A Generic Segmental Analysis of all types of RC Members

Phillip Visintin

B.E. Civil & Structural Engineering (Hons)

Thesis submitted for the degree of Doctor of

Philosophy at The University of Adelaide

(The School of Civil, Environmental and

Mining Engineering)

Australia

-March 2012-

Contents

Abstract

This thesis contains a series of journal papers in which a new segmental moment-rotation (M/θ) approach is developed for both instantaneous and long term loading. The analysis technique is based on the starting position of moment-rotation rather than moment-curvature and the assumption that plane sections remain plane, but not on the often applied corollary of a linear strain profile. Using the well-established mechanics of partial-interaction theory, the M/θ approach simulates the formation and gradual widening of cracks as well as tension stiffening, as the reinforcement slips relative to the concrete which encases it, and, using the mechanics of shear-friction theory, the approach simulates the formation and failure of concrete softening wedges. Moreover, being mechanics based, the M/θ approach can in theory be applied to any type of member, that is any cross section, with any concrete properties, and any reinforcement type with any bond characteristic. Hence using partial-interaction and shear friction theories, the M/θ approach obviates the need for both empirically derived effective flexural rigidities and hinge lengths. This leads to the establishment of a new equivalent flexural rigidity that accounts for both concrete cracking and concrete softening and can be applied to both instantaneous and long term loading.

Having established the equivalent flexural rigidity from segments of a member, it can then be used to predict the effective flexural rigidity of an entire member, and hence the load deflection behaviour through the application of a numerical segmental analysis procedure. It is further shown that with simplifying assumptions closed form solutions to describe the equivalent flexural rigidity of a segment can be obtained and member deflections described using standard analysis techniques.

Having established that the M/θ technique can be applied using both numerical and closed form solutions, it is used to predict a broad range of reinforced concrete behaviours. These behaviours include: the instantaneous deflection of beams reinforced with both ductile steel and brittle fiber reinforced polymer bars and the instantaneous deflection of laterally and eccentrically loaded columns, including those in which second order effects are considerable and the long term deflection of simply supported beams. Through these broad applications, it is shown that the M/θ approach represents a mechanics based solution to reinforced concrete analysis, capable of accurately predicting both instantaneous and long term deflections from serviceability through to peak loading and collapse, where the only empirically derived requirements are material properties. Hence, the M/θ approach can be considered an extension of traditional analysis techniques in that it removes the need to empirically define effective flexural rigidities and hinge lengths to determine member behaviour.

Statement of Originality

This work contains no material which has been accepted for the award of any other degree or diploma in any university or any tertiary institution to Phillip Visintin and, to the best of my knowledge and belief, contains no material previously published or written by another person, except where due reference has been made in the text.

I give consent to this copy of my thesis when deposited in the University Library, being made available for load and photocopying, subject to the provisions of the Copyright Act 1968.

The author acknowledges that copyright of published works contained within this thesis (as listed below) resides with the copyright holder(s) of those works.

I also give permission for the digital version of my thesis to be made available on the web, via the University's digital research repository, the Library catalogue, the Australasian Digital Theses Program (ADTP) and also through web search engines, unless permission has been granted by the University to restrict access for a period of time.

…… ……..……

Phillip Visintin Date

List of Publications

Oehlers, D.J., Mohamed Ali M.S., Haskett, M., Lucas, W., Muhamad, R., and Visintin, P., (2011) "FRP reinforced concrete beams – a unified approach based on IC theory". *ASCE Composites for Construction*, May/June, Vol. 15, No. 3, pp293-303.

Visintin, P., Oehlers, D.J., Wu, C., and Haskett, M., (2012) "A mechanics solution for hinges in RC beams with multiple cracks". *Engineering Structures*, Vol. 36, pp 61-69.

Visintin, P., Oehlers, D.J., Wu, C., and Haskett, M., (2012) "A Mechanics Based Hinge Analysis for Reinforced Concrete Columns". Submitted to *Journal of Structural Engineering*

Visintin, P. Oehlers, D.J., Wu, C. and Griffith, M.C., (2012) "The Reinforcement Contribution to the Cyclic Behaviour of Reinforced Concrete Beam Hinges". Accepted for publication in *Earthquake Engineering and Structural Dynamics*.

Haskett, M., Oehlers, D.J., Visintin, P., Ali Mohamed, M.S., (2012) "Using shear-friction properties to simulate concrete softening in reinforced concrete flexural members" Submitted to: *Cement and Concrete Research*

Visintin, P., Oehlers, D.J., Haskett, M., Wu, C and Chen JF., (2012) "A moment-rotation approach for analysing the behaviour of RC columns". Submitted to *Computers and Structures*.

Visintin, P, Oehlers, D.J., Haskett M., (2013) "Partial-interaction time dependent behaviour of reinforced concrete beams". Submitted to *Magazine of Concrete Research.*

Visintin, P., Oehlers, D.J. Muhamad, R. and Wu, C. (2012) "Partial-interaction short term serviceability deflection of FRP RC beams". Submitted to *Engineering Structures.*

Oehlers, D.J., Visintin, P., Haskett, M. and Sebastian, W., (2013) "The fundamental mechanisms that govern the flexural ductility of all RC members". Invited paper for *Construction and Building Materials.*

Acknowledgements

My sincerest thanks go to Professor Deric Oehlers; this thesis owes much to his passion for research and knowledge of all things related to reinforced concrete.

I would also like to thank Dr Chengqing Wu and Professor Mike Griffith for their input and guidance when this research crossed into the area of their expertise.

Finally, thanks go to those friends, who despite having no idea what I've been working on, have managed to offer tremendous encouragement and motivation.

Introduction and General Overview

Current analysis techniques for the flexural analysis of reinforced concrete (RC) members are based on a full-interaction (FI) moment-curvature (M/χ) technique which assumes plane sections remain plane at all cross sections as well as the corollary of a linear strain profile. These assumptions mean that the M/χ approach cannot simulate what is seen in practice, that is, the formation and widening of cracks as the reinforcement slips relative to the concrete which surrounds it, and the formation and failure of concrete softening wedges. Consequently, the FI M/χ approach relies on empirically derived effective flexural rigidities and hinge lengths in order to determine member deflection. Being empirically derived, these should in theory only be applied within the bounds of the tests from which they were calibrated, and hence the FI M/χ approach requires large scale testing prior to its application to new materials, such as has been the case with the introduction of brittle FRP reinforcement.

In this work, an alternative analysis technique: the partial-interaction (PI) moment-rotation (M/θ) approach is developed. The approach is based on the starting position of moment-rotation rather than moment-curvature and the assumption that plane sections remain plane, but not the corollary of a linear strain profile. Using the well-established mechanics of partial-interaction theory, the formation and gradual widening of cracks as the reinforcement slips relative to the concrete which encases it is simulated, and, using the mechanics of shear-friction theory, formation and failure of concrete softening wedges is considered. Being entirely mechanics based, the PI M/θ approach can therefore in theory be applied to any type of member, that is any cross section, with any concrete properties, and any reinforcement type with any bond characteristic. Hence, using partial-interaction and shear-friction theories, the PI M/θ approach obviates the need for both empirically derived effective flexural rigidities and hinge lengths required for the FI M/χ approach. Moreover, the application of this approach has lead to the establishment of a new mechanics based equivalent flexural rigidity, which accounts for both concrete cracking and concrete softening and can be applied to both instantaneous and long term loading.

This thesis contains a collection of manuscripts published, accepted or submitted to internationally recognised journals. Each of the chapters 1-3, which are titled according to the research objective, contain: an introduction explaining the aim of the chapter and how the work fits into the overall objective; a list of manuscripts contained within the chapter; and finally the presentation of each manuscript.

Chapter 1 provides background information on the current methods applied to the design of RC beams and details the alternative single crack PI M/θ approach. This approach can be applied to members where it is known that a weak bond exists between the reinforcement and

the surrounding concrete or as a reliable lower bounds approximation to the analysis of all members.

Chapter 2 contains four journal papers which show how the PI M/θ approach can be used to derive cross-section behaviour or properties such as flexural rigidities. The first two of these papers develop the segmental PI M/θ approach, which is the major focus of this thesis, for the analysis of reinforced concrete beams and columns. The segmental approach is different from the single crack approach in that it simulates the partial interaction tension stiffening which takes place between a pair of cracks. The segmental approach is therefore more applicable to members in which a strong bond forms between the reinforcement and the concrete, and in which the moment gradient is shallow, the extremity of which would be a constant moment region. Importantly, these two papers outline the development of a new cross sectional equivalent flexural rigidity which can be used to predict member deflection using standard analysis techniques. The third paper covers the development of shear friction material properties which are required to carry out a M/θ analysis to failure, and finally, the fourth paper describes the development of a numerical partial-interaction approach which allows for load reversals and hence for analysis of the cyclic load case.

Chapter 3 then focuses on the use of the equivalent flexural rigidity derived in Chapter 2 to describe member behaviour. The first paper in this chapter applies the segmental PI M/θ approach to both laterally and eccentrically loaded columns where second order effects are significant, and it is shown that the approach can accurately simulate the load-deflection behaviour from serviceability to peak loading and through to collapse. The second and third publications in this chapter focus on the serviceability behaviour of reinforced concrete beams; they outline an extension of the segmental PI M/θ approach to allow for concrete shrinkage and creep, as well as the development of closed form flexural rigidity and deflection equations. Finally the fourth publication brings together the single crack and segmental PI M/θ approaches, showing how they can be used in conjunction to quantify, entirely through mechanics, the deflection of members at all limit states, as well as to quantify moment redistribution and energy absorption throughout.

Chapter 1 – Background

Introduction

This chapter contains the paper "FRP reinforced concrete beams – a unified approach based on IC theory" which provides background information on the fundamental mechanisms used throughout the remainder of this thesis as well as inducing the single crack M/θ approach. Significantly, it will be shown that the M/θ approach, through the use of mechanics, simulates what is observed in practice and hence can be used to develop numerical and closed-form models for: moment-rotation and confinement; crack widths, crack spacings and deflections; moment redistribution and energy absorption; the stirrup and concrete component of shear failure; and the effect of fibers in concrete. Being mechanics based it is also shown that the approach is generic and therefore can in theory be applied to any concrete or reinforcement, type.

List of manuscripts

Oehlers, D.J., Mohamed Ali M.S., Haskett, M., Lucas, W., Muhamad, R., and Visintin, P., (2011) "FRP reinforced concrete beams – a unified approach based on IC theory". *ASCE Composites for Construction* , May/June, Vol. 15, No. 3, pp293-303.

Statement of Authorship

FRP reinforced concrete beams – a unified approach based on IC theory
ASCE Composites for Construction 2011, May/June, Vol. 15, No. 3, pp293-303.

Oehlers, D.J.

Supervised research and wrote paper.

I hereby certify that the statement of contribution is accurate and I give permission for the inclusion of the paper in the thesis

Signed……..Date……

Mohamed Ali, M.S.

Contributed and supervised research.

I hereby certify that the statement of contribution is accurate and I give permission for the inclusion of the paper in the thesis

Signed…….Date……

Haskett, M

Contributed to moment redistribution and energy absorption research and assisted in manuscript evaluation.

I hereby certify that the statement of contribution is accurate and I give permission for the inclusion of the paper in the thesis

Signed…….Date……

Lucas, W

Contributed to shear loading research and assisted in manuscript evaluation.

I hereby certify that the statement of contribution is accurate and I give permission for the inclusion of the paper in the thesis

Muhamad, R

Contributed to crack spacing and deflection research and assisted in manuscript evaluation.

I hereby certify that the statement of contribution is accurate and I give permission for the inclusion of the paper in the thesis

Signed… ……Date……..

Visintin, P (candidate)

Contributed to confinement research, performed confinement analysis and assisted in manuscript evaluation.

I hereby certify that the statement of contribution is accurate

Signed……Date……

FRP reinforced concrete beams – a unified approach based on IC theory

Deric John Oehlers, Mohamed Ali M.S., Matthew Haskett, Wade Lucas, Rahimah Muhamad and Phillip Visintin

ABSTRACT

In general, steel reinforced concrete deals with a ductile steel material and a very strong and ductile bond between the steel reinforcement and concrete, so that debonding rarely governs the design. In contrast, FRP reinforcement is a brittle material with a weak and brittle bond so that debonding is a major issue. Consequently, there has been an extensive amount of research on FRP debonding and in particular intermediate crack (IC) debonding. This paper shows that the very good research by the FRP research community on the mechanics of IC debonding can be applied to a wide range of apparently disparate reinforced concrete behaviours to produce a unified approach. Hence a single mechanism, or unified approach, based on IC debonding is proposed in this paper for dealing with moment rotation, tension stiffening and deflections, member ductility and moment redistribution, shear capacity, confinement, and fibre concrete for FRP RC beams.

Keywords: FRP; reinforced concrete beams; moment rotation; tension stiffening; deflection; ductility; moment redistribution; shear capacity; confinement; and fibre concrete.

INTRODUCTION

There has been an extensive amount of research over the past twenty years on FRP reinforced concrete (fib 2001; Teng et al 2002; Oehlers and Seracino 2004; Oehlers et al 2008a; ACI 2008) which has encompassed the seemingly disparate problems of flexure, shear, moment redistribution, ductility, confinement and fibre concrete. It is shown in this paper that these apparently disparate behaviours can be modelled using a *unified approach* that is based on a partial-interaction (that is interface slip between the reinforcement and its surrounding concrete) structural mechanics mechanism that uses IC debonding as its main cornerstone. However, the model is not only concerned with the ultimate limit of IC debonding but also the partial-interaction (PI) behaviour (interface slip) from the commencement of crack widening to debonding which will be referred to as *IC theory*.

The philosophy behind this *unified approach* is first described. It is then shown that central to this new model is the *discrete rotation* that occurs through crack widening at each individual crack and that crack widening is due to slip between the reinforcement and concrete that is *IC theory*. Furthermore, that *IC theory* and its associated *discrete rotation* can be used to develop structural mechanics numerical and closed form models not only for (i) moment

rotation but also for: (ii) crack spacings, crack widths and subsequently tension stiffening and member deflections; (iii) moment redistribution and the ability of a member to absorb energy; (iv) the shear deformation and capacity of a reinforced concrete (RC) member, where it is shown that shear failure is simply a limit to the moment rotation behaviour and not an alternative mechanism; (v) quantifying the confinement forces due to stirrups and wraps; and for (vi) quantifying the effect of fibres in concrete.

In general, civil engineering research comprises the following steps. (1) The development of the *mechanics model* to simulate the mechanism being studied. (2) The *qualitative validation* of the mechanics model to show that it physically simulates the mechanism being studied that is it physically simulates what may be seen in practice; as an example, it may be necessary to show that the mechanics model has the ability to simulate crack development and spacings or to simulate rotations. This is followed by (3) the *quantitative calibration* of the mechanics model to ensure that the magnitudes predicted by the mechanics model are close to those determined by tests; for example this could be done by changing the coefficients or material properties used in the mechanics model. And finally, there is (4) the development of the *design rules*; these could be the direct use of the mechanics model, which would generally has a wide application, or the development of simple and more convenient design approaches from parametric studies using the mechanics models, which have a limited width of application within the bounds f the parametric study. It is felt that developing a mechanics model that closely simulates the actual behavior of the mechanism being studied (that is steps (1) and (2) and which is the thrust of this paper) is important in research as it should be easier to calibrate and to develop design rules (that is steps (3) and (4)). The aim of this paper is to qualitatively illustrate the *IC theory* structural mechanics mechanisms of this new *unified approach* for FRP reinforced concrete, that is Steps (1) and (2), and not to quantify the behaviour, that is Steps (3) and (4), which is given elsewhere in referenced published papers.

PHILOSOPHY BEHIND UNIFIED APPROACH

A two span continuous beam that had originally been plated with FRP externally bonded (EB) tension face plates that have now debonded is shown in Fig. 1. A reinforced concrete beam can be considered to consist of undisturbed regions between cracks and disturbed regions at each individual crack.

The philosophy behind the *unified approach* is that the behaviour of reinforced concrete beams as in Fig. 2(a) can be separated into: undisturbed regions between cracks where linear strain profiles govern as in Fig. 2(b); and disturbed regions at each individual crack where discrete rotations occur through linear rigid body displacements as in Fig. 2(c). The deformation of the undisturbed regions is governed by elementary and well understood and documented fundamental full-interaction (that is no slip between the reinforcement and its

adjacent concrete) moment-curvature (M/χ) analyses (Oehlers and Seracino 2004; Oehlers 2007). This full-interaction (FI) analysis is based on Bernoulli's linear strain profiles where integration of the curvature along the beam, as in Fig. 2(b), can lead to continuity of rotations and deflections along the beam. In contrast, the deformation of a disturbed region is governed by a discrete rotation, that is a sudden change in rotation, that is directly proportional to the crack width at the level of the longitudinal reinforcement as shown in Fig. 2(c). In this case, the crack width is simply the partial-interaction (PI) slip between the longitudinal reinforcement and the concrete at each crack face and which is governed by *IC theory*. Hence, full-interaction (FI) analyses apply in undisturbed regions and partial-interaction (PI) analyses apply in disturbed regions.

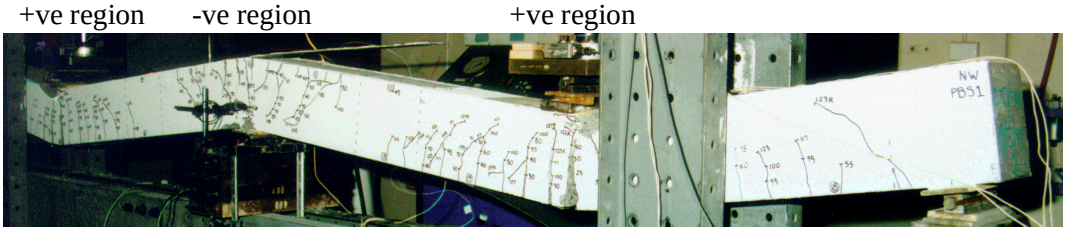

Fig. 1. Two span FRP EB plated continuous beam

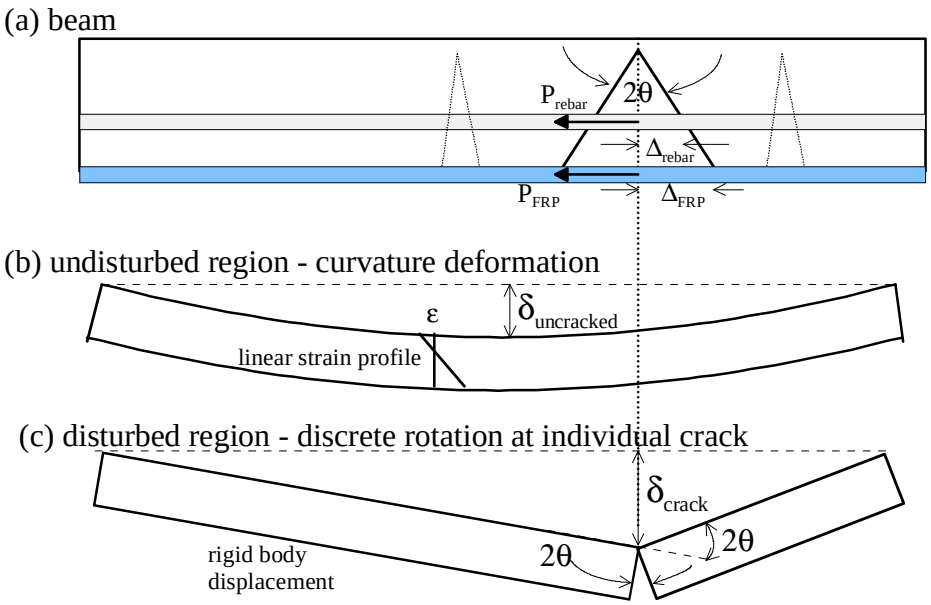

Fig. 2. Unified approach philosophy

It is the *discrete rotation* at each individual crack, that is governed by *IC theory*, which is central to this unified approach. The concept of hinge rotation is fundamental to understanding the behaviour of RC beams as it governs the ability to deform and redistribute moment and absorb energy. It can be seen in Fig. 1 that the rotation of the so called hinge in

the –ve or hogging region and the ‘hinge’ in the +ve or sagging region can comprise of numerous discrete rotations at each individual crack within the hinge region. However, yielding of any steel reinforcement can cause much of the rotation to be concentrated at an individual crack as in the +ve region in Figs. 1 and 2 and also at the crack in the fibre concrete beam in Fig. 3 that had been subjected to blast loads (Wu et al. 2007).

DISCRETE ROTATION AT EACH INDIVIDUAL CRACK

The components required for a discrete rotation at an individual crack are shown in Fig. 3. Even though the crack faces in the tension zone may be non-linear, flexure causes the crack faces to separate so that there is a linear variation in crack width from the soffit to the apex of the crack. To accommodate the crack width and further crack widening, slip must occur between the reinforcement and concrete; this is an absolutely essential prerequisite as straining or yielding of the reinforcement does not by itself widen a crack as this would require infinite strains. Furthermore, if the compressive forces in the concrete are large enough, wedges can form which can slide off to cause failure. These deformations form the basis for the discrete rotation model which is illustrated in Fig. 4. The discrete rotation model or mechanism in Fig. 4 is based on the following three well researched fundamental principals: rigid body displacements; shear friction or aggregate interlock; and *IC theory*.

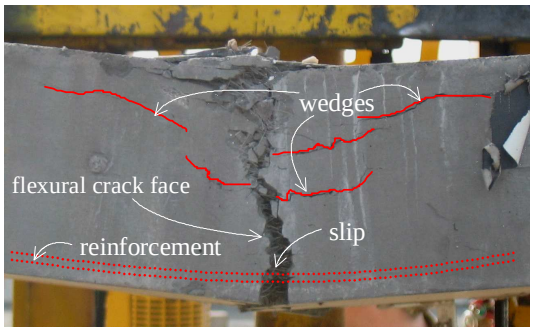

Fig. 3. Discrete rotation at a single crack

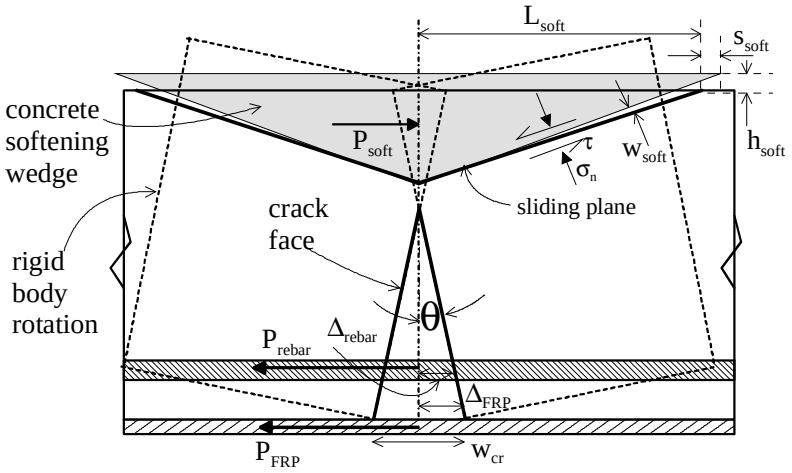

Fig. 4. Discrete-rotation mechanism

The opening of the vertical crack in Fig. 4 consists of two rigid bodies rotating as shown and, hence, is an example of a rigid body displacement. This rigid body rotation can also cause the wedges to slide across the sliding planes a distance s_{soft} and to separate across the sliding plane by *w* through aggregate interlock such as by w_{soft}; this relative movement between the softening wedge and the adjacent beam concrete is also an example of a rigid body displacement. Shear friction or aggregate interlock research simply quantifies the rigid body displacements and stresses across a sliding plane as shown in Fig. 5. Shear friction research is the relationship at a specific point in the sliding plane between the normal stress across the sliding plane σ_n, the shear stress across the sliding plane τ, and the rigid body slip and separation δ and *w*. These shear friction properties (σ_n, τ, δ and *w*) and their limits or capacities have been quantified for initially cracked interfaces (Mattock and Hawkins 1972; Walraven 1981; Walraven et al 1987; Haskett et al 2010a) such as across the flexural crack in Fig. 4 when subjected to shear, and also for initially uncracked interfaces (Mattock and Hawkins 1972; Haskett et al 2010a) such as at the wedge interface shown in Fig. 4 and also across the vertical plane in the compression zone above the crack when subjected to shear forces.

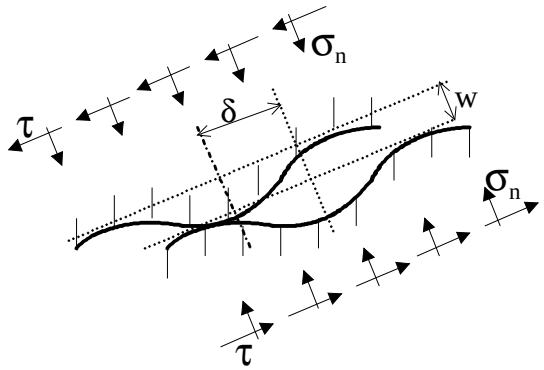

Fig. 5. Shear friction components

The third component of the discrete rotation model in Fig. 4 is the partial-interaction between the reinforcement and the concrete, that is *IC theory*, which allows the reinforcement to slip relative the crack face Δ and without which the crack could not open or widen. It is the relationship between the force and slip in the reinforcement at the crack face, shown as P and Δ in Fig. 4.

IC THEORY

Figure 6 is an example of intermediate crack (IC) debonding for a near surface mounted (NSM) FRP plate. IC debonding may be defined as when there is sufficient separation of the reinforcement from the concrete to cause a reduction in the reinforcement strain. IC debonding deals with debonding of reinforcement that intercepts a crack due to stress concentrations that occur due to the sudden discontinuity between the reinforcement and the concrete at the crack face. We will define *IC theory* as not only what is happening at IC debonding but what is happening from the onset of the intermediate crack and its interception of the reinforcement all the way through to IC debonding.

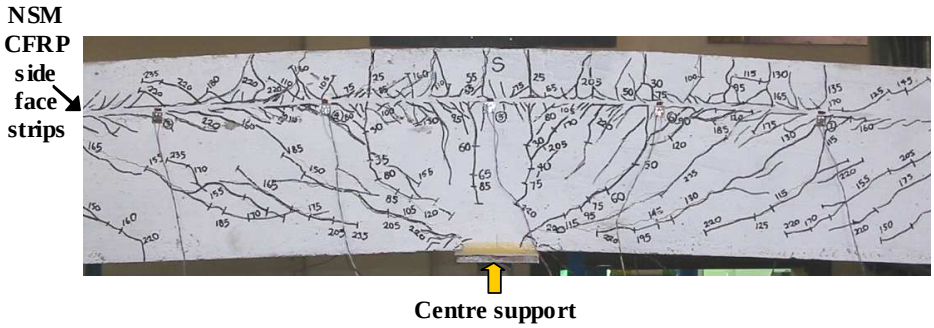

Fig. 6. IC debonding of FRP NSM side plate

Central to IC debonding and *IC theory* is the material bond characteristics between the reinforcement and the concrete (De Lorenzis et al 2002; Lu et al 2005; Dai et al 2005; Seracino et al 2007; Haskett et al 2008; Rashid et al 2008; Oehlers et al 2008b; Eligehausen et al 1983; Malvar 1995, Harajli et al 2004) that is the shear-stress/slip (τ-δ) relationship. Examples of idealised bond-slip characteristics are show in Fig. 7 where: the peak shear stress τ_f occurs at a slip δ_1; and δ_f is the peak slip beyond which the shear stress can be assumed to be zero. It is these τ-δ bond-slip characteristics that allow *IC theory* to be developed as it allows the variation of slip along the reinforcement, that is the partial-interaction behaviour to be quantified which is the essence of *IC theory*. The fundamental characteristics of *IC theory* is illustrated in the following numerical simulation that uses a shooting approach. A shooting approach is useful as it incorporates all the structural mechanics principles and boundary conditions required to find a solution which,

consequently, can also be used to develop closed form structural mechanics solutions for *IC theory*.

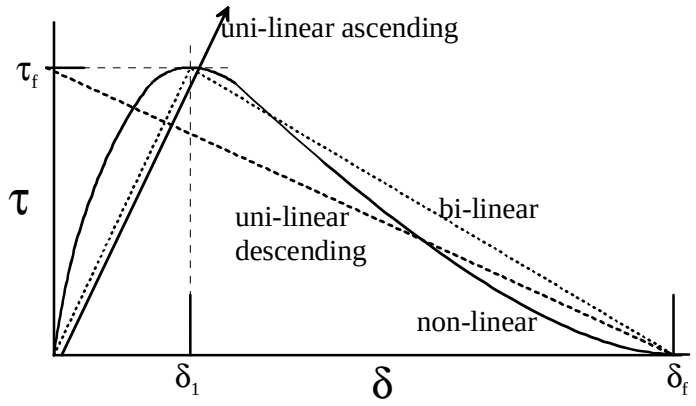

Fig. 7. Bond-slip characteristics

A numerical simulation of partial-interaction *IC theory* (Haskett et al 2008) is illustrated in Fig. 8 for the case of a reinforcing bar (which can have any material property) of cross-sectional area A_r which is being pulled out with a force P_{r1} from a restrained concrete block of cross-sectional area A_c such that P_{r1} equals P_{c1}. This simulates a standard test that is used to directly measure the bond-slip characteristics of FRP or steel reinforcement (Haskett et al 2008). To understand the behaviour, the pull-test is sliced into very fine segments of length L_s such that L_s is much less than the length of the reinforcement L_r. Each segment is shown separated so that the forces between segments can be inserted and, furthermore, shear lag is ignored so that the strain in the concrete is uniform over a cross-sectional area A_c.

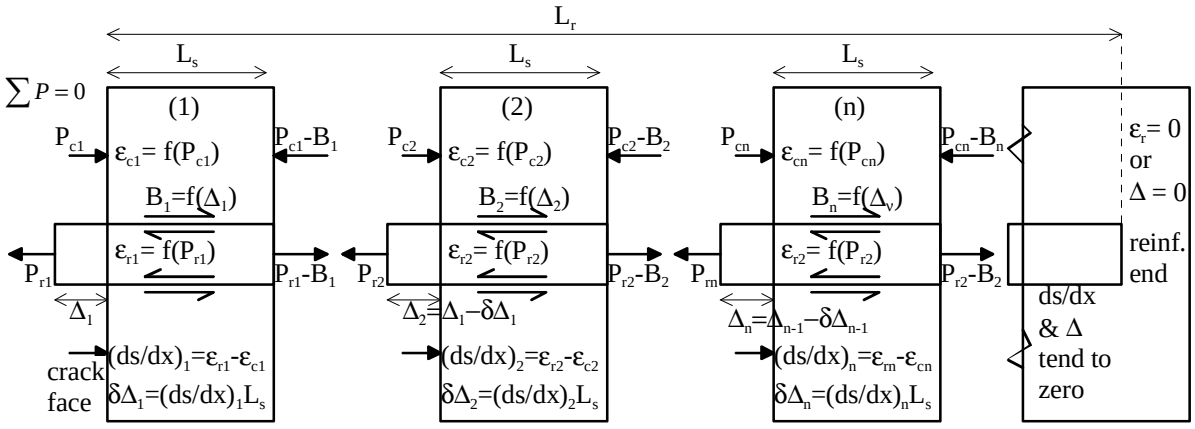

Fig. 8. IC theory numerical simulation of pull-test

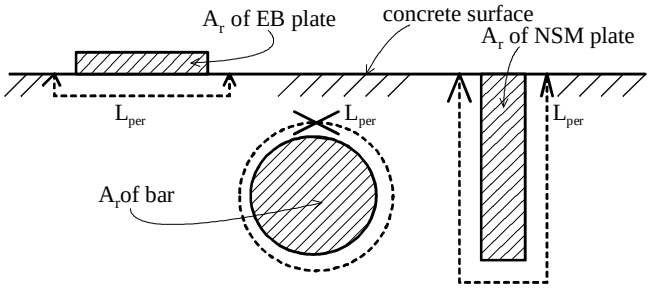

Fig. 9 IC debonding failure planes

At the crack face in Fig. 8: the bar slips Δ_1; the reinforcement strain is ε_{r1} which is a function of P_{r1}; the concrete strain is ε_{c1} which is a function of P_{c1}; the algebraic summation of P_{r1} and P_{c1} is zero; the slip-strain $(ds/dx)_1$ is ε_{r1}-ε_{c1}; and the bond stress is τ_1 which is a function of Δ_1 from the material bond-slip relationship such as in Fig. 7. For very thin segment lengths L_s: the bond force B_n in segment (1) is very close to $\tau_n L_{per} L_s$ where L_{per} is the width of the failure plane encompassing the reinforcement as shown in Fig. 9 (Seracino et al 2007; Haskett et al 2008; Oehlers et al 2008b; Rashid et al 2008); the change in slip within a segment $\delta\Delta_n$ in Fig. 8 is close to $(ds/dx)_n L_s$; so that the slip in segment n that is Δ_n is Δ_{n-1}-$\delta\Delta_{n-1}$. Hence the variation along the reinforcement of the slip (Δ), slip-strain (ds/dx), and strains ε_r and ε_c can be determined. Any of the following three boundary conditions can govern the behaviour. For long lengths of reinforcement L_r, full interaction conditions, that is both the slip-strain (ds/dx) and slip (Δ) tend to zero at the same section and before the end of the reinforcement at L_r. For short reinforcing bars anchored at L_r such as may occur at a bend in the reinforcement, the boundary condition at L_r is $\Delta = 0$. And for short reinforcing bars not anchored at L_r but free, the boundary condition at L_r is $\varepsilon_{r1} = 0$. In general, an iterative shooting approach is used to find a solution (Haskett et al 2008). These structural mechanics fundamental principles illustrated in this numerical analysis are the basis of *IC theory*.

The partial-interaction numerical solution described above has been applied in Fig. 10 to the analysis of a pull-test in which an EB plate has been bonded to a concrete prism. In this case, the bi-linear bond-slip relationship in Fig. 7 has been used (Yuan et al 2004; Mohamed Ali M.S. 2008; Haskett et al 2008). The variation in the bond stress along the reinforcement as the slip at the crack face Δ_1 is gradually extended is shown in Figs. 10(a) –(c). Figure 10(a) shows the distribution of shear stress (τ) at the start of loading where the full interaction boundary condition governs and Fig. 10(c) shows debonding where the unrestrained plate end boundary condition governs as shown. Often the cross-sectional area of the concrete A_c is several orders of magnitude greater than that of the reinforcement A_r so that the strains in the concrete in the numerical simulation in Fig. 8 can be ignored.

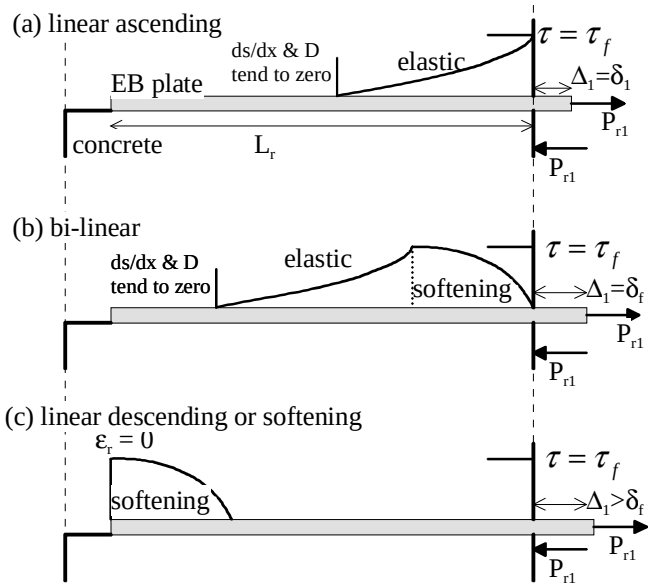

Fig. 10. Variation of shear stress in a pull test

Having defined the behaviour and boundary conditions such as in Fig. 10, this *IC theory* procedure can be used to develop closed form solutions for a variety of bond-slip relationships and reinforcement material properties (Muhamad et al 2010). For example, the following equation uses the linear descending bond-slip relationship in Fig. 7 for any elastic reinforcement such as FRP or for steel prior to yield

$$P_r = \frac{\tau_f L_{per}}{\lambda_1} \sin\left\{\arccos\left\{\frac{\delta_f - \Delta_{reinf}}{\delta_f}\right\}\right\} \tag{1}$$

where

$$\lambda_1 = \sqrt{\frac{\tau_f L_{per}}{\delta_f (AE)_r}} \tag{2}$$

and where E_r is the Young's modulus of the reinforcement. The P/Δ relationship from *IC theory* can now be used in the hinge model in Fig. 4 to determine the moment rotation relationship of a given reinforced concrete section.

MOMENT DISCRETE-ROTATION

The rigid body deformations shown in Fig. 4 are brought together in the analytically convenient form in Fig. 11 (Haskett et al 2008; Oehlers et al 2008c; Oehlers et al 2009; Haskett et al 2009a; Haskett et al 2009b; Haskett et al 2009c). The position of the neutral

axis at level C can be determined from standard well established procedures. For example at serviceability, the neutral axis can be determined from the elastic analysis of the transformed cracked section. At the ultimate limit state the neutral axis can be determined from rectangular stress blocks and the well known gamma factor given in national codes and standards which also give the positions of the compressive forces. It can be seen that once the position of the neutral axis is established, the discrete rotation θ in the tension zone is directly proportional to the reinforcement slip Δ or, inversely, for a given rotation θ the tensile reinforcement forces P can be determined from IC theory as Δ is known. And consequently the moment M for that rotation θ.

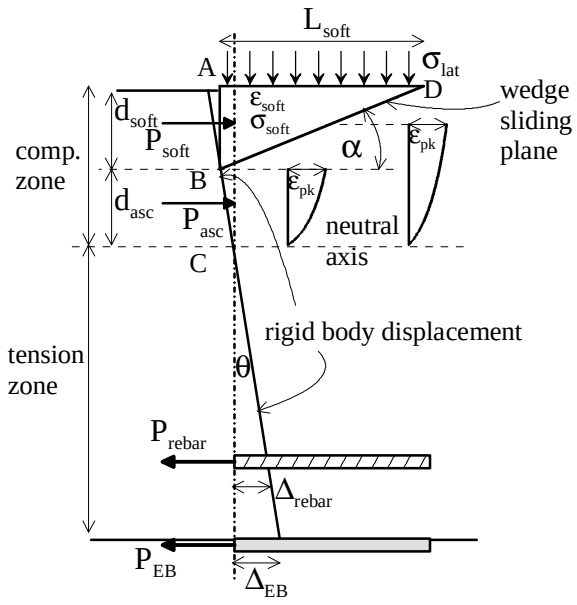

Fig. 11. Moment/discrete-rotation analysis

If the compression zone in Fig. 11 is unlikely to limit the rotation by compression failure (such as might occur in shallow slabs where the wedges or unlikely to slide or in reinforced concrete beams made with fibre concrete as fibre concrete is known to be highly ductile in compression) then the above analysis that is based solely on *IC theory* and rigid body displacements will suffice to give the moment/discrete-rotation. This is depicted in Fig. 12 where the limits to the rotation are at either tension reinforcement fracture or debonding. However sliding failure of the compression wedge, as in the eccentrically loaded prism in Fig. 13 that is used to directly study concrete softening (Daniell et al 2008; Mohamed Ali M.S. et al 2010), can often precede reinforcement failure in beams that have normal concrete. In this case, it is necessary to directly link the rigid body deformations in the tension and compression zones in Fig. 11 as the rectangular stress block approach cannot predict the rigid body displacement at failure of the compression zone as it is strain based and not displacement based.

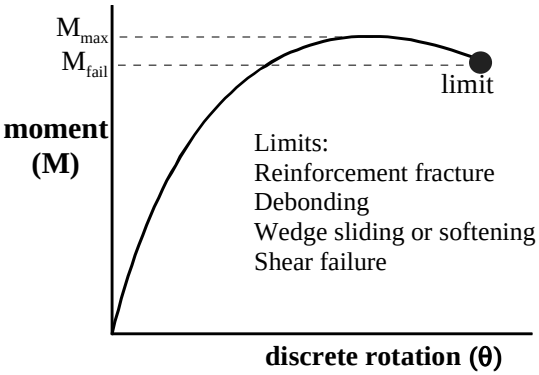

Fig. 12. Moment/discrete rotation

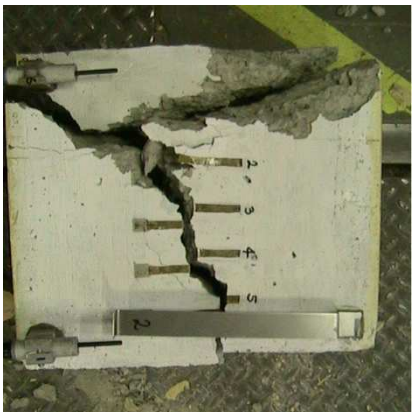

Fig. 13. Sliding failure of wedge

The concrete in the compression zone in Fig. 11 has two components. Immediately above the crack apex from C to B (below the sliding plane B-D) the concrete is in the ascending portion of its material stress-strain relationship which has a strain of ε_{pk} at its peak stress prior to softening as shown (Haskett et al 2009a). Hence immediately below and adjacent to the sliding plane and over the length of the wedge L_{soft} the concrete strain is ε_{pk}. Above the sliding plane B-D, the concrete is softening as depicted by the wedge (Haskett et al 2009a; Mohamed Ali M.S. et al 2010). In this softening region, the force P_{soft} that a wedge of depth d_{soft} can resist has been found to depend on the Mohr Coulomb cohesive, *c*, and frictional, *m*, components of the concrete (Mattock et al 1972; Mattock 1974; Haskett et al 2009a; Mohamed Ali M.S. et al 2010) and is given by the following equation.

$$P_{soft} = d_{soft} b_{soft} \frac{c + \sigma_{lat} \cos\alpha(\sin\alpha + m\cos\alpha)}{\sin\alpha(\cos\alpha - m\sin\alpha)} \quad (3)$$

where the angle of the wedge α in both Eq. 3 and Fig. 11 is also a function of *m* and σ_{lat} is any lateral restraint imposed on the wedge which is discussed in the next section on confinement.

The slip *s* along the wedge interface or sliding plane in Fig. 4 varies from zero above the vertical crack to s_{soft} at the end of the wedge. As P_{soft} in Fig. 11 is known for a given d_{soft} so to is the stress in the wedge σ_{soft} and from the ascending portion of the concrete stress-strain relationship the strain in the wedge ε_{soft}. Hence from the slip-strain across the sliding plane ε_{pk}- ε_{soft}, the maximum slip s_{soft} can be determined from $(\varepsilon_{pk}- \varepsilon_{soft})L_{soft}$. For analytical considerations, this rigid body displacement s_{soft} is shown as point B in Fig. 11 and in line with the rigid body displacement of the crack face. Hence the rigid body displacement in the compression zone has now been linked to that in the tension zone so that the limit to the discrete rotation due to wedge sliding can also be incorporated in Fig. 12. There is one other limit to the discrete rotation which is labeled 'shear failure' in Fig. 12 which will be discussed later and where it will be shown that the shear capacity is directly related to the discrete-rotation and *IC theory*.

Having now defined the discrete rotation as a function of both the softening wedge in the compression zone and *IC theory* in the tension zone it is now possible to derive closed form solutions. For example, for the following conditions (one level of reinforcement of area A_r which is at a distance h_1 from the crack apex and d_1 from the resultant compressive force; for a linear descending bond-slip characteristic as in Fig. 7; and for a linear elastic material at fracture such as FRP), the moment (M_f) and rotation (θ_f) at fracture is given by Eqs. 4 and 5:

$$M_f = A_r f_f d_1 \tag{4}$$

where f_f is the fracture stress

$$\theta_f = \frac{\delta_f}{h_1}\left(1-\sqrt{1-\frac{A_r f_f \varepsilon_f}{L_{per}\tau_f \delta_f}}\right) \tag{5}$$

and where ε_f is the fracture strain.

CONCRETE CONFINEMENT ON MOMENT/DISCRETE-ROTATION

It is well known that FRP confinement of concrete in cylinders and prisms can increase the concrete ductility (Fam and Rizkalla 2001; Lam and Teng 2004; Griffith et al 2005; Wu et al 2006) which in turn can increase the ductility or rotation capacity of a member (Wu et al 2006; Haskett et al 2008). To illustrate the confinement mechanism that increases the member ductility, let us consider the beam in Fig. 14(a) which is wrapped externally with

FRP and confined internally with stirrups as in Fig. 14(c). The same discrete hinge mechanism as in Fig. 4 occurs in this wrapped member as shown in Fig. 14(b).

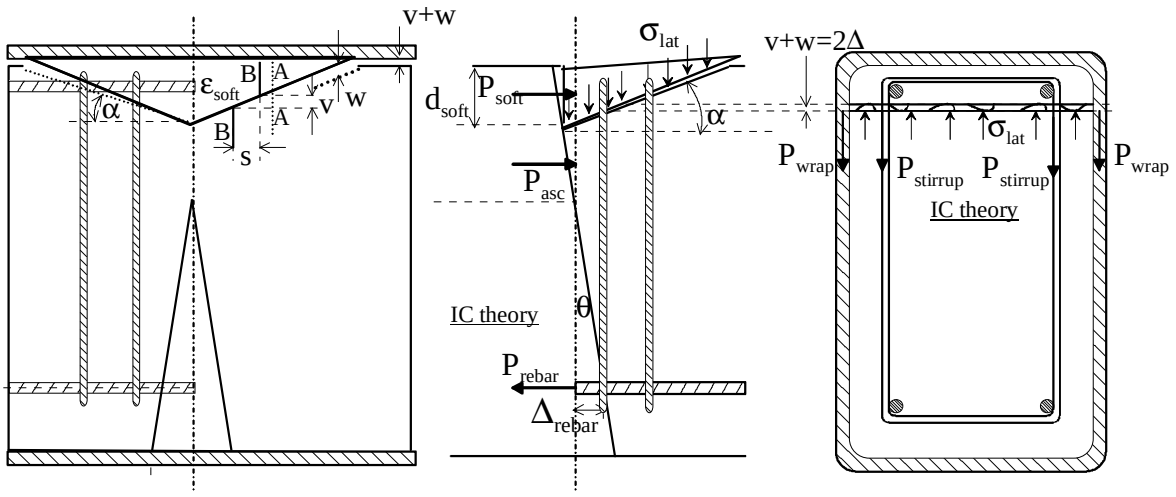

(a) wedge restraints (b) wedge deformation (c) IC wedge confinement

Fig. 14 Confinement mechanism

Let us consider the line A-A in Fig. 14(a) that is drawn prior to sliding. After sliding, line A-A moves to the two lines, shown as B-B with a slip separation *s*; the separation *s* is due to the different strains in the concrete above and below the sliding plane. For a smooth sliding plane interface, this slip *s* causes a vertical separation *v* as shown which depends on the angle of the wedge α. However, there is also a further vertical separation *w* induced by the slip *s* due to aggregate interlock as shown in Fig. 5 which can be quantified through the shear friction properties, σ_n, τ, δ and *w*, (Mattock et al 1972; Haskett et al 2010a; Mohamed Ali M.S. et al 2010). Hence, the wedge rises at a section by *v*+*w* (Farrall et al 2008) as shown in Fig. 14(a). The wedge interface is simply an intermediate crack and, therefore, for a given separation (*v*+*w*) as in Figs. 14(a) and (c), *IC theory* can be used to determine the forces P in the wrap and in the stirrups which induces the lateral confinement σ_{lat} across the sliding plane. From shear-friction research (Mattock et al 1972; Jensen 1975; Haskett et al 2010a; Mohamed Ali M.S. et al 2010), this lateral confinement σ_{lat} can not only increase the force in the wedge P_{soft} in Fig. 14(b) as shown in Eq. 3 but it also suppresses sliding, s_{soft} in Fig. 14(b) and consequently sliding failure.

It is this suppression of the sliding failure in the moment/discrete-rotation response in Fig. 12 that can make the beam more ductile, that is it can rotate more without an increase in flexural strength. This increase in ductility is indicated in the analysis depicted in Fig. 14(b) where no axial forces are attributed to the wrap. It can now be seen that *IC theory* not only controls the behaviour in the tensile zone in Fig. 14(b) but also the confinement forces in the compression zone. Furthermore, that shear-friction properties and limits are required to quantify the movements and, therefore, the *IC theory* forces. And that the third prerequisite of rigid body

displacements are required to simulate the deformations in both the tension and compression zones to which *IC theory* can be applied. In short, the unified approach is based on three fundamental prerequisites: *IC theory*, *shear-friction* and *rigid-body-displacements*.

CRACK SPACINGS, WIDTHS AND DEFLECTIONS

Having illustrated how *IC theory* is central to the discrete rotation at a single crack, let us now consider multiple cracks as in the hinge vicinities in Fig. 1. A positive hinge region is shown in Fig. 15(a) where the first crack to form is at the centre after which primary and secondary cracks occur. It is common practice in tension stiffening research to first idealise the problem as that of a concentrically loaded prism (CEB-FIP 1985 & 1992, Eurocode 2, Chang 1996, David 2008, Gilbert 2007, Marti 1998, Wu 2009) as in Fig. 15(b) which is simply an *IC theory* problem. It may be worth noting that in the *IC theory* pull-test in Fig. 8 the algebraic sum of forces at a section is zero, whereas, in the tension stiffening simulation in Fig. 15(b) the sum of forces at a section equals P. In all other respects the analysis is the same.

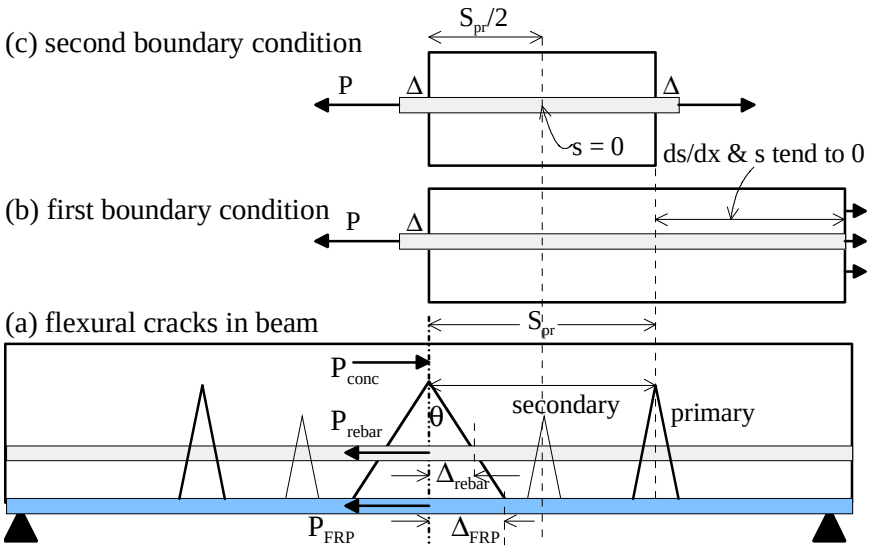

Fig. 15. IC theory simulation of tension stiffening

The maximum stress in the concrete element in Fig. 15(b) occurs in the region where full-interaction is approached that is the boundary condition where both the slip-strain and slip tend to zero as shown. This is, therefore, the minimum crack spacing S_{pr} of the primary cracks as shown. After the primary cracks have formed at spacings S_{pr}, we now deal with the partial-interaction model in Fig. 15(c) where by symmetry the boundary condition is that the slip at the centre at $S_{pr}/2$ is zero as shown where the secondary crack would form if the bond

strength is sufficient. It can be seen that the formation of the primary cracks and secondary cracks require different boundary conditions.

The distribution of cracks and crack widths can be determined using the same partial-interaction numerical procedure as outlined in Fig. 8 which can also form the basis for structural mechanics closed form solutions. For example, a partial-interaction analysis of Fig. 15(b) using a linear ascending bond-slip relationship in Fig. 7 gives the primary crack spacing as

$$S_{pr} = \frac{2}{\sqrt{\frac{\tau_f}{\delta_1} \cdot \frac{L_{per}}{A_r}\left[\frac{1}{E_r} + \frac{A_r}{(EA)_c}\right]}} \tag{6}$$

where E_r is the elastic modulus of the reinforcement and $(EA)_c$ is the axial rigidity of the concrete prism. It can be seen that the crack spacing is independent of the tensile strength of the concrete and directly dependent of the bond stiffness τ_f/δ_1. Furthermore, an *IC theory* analysis of Fig. 15(c) gives the following primary half crack widths Δ_{pr} in relationship to the force in the reinforcement at the crack P_r which is directly dependent on the primary crack spacing S_{pr}.

$$\Delta_{pr} = \frac{P \tanh(2) S_{pr}}{2(EA)_r} \tag{7}$$

where $(EA)_r$ is the axial rigidity of the reinforcement.

Having now shown how *IC theory* can be used to quantify both the crack spacings and crack widths either numerically or through closed form solutions, the results can be used in Fig. 2(c) to determine the deflection due to the discrete-rotation at each individual crack which can be added to that in the undisturbed region in Fig. 2(b) to derive the total deflection.

MOMENT REDISTRIBUTION AND ENERGY ABSORPTION

Moment redistribution is the ability of a hinge, such as that in the –ve region in Fig. 1, to rotate and hold much of its moment whilst the moment in another potential hinge region, such as that in the +ve region, achieves its required moment. Moment redistribution is illustrated in Fig. 16 for a continuous span of a beam which could be plated as shown in Fig. 16(a). Within the span of the beam, there are four possible discrete-rotation hinges as in Fig. 16(b). As described previously, it is now possible to derive the moment/discrete-rotation response, as in Fig. 12, for each possible hinge rotation from *IC theory*. The first hinges to form are labeled the ‘primary hinges’ in Fig. 16(b).

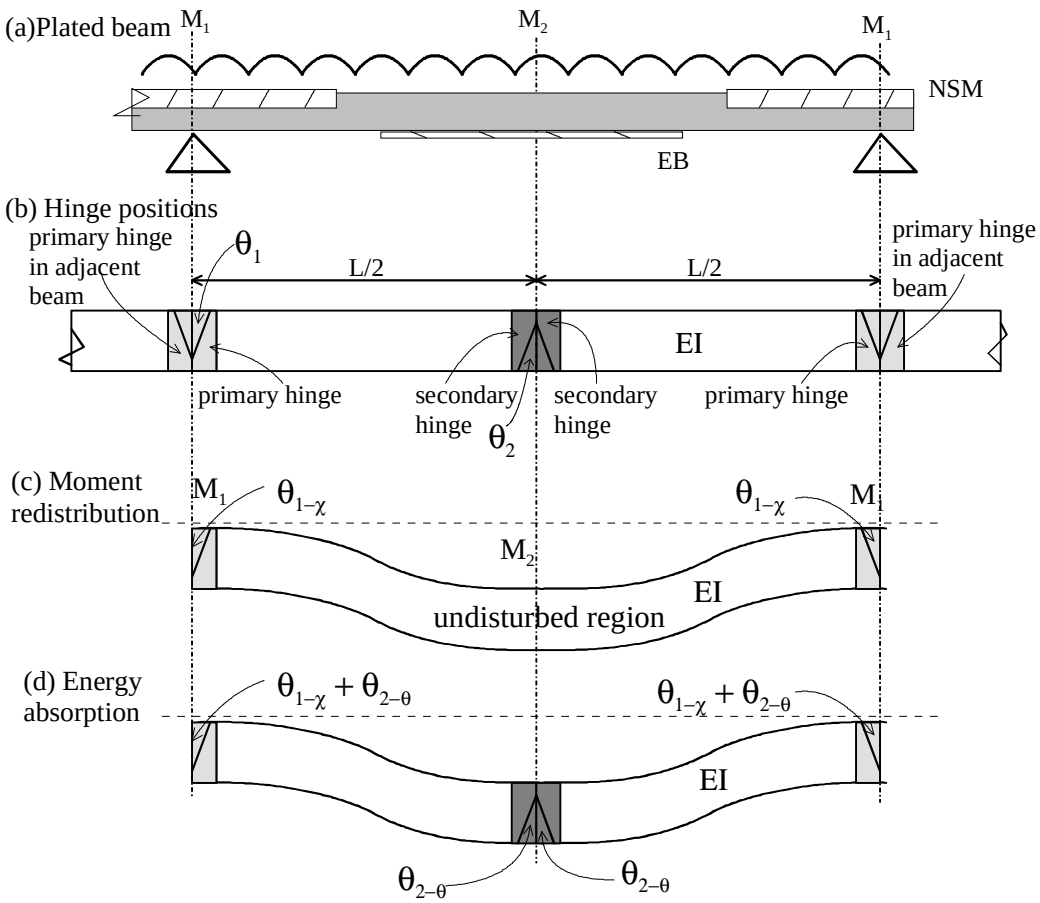

Fig. 16. Moment redistribution in a continuous beam

Let us assume that the distribution of moment in the beam in Fig. 16(a) is known and varies from M_1 to M_2 as shown. Let us also assume that this distribution occurs after moment redistribution. It is a straightforward procedure to integrate the variation of curvature within the undisturbed region of flexural rigidity EI to determine the rotation $\theta_{1-\chi}$ in Fig. 16(c) that is required in the primary hinge to accommodate this distribution of moment. If the rotation capacity of the primary hinge is greater than $\theta_{1-\chi}$ then this moment redistribution can be accommodated. Alternatively, if the moment-rotation relationship, M-θ, of the primary hinge is known such as that shown in Fig. 12 then the moment redistribution capacity K_{MR} can be determined (Oehlers et al 2010; Haskett et al 2010b; Haskett et al 2010c) as follows

$$K_{MR} = \frac{2(EI)\theta}{2(EI)\theta + M.L} \tag{8}$$

where EI is the flexural rigidity of the undisturbed region of the beam and where K_{MR} is the moment redistributed as a portion of the undistributed static moment, that is the well used 'percentage' moment redistribution factor but not as a percentage here. Hence, knowing the moment-rotation response as in Fig. 12 it is possible not only to determine the moment

redistribution factor K_{MR} at its limit but also at the position of the maximum moment or at any moment.

The ability to absorb energy depends on the ability to deform at all hinge locations as shown in Fig. 16(d). If the rotation capacity at the secondary hinges is $\theta_{2\text{-}\theta}$ then the primary hinge has to rotate $\theta_{1\text{-}\chi}+\theta_{2\text{-}\theta}$ as shown. If this can be accommodated by the primary hinge then this is the deformation at failure. Hence, not only the ability to redistribute moment but also the ability to absorb energy can also be determined from *IC theory*.

SHEAR DEFORMATION AND CAPACITY

The moment/discrete-rotation response in Fig. 12 is not only limited by reinforcement fracture or debonding, and wedge sliding but can also be limited by shear failure. The discrete rotation analysis shown in Fig. 4 which is shown with a vertical crack can also be applied to inclined cracks as in Fig. 17. These cracks are subjected to both shear and flexure (Lucas et al 2010). To understand this flexure-shear mechanism, let us first consider a reinforced concrete beam with an inclined crack and with only longitudinal reinforcing bars as in Fig. 18 (Lucas et al 2010).

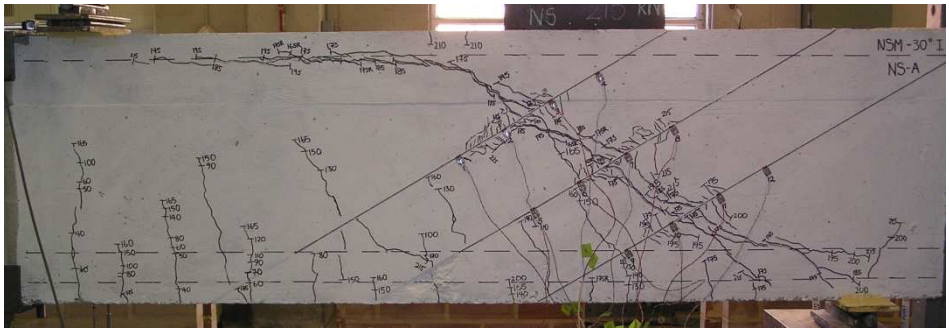

Fig. 17. Discrete rotation at an inclined crack.

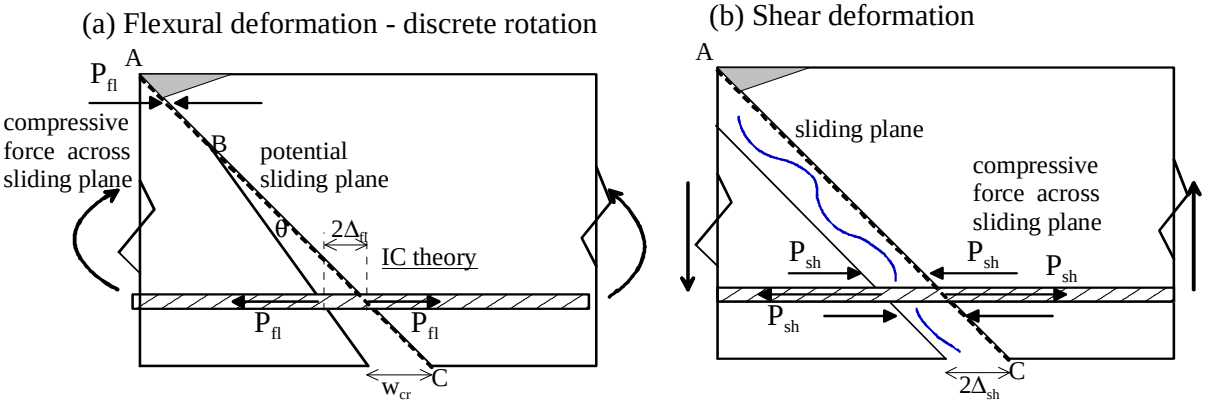

Fig. 18. Flexure-shear mechanism

The analysis of the flexural deformation in Fig. 18(a) is the same as for the vertical crack in Fig. 11. A crack width w_{cr} can be imposed at the soffit of the beam at C in Fig. 18(a) from which the total slip at the level of the reinforcement $2\Delta_f$ can be determined. Consequently from *IC theory*, the force in the reinforcement P_{fl} can be determined which from longitudinal equilibrium is also the compressive force P_{fl} at an offset *d* for rotational equilibrium. From these forces and the beam properties can be determined both the applied moment M_{apl} and shear force V_{apl} at this hinge.

The analysis of a uniform shear deformation is shown in Fig. 18(b) where through aggregate interlock the crack widens a further distance $2\Delta_{sh}$ (to give a total slip of $2(\Delta_{fl}+\Delta_{sh})$). This widening further stretches the reinforcement to induce an increase in the tensile reinforcement force by P_{sh} (to give a total force of $P_{fl}+P_{sh}$) that can be derived from *IC theory*. For longitudinal equilibrium, there must be an additional equal compressive force P_{sh} across the sliding plane the resultant of which must be in line with that in the reinforcement to ensure rotational equilibrium.

The possible sliding plane A-C in Fig. 18 is subjected to a compressive force P_{fl} in the region A-B in Fig. 18(a) prior to sliding and then after sliding commences it is subjected to an additional compressive force P_{sh} in Fig. 18(b). Hence, there is a total force when sliding commences of $P_{fl}+P_{sh}$. It is these compressive forces across the sliding plane which govern the shear capacity of the sliding plane though shear friction theory (Walraven 1981, Walraven and Reinhardt 1981, Mattock and Hawkins 1972, Lucas et al. 2010b). The vertical component of this shear capacity is the commonly referred to 'concrete component' of the shear capacity V_c. It may also be worth noting that even though the compressive force after sliding commences $P_{fl}+P_{sh}$ is greater than that prior to sliding P_{fl}, the shear capacity after sliding may be less than that prior to sliding due to shear friction properties. This is because sliding reduces the shear resistance for a given normal force but sliding increases the normal force increasing the shear resistance. These two effects counteract each other so that the rate of change of each component determines whether sliding reduces or increases the shear capacity which explains the difference between rapid or gradual shear failure (Lucas et al 2010; Zhang 1997).

Let us now consider the case of a beam with both internal and external stirrups as shown in Fig. 17. The flexural behaviour is shown in Fig. 19. For an imposed crack width w_{cr}, the reinforcement slips are Δ_{stp}, Δ_{NSM} and $\Delta_{long.fl}$ as shown. Hence, from *IC theory* the reinforcement forces P_{stp}, P_{NSM} and $P_{long.fl}$ can be determined. It is the sum of the vertical components of the stirrup forces P_{stp-fl} and P_{NSM-fl} which is the shear force directly resisted by the stirrups V_{stir}.

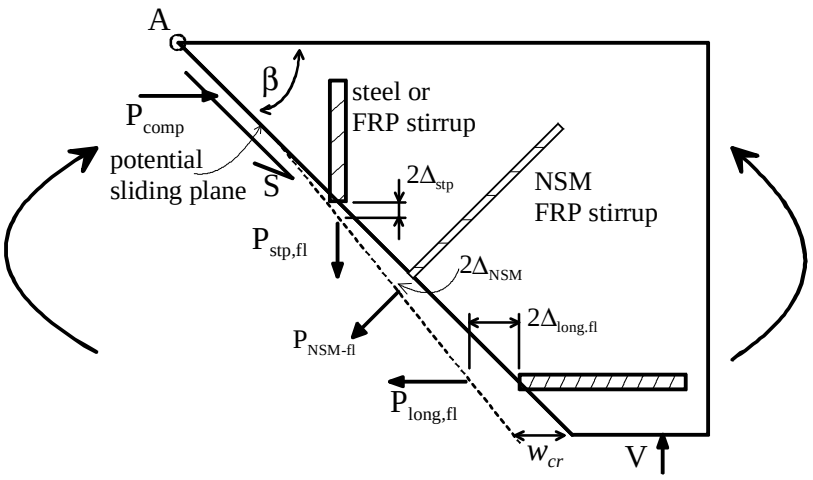

Fig. 19. Stirrup component of the shear capacity

The analysis for the concrete component of the shear capacity is shown in Fig. 20. As explained in Fig. 18, the compressive forces across the potential sliding plane are shown as P_{fl} and P_{sh}. These can be resolved as normal forces to the sliding plane *N* and as shear forces along the sliding plane *S* as shown. From shear-friction theory as explained previously, it is the normal forces *N* that determine the shear capacity along the sliding plane which is shown as $(V_c)_{plane}$. However, this shear capacity must provide the shear forces *S* as shown leaving the capacity along the sliding plane to resist the vertical shear as $(V_c)_{plane} - \sum S = (V_c)_{\beta}$; the vertical component of which is the concrete component of the shear capacity V_c as shown.

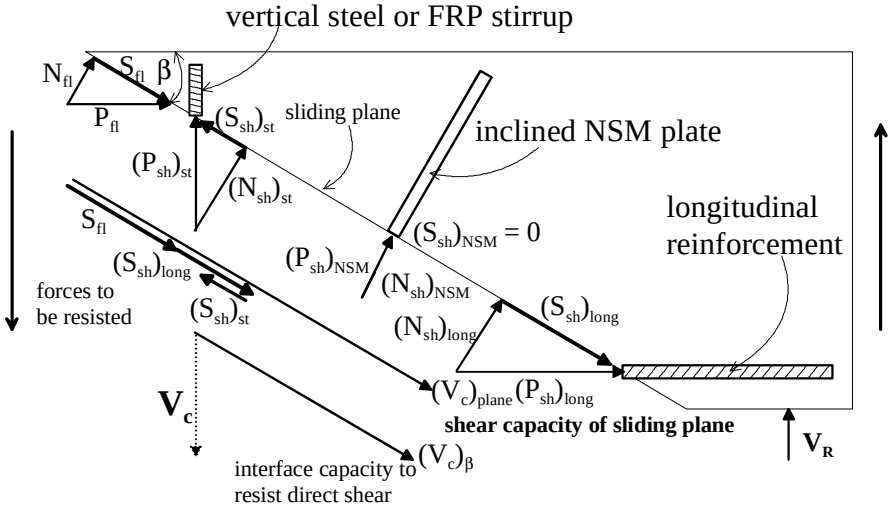

Fig. 20. Concrete component of shear capacity

It can be seen from the previous paragraph that using the total shear-friction shear capacity along the sliding plane $(V_c)_{plane}$ without allowance for the shear forces that are needed to maintain equilibrium $\sum S$ will always overestimate the concrete component of the shear capacity. This maybe a reason why shear-friction is seldom used in practice to quantify the

concrete component of the shear capacity. It is also worth noting in Fig. 20 that the shear force $(S_{sh})_{st}$ associated with vertical stirrups is beneficial in that it increases $(V_c)_\beta$ while that associated with longitudinal bars $(S_{sh})_{long}$ is detrimental that is it reduces $(V_c)_\beta$. It can now be seen how *IC theory* controls both the stirrup and concrete components of the shear capacities.

FIBRE CONCRETE

Figure 3 shows the failure of a beam with fibre concrete. The effect of fibre on the tensile behaviour of concrete is often determined from tensile tests such as in Fig. 21. Gauges positioned at *a-a* can be used to measure the extension and consequently the strain ε_t up to cracking that is along O-A in Fig. 22; this is a material property. After cracking, the gauges not only record the extension due the strains in the uncracked concrete but also the extension due to the crack width w_{cr} and, hence, are recording an effective strain. If the gauge length is increased from *a-a* to *b-b* in Fig. 21 the effective strain will reduce and, hence, there is no effective strain that can be used. However, what can be determined from these tests is the variation in stress with crack width as shown as B-C in Fig. 22 which is the *IC theory* P/Δ relationship described previously.

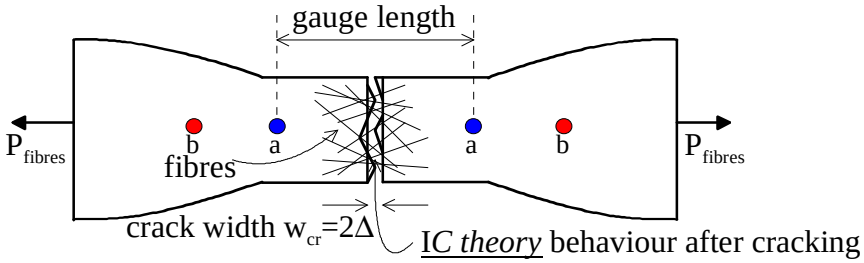

Fig. 21. Tensile test on fibre concrete

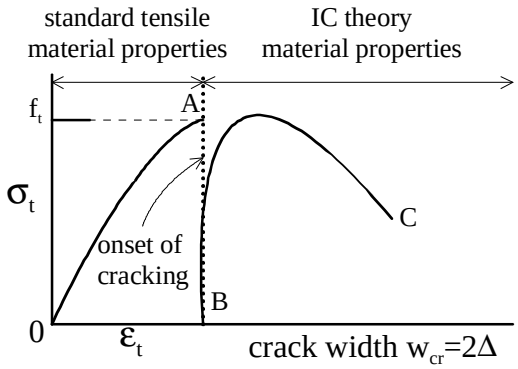

Fig. 22. Fibre concrete tensile properties

Fibres are simply small bits of reinforcement although generally distributed in a random fashion. Hence the effect of fibre reinforcement across a crack is the same as the effect of reinforcement across a crack. Fibres cross the flexural crack in Fig. 3 and, hence, their contribution to the tensile forces in the moment/discrete-rotation analysis in Fig. 4 can be obtained from B-C in Fig. 22 which can be determined directly from tests (Schumacher et al 2009, Suwannakarn 2009, Yuguang et al 2009) or from much good research on the micromechanics of fibre concrete (Bischoff 2003, Fantili et al 2009 & 2007, Jungwirth et al 2004, Redaelli et al 2007) which is in many ways closely related to *IC theory*. Fibres also cross the wedge sliding plane cracks in Fig. 3 and, hence, their effect on wedges is the same as for stirrups and wraps as in Fig. 14. Consequently fibres provide an additional confinement stress σ_t from Fig. 22 which will inhibit wedge sliding and increase the ductility as has been found in practice (Yuguang 2009, Suwannakarn 2009). Finally, fibres cross the potential shear sliding planes. By so doing they induce: additional tensile forces transmitted by the fibres across the crack in Fig. 14 so that the stirrup resistance V_{stir} is increased; and additional compressive confinement forces in Fig. 20 which enhance the concrete component of the shear capacity $V_{c.}$.

It can be seen that fibres can increase the flexural capacity but in particular the flexural ductility and the shear capacity which has been found in practice. It has been shown that all the reinforced concrete behaviours described previously in terms of *IC theory* can also be used to explain the behaviour of reinforced concrete beams with fibre concrete.

SUMMARY

A unified reinforced concrete model for beams with FRP reinforcement or for steel reinforced concrete beams retrofitted with FRP reinforcement has been described. The model makes a direct distinction between the undisturbed region where conventional moment-curvature analyses can be applied and disturbed regions at each individual crack where a new discrete moment-rotation model can be applied. The discrete-rotation is the step change in rotation at each individual crack due to widening of the flexural crack due to slip of the reinforcement. It is shown that the discrete rotation model depends on three fundamental principles: shear-friction, rigid-body-displacements and most importantly the IC theory developed specifically to prevent IC debonding of FRP reinforcement. It is shown that this discrete rotation approach can be used to develop numerical and closed form structural mechanics models for: moment-rotation and confinement; crack widths, crack spacings and deflections; moment redistribution and energy absorption; the stirrup and concrete component of shear failure; and the effect of fibres in concrete. The unified reinforced concrete model is generic as it can in theory be applied to any concrete or reinforcement but it was specifically developed for FRP reinforcement using IC theory developed in large by the FRP research community.

REFERENCES

ACI 440.2R-08 (2008): Guide for the Design and Construction of Externally Bonded FRP Systems for Strengthening Concrete Structures, American Concrete Institute, Detroit(USA).

Bischoff, P.H.(2003) " Tension stiffening and cracking of steel fiber-reinforced concrete" ASCE Journal of Materials in Civil Engineering, Vol 15, No 2, pp. 174-182.

CEB-FIP. (1985) : CEB Manual-Cracking and Deformations, Swiss Federal Institute of Technology.

CEB-FIP. (1992) : CEB-FIP Model Code 90, London.

CEN Eurocode 2 (1992): Design of concrete structures-Part 1-1: General rules and rules for buildings, ENV 1992-1-1:1991.

Chang, K.C. & Sung, H.C. (1996) "Tension stiffening model for planar reinforced concrete members". Journal of Computers & Structures, Vol 59, Issue 1, pp. 179-190.

Dai, J., Ueda, T., and Sato, Y. (2005). "Development of the Nonlinear Bond Stress–Slip Model of Fiber Reinforced Plastics Sheet–Concrete Interfaces with a Simple Method". Journal of Composites for Construction, Volume 9, Issue 1, Jan-Feb: 52-62.

Daniell, J.E., Oehlers, D.J., Griffith, M.C., Mohamed Ali, M.S. and Ozbakkaloglu, T., (2008). "The softening rotation of reinforced concrete beams", Engineering Structures, Vol. 30, 3159-3166.

David, Z.Y., Mahmood, J. & Amir, D.A. (2008) "One dimensional analysis of tension stiffening in reinforced concrete with discrete cracks". Engineering Structures, Vol 30, pp. 206-217.

De Lorenzis, L., and Nanni, A. (2002). "Bond between Near-Surface Mounted Fiber-Reinforced Polymer Rods and Concrete in Structural Strengthening." *ACI Structural Journal*, Vol. 99, No. 2, March-April:123-132.

Fam, A.Z., and Rizkalla, S.H., (2001). "Confinement model for axially loaded concrete confined by circular fibre-reinforced polymer tubes". ACI Structural Journal: 98 (4): 451-61.

Fantili, P.A., Mihashi, H. & Vallini, P. (2007) " Crack profile in R/C, R/FRCC and R/HPFRCC members in tension" Materials and Structures, Vol 40, pp. 1099-1114.

Fantili, P.A., Mihashi, H. & Vallini, P. (2009) " Multiple cracking and strain hardening in fiber-reinforced concrete under uniaxial tension" Cement and Concrete Research, Vol 39, pp. 1217-1229.

Farrall, J., Kotomski, R., Paterson, L. and Visintin, P., (2008) "Moment rotation of confined beams". Final year research report, School of Civil, Environmental and Mining Engineering, The University of Adelaide.

Fib bulletin 14(2001). Externally bonded FRP reinforcement for RC structures. Design and use of externally bonded fibre reinforced polymer reinforcement (FRP EBR) for reinforced concrete structures. Task Group 9.3 FRP reinforcement for concrete structures, Lausanne, Switzerland; 2001.

Gilbert, R.I. (2007) " Tension stiffening in lightly reinforced concrete slabs". Journal of Structural Engineering, Vol 133, Issue 6, pp. 899-903.

Griffith, M.C., Wu, Y.F. and Oehlers, D.J. (2005) "Behaviour of steel plated RC columns subject to lateral loading". Advances in Structural Engineering, Vol.8. No.4, pp 333-347.

Harajli, M.H., Hamad, B.S., and Rteil, A.A.(2004), "Effect of confinement of bond strength between steel bars and concrete", *ACI Structural Journal*, Vol. 101, No. 5, pp. 595-603

Haskett, M., Mohamed Ali M.S., Oehlers D.J., and Wu, C., (2009c) "Influence of bond on the hinge rotation of FRP plated beams", special edition of *Advances in Structural Engineering,* Vol. 12, No. 6, pp 833-843.

Haskett, M., Oehlers, D.J., and Mohamed Ali M.S. (2008) "Local and global bond characteristics of steel reinforcing bars", Engineering Structures, Vol. 30, Issue 2, 376-383, Feb..

Haskett, M., Oehlers, D.J., and Mohamed Ali, M.S., (2010b) "Design for moment redistribution in RC beams retrofitted with steel plates". Advances in Structural Engineering, Vol. 13, No. 2, pp 379-391.

Haskett, M., Oehlers, D.J., Mohamed Ali and Wu, C. (2009b) "Yield penetration hinge rotation in reinforced concrete beams". *ASCE Structural Journal*, Vol. 135, Issue 2, Feb., 130-138.

Haskett, M., Oehlers, D.J., Mohamed Ali M.S. and Wu, C.. (2010c) "Analysis of moment redistribution in FRP plated RC beams". Composites in Construction, ASCE, Vol. 14, Issue 4, July/August, pp 424-433.

Haskett, M., Oehlers, D.J., Mohamed Ali M.S., and Sharma, S. K.. (2010a) "The shear-friction aggregate-interlock resistance across sliding planes in concrete". Accepted Magazine of Concrete Research.

Haskett, M., Oehlers, D.J., Mohamed Ali, M.S., and Wu, C., (2009a) “Rigid body moment-rotation mechanism for reinforced concrete beam hinges” Engineering Structures, 31 (2009) 1032-1041.

Jenson, B.C., (1975). Line of discontinuity for displacements in the theory of plasticity of plain and reinforced concrete, Magazine of Concrete Research, Vol.27, No.92, September., 143-150.

Jungwirth, J. & Muttoni, A. (2004) “ Structural behaviour of tension members in ultra high performance concrete” International Symposium on UHPC 2004, Kassel Germany.

Lam, L., and Teng, J.G., (2004). “Ultimate condition of fibre reinforced polymer-confined concrete”. Journal of Composites for Construction, Vol. 8, No. 6, 539-548.

Lu, X.J., Teng, J.G., Ye, L.P. and Jiang, J.J. (2005). “Bond-slip models for FRP sheets/plates bonded to concrete.” Engineering Structures, Vol.27: 920-937.

Lucas, W., Oehlers, D.J. and Mohamed Ali M.S. (2010) “A Shear Resistance Mechanism for Inclined Cracks in RC Beams”. Submitted ASCE Journal of Structural Engineering

Lucas, W., Oehlers, D.J., Mohamed Ali M.S., Griffith, M.C., (2010b) “The shear-friction mechanism of reinforced concrete”. Submitted ACI Materials Journal.

Malvar, L., (1995), “Tensile and bond properties of GFRP reinforcing bars”, *ACI Materials Journal*, Vol. 92, No. 3, pp. 276-285.

Marti, P., Alvarez, M., Kaufmann, W. & Sigrist, V. (1998) “ Tension chord model for structural concrete” Structural Engineering International, pp. 287-298

Mattock, A.H., and Hawkins, N.M., 1972. Shear transfer in reinforced concrete recent research. Precast Concrete Institute Journal, March-April, 55-75

Mattock,A.H. (1974). “Shear transfer in concrete having reinforcement at an angle toshear plane”, *ACI Publication SP-42-Shear in Reinforced Concrete*, American Concrete Institute (Detroit), Vol.1, 17-42..

Mohamed Ali, M.S., Oehlers, D.J., and Griffith, M.C. (2010) “The residual strength of confined concrete”, Advances in Structural Engineering, Vol. 13, No. 4, pp 603-618.

Mohamed Ali, M.S., Oehlers, D.J., Griffith, M.C., and Seracino, R., (2008) “Interfacial stress transfer of near surface mounted FRP-to-concrete joints”, Engineering Structures, Vol. 30, Issue 7, July, 1861-1868.

Muhamad, R., Mohamed Ali M.S., Oehlers, D.J. and Sheikh, A.H.. “Load-slip relationship of tension reinforcement in reinforced concrete members”. Submitted to Engineering Structures.

Oehlers, D.J. (2007) “Teaching the fundamental principles in reinforced concrete design”. Australian Journal of Structural Engineering, Vol. 7, No.3, pp 99-108.

Oehlers, D.J. and Seracino, R. (2004) “Design of FRP and Steel Plated RC Structures: retrofitting beams and slabs for strength, stiffness and ductility.” Elsevier. 228 pages.

Oehlers, D.J., Griffith, M.C. and Mohamed Ali, M.S. (2009) “Ductility components and limits of FRP plated RC structures”. Construction and Building Materials. Vol.23, Issue 4, Special issue, April 1538-1543.

Oehlers, D.J., Haskett, M., Mohamed Ali, M.S. and Griffith, M.C. (2010) “Moment redistribution in reinforced concrete beams”. Accepted, Proceedings ICE, Structures and Buildings.

Oehlers, D.J., Mohammed Ali, M.S., and Griffith, M.C. (2008c) “Concrete component of the rotational ductility of reinforced concrete flexural members”. Advances in Structural Engineering, Vol. 11, No.3, June, 293-303.

Oehlers, D.J., Rashid, R., and Seracino, R., (2008b) “IC debonding resistance of groups of FRP NSM strips in reinforced concrete beams” Construction and Building Materials. 22, 1574-1582.

Oehlers, D.J., Seracino, R., and Smith, S (2008a) “Design Guideline for RC structures retrofitted with FRP and metal plates - beams and slabs”. Standards Australia HB 305. Publishers SAI Global Limited. ISBN 0 7337 87444, June 4th.

Rashid, R., Oehlers, D.J. and Seracino, R., (2008) “IC debonding of FRP NSM and EB retrofitted concrete: plate and cover interaction tests”, ASCE, Journal of Composites for Construction. Vol. 12, No. 2, March-April, 160-167.

Redaelli, D. & Muttoni, A (2007) “Tensile behaviour of reinforced ultra high performance fiber reinforced concrete elements”

Seracino, R., Jones, N.M., M.S.M. Ali, Page M.W. and Oehlers, D.J. (2007) “Bond strength of near-surface mounted FRP-to-concrete joints” ASCE Composites for Construction. July/August pp401-409

Suwannakarn, S. W. “Postcracking characteristics of high performance fiber reinforced cementitious composites’. Thesis (2009), University of Michigan.

Teng, J.G., Chen, J.F., Smith, S.T., and Lam, L. (2002). FRP Strengthened RC Structures. Wiley, London, England.

Walraven, J., Frenay, J., and Pruijssers, A., 1987. Influence of Concrete Strength and Load History on the Shear Friction Capacity of Concrete Members, PCI Journal, V.32, No.1, Jan-Feb., 66-84.

Walraven, J.C. & Reinhardt, H.W. 1981, "Theory and Experiments on Mechanical Behaviour of Cracks in Plain and Reinforced Concrete Subjected to Shear Loading", *Heron*, 26(1A), pp. 1-68.

Walraven, J.C., (1981). Fundamental analysis of aggregate interlock. Journal of Structural Engineering, ASCE, Vol. 107, No. ST11, Nov., 2245-2271.

Wu, C.Q., Oehlers, D.J., Waschl, J., Glynn, C., Spencer, Merrigan, M., and Day, I., (2007) "Blast testing of RC slabs with NSM CFRP plates", Advances in Structural Engineering, 10 (4), Aug., 397-414.

Wu, H.Q. & Gilbert, R.I. (2009) " Modelling short term tension stiffening in reinforced concrete prisms using a continuum-based finite element model". Engineering Structures, Vol 31, Issue 6, pp. 2380-2391.

Wu, Y.F., Liu, T. and Oehlers, D.J. (2006) "Fundamental principles that govern retrofitting of reinforced concrete columns by steel and FRP jacketing". Advances in Structural Engineering, Vol. 9, No. 4, pp 507-533.

Yuan, H., Teng, J.G., Seracino, R., Wu, Z.S., and Yao, J. (2004). "Full-range behavior of FRP-to-concrete bonded joints", Engineering Structures, Vol. 26, No. 5, April, pp 543-691.

Yuguang, Y., Walraven, J.C. & Uijl, J.A. (2009) " Combined effect of fibers and steel rebars in high performance concrete". *Heron* 54(2/3). pp. 205-224.

Zhang, J.P., (1997) "Diagonal cracking and shear strength of reinforced concrete beams", Magazine of Concrete Research, Vol. 49, No. 178, March, pp 55-65.

Chapter 2 – Cross Sectional Analysis

Introduction

In this chapter it is shown that the fundamental mechanisms outlined in Chapter 1, that is, partial-interaction and shear-friction, can be used to quantify the variation in flexural rigidity using a segmental approach. This segmental approach is fundamentally different from that presented in Chapter 1 in that partial-interaction theory is used to describe tension stiffening between a pair of cracks. Hence, the approach presented here more closely simulates the behaviour of a section with ductile reinforcement where a strong bond forms between the bar and concrete encasing it. This is in contrast to the analysis in Chapter 1 which more accurately simulates behaviour where a weak bond between the reinforcement and concrete exits, for example under the case for cyclic loading where the bond is degraded by load reversals.

The first two papers contained in this chapter namely "A mechanics solution for hinges in RC beams with multiple cracks" and "A Mechanics Based Hinge Analysis for Reinforced Concrete Columns" develop the segmental PI M/θ approach for reinforced concrete beams and columns and describe the newly defined equivalent flexural rigidity. The derivation of the shear friction material properties required for the simulation of the softening wedge is then presented in the paper "Using shear-friction properties to simulate concrete softening in reinforced concrete flexural members". Finally, a new cyclic partial interaction model is developed in the paper "The Reinforcement Contribution to the Cyclic Behaviour of Reinforced Concrete Beam Hinges" and the single crack PI M/θ approach is used to describe the load deflection behaviour of RC beams subjected to large load reversals.

List of manuscripts

Visintin, P., Oehlers, D.J., Wu, C., and Haskett, M., (2012) "A mechanics solution for hinges in RC beams with multiple cracks". *Engineering Structures*, Vol. 36, pp 61-69.

Visintin, P., Oehlers, D.J., Wu, C., and Haskett, M., (2012) "A Mechanics Based Hinge Analysis for Reinforced Concrete Columns". Submitted to *Journal of Structural Engineering*

Haskett, M., Oehlers, D.J., Visintin, P., Ali Mohamed, M.S., (2012) "Using shear-friction properties to simulate concrete softening in reinforced concrete flexural members" Submitted to: *Cement and Concrete Research*

Visintin, P. Oehlers, D.J., Wu, C. and Griffith, M.C., (2012) "The Reinforcement Contribution to the Cyclic Behaviour of Reinforced Concrete Beam Hinges". Accepted for publication in *Earthquake Engineering and Structural Dynamics*.

Statement of Authorship

A mechanics solution for hinges in RC beams with multiple cracks
Engineering Structures 2012, Vol. 36, pp 61-69

Visintin, P. (candidate)

Prepared manuscript, performed all analyses, developed model and theory.

I hereby certify that the statement of contribution is accurate

Signed……..Date……

Oehlers, D.J..

Supervised research, provided critical manuscript evaluation and acted as corresponding author.

I hereby certify that the statement of contribution is accurate and I give permission for the inclusion of the paper in the thesis

Signed…….Date……

Wu, C.

Assisted in manuscript evaluation.

I hereby certify that the statement of contribution is accurate and I give permission for the inclusion of the paper in the thesis

Signed …….Date……

Haskett, M

Assisted in manuscript evaluation.

I hereby certify that the statement of contribution is accurate and I give permission for the inclusion of the paper in the thesis

Signed …….Date……

A Mechanics Solution for Hinges in RC Beams with Multiple Cracks

Visintin, P., Oehlers, D.J., Wu, C., and Haskett, M..

ABSTRACT

The formation of hinges in reinforced concrete beams is important as hinges influence the ability of the beam and, subsequently, the frame to absorb energy and resist extreme loads such as hurricane or seismic loads. A common approach for quantifying the rotational capacity of beams at the ultimate limit is to use a strain based moment-curvature analysis combined with an empirical hinge length to determine the rotation capacity of the member. Being empirically based, this approach is very restrictive as it can only be applied within the bounds of the tests from which they were derived. In this paper, a mechanics displacement based hinge approach is described that can simulate the formation of cracks, the discrete rotation at each individual crack and the formation of wedges. Being mechanics based, this hinge model can be applied to any type of reinforced concrete, such as those with brittle reinforcement and also to all strengths of concrete. This mechanics based model is shown to have good agreement with test results and can be used at all stages of loading from serviceability to failure. Furthermore, it can also used to develop closed form solutions that do not require the moment-curvature assumption of full interaction but specifically allow for partial interaction that is slip between the reinforcement and the concrete.

Keywords: RC beams; RC hinges; ductility; concrete softening; reinforcement bond; shear friction; and partial interaction.

INTRODUCTION

A two span continuous beam that has been loaded beyond its peak strength is shown in Fig. 1. In each of the regions between the points of contraflexure, the first flexural or initial crack occurs at a very early stage of loading and can be predicted using a full-interaction moment-curvature (M/χ) analysis; full-interaction implies that there is no slip between the reinforcement and adjacent concrete so that the reinforcement and adjacent concrete are subject to the same strain. Subsequent flexural cracks depend on the bond and slip between the reinforcement and the concrete which is a partial-interaction consideration [1-13]; partial-interaction implies that there is slip between the reinforcement and the adjacent concrete such that there is a step change in the strain between the reinforcement and the adjacent concrete. As such, the moment at which subsequent cracks occur and their spacings cannot be predicted by a full-interaction M/χ analysis. As the load is increased, these cracks widen through slip between the reinforcement and the concrete so that the full-interaction assumption implicit in a M/χ analysis cannot be used to predict crack widths. Hence, it can be seen that a M/χ analysis can only directly predict the occurrence of the first crack in an uncracked region, after which the M/χ analysis has to be supplemented with empirical approaches to predict crack spacings and crack widths [4,14,15]

At the ultimate limit state, some of the cracks widen significantly so that most of the rotation is due to the discrete rotation between crack faces [16] as can be seen in Fig. 1. Hence this localised or concentrated rotation at high moment regions, often referred to as hinges, is primarily due to slip between the reinforcement and the concrete that a M/χ analysis cannot simulate. As a consequence, a M/χ analysis requires empirically derived hinge lengths [17-23] over which the full-interaction curvature can be integrated in an attempt to simulate this partial-interaction discrete rotation. And finally, compression wedges form as can be seen in Fig. 1 where the wedge slides relative to the adjacent concrete [24,25]. This behaviour cannot also be simulated directly by a strain based M/χ analysis as this is a mechanism, but has to resort to the use of softening compression stress-strain relationships which are often found to be size dependent.

Figure 1: Disturbed regions in RC beam

It can be seen that a M/χ analysis does not directly simulate the behaviour of a reinforced concrete beam after the first crack has formed and as such has to resort to empirically derived components. Being empirically based, these M/χ approaches can only be applied within the bounds of the testing regimes from which they were derived and, consequently, are of limited help outside these bounds. Hence the need for a mechanics based approach which is the subject of this paper.

In this paper, a mechanics approach is described which is based on the principle of plane sections remaining plane at discrete locations, that is the bisection of cracks and at the mid-point between cracks, but not on the commonly used consequential assumption of a linear strain profile along the depth of the beam. Established partial-interaction theory [5,6,9,10,12,26,27], that is slip between the reinforcement and the concrete, is used to simulate the cracked region and established shear-friction theory [28-37] is used to simulate the formation of wedges. Hence this model can simulate the formation and widening of cracks and the formation of wedges. That is, this mechanics model can directly simulate, as opposed to indirectly simulate, what is actually seen in practice.

This paper deals with flexural behaviour and failure. However, these mechanics hinges are equally applicable in the serviceability limit state [38], and can also be used to quantify shear failure but this is dealt with elsewhere [39]. The fundamental principles of the hinge mechanism are first described. This is then followed by idealisations that can be used, but do

not have to be used, to develop a mechanics solution. The mechanics model is then compared with test results of eccentrically loaded prisms and it is also shown how the mechanics model can be used to develop closed form solutions.

HINGE MECHANISM

The basic fundamental principles on which the hinge model is based, that is the fundamental mechanics that controls the hinge behaviour and which is independent of the material properties, is first described. This is followed by idealised assumptions that are required to develop mechanics based numerical models or mechanics based closed form solutions. It may be worth noting that these idealised assumptions are not an essential component of the model but can be refined in the long term to achieve better correlation with test results. The major component of the rotation of a beam occurs over a very small region, as can be seen in Fig. 1, which can be two orders of magnitude smaller than the beam span. Hence, it is reasonable to assume that within the hinge region the moment is constant. This helps in the following explanation but it may be worth noting that variations in moment can be incorporated.

Basic fundamental principles of hinge mechanism

The beam, such as in Fig. 1, is divided by adjacent flexural cracks into elements of length L_{cr} of half length L_{def}. Three adjacent elements are shown Fig. 2. They are in a constant moment region and, hence, have identical behaviours. Flexural cracks occur at Sections A-A and C-C; the behaviour at C-C is a mirror image of that at A-A. Let us first consider Section A-A. Prior to bending, the left side of Element 1 is a single line *c-h-k-n*. An applied moment will cause the reinforcing bar to pull out of Element 1 by Δ (which is the slip between the reinforcing bar and the crack face at *h*) and out of Element 2 by an equal amount Δ. Furthermore, the moment will cause the face of Element 1 to compress by the shaded region *k-n-o*, where D is the contraction at the top fibre, and Element 2 to compress an identical amount *k-p-o*. Hence by symmetry, *b-g-k-o* is a straight line and remains a straight line under varying moment, that is, the principle of plane sections remaining plane applies to *b-g-k-o*. In contrast, it can be seen that if a line were drawn adjacent to the crack face then this would deform to *c-h-k-o* which is not a straight line and, hence, the principle of plane sections remaining plane is not applicable. It needs to be stressed that the crack-face such as *a-k* or *c-k* does not need to be linear but that there is a linear variation in crack width such as that shown on the right hand side of element 3 where the crack width w_{cr} varies linearly from zero at the crack apex to a maximum at the soffit of the beam.

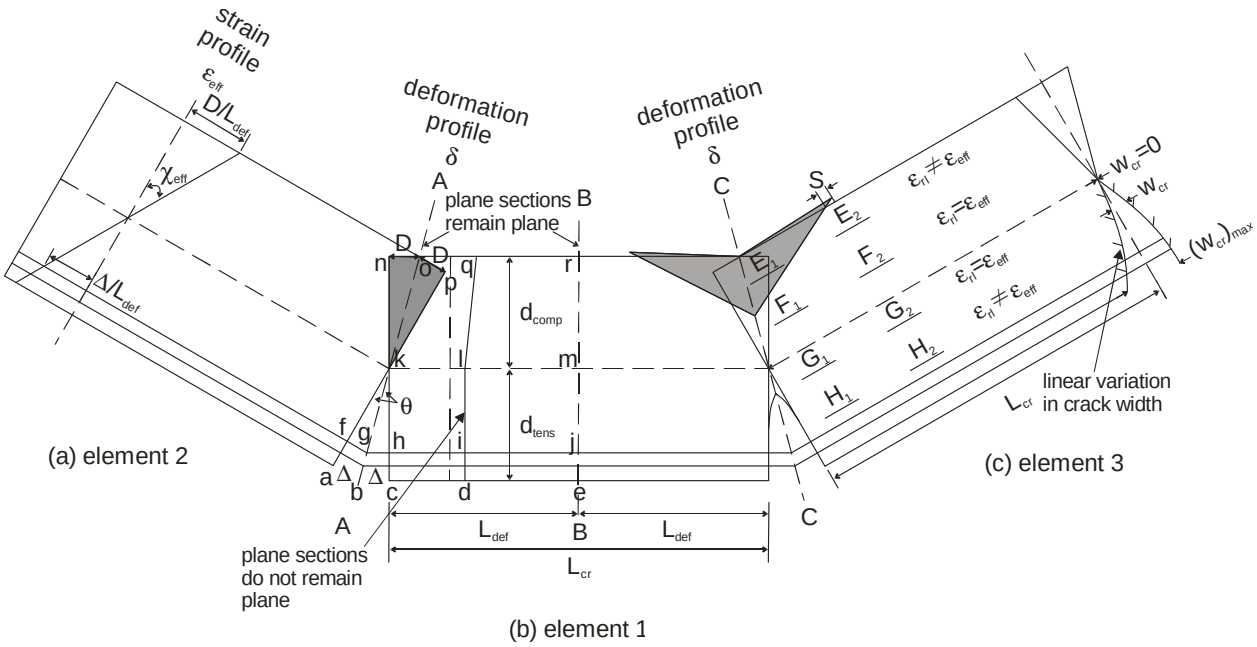

Figure 2: Mechanics based beam hinge model in constant moment region

A line drawn at the centre of an element such as *e-j-m-r* in Element 1 in Fig. 2(b) also remains straight as the moment is varied because of symmetry, that is because the deformation to the left at Section A-A is equal and opposite to the deformation to the right at Section C-C. Hence the section at mid-span of the element *e-j-m-r* also obeys the plane sections remain plane principle. In conclusion, the principle of plane sections remaining plane applies at a section that bisects the crack i.e. *b-g-k-o* and at a section that bisects the element i.e. *e-j-m-r* but does not apply elsewhere such as at *d-i-l-q* as this now has a bilinear shape.

Having shown that plane sections remain plane at Sections A-A and B-B in Fig. 2, now let us consider the deformations encompassed by these sections. The length of this region is shown as L_{def} which is simply half the crack spacing L_{cr}. There is a linear variation of deformation in the compression region *k-n-o* and a linear variation in deformation in the tension region *k-c-b*. These deformations divided by the length of the region over which these deformations act (L_{def}) provides a linear variation of strain as plotted in the strain profile in Fig. 2(a) where at the top fibre the strain is D/L_{def} and that at the level of the reinforcement of Δ/L_{def}. It should be noted that these are either real strains or effective strains. Consider for example Element 3. If strain gauges were placed at G_1 and G_2 or at F_1 and F_2, where there are no disturbance at these levels associated with flexural cracking or the formation of wedges that is these are undisturbed levels, then the strains plotted in the strain profile in Element 2 at these levels are real strains as these are the strains that would be measured by the strain gauges. If strain gauges were placed at H_1 and H_2 within the flexural crack region, then these would not register the strains in the strain profile as they are mainly due to the deformation

due to crack widening and are, therefore, effective strains. Similarly if strain gauges were placed at E_1 and E_2 that is within a wedge and outside a wedge, they would measure the same value but would not be the same as in the strain profile as part of the deformation is due to sliding of the wedge shown as S.

Hence the strain profile plotted in Element 2 in Fig. 2 is an effective (that is it cannot be physically measured) strain profile which gives effective curvatures χ_{eff} and effective flexural rigidities if required. It can also be seen that these effective values depend on the element length L_{def} which depends on the spacing of cracks L_{cr}, reinforcement slip Δ which depends on the bond-slip properties and on the slip of the wedge S which depends on shear-friction properties. Figure 2 summarises all aspects of the mechanics hinge model, where it can be seen that all aspects of reinforced concrete beam behaviour are simulated. Its application is described in the following section.

Idealisations for a mechanics solution

The mechanics hinge model is illustrated in Fig. 2. It is simply a question of rotating the element ends, such as *c-h-k-n*, by θ and adjusting the neutral axis depth at *k* until equilibrium is achieved. To help find a solution, it is often best to make reasonable assumptions which can often be improved with time but it needs to be stressed do not affect the fundamental mechanics of the hinge. Let us first consider the tension region.

Tension region

The left hand side of Element 1 in Fig. 2(b) is shown in Fig. 3. The first component that is required for the analysis is the half crack spacing L_{def} as this is the length of the element that the deformations shown at Section A-A have to be accommodated within. It is now common practice to derive the crack spacing from a partial-interaction analysis of the prism of depth d_{prism} that is encapsulating the reinforcement [4,12,14,15]. The partial-interaction analysis is illustrated in Fig. 4(a) and depends on the bond-slip (τ/δ) characteristics which allows slip at the crack face Δ for a given reinforcement force P to be derived. This analysis can be used to determine the variation in strain in the concrete and reinforcement ε_c and ε_r respectively along the prism, and in particular the variation in the slip-strain $d\delta/dx$ that is ε_c-ε_r and slip δ as shown. From this can be determined the position of full-interaction where both the interface slip and the interface slip-strain approaches zero which is also the position L_{cr} of the next crack when the strain in the concrete is equal to the cracking strain.

Let us now impose a rotation θ, where the face *a-b-c* at Section A-A in Fig. 3(b) is linear, and in which the neutral axis is shown to be constant for ease of reading but which varies with the imposed actions. Let us keep rotating until the tensile strain capacity of the concrete ε_t is about to be achieved, that is D_1 is almost $\varepsilon_t L_{def}$ at deformation 1-1 in Fig. 3(a) where the rotation is θ_1. The deformation 1-1 still has a linear variation *d-b-e* so the corresponding

strain distribution 1-1 in Fig. 3(a) is a real strain distribution ε_{rl} so that the Euler-Bernoulli elastic beam equation applies. However, increasing the rotation to θ_2 that is deformation 2-2 in Fig. 3(b) *f-g-k-b-h* will cause the strain profile 2-2 in Fig. 3(a) in which the strain over the cracked region $d_{ten\text{-}cr}$ is an effective strain ε_{eff} and that over the uncracked region $d_{ten\text{-}uncr}$ is a real strain distribution ε_{rl}. The crack face is now *k-i-l* where for example *i-j* is the deformation in the concrete due to tensile stresses in the concrete. The tensile stresses in the concrete must be zero at the crack face and less than the tensile capacity at B-B otherwise another flexural crack would have occurred. Furthermore, if total debonding has occurred at the ultimate limit state then the tensile stress in the concrete at B-B would be zero. Hence the deformation *i-j* shown as $d\Delta$ can be assumed to be zero that is all of the deformation *f-g-k-b* is due to crack widening and slip Δ of the reinforcement and, furthermore, the slip and crack-width variation is linear.

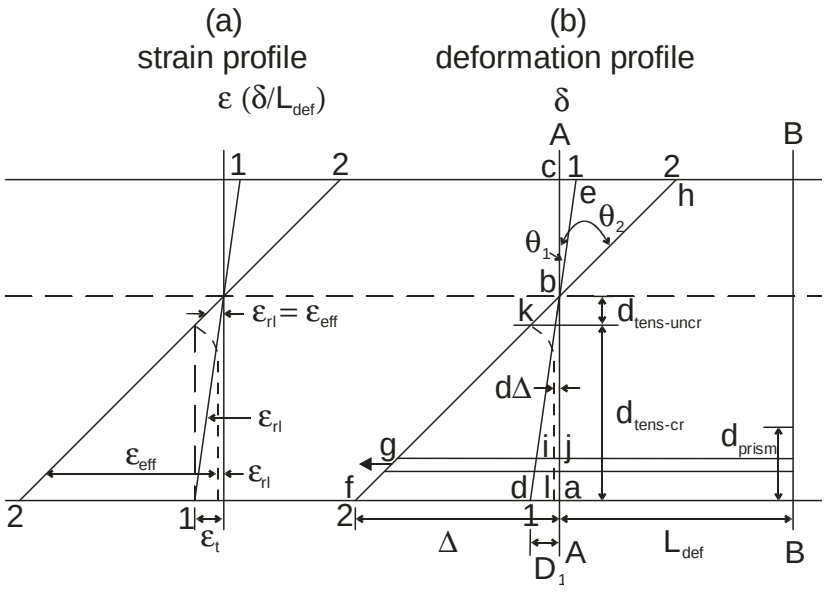

Figure 3: Idealised tensile deformations

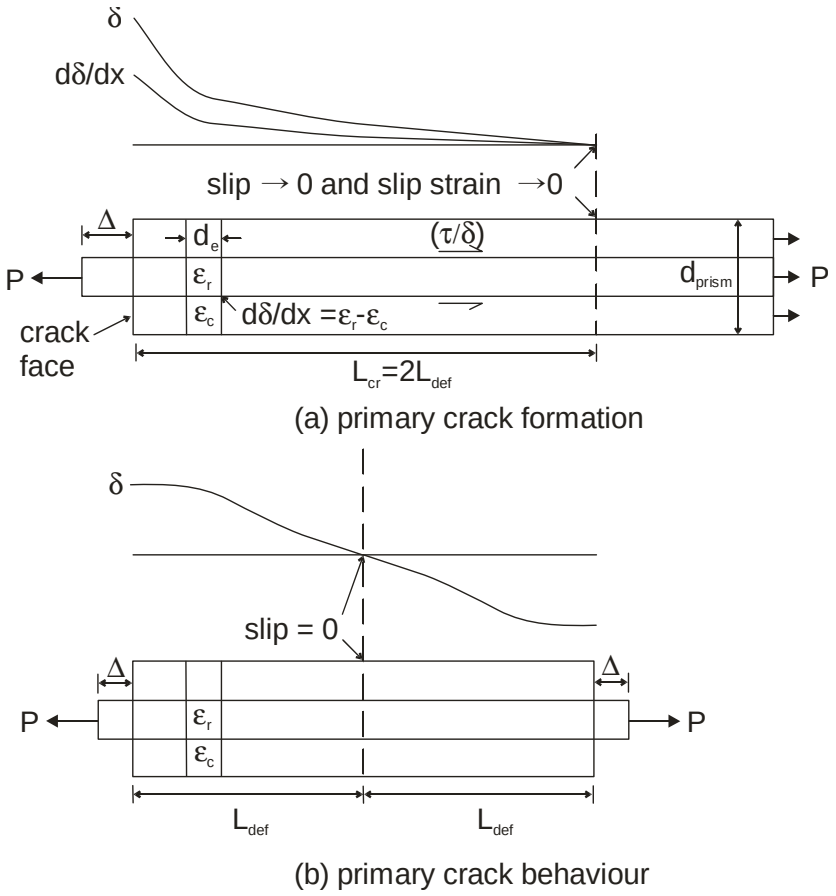

Figure 4: Tension stiffening analysis

The analysis in Fig. 4(b) gives the relationship between P and Δ for an element between two cracks in which case the boundary condition is slip is zero at L_{def} from the crack face as shown. The analysis in Fig. 4(b) represents the analysis of the tension region in Element 1 in Fig. 2(b) and, hence, gives the P/Δ relationship required for the analysis in Fig. 3(b). Numerical models have been developed that can cope with any bond-slip characteristic [6,10,27] and closed form solutions [12] have been derived for a range of idealised bond-slip characteristics.

Compression region

A wedge may form in the compression region of the mechanics hinge as can be seen in Fig. 1 and illustrated in Fig. 2. This can be simulated indirectly by using a softening branch in the compressive stress-strain relationship or it can be simulated directly using well established shear-friction theory [30,31,35-37,40].

To understand the shear-friction mechanism, let us first consider the rectangular prism in Fig. 5(a) of height L_{def} and width *b* and of a depth into the page that is much larger than L_{def}, such

that the behaviour can be considered as two dimensional so that the deformations shown in Figs. 5(b) to (e) apply at any cross section throughout the depth of the prism. The prism can be loaded to failure and the stress-strain relationship recorded as in Fig. 6(a) where the strain is the overall contraction of the prism as a proportion of the prism height L_{def}. There is an ascending path *a-b-c* in Fig. 6(a) up to the peak stress f_c at a strain ε_{pk}. Followed by a horizontal component on further contraction of the prism where the stress f_c is maintained whilst the concrete softens up to a strain ε_{sft} after which the concrete weakens with a descending stress with increasing strain.

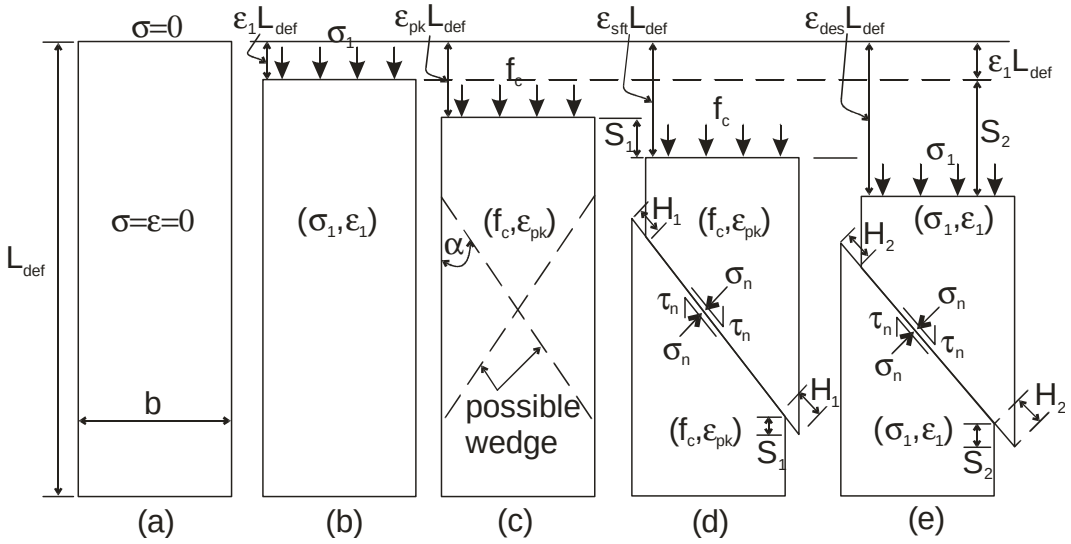

Figure 5: Shear friction mechanism

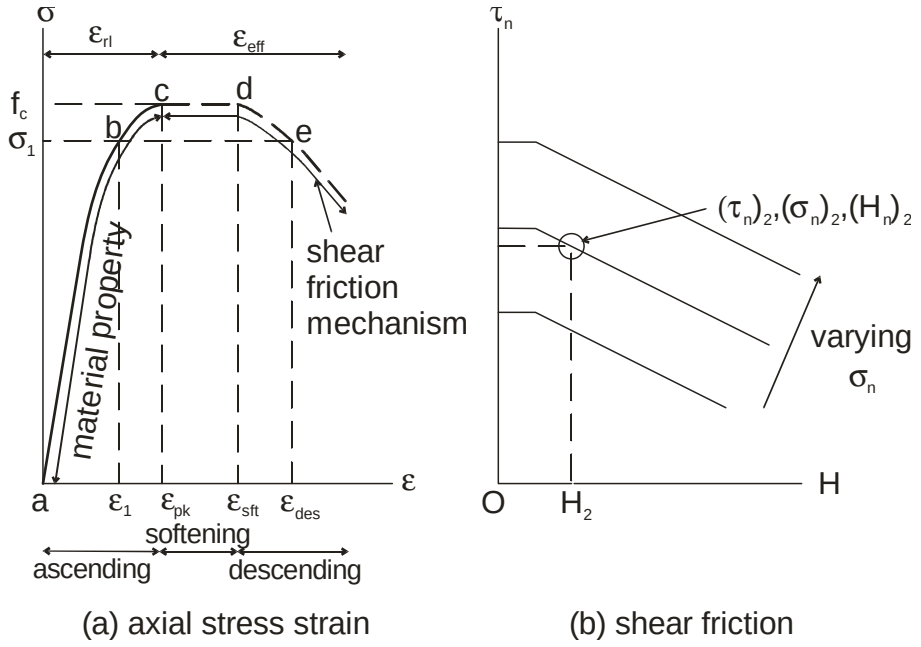

Figure 6: Concrete material properties

The mechanism that causes the stress strain relationship in Fig. 6(a) is illustrated in Fig. 5. The ascending path *a-b-c* in Fig. 6(a) may be considered to be a material property such that the deformation in Fig. 5(b) of $\varepsilon_1 L_{def}$ and that in Fig. 5(c) of $\varepsilon_{pk} L_{def}$ at the peak strength are due to the measurable strain in the concrete. Once the peak stress f_c at ε_{pk} is achieved at Point *c* in Fig. 6(a) and at the deformation in Fig. 5(c), any further axial deformation can no longer be accommodated by the material, so wedges form and the corresponding stress strain relationship, c-d-e in Fig. 6(a) is a mechanism dependent on the shear friction properties in Fig 6(b). These wedges can form as in Fig. 5(c) or as in Fig. 5(d), depending on the restraints at the top and bottom of the prism and on the height to width ratio L_{def}/b of the prism. The angle of the wedge α depends on the cohesive and frictional properties of the concrete [33] and also on the height L_{def} which if small may force α to increase so that the wedge can be accommodated between the end restraints.

Let us now increase the axial deformation of the prism to follow the path *c-d* in Fig. 6(a) in which the stress remains constant at f_c. As the stress remains constant at f_c, the strain in the concrete material remains constant at ε_{pk} as shown in Fig. 5(d), so that the additional deformation during softening S_1 must be accommodated by sliding of the wedge H_1, such that the vertical movement S_1 is equal to $(\varepsilon_{sft}-\varepsilon_{pk})L_{def}$ where ε_{sft} is defined in Fig. 6(a). Any further axial deformation as in Fig. 5(e) may cause the applied stress to drop to σ_1 at the apparent strain ε_{des} in Fig. 6(a). In this case, the strain in the concrete material is now ε_1, from the concrete material property *a-b-c* in Fig. 6(a), as shown in Fig. 5(e). Hence the total axial deformation $\varepsilon_{des} L_{def}$ consists of the material deformation $\varepsilon_1 L_{def}$ plus that due to wedge sliding H_2 such that S_2 equals $(\varepsilon_{des}-\varepsilon_1)L_{def}$.

It can be seen that shear-friction theory can be used to simulate the formation of wedges. It also helps explain the difference between real strains ε_{rl} in Fig. 6(a), which are strains in the concrete that can be physically measured, and effective strains $\varepsilon_{eff,}$ which are not the actual strains in the concrete material but which allow for disturbances, in this case wedge sliding. It can also be seen in Figs. 5(d) and (e) that these prism tests can also be used to quantify the shear-friction properties along the sliding plane that is the relationship between the normal stress, shear stresses and slip along the sliding plane (σ_n, τ_n, H) which can be given in the form shown in Fig. 6(b) [35-37].

The application of the above shear-friction mechanism to the left hand side of beam element 1 in Fig. 2(b) is illustrated in Fig. 7 for the compression region where for convenience the wedge is shown to the right. Furthermore, for convenience in the explanation, the position of the neutral axis has been drawn as unchanged but it will be shown later in the paper in the application of this procedure that this does change slightly and that the analysis can accommodate this change. Let us impose a rotation θ_1 so that the face at A-A in Fig. 7(b) rotates to 1-1 at which point the strain in the top fibre reaches ε_{pk} in Fig. 7(a), and the deformation $\varepsilon_{pk} L_{def}$ in Fig. 7(b). This deformation 1-1 can be accommodated by the concrete material as the strains lie within *a-b-c* in Fig. 6(a).

Let us now increase the deformation to 2-2 in Fig. 7(b) such that the effective top fibre strain is ε_{sft} in Fig. 6(a) so that the stress where the effective strain exceeds ε_{pk} remains at f_c. The region 1-2-4 in Fig. 7(b) and which has been shaded is the deformation that cannot be accommodated by the material deformation as this has a maximum value of $\varepsilon_{pk}L_{def}$. Hence this deformation 1-2-4 has to be accommodated by slip of a wedge of depth $(d_w)_{sft}$ shown as a broken line in Fig. 7(c). It is also worth noting that the stress in the beam over the depth $(d_w)_{sft}$ remains at f_c in the wedge and also outside the wedge. Furthermore, below the wedge the strains are real so that the stresses are given by *a*-*b*-*c* in Fig. 6(a).

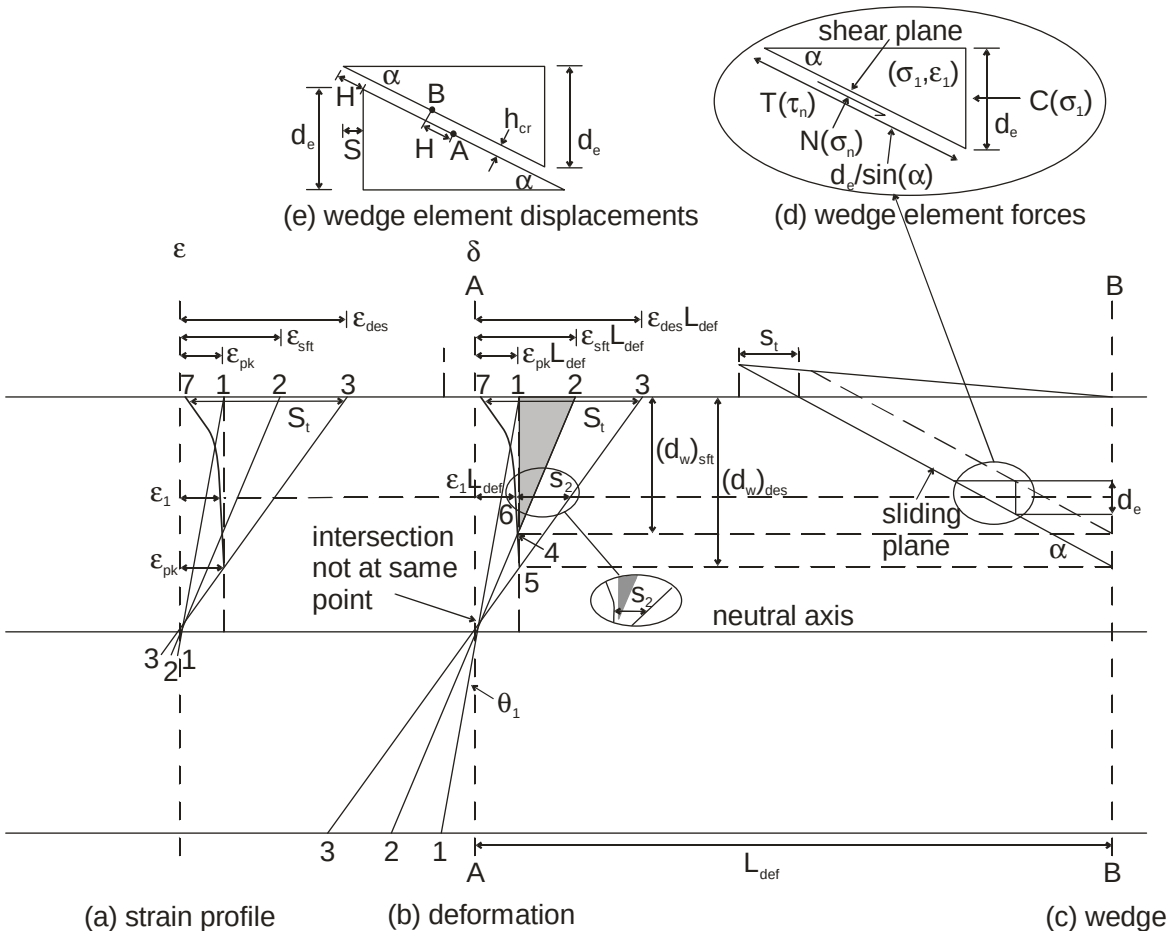

Figure 7: Idealised compression deformation

Let us now further increase the rotation to 3-3 in Fig. 7(b) such that the effective fibre strain ε_{des} in the top fibre exceeds ε_{sft} in Fig. 6(a). The depth of the wedge now increases to $(d_w)_{des}$ in Fig. 7(b) below which the deformation can be accommodated by material contraction. In this case, the contraction of the material over the depth $(d_w)_{des}$ is in part less than $\varepsilon_{pk}L_{def}$ i.e. the line 1-4-5 but reduces to 7-6-5 so that the wedge slip required increases from the shaded region 1-2-4 to 1-2-3-5-6.

The force the wedge in Fig. 7(c) can resist can be determined from the shear friction properties illustrated in Fig. 6(b) where an iterative approach may be required to solve. For example, consider the element of wedge of depth d_e in Fig. 7(c) which is enlarged in Fig. 7(d). Let the deformation at this level to be accommodated by wedge slip be estimated to be $S_{2,}$ as in Fig. 7(b), so that the remaining deformation required is $\varepsilon_1 L_{def}$ as shown and is due to the material strain ε_1; hence ε_1 is an estimated value $(\varepsilon_1)_{est}$ derived for an estimated S_2. For the contraction S_2, the slip along the sliding plane at the angle α in Fig. 7(c) H_2 can be determined as described in the following paragraph. It is then a question of moving vertically up the line at H_2 in Fig. 6(b) to find the combination of $(\tau_n)_2$ and $(\sigma_n)_2$ that gives a horizontal force component C in Fig. 7(d). From the force C can be determined the stress σ_1 and from the material property *a*-*b*-*c* in Fig. 6(a) can be determine the material strain ε_1 and if this is not what is required for S_2 that is $(\varepsilon_1)_{est}$, S_2 has to be iterated to find a solution.

The relationship between the shear-friction sliding component H, and the non-material contraction S [36, 37] is illustrated in Fig. 7(e) for an element of depth d_e. Prior to sliding, points A and B are opposite and adjacent. Sliding H causes these points on adjacent planes to move apart h_{cr} as shown due to aggregate interlock in addition to the dispalcement H. From the geometry in Fig. 7(e), it can be deduced that H is equal to the sum of $S/\cos\alpha$ and $h_{cr}\tan\alpha$. As h_{cr} is an order of magnitude smaller than S it is convenient to assume that H is equal to $S/\cos\alpha$. However as for the relationship between τ_n, σ_n and H in Fig. 6(b) which is known [36, 37], the relationship between h_{cr}, σ_n and H is also known [36, 37] and this can be used to the quantify the $h_{cr}\tan\alpha$ component of H if a greater degree of accuracy is required.

Accommodation of multiple cracks

The analysis procedure outlined above is also applicable when the softening wedge crosses multiple cracks. Let us consider the case shown in Figure 8(a) where the cracks can be considered to occur in a constant moment region within which there are five cracks. The deformation of each individual element, already described in Fig. 2, has been shown for the four elements in Fig. 8(a). The constant moment region consists of two symmetrical hinges that are to the left of A-A and to the right of A-A. If for example Fig. 8(a) was inverted by rotating about a horizontal axis, then A-A would be at the support of a continuous beam or encased beam in which the hinge at the support would be the left hand hinge that is from B-B to A-A.

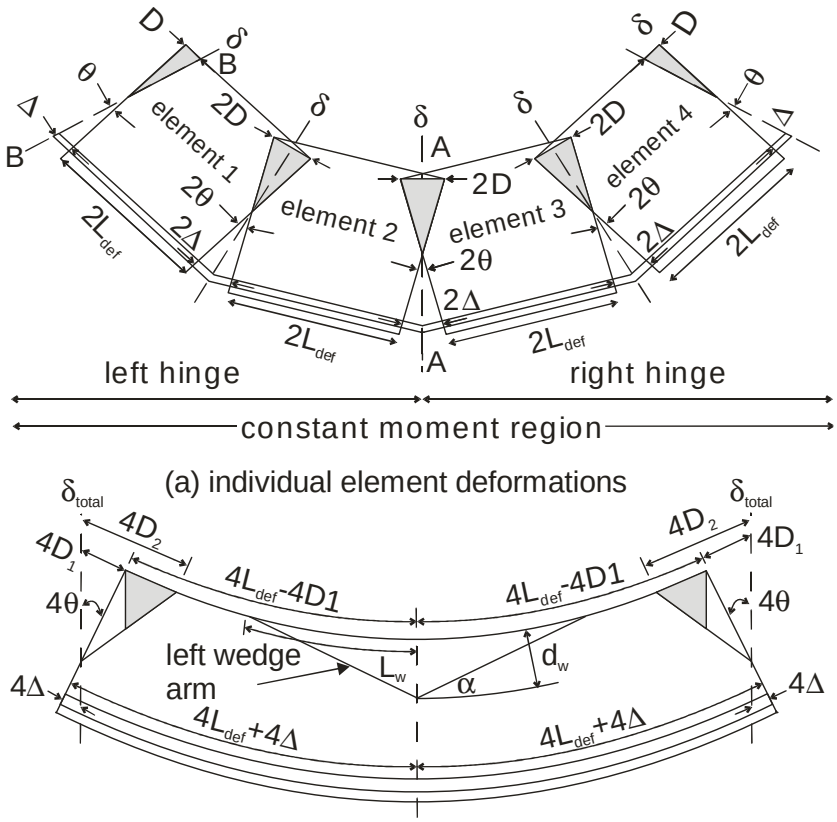

Figure 8: Multiple cracks in hinge region

Let us consider the left hand hinge in Fig. 8(a). For each element of length $2L_{def}$, the top compressive fibre deforms 2D, the reinforcing bars pull out by 2Δ and the crack faces rotate by 2θ. Hence for this specific hinge comprising of two elements and length $4L_{def}$, the total contraction of the top fibre is 4D, the total rotation is 4θ and the total slip of the reinforcement is 4Δ as shown in Fig. 8(b). Hence the compression zone of length $4L_{def}$ within the hinge has to accommodate a deformation of 4D. The maximum compressive strain that the material can withstand is ε_{pk} as in Fig. 6(a). Hence the maximum compressive deformation this hinge of length $4L_{def}$ can withstand is $\varepsilon_{pk}4L_{def}$ which is shown as $4D_1$ in Fig. 8(b). If a further rotation is imposed to cause the deformation $4D_2$, then the deformation shown shaded must be accommodated by the left arm of the wedge; the right arm of the wedge accommodates the deformation in the right hand hinge should it exist.

For the double hinge shown in Fig. 8(b) which is in a constant moment region, in theory the wedge can occur anywhere within the constant moment region. However only one wedge will form as seen in practice; this behaviour cannot be simulated with the strain based M/χ approach. The maximum slip the wedge has to accommodate is $4(D_2-\varepsilon_{pk}L_{def})$ which is the accumulation of the slips from each half element of length L_{def}. The deeper the beam the more elements the hinge encompasses. The crack spacing $2L_{def}$ is a function of the bar

diameter and concrete cover, whereas, the depth of the wedge d_w and consequently the length of the wedge L_w in Fig. 8(b) is a function of the depth of the compression zone and consequently a function of the depth of the beam. Hence the wedge length L_w encompasses more cracks at a spacing of $2L_{def}$ as the depth of the beam increases. Hence deep beams require more slip than shallow beams like slabs. As slip reduces the wedge capacity as in Fig. 6(b), deeper beams are more prone to wedge failure as seen in practice and which is a further behaviour that the M/χ approach cannot simulate.

VALIDATION OF HINGE MODEL

It is difficult to test hinges in isolation. Possibly the closest test model is an eccentrically loaded prism [23,24]. The hinge model is first applied to the analysis of eccentrically loaded prisms and then compared with test results. This paper is on the formation of hinges. However it may be worth noting that the moment rotation model depicted in Fig. 2 applies at all stages of loading that is at both serviceability and at ultimate. This partial interaction model has been used to determine the deflection of beams at serviceability [38] using closed form solutions for the tension stiffening [12] and gives good correlation with test results. In these analyses the element lengths as depicted in Fig. 2 were equal to the theoretical crack spacing which are in general two orders of magnitude smaller than the beam span so that the assumption of a constant moment region between cracks was shown not to affect the deflection.

Analysis of eccentrically loaded prism

The analysis of an eccentrically loaded prism is summarised in Fig. 9 where the prism is of length $2L_{def}$. Thick steel plates are often glued to the specimen faces A-A of the concrete in Fig. 9(d) so that the interface can take tension. A load P is then applied at an eccentricity *e* which causes a rotation θ as shown. It is, therefore, simply a question of fixing the rotation θ and varying the neutral axis $d_{n\text{-}a}$ until the resultant force is in line with the position of the applied force P after which moments are taken. The deformation is shown in Fig. 9(c), the stresses from these deformations in Fig. 9(b) and the resulting forces in Fig. 9(a). It is common practice to ignore the tensile capacity of the concrete but this can be included if the serviceability behaviour is important. The analysis can cope with compression steel as the deformation at the level of the compression steel $\delta_{reinf\text{-}comp}$ gives the real strain in the compression reinforcement of $\delta_{reinf\text{-}comp}/L_{def}$ and, consequently, the force in the reinforcement $P_{reinf\text{-}comp}$. It is also worth noting that the rotation of the prism face θ is equal to the rotation of the adjacent crack face. Hence as the analysis also gives the height of the crack, the slip of the reinforcement Δ and consequently the force in the reinforcement, should tension reinforcement be present, it can be determined from the partial interaction analyses depicted in Fig. 4.

The analysis in Fig. 9 will now be applied to eccentrically loaded prisms without any reinforcement as these are available in published literature. The tensile capacity of the concrete will be ignored as this has a very minor effect. Hence only the compressive material properties are required which are the ascending properties *a-b-c* in Fig. 6(a) and the shear-friction properties in Fig. 6(b).

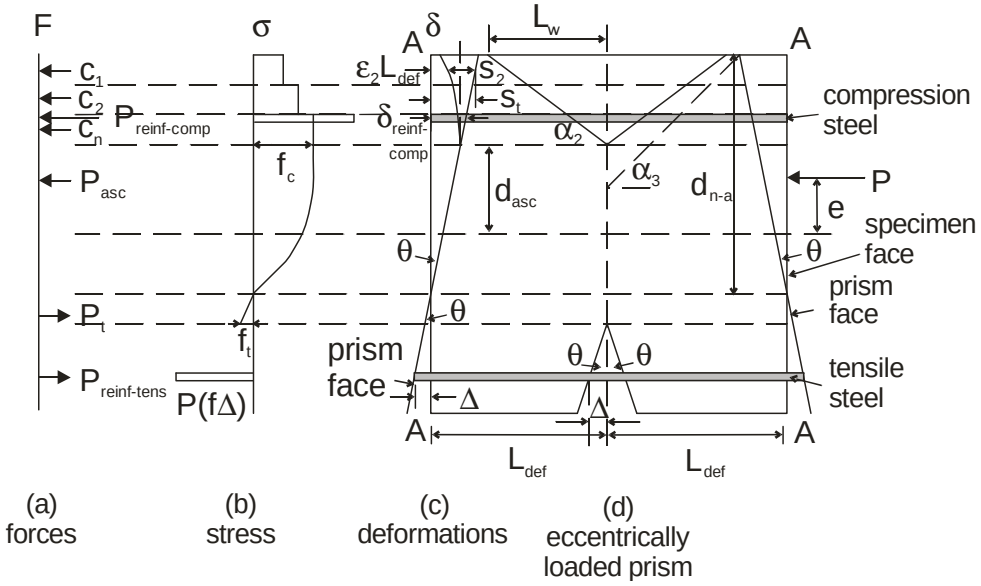

Figure 9: Analysis of eccentrically loaded prism

The analysis procedure can be split into two stages. Firstly for low levels of applied loads where the total rotation can be accommodated for through material deformation, the strain in the concrete remains within the ascending branch *a-b-c* in Fig. 6(a). Assuming Hognestad's parabolic stress distribution [41]

$$\sigma = f_c \left[\frac{2\varepsilon}{\varepsilon_{pk}} - \left(\frac{\varepsilon}{\varepsilon_{pk}} \right)^2 \right] \tag{1}$$

in which the peak strain can been determined using, [42]

$$\varepsilon_{pk} = (-0.067 f_c + 29.9 f_c + 1053).10^{-6} \tag{2}$$

the compressive load P_{asc} for a given depth of the neutral axis d_{n-a}, width of beam *b*, and peak compressive strain ε_m, which occurs at the top surface in Fig. 9(d) and in which ε_m is less than ε_{pk}, can be determined as follows

$$P_{asc} = b f_c d_{n-a} \left(\frac{\varepsilon_m}{\varepsilon_{pk}} \right) \left(1 - \frac{\varepsilon_m}{3\varepsilon_{pk}} \right) \tag{3}$$

In the second case, a softening wedge forms when the maximum material deformation has occurred, that is when the maximum effective strain in the concrete has exceeded the peak

material strain ε_{pk}. The force developed in the ascending region, P_{asc} in Fig. 9(a), is now be given by

$$P_{asc} = {}^{2}/_{3}\, f_c d_{asc} b \tag{4}$$

where the depth of the ascending region d_{asc} can be calculated from the displacement profile in Fig. 9(c) where d_{asc} is the region where the displacement is less than $\varepsilon_{pk}L_{def}$.

From the displacement profile in Fig. 9(c), the slip of the wedge can be determined; this is an iterative process and is carried out for each slice of the wedge. The analysis begins by guessing a concrete strain in the wedge ε_2 in Fig. 9(c) of $(\varepsilon_2)_g$, and based on the length of deformation, L_{def}, calculating the material deformation $(\varepsilon_2)_g L_{def}$. The wedge must then slip a distance S_2 as shown to make up the total required deformation S_t.

The analytical procedure has already been described previously using Fig. 7. The slip S_2 is resolved to give the slip of H_2 along the shear plane in Fig. 7(d). Hence from the shear-friction properties in Fig. 6(b), the combination of σ_n and τ_n must lie along the vertical line at the slip H_2. It is a question of finding the combination of σ_n and τ_n along this vertical line such that the resulting force C in Fig. 7(d) is horizontal, that is the algebraic sum of the vertical components of T and N in Fig. 7(d) is zero. The shear force T in Fig. 7(d) is given by

$$T = \frac{\tau_n d_e w}{\sin\alpha} \tag{5}$$

and the normal force N by

$$N = \frac{\sigma_n d_e w}{\sin\alpha} \tag{6}$$

where the angle of the wedge α which depends on the Mohr-Coulomb frictional property can be assumed to be 37^{o} and where the shear-friction properties are given by [37] and the units are in N and mm

$$\tau = \left[\left(-30.142 + 51.623\frac{\sigma_n}{f_c}\right)H\right]\left(\frac{f_c}{30}\right)^{0.91} + 0.497 f_c \tag{7}$$

Knowing the force C in Fig. 7(d) and, therefore, the stress developed in the wedge σ_2, the strain ε_2 in Fig. 9(d) can be determined using Eq. 1. If the strain is not equal to that which was initially guessed $(\varepsilon_2)_g$, the procedure has to be iterated until it does so. This procedure can be repeated for each wedge element to derive the wedge element forces C_1 to C_n in Fig. 9(a).

Having found the forces developed in both the wedge and the ascending region in Fig. 9(a) and for the case where reinforcing bars are not present, the location of the resultant force can be determined, and the depth of the neutral axis $d_{n\text{-}a}$ adjusted until the resultant force lies in

line with the applied load P. If the length of the wedge L_w in Fig. 9(d) exceeds L_{def}, then this forces the angle of the wedge to change to α_3 as shown to allow sliding; this does not occur in beams but is peculiar to eccentrically loaded prisms.

Comparison with test results

In order to quantify the full range stress-strain behaviour of concrete, Debernardi and Taliano [24] conducted a series of compression tests under displacement controlled conditions on prisms with the dimensions of 500x200x100 with the middle 336mm of the section having a reduced cross section of 150x100mm. During these tests, the deformations were recorded using a series of extensometers placed along both the tension and compression faces, and the resulting deformations were used to construct moment-rotation plots as in Fig. 10 for specimens with eccentricities of 24, 36 and 48mm.

The moment-rotation analysis depicted in Fig. 9 are shown as the 'theoretical' results in Figs. 10 where the moment at the start of cracking and at the start of softening or wedge formation are also shown. Importantly it can be seen that the 'theoretical' results have the same shape as the experimental results as well as good correlations in magnitude over the entire range of behaviour, including post cracking and softening of the section especially considering the variation in experimental results. It is suggested that the good correlation in shape would imply that this mechanics model simulates the test results, in contrast to the magnitudes which are dependent on the accuracy of the measured material properties which can be refined with time.

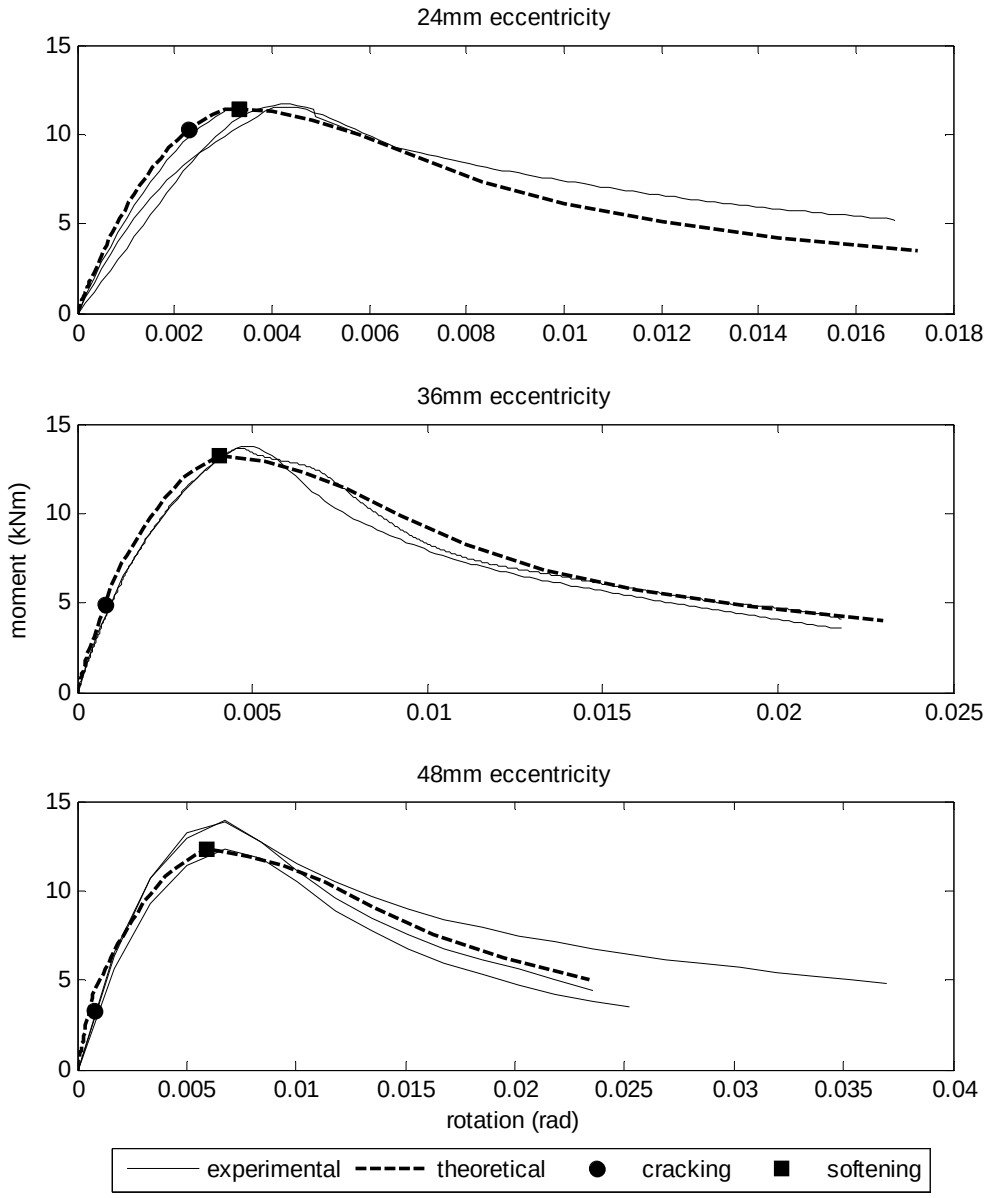

Figure 10: Comparison of Debernardi and Taliano test results

EXAMPLES OF MECHANICS SOLUTIONS

As the moment-rotation analysis is mechanics based, it is possible to develop closed form solutions to describe member behaviours which are purely dependent on material properties. As an example, a closed form solution has been developed to determine the crack height for a singly reinforced section such as that shown in Fig. 11 under serviceability loads.

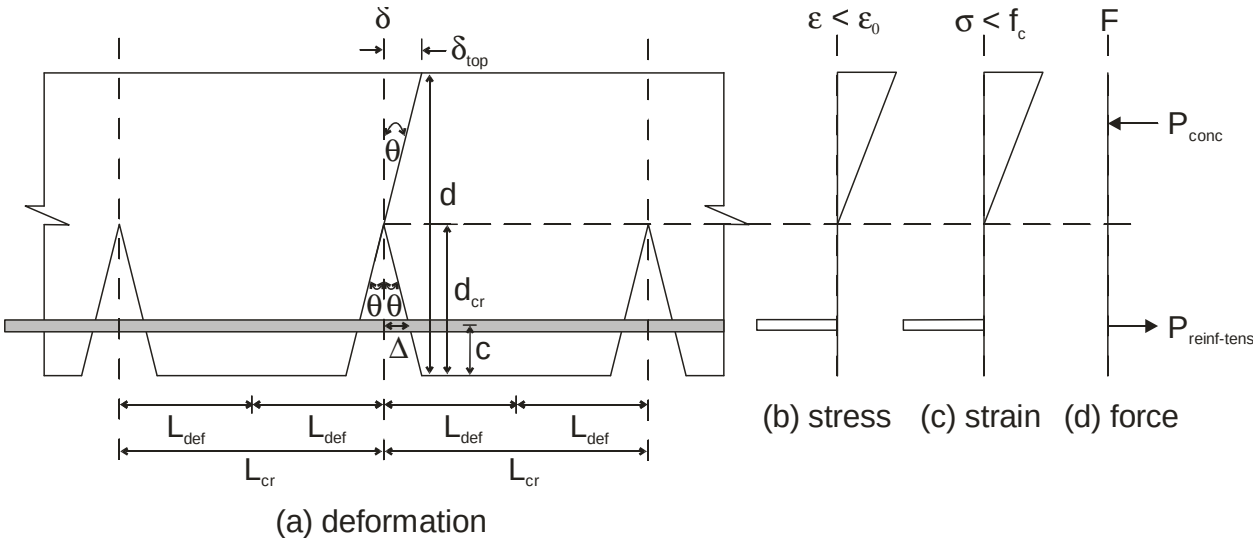

Figure 11: Idealisation for closed form solution

From the tension region in Fig. 11, the crack rotation θ is given by

$$\theta = \frac{\Delta}{d_{cr}-c} \tag{8}$$

where Δ is the reinforcement slip relative to the crack face, d_{cr} is the depth of the crack and d_{cr}-c is the distance of the reinforcement from the crack apex. From the compression region

$$\theta = \frac{\delta_{top}}{d-d_{cr}} \tag{9}$$

where δ_{top} is the maximum deformation in the compression zone and *d* is the depth of the beam. From Eqs. 8 and 9

$$\delta_{top} = \frac{\Delta(d-d_{cr})}{d_{cr}-c} \tag{10}$$

The maximum strain in the concrete is

$$\varepsilon = \frac{\delta_{top}}{L_{def}} \tag{11}$$

where, L_{def} is half the crack spacing, which for a linear ascending bond stress distribution [11] is

$$L_{def} = \frac{1}{\lambda_1} \tag{12}$$

where

$$\lambda_1 = \sqrt{k_e \beta_2} \tag{13}$$

in which k_e is the bond stiffness and β_2 is given by

$$\beta_2 = \frac{L_p}{A_r}\left(\frac{1}{E_r} + \frac{A_r}{E_c A_c}\right) \tag{14}$$

in which L_p is the perimeter of the reinforcing bar, A_r the area of the reinforcing bar, E_r Young's Modulus of the reinforcing bar, E_c Young's Modulus of the concrete and A_c is the area of concrete surrounding the reinforcing bar which interacts with the bar. From Eqs. 11 and 12, the force developed in the concrete is given by

$$P_{conc} = \frac{0.5\Delta(d-d_{cr})^2 \lambda E_c b}{(d_{cr}-c)} \tag{15}$$

where E_c is the modulus of the concrete as we are dealing with serviceability conditions and *b* is the width of the beam.

Now consider the tensile reinforcement in Fig. 11(a) which is surrounded by concrete of area A_c, as defined above, over a length $2L_{def}$ between adjacent cracks. The force developed for a given slip Δ using partial interaction theory [12] is given by

$$P_{reinf-tens} = \frac{n\Delta A_r E_r \lambda_1}{\tanh(1)} \tag{16}$$

where n is the number of reinforcing bars and E_r is the modulus of the steel reinforcement as we are dealing with serviceability. It may be worth noting that the partial-interaction mechanics principles that are used to derive Eq. 16 for the force in a reinforcing bar between adjacent cracks, are the same as that used to derive the force in the reinforcing bar when only one crack exists by Mohamed Ali et al [43]. Hence the equivalent expression to Eq. 16 from [43] could be substituted when dealing with a single crack.

As $P_{conc} = nP_{reinf\text{-}tens}$ at equilibrium, the crack height is given by

$$d_{cr} = \frac{dbE_c \tanh(1) + nA_r E_r \mp \sqrt{2dbE_c nA_r E_r \tanh(1) + n^2 A_r^2 E_r^2 - 2bE_c nA_r E_r c \tanh(1)}}{bE_c \tanh(1)} \tag{17}$$

It can be seen that the crack height is fixed for a given beam geometry and interestingly is independent of the applied moment and the bond characteristics. As a comparison, for a singly reinforced beam of depth 450 mm and width 300 mm with 4 No. 28 mm bars, Eq. 16 based on partial-interaction gives a crack height of 249 mm which is in close agreement with the 276 mm obtained using full-interaction moment-curvature transformed sections.

SUMMARY

A mechanics based moment rotation hinge model has been developed for beams at all stages of loading from serviceability to ultimate and during collapse. The mechanics hinge model is based on the principle of plane sections remaining plane and a linear real strain profile prior to the formation of disturbances such as flexural cracks in the tension zone and wedges in the compression zone. However after the formation of disturbances, the well established principle of plane sections remaining plane only applies at discrete locations and a linear effective, as opposed to real, strain profile is only applicable. The mechanics hinge model uses the well established principle of shear-friction to model concrete compressive failure and, hence, directly models the formation of wedges without the need for empirical hinge lengths or softening stress-strain concrete properties. Furthermore, the mechanics hinge model uses partial-interaction theory to model the development of flexural cracks and their widening and the consequential deflection of beams without the need for empirical models such as effective flexural rigidities or empirical hinge lengths. The mechanics based hinge model is shown to model the behaviour of eccentrically loaded prisms well and being a mechanics based model closed form solutions can be obtained as described.

Unlike empirically based models which should only be used within the bounds of the tests from which they were developed, this mechanics based model can in theory be used for any type of reinforced concrete beam just as long as the material properties are available. Hence it should help in the rapid development of new products such as the application of new types of reinforcement and new types of concrete as well as better refinement of existing design rules.

ACKNOWLEDGEMENTS

The financial support of the Australian research Council ARC Linkage Project LP 0883451 “Blast resistance of flexural high performance concrete members’ and ARC Discovery project DP0985828 ‘A unified reinforced concrete model for flexure and shear’ are gratefully acknowledged.

REFERENCES

[1] Gupta AK, Maestrini SR. Tension stiffening model for reinforced concrete bars. Journal of Structural Engineering 1990; 116 (3): 769-790.

[2] Wu Z, Yoshikawa H, Tanabe T. Tension stiffness model for cracked reinforced concrete. Journal of Structural Engineering 1991; 117 (3): 715-732

[3] Choi CK, Cheung SH. Tension stiffening model for planar reinforced concrete members. Computers & Structures 1996; 59 (1): 179-190.

[4] Marti P, Alvarez M, Kaufmann W. and Sigrist V. Tension chord model for structural concrete. Structural Engineering International 1998; 8 (4): 287-298.

[5] Yuan H, Teng JG, Seracino R, Wu ZS, Yao J. Full-range behavior of FRP-to-concrete bonded joints, Engineering Structures 2004; 26 (5): 543-691.

[6] Oehlers DJ, Liu IST, Seracino, R. The gradual formation of hinges throughout reinforced concrete beams. Mechanics Based Design of Structures and Machines 2005; 33 (3-4): 375-400.

[7] Warner RF, Foster SJ, Kilpatrick AE. Reinforced Concrete Basics: Analysis and Design of Reinforced Concrete Structures. Pearson Education, Australia 2007.

[8] Haskett M, Oehlers DJ, Mohamed Ali MS. Local and global bond characteristics of steel reinforcing bars. Engineering Structures 2008; 30 (2): 376-383.

[9] Mohamed Ali MS, Oehlers DJ, Griffith MC, Seracino R. Interfacial stress transfer of near surface mounted FRP-to-concrete joints. Engineering Structures 2008a; 30 (7): 1861-1868.

[10] Mohamed Ali MS, Oehlers DJ, Griffith MC. Shear transfer across cracks in FRP strengthened RC structures. ASCE Journal of Composites in Construction 2008b; 12 (4): 416-424.

[11] Yankelevsky DZ, Jabareen M, and Abutbul AD. One-dimensional analysis of tension stiffening in reinforced concrete with discrete cracks. *Engineering Struct*ures 2008; 30: 206-217.

[12] Muhamad R, Mohamed Ali MS, Oehlers DJ, and Griffith MC. The tension stiffening mechanism in reinforced concrete prisms. Submitted International Journal of Advances in Structural Engineering 2011.

[13] Mohamed Ali MS, Oehlers DJ, Haskett M, and Griffith MC. The discrete rotation in reinforced concrete beams. Submitted to ASCE Journal of Structural Engineering

[14] CEB. *CEB-FIP Model Code 90*. London; 1992.

[15] Eurocode- 2. ENV 1992-1-1. Eurocode 2: Design of concrete structures-Part 1-1: General Rules and Rules for Buildings, CEN; 1992.

[16] Bachmann, H. Influence of shear and bond on rotational capacity of reinforced concrete beams, Publications, IABSE, Zurich, 1970: Vol. 30, Part II, pp. 11-28.

[17] Baker ALL. Ultimate load theory applied to the design of reinforced and prestressed concrete frames, Concrete Publications Ltd., London (1956).

[18] Sawyer HA. Design of concrete frames for two failure states. In: Proceedings of the international symposium on the flexural mechanics of reinforced concrete, ASCE-ACI, Miami, 1964; p. 405–31.

[19] Corley GW. Rotation capacity of reinforced concrete beams, J Struct Eng ASCE 1966; 92 (ST10): 121–146.

[20] Mattock AH. Discussion of rotational capacity of reinforced concrete beams, by W.D.G. Corley. J Struct Div ASCE 1967; 93(2): 519–22.

[21] Priestley MJN, Park R. Strength and ductility of concrete bridge columns under seismic loading. ACI Struct J 1987; 84(S8): 61–76.

[22] Coleman J and Spacone E, Localization issues in force-based frame elements, J Struct Eng 2001; 127 (11): 1257–1265.

[23] Panagiotakos TB and Fardis MN, Deformations of reinforced concrete members at yielding and ultimate, *ACI Struct J* 2001; (March/April).

[24] Debernardi PG, Taliano M. Softening behaviour of concrete prisms under eccentric compressive forces. Magazine of Concrete Research 2001; 53 (4): 239-249

[25] Daniell JE, Oehlers DJ, Griffith MC, Mohamed Ali MS, Ozbakkaloglu T. The softening rotation of reinforced concrete members. Engineering Structures 2008; 30 (11) 3159-3166

[26] Haskett M. Oehlers DJ, Mohamed Ali MS Wu C. Rigid body moment-rotation mechanism for reinforced concrete beam hinges. Engineering Structures 2009a; 31 (5): 1032-1041.

[27] Oehlers D J, Mohamed Ali MS, Haskett M, Lucas W, Muhamad R Visintin P. (2011) FRP reinforced concrete beams - a unified approach based on IC theory. ASCE Composites for Construction, May/June, Vol. 15, No. 3, pp 293-303.

[28] Birkeland PW and Birkeland HW. Connections in Precast Concrete Construction, ACI Journal Proceedings 1966; 63 (3): 345-368.

[29] Hofbeck JA, Ibrahim IO, and Mattock AH. Shear Transfer in Reinforced Concrete, ACI Journal Proceedings 1969; 66 (2): 119-128.

[30] Walraven JC and Reinhardt HW. Theory and Experiments on mechanical behaviour of cracks in plain and reinforced concrete subjected to shear loading, Heron 1981; 26 (1A): 68 pp.

[31] Walraven JC, Frenay J. and Pruijssers A. Influence of Concrete Strength and Load History on the Shear-friction Capacity of Concrete Members, Prestressed Concrete Institute 1987; 32 (1): 66-85.

[32] Mansur MA, Vinayagam T, and Tan KH. Shear transfer across a crack in reinforced high-strength concrete", Journal of Materials in Civil Engineering 2008; 20 (4): 294-302.

[33] Mohamed Ali MS, Oehlers DJ, and Griffith MC. The residual strength of confined concrete, Advances in Structural Engineering 2010; 13 (4): 603-618.

[34] Lucas W, Oehlers DJ, Mohamed Ali MS and Griffith MC. The FRP reinforced concrete shear-friction mechanism. Accepted Advances in Structural Engineering 2011.

[35] Haskett M, Oehlers DJ, Mohamed Ali MS, and Sharma SK. The shear-friction aggregate-interlock resistance across sliding planes in concrete", Magazine of Concrete Research 2010; 62 (12): 907-924.

[36] Haskett M, Oehlers DJ, Mohamed Ali MS, and Sharma SK. Evaluating the shear-friction resistance across sliding planes in concrete", Engineering Structures 2011; 33:1357-1364.

[37] Haskett M, Oehlers DJ, Visintin P., and Mohamed Ali, MS. "Using shear-friction to simulate concrete softening in RC flexural members", submitted to Cement and Concrete Research 2011.

[38] Muhamad, R., Oehlers, D.J., and Mohamed, Ali, M.S. "Discrete rotation deflection of RC beams at serviceability". Accepted Proc. ICE Structures and Buildings

[39] Lucas W, Oehlers DJ and Mohamed Ali MS. The formulation of a shear resistance mechanism for inclined cracks in RC beams. Accepted ASCE Journal of Structural Engineering 2011.

[40] Mattock AH and Hawkins NM. Shear Transfer in Reinforced Concrete – Recent Research, Journal of Prestressed Concrete Institute 1972; 17 (2): 55-75.

[41] Hognestad E, Hanson NW and McHenry D. Concrete stress distribution in ultimate strength design. Journal of ACI 1955; 27 (4): 455-479.

[42] Tasdemir MA, Tasdemir C, Akyuz S, Jefferson AD, Lydon FD and Barr BIG. Evaluation of Strains at Peak Stresses in Concrete: A Three-Phase Composite Model Approach, Cement and Concrete Composites 1998; 20 (4): 301-318.

[43] Mohamed Ali, M.S., Oehlers, D.J., Griffith, M.C., and Seracino, R., (2008) "Interfacial stress transfer of near surface mounted FRP-to-concrete joints", Engineering Structures, Vol. 30, Issue 7, July, 1861-1868.

Statement of Authorship

A Mechanics Based Hinge Analysis for Reinforced Concrete Columns

ASCE Journal of Structural Engineering: submitted paper

Visintin, P. (candidate)

Prepared manuscript, performed all analyses, developed model and theory.

I hereby certify that the statement of contribution is accurate

Signed……..Date……

Oehlers, D.J..

Supervised research, provided critical manuscript evaluation and acted as corresponding author.

I hereby certify that the statement of contribution is accurate and I give permission for the inclusion of the paper in the thesis

Signed…….Date……

Wu, C.

Assisted in manuscript evaluation.

I hereby certify that the statement of contribution is accurate and I give permission for the inclusion of the paper in the thesis

Signed …….Date……

Haskett, M

Assisted in manuscript evaluation.

I hereby certify that the statement of contribution is accurate and I give permission for the inclusion of the paper in the thesis

Signed …….Date……

A Mechanics Based Hinge Analysis for Reinforced Concrete Columns

Visintin, P., Oehlers, D.J., Haskett, M. and Wu, C..

ABSTRACT

The lateral deformation behaviour of a reinforced concrete column is particularly important as it not only magnifies the moment but also affects the ability of the column and, subsequently, frame to sway and absorb energy at all stages of loading. The lateral deformation is affected by disturbed regions, such as tensile cracks or compression wedges, which are often simulated with the help of hinges whose properties are derived empirically. Being empirical, these hinges can only be used within the bounds of the tests from which they were derived, and in this respect are of limited use. In this paper, a mechanics based hinge is developed which can be used at all stages of loading, that is, at serviceability through to ultimate and also during failure. The mechanics based model is based on the principle of plane sections remaining plane, shear-friction theory which quantifies the behaviour of reinforced concrete across sliding planes, and partial-interaction theory that allows for slip between the reinforcement and the encasing concrete. Being mechanics based, it can be used for any type of reinforced concrete column, that is for any type of reinforcement and for any type of concrete just as long as the material properties are known. The mechanics model is shown to be in good agreement with published test results and can simulate not only multiple cracks if necessary but also the formation of wedges.

Keywords: reinforced concrete; reinforced concrete columns; reinforced concrete hinges; hinge lengths; shear friction; partial interaction; ductility; moment rotation.

INTRODUCTION

The resistance of a reinforced concrete frame against lateral loads such as earthquake and hurricane loads, depends not only on the applied lateral loads, but also on the position at which hinges form, whether in beams or columns, and also on the ability of these hinges to rotate and absorb energy, not just at the ultimate capacity but also during failure. It is common practice to use a strain based full-interaction moment-curvature analysis to quantify the curvature at the ultimate limit. And as this is a two-dimensional analysis, to then use an empirically derived hinge length over which the curvature can be integrated to ensure the rotation at the ultimate limit is equal to that determined experimentally at the ultimate limit. This approach has the following limitations. Being empirically based, this strain based approach can only be used within the bounds of the tests from which the empirical hinge lengths were derived and research has shown (Panagiotakos and Fardis 2001) that use outside these empirical bounds can lead to large scatter of results. These empirical hinge lengths generally only apply at the limit of the maximum moment capacity and so cannot be used at serviceability which means that very careful consideration has to be made as to where these

hinges occur and, furthermore, these empirical hinge lengths do not simulate the failure process.

A displacement based partial-interaction moment-rotation approach for simulating reinforced concrete hinges is described in this paper. It is based on the fundamental principle of plane sections remaining plane but not on the corollary of a linear strain profile where disturbances such as cracks or wedges have formed. This mechanics model simulates what is actually seen in practice. The model simulates the formation of cracks and the widening of cracks through partial interaction theory (Bachmann 1970; Yuan et al. 2004; Oehlers et al. 2005; Mohamed Ali et al. 2008a,b; Haskett et al. 2009; Muhamad et al. 2011) and the development of compression wedges, which leads to concrete softening, through the use of shear-friction theory (Birkeland and Birkeland 1966; Hofbeck et al. 1969; Walraven and Reinhardt 1981; Walraven et al. 1987; Mansur et al. 2008; Haskett et al. 2010; Haskett et al. 2011a,b). The model quantifies reinforcement debonding, yield and fracture and the gradual formation of compression wedges and their sliding and eventual failure. The model can also cope with shear failure (Lucas et al. 2011) if required, but this has not been included in this paper. Furthermore extension to allow for cyclic loading is possible through the use of a cyclic partial interaction model such as Visintin et al. (2011).

The basic fundamental mechanics principles of the mechanics hinge model for reinforced concrete columns are first described. A numerical simulation of this hinge model is then described although any convenient approach can be used. Furthermore, in order to simulate this hinge model, idealised assumptions are then given such as material properties which can be refined with time. The model is then validated with a comparison with tests on eccentrically axially loaded prisms.

FUNDAMENTAL PRINCIPLES OF COLUMN HINGE MECHANISM

An example of a hinge that occurs between column ends, which may occur in the case of an eccentrically loaded column, is shown in Fig. 1(a). The boundaries of the hinge A-A and B-B need to be placed at sections where the Euler-Bernoulli principle of plane sections remaining plane applies. It is convenient, but not essential in the analysis, to choose total hinge lengths or deformation lengths $2(L_{hg})_1$ which encompass the disturbances within the column such as that due to major tensile cracking and that due to the formation of wedges should they occur. And, furthermore, to choose total hinge or deformation lengths in which the moment can be assumed to be constant which is generally the case as the disturbed region is usually at least an order of magnitude smaller than the length of the column. Hence unlike the moment-curvature strain based approach where the hinge length is fixed for a given column cross-section, in this approach any convenient hinge length can be chosen as long as it encompasses the softening wedge. For example, the hinge boundary could have been taken at C-C in which the total hinge length is $2(L_{hg})_2$. In this case, the change in rotation between the

boundaries A-A and C-C is simply that due to the rotation between these boundaries which can be obtained by integrating the curvature should disturbances not occur within this region.

As the hinge in Fig. 1(a) is symmetrical about the mid-hinge section at D-D, the deformation A'-A' at rotation θ_A is the mirror image of that at B'-B' so that plane sections remain plane at the mid-height D-D. Hence the deformation at the boundary A-A shown as A'-A' has to be accommodated over the length $(L_{hg})_1$ and that due to B'-B' over the adjacent length of equal magnitude. Hence the length L_{hg} has to accommodate the adjacent boundary deformations so it may be more convenient to consider L_{hg} as one hinge length such that in Fig. 1(a) there are in effect two identical hinges which form about an axis of symmetry at D-D and with each hinge having a length of $(L_{hg})_1$. The cracks in the upper hinge in Fig. 1(a) rotate by θ_c by slip between the reinforcement and the crack face of Δ and the wedges at an angle α slip up to a maximum value of S as shown. The deformation A'-A' has to accommodate not only the material strains within the hinge boundaries but also the non-material deformations due to the wedge slip S and reinforcement slip Δ. This non-material deformation only occurs in disturbed regions.

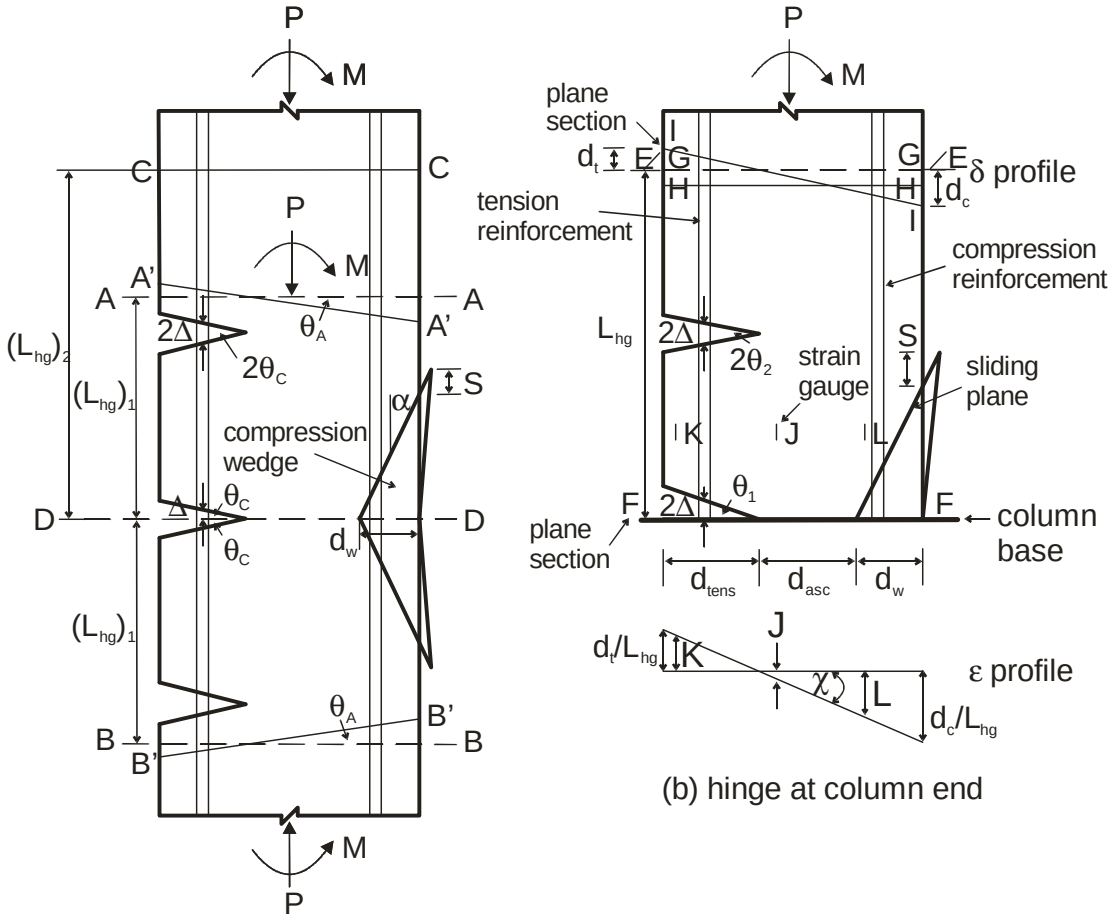

Fig. 1 Column hinges

A hinge at the base of a column, which may occur for example in a cantilever column is shown in Fig. 1(b). In this case, there is only one hinge of length L_{hg} as no axis of symmetry exists around the hinge and hence the principle of plane sections remaining plane applies not only at E-E but also at the base at F-F. Hence the linear variation in deformation I-I which has to be accommodated over the length L_{hg} produces a linear variation in strain as shown. For example, the deformation at the compression face d_c induces an overall strain d_c/L_{hg} and that at the tension face d_t/L_{hg}.

If disturbances do not occur within the hinge such as over the depth d_{asc} in Fig. 1(b), then the overall strains in this region in the strain profile are real strains and are what would be recorded by a strain gauge at J which is shown as point J on the strain profile in Fig. 1(b). Flexural cracks may form in the tension region of depth d_{tens} making it a disturbed region. These cracks widen through slip between the reinforcement and the concrete which at the crack face is shown as Δ and which causes the discrete rotation at each crack θ. Hence in the cracked region of depth d_{tens}, the deformation is due to both strain in the concrete and crack widening that is the strain in this region is an effective strain such that strain gauge K would not measure the corresponding strain in the strain profile. Concrete softening takes place as wedges of depth d_w form in the compression region. The wedges have a vertical component of slip S along the sliding plane such that the deformation I-I is a result of both this slip and the concrete strains so that the strains over d_w are effective and are strains that would not be recorded by a strain gauge at L.

In summary, when disturbances do not occur within the hinge, the strain profile in Fig. 1(b) is a real strain profile. Hence the corollary to the Euler-Bernoulli principle of a linear real strain profile, which gives real curvatures χ and real flexural rigidities EI, applies and which depends on material properties. In these circumstances a strain based approach is applicable. In comparison, when disturbances do occur, there is a linear effective strain profile, which gives an effective curvature and an effective flexural rigidity which depends not only on material properties but also on the crack widening mechanism and the wedge sliding mechanism. In these circumstances a deformation based approach is required, as presented in this paper.

MODELLING OF MECHANICS HINGE

A numerical procedure for quantifying the behaviour of hinges is proposed. The model is described for the full range of stress resultants that can be applied, which ranges from concentrically loaded hinges with zero moment (e.g. a column in pure compression), to hinges subjected to predominantly moment (e.g. a beam). As we are dealing with a small region of the column that is the hinge, it will be assumed, for convenience of explanation, that the hinge is in a constant moment region although variable moments can be accommodated.

Deformation of hinges under pure compression

Consider the concentrically loaded hinge in Fig. 2(a) in which G-G and F-F are the Euler-Bernoulli boundaries where plane sections remain plane. As the hinge boundary G-G is moved downwards under increasing applied stress, the contraction as a proportion of L_{hg} is a real strain so that the stress-strain relationship follows the ascending path O-A-B in Fig. 3 which may be considered a material property. The peak stress f_c in Fig. 3 is the maximum stress that the concrete material can resist and the peak strain ε_{pk} at the onset of f_c is the maximum strain the concrete material can resist. Hence the maximum deformation the hinge material can resist is $\varepsilon_{pk}L_{hg}$ which is shown as line H-H in Fig. 2.

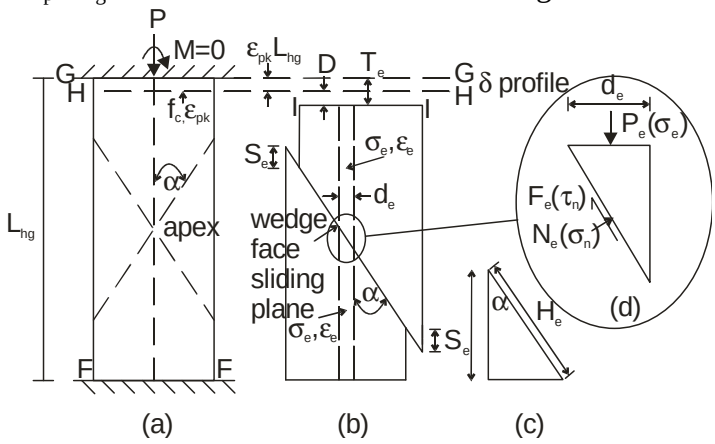

Fig. 2 Concentrically loaded hinge

If a further displacement D is now applied from H-H to I-I in Fig. 2(b), then this increase in displacement D cannot be accommodated by concrete material strains but has to be accommodated by slip of the wedge which has a vertical component S_e as shown and this slip of the wedge results in concrete softening. The wedge can form as in Fig. 2(a) or as in Fig. 2(b) depending on the restraints at the boundaries and their distance apart. However, the mechanics are virtually the same except that in Fig. 2(a) localised crushing of the apex is required to accommodate interface slip. The angle of the wedge α depends on the frictional properties of the concrete (Mohamed Ali et al. 2010) and for normal concrete is about 30^o. The total displacement T_e from G-G to I-I in Fig. 2(b) is accommodated by strains in the concrete ε_e and by the vertical component of the slip S_e such that the effective strain is given by

$$\varepsilon_{eff} = \frac{T_e}{L_{hg}} = \varepsilon_e + \frac{S_e}{L_{hg}} \tag{1}$$

That is the falling branch of the concrete stress-strain relationship, B-D in Fig. 3, is not a material property, but rather the strains are effective strains because they are the result of both material and non-material deformation. The falling branch must therefore be considered

a mechanism where the material deformation is controlled by the stress-strain relationship A-B in Fig. 3, and the non material deformation S_e is controlled by the shear friction properties in Fig. 4.

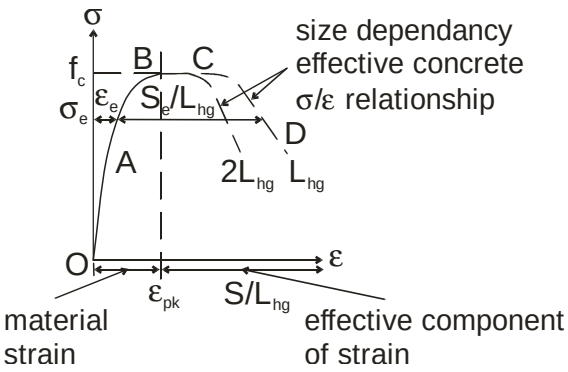

Fig. 3 Concrete material properties

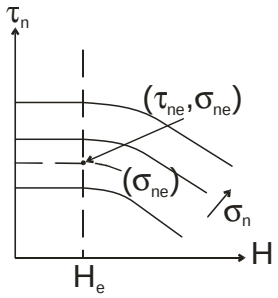

Fig. 4 Concrete shear-friction properties

For example, if the applied stress at displacement T_e at I-I is σ_e in Fig. 3, then the material strain throughout the hinge is ε_e. Therefore from Eq. 1, the slip S_e required is the deformation T_e less that which is accommodated by the concrete material $\varepsilon_e L_{hg}$. It can be seen in Fig. 3 that at a stress level σ_e, the real strain is ε_e and the effective component of strain is S_e/L_{hg}. It can also be seen in Eq. 1 and in Fig. 3 that if the hinge length is doubled to $2L_{hg}$ then the effective component of strain is halved. Hence effective concrete stress-strain relationships are size dependent and, consequently, have to be used with care. The alternative is to use a shear-friction approach which automatically accounts for size dependency as follows.

Because of the uniform displacement that is applied to the hinge in Fig. 2(b), the vertical component of the slip S_e is uniform along the width of the hinge and has a component along the sliding plane of H_e as shown in Fig. 2(c). Let us now consider an element of width d_e in Fig. 2(b) that is shown enlarged in Fig. 2(d), that is subjected to an applied stress σ_e (material strain ε_e) and consequently applied force P_e in which there is a vertical component of slip S_e that can be derived from the applied displacement T_e as in Eq. 1. From equilibrium of the forces in Fig. 2(d), can be derived the normal force N_e and shear force F_e adjacent to the sliding plane from which can be derived the normal stress to the sliding plane σ_n and the

shear stress across the sliding plane τ_n. Hence the shear-friction properties in Fig. 4 can be derived from this type of test (Haskett et al. 2010, Haskett 2011a,b).

Conversely the shear-friction properties in Fig. 4 can be used to analyse the hinge in Fig. 2(b). The applied displacement T_e is accommodated by material strain $\varepsilon_e L_{hg}$ and the vertical component of the wedge slip S_e which has a sliding component H_e; it may be worth noting that this is only a good approximation as it does not include the second order effect of the crack widening due to aggregate interlock (Haskett et al 2010). A solution can be found by iterating. Let us guess that to induce the applied displacement T_e the applied stress is $(\sigma_e)_{guess}$ at which the material strain is $(\varepsilon_e)_{guess}$. The vertical component of the wedge slip S_e can be derived from Eq. 1 and consequently the sliding component of the slip H_e from Fig. 2(c). It is simply a question of moving along the vertical line at H_e in Fig. 4 until the combination of τ_n and σ_n when input into Fig. 2(d) gives a vertical component of P_e. If the resulting σ_e is not equal to $(\sigma_e)_{guess}$ then the procedure has to be iterated until it does so.

Rotation of hinges whilst in compression

The column hinge in Fig. 5(b) is subjected to a moment and axial load of magnitudes such that the extending displacements induced by the moment are less than the contracting displacements induced by the axial load, and therefore the remains purely in compression. This case allows for the illustration of the formation of wedges. The axial load P is first applied at the hinge boundary G-G and the moment M gradually increased until the strain on the surface of the concrete on the right hand side just reaches the concrete material peak strain ε_{pk} in Fig. 3. This is shown as deformation I-I' in Fig. 5(a) where the contraction G-I' is equal to $\varepsilon_{pk} L_{hg}$. Up to this point, the wedge has not formed as the deformation can be accommodated by the strain in the material. Hence a strain based moment-curvature (M/χ) analysis when integrated over the hinge length L_{hg} will give exactly the same results as the displacement based moment-rotation (M/θ) analysis. This is shown as O-A in Fig. 6 to emphasise the fact that there are no differences between the two approaches prior to disturbances being formed and also the fact that the M/θ applies at serviceability.

Let us now increase the rotation in Fig. 5(a) to J-J'. Any component of the deformation that exceeds $\varepsilon_{pk} L_{hg}$ shown as the shaded region adjacent to I'-J' cannot be accommodated by material deformation. This shaded deformation can only be accommodated by wedge slip so that a wedge of depth d_{w1} has to form. If in this example we assume that the peak material strength f_c can be maintained over the depth d_{w1} such that we are moving along B-C in Fig. 3 so that the material strain in this region remains at ε_{pk}, then the slip of the wedge at the surface of the column is I'-J'.

Let us now increase the rotation in Fig. 5(a) to θ_K that is line K-K' such that the stress on the right hand surface of the column is now reducing along C-D in Fig. 3, that is it is less than f_c

so that the material strain is less than ε_{pk}. The deformation M-I'-K' in Fig. 5(a) cannot be accommodated by material deformation as the deformation in this region exceeds $\varepsilon_{pk}L_{hg}$ so that the depth of wedge required is now d_{w2}. Consider the element of the wedge of width d_2 where the strain is ε_2 which is less than ε_{pk} so that the material can accommodate a deformation of $\varepsilon_2 L_{hg}$ which means that the wedge has to take up the remaining deformation that is to accommodate a slip S_2 as shown. Hence the slip that the wedge has to accommodate is now M-P-K' being zero at M with a maximum value at the column surface of S_s as shown.

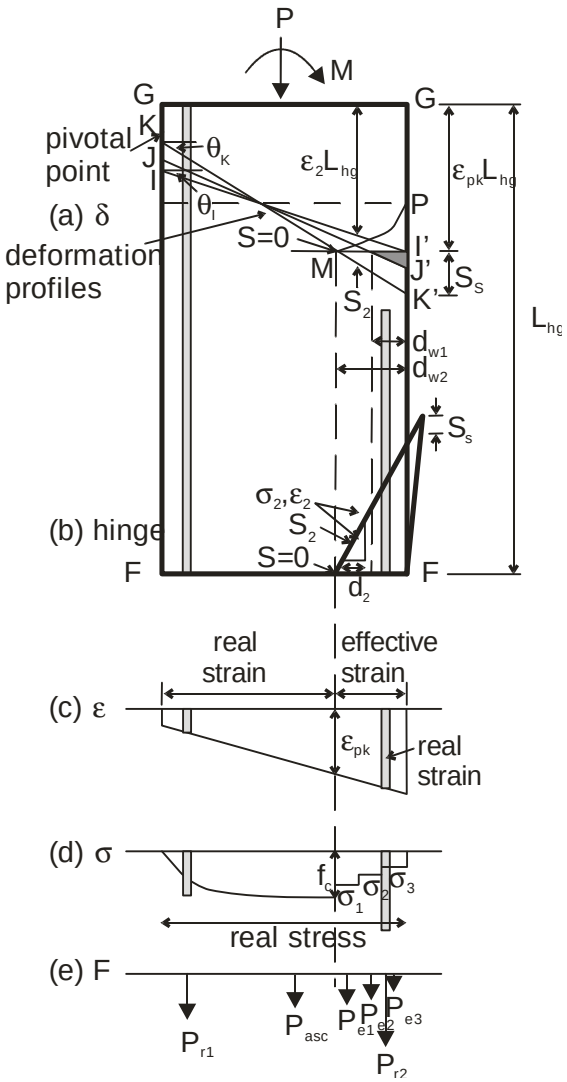

Fig. 5 Rotation of hinge whilst in pure compression

A numerical solution can be obtained by iteration. As an illustration, let us impose a displacement G-K on the left hand surface of the column in Fig. 5(a). Using K as a pivotal point, rotate K-K', that is vary θ_K, until equilibrium is achieved. For example for the displacement K-K', the effective strain variation is given in Fig. 5(c). For the longitudinal reinforcement on either side of the column and for the concrete where the strain is less than ε_{pk}, these are real strains so from their material properties the stresses in Fig. 5(d) can be

obtained so that the forces in Fig. 5(e) for P_{r1}, P_{asc} and P_{r2} can be derived as explained previously. This leaves the force in the wedge region to be determined, as explained previously using Fig. 2, an iterative procedure, which has also been used in Visintin et al. (2011), can be used. Take the wedge element of width d_2 in Fig. 5(b). Start by guessing the stress $(\sigma_2)_{guess}$ from which the material strain ε_2 can be determined using any material stress-strain relationship, that is O-B in Fig.3. Since it is known the stress σ_2 lies between 0 and f_c and the material strain between 0 and ε_{pk} a simple bisection method can be used to iterate as follows. For the guessed stress the material deformation $\varepsilon_2 L_{hg}$ in Fig. 5(a) is known and consequently for the given deformation shown in Fig. 5(a) so too is the vertical component of the wedge slip S_2. From Fig. 2(c) can be derived the sliding component H_2 and for this value of H_2 in Fig. 4, it is a question of finding the combination of τ_{n2} and σ_{n2} that gives a vertical component of P_e in Fig. 2(d) that is P_2. If the associated stress σ_2 is not equal to $(\sigma_2)_{guess}$ then iterate until it is. This gives the stress σ_2 in Fig. 5(d) and P_{e2} in Fig. 5(e). As a termination criterion, it is sufficient that the calculated stress is within 5% of the guessed stress, and convergence can often be achieved in less than 20 iterations. When implementing it is known that the strain in the wedge is initially close to ε_{pk} and hence an initial guess of close to ε_{pk} leads to a rapid solution, this solution can then be used as the initial starting guess for subsequent analyses where the rotation has increased.

The procedure needs to be repeated for the other elements of the wedge as unlike the concentrically loaded prism in Fig. 2, in the case in Fig. 5 the slips vary over the section depth. For the case of a column subjected to a fixed applied load P and then increasing moments, it is simply a case of rotating θ_K until the resultant force from Fig. 5(e) is P and then taking moments. Alternatively if an axial load P is applied gradually at an eccentricity *e*, then θ_K can be rotated until the resultant force from Fig. 5(e) is in line with the eccentricity *e*.

The procedure described above can be repeated at different pivotal points such as I and J in Fig. 5(a) to derive the M/θ response such as in Fig. 6. This moment-rotation procedure gives the full range of M/θ: from serviceability to the peak capacity that is O-A; at the ultimate limit state whilst the maximum moment capacity M_{max} is being maintained along A-B; and also during failure B-C. However, it may be worth bearing in mind that this is in contrast to the M/χ empirical hinge length approach which is normally only applied at the ultimate limit of the maximum moment M_{max} to quantify the rotation capacity at B.

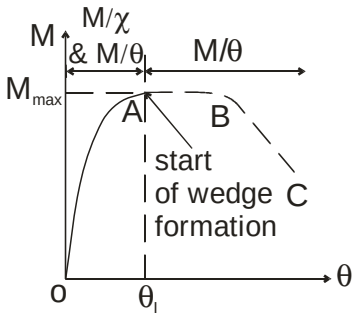

Fig. 6 Hinge moment-rotation

Rotation of hinges that accommodate flexural cracks

Figure 7 illustrates a column hinge in which flexural cracking has occurred. The deformation H-H has to accommodate flexural cracking and its associated tension stiffening that is the interaction between the tension reinforcement and the concrete. It is now common practice to simulate tension stiffening, that is the post cracking behavior of the concrete, by considering individual reinforcing bars of area A_r embedded in individual concrete prisms of area A_c and in which the bond-slip properties τ/δ allow for slip between the reinforcement and concrete (Gupta and Maestrini 1990; Wu et al 1991; Choi and Cheung 1996; Marti et al 1998; Yuan et al 2004; Oehlers et al 2005; Warner et al 2007; Mohamed Ali M.S. et al 2008a,b; Haskett et al 2008; Mohamed Ali M.S. et al 2011; Muhamad, R., 2011).

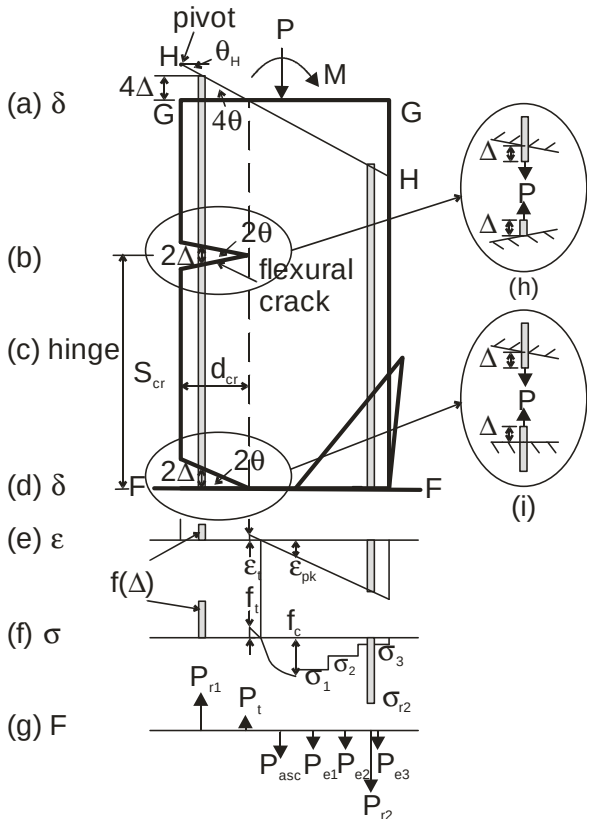

Fig. 7 Rotation of hinge accommodating cracks

A numerical model that explains the mechanics behind the partial-interaction tension stiffening model (Haskett et al 2008; Oehlers et al. 2011) is illustrated in Fig. 8 where three elemets for the analusis and the associated equations are shown. The prism is sliced into elements of very short lengths L_s which are shown separated and where A-A is any crack face. The bar is pulled out from the crack face a distance Δ_1 so that, from the known material bond-slip properties τ/δ, the bond force in the first element B_1 can be determined. It is a question of finding the force P_{r1} that induces this imposed crack face slip Δ_1. This can be done by first guessing P_{r1} in which case the stress in the bar and the accompanying strain ε_{r1} is known. At the crack face, the stress in the concrete is zero so that the strain in the concrete ε_{c1} can be taken as zero as the element thickness L_s is deliberately very small. The slip-strain (ds/dx) is the algebraic difference in strain between the reinforcement and the concrete which for Element 1 is ε_{r1}-ε_{c1} as shown. The change in slip over Element 1, $\delta\Delta_1$, is the integration of the slip-strain over L_s as shown. Hence both the slip and slip-strain in Element 1 are known. The analysis can be repeated for Element 2 where the force in the reinforcing bar P_{r2} is now P_{r1}-B_1, the force in the concrete prism P_{c2} which is now B_1 and the slip between the reinforcing bar and the concrete Δ_2 is now Δ_1-$\delta\Delta_1$ from which the bond force B_2 can be derived. From these quantities can be derived the slip strain in Element 2 $(ds/dx)_2$ and the increase in slip $\delta\Delta_2$ that affects the next element along.

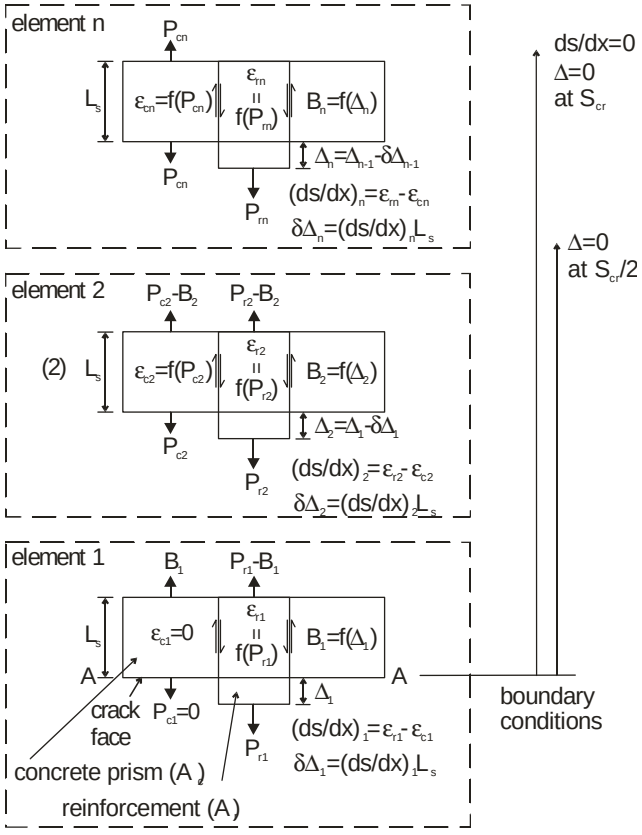

Fig. 8 Tension stiffening

The above analysis gives the variation in slip-strain, ds/dx, and slip, Δ, along the prism. It is a question of finding the force P_{r1} such that the slip-strain and slip tend to zero at the same position shown as S_{cr} in Fig. 8 as this is a position of full-interaction and it is also the position of the next crack that is the crack spacing S_{cr} in Fig. 7(c). This analysis can also be used to determine the force in the reinforcing bar P_{r1} in Fig. 8 that causes the concrete prism to crack at the tensile strength of the concrete f_{ct} so that it gives not only the crack spacing S_{cr} in Fig. 7(c) but also the force in the reinforcing bar in Fig. 7(d) that causes the crack at Fig. 7(b). Once the next crack or cracks at spacing S_{cr} in the hinge occurs, the procedure illustrated in Fig. 8 can also be used to determine the P/Δ relationship at the cracks by simply changing the boundary condition to $\Delta = 0$ at $S_{cr}/2$.

Prior to disturbances being present, that is prior to the formation of flexural cracks or wedges, a strain based M/χ analysis and the displacement based M/θ analysis as illustrated in Fig. 5 will give the formation of the initial crack at F-F in Fig. 7(d). After this initial crack has formed, the strain based M/χ analysis will not give the formation of subsequent cracks as the hinge is now disturbed. In this case, the partial-interaction analysis in Fig. 8 can be used to: quantify the P/Δ relation at F-F in Fig. 7(d) shown enlarged in Fig. 7(i); when and where the next crack or cracks at the spacing S_{cr} occur or should they occur; and also the P/Δ relationships at both F-F and at the position S_{cr} shown enlarged in Fig. 7(h) after the cracks have formed. Full details are given elsewhere (Haskett et al 2008; Oehlers et al. 2011).

The analysis of multiple cracks is similar to that described for Fig. 5. Point H in Fig. 7(a) can be used as a pivot and the Euler-Bernoulli boundary H-H rotated θ_H to find a solution. It is often convenient to assume that the tensile strain in the concrete over the cracked region of width d_{cr} is zero. In this case, the imposed rotation θ_H is also the total rotation of the cracks which for the two cracks shown is 4θ. Hence from the linear variation in crack width, can be determined the slip of the reinforcement Δ and from the analysis in Fig. 8, the force in the reinforcement at the crack face P_{r1} as required in Fig. 7(g). As explained for the analysis in Fig. 5, it is simply a question of rotating θ_H to be in equilibrium with the applied forces and varying the displacement 4Δ to get the full moment rotation in Fig. 6. In this case, the M/χ and M/θ approaches give identical results in Fig. 6 until the initial crack or wedge occurs that is whichever occurs first. It may be worth noting that the crack faces in Fig. 7 have been drawn as straight lines for convenience. They could have been drawn as curved but what is important is that there is a linear variation in crack widths from zero at the apex to a maximum at the column surface.

VALIDATION OF HINGE MECHANISM

In order to validate the hinge mechanism, reinforced eccentrically loaded prisms, where second order effects are minimal, have been simulated. In the simulations, the following

material stress-strain relationship used for the ascending branch O-A-B in Fig. 3 is that of Hognestad (1955)

$$\sigma = f_c \left[\frac{2\varepsilon}{\varepsilon_{pk}} - \left(\frac{\varepsilon}{\varepsilon_{pk}} \right)^2 \right] \tag{2}$$

where the peak strain has been calculated using either the empirically derived relationship developed by Wee et al. (1996)

$$\varepsilon_{pk} = 0.00078 f_c^{0.25} \tag{3}$$

or by Tasdemir et al (1998)

$$\varepsilon_{pk} = \left(-0.067 f_c + 29.9 f_c + 1053 \right).10^{-6} \tag{4}$$

and the following shear-friction properties that were used, Fig. 4, are those of Haskett et al. (2011b)

$$\tau = \left[\left(-30.142 + 51.623 \frac{\sigma_N}{f_c} \right) H \right] \left(\frac{f_c}{30} \right)^{0.91} + 0.497 f_c \tag{3}$$

where the units are in N and mm. Finally, the bond slip properties suggested by CEB (1992) have been used, as well as the stress-strain relationship developed by Dhakal and Maekawa (2002) to allow for buckling of the compression reinforcement.

The eccentrically loaded prisms tested by Kim and Yang (1995) with a length of 240mm have been simulated. While longer specimens were also tested, these were not considered as the second order effects were found to be significant. The specimens all have 80mm x 80mm cross sections and are reinforced with 4 #2 bars to give a reinforcing ratio of 1.98%, or 8 #2 bars to give a reinforcing ratio of 3.95%. For each reinforcing ratio, three concrete strengths were tested, namely 25.5MPa, 63.5MPa and 82.6MP.

The theoretical results are shown as broken lines in Fig. 9 which also shows the onset of cracking, buckling and softening. In the case of the specimen with ρ = 1.98% and f_c = 25.5MPa, this test was reported to have failed prematurely which is in line with the theoretical prediction. In order to show the sensitivity of the analysis to the material properties, the peak strain models of both Wee et al. (1996) and Tasdamir et al.(1998) have been used and as can be seen can influence the magnitudes of the theoretical results significantly, particularly at higher concrete strengths. It can be seen that the theoretical results have the same shape as the experimental results which suggest that the mechanics

model is capable of simulating the tests. While a reasonable correlation with the magnitudes of the results is seen over the entire range of behavior, that is before cracking, after cracking and during softening, it can be expected that the magnitudes can be improved as the shear-friction material properties are refined with time.

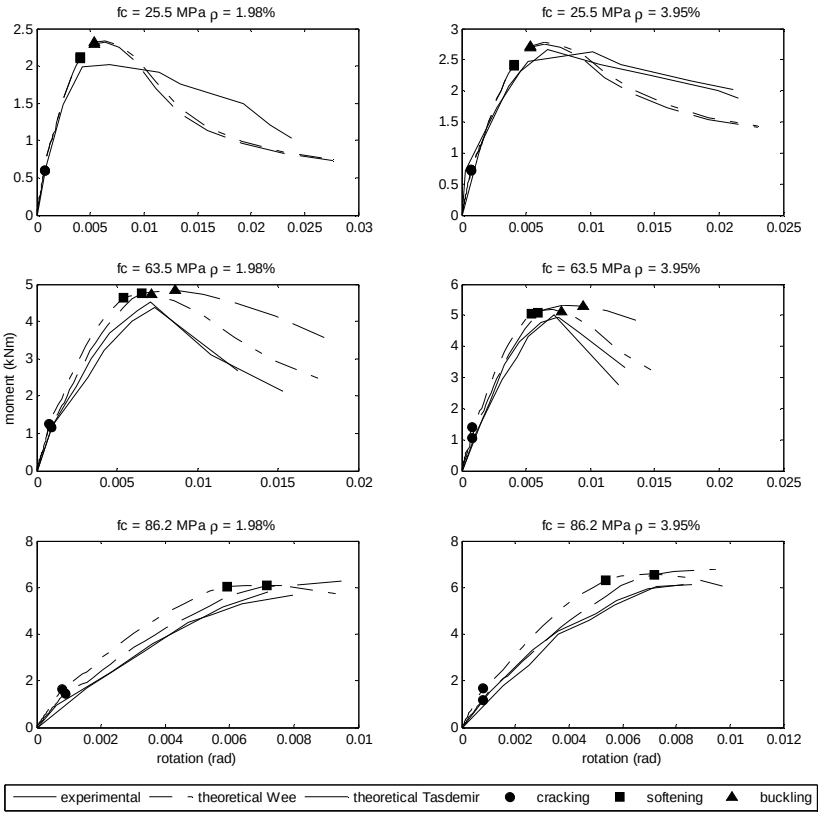

Fig. 9 Simulation of reinforced eccentrically loaded prisms

It is important to note, as seen in Fig. 10, that the M/θ relationship can be converted into a moment-equivalent flexural rigidity (EI_{equ}) relationship. This is done by fist deriving the curvature, which is simply the rotation divided by the length over which is acts, that is $\chi = \theta \backslash L_{def}$. The equivalent EI is not the same as the effective EI derived from transformed sections as the M/θ approach accounts for partial interaction between the reinforcement and the concrete as well as the formation and failure of softening wedges. Having derived the (M/EI_{equ}) relationship calculating member deflection simply becomes a matter of determining the curvature distribution for a given moment distribution and integrating twice as in a traditional analysis.

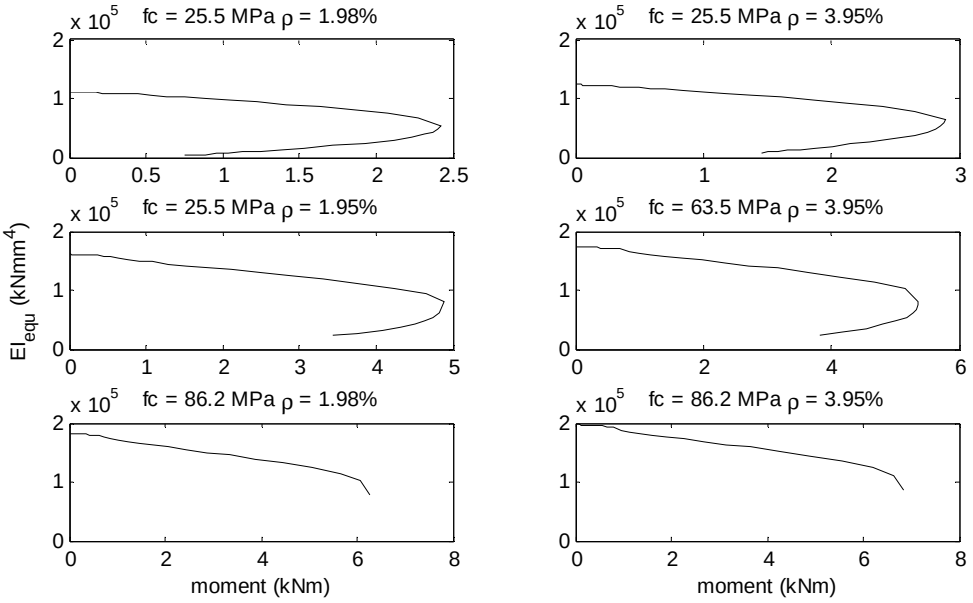

Fig. 10 Moment-EI_{equ} relationships for eccentrically loaded prisms

CONCLUSIONS

A mechanics based model for hinges in reinforced concrete columns has been described and shown to simulate test results closely. The model is based on the Euler-Bernoulli principle of plane sections remaining plane. It is also based on the Euler-Bernoulli strain based corollary of a linear strain profile prior to the formation of flexural cracks or wedges but not after these disturbances have occurred. After disturbances, the mechanics model shows that an effective linear strain profile does occur but which does not just depend on strains but also on the partial-interaction mechanisms that allow wedges to form and reinforcement to slip allowing cracks to widen. The mechanics model also uses the well-established principles of partial-interaction theory and shear-friction theory to model disturbances. Unlike current hinge models, this mechanics model can be applied at all stages of loading from initial loading at serviceability to the maximum capacity at ultimate and beyond to failure whilst softening. Being a mechanics based model it can be applied to any type of reinforced concrete column, with any type of reinforcement and any type of concrete. And being a mechanics based model it does not require empirical testing to develop components of the model but just to determine the material properties.

ACKNOWLEDGEMENTS

The financial support of the Australian research Council ARC Linkage Project LP 0883451 "Blast resistance of flexural high performance concrete members' and ARC Discovery project DP0985828 'A unified reinforced concrete model for flexure and shear' are gratefully acknowledged.

REFERENCES

Bachmann, H. (1970). “Influence of shear and bond on rotational capacity of reinforced concrete beams.” Publications, IABSE, Zurich,: Vol. 30, Part II, 11-28.

Birkeland, P. W., and Birkeland, H. W. (1966). “Connections in Precast Concrete Construction.” *ACI Journal Proceedings*, 63(3), 345-368.

CEB.1992. CEB-FIP Model Code 9*0*. London.

Choi, C. K., and Cheung, S. H. (1996). “Tension stiffening model for planar reinforced concrete members.” *Computers & Structures*, 59(1), 179-190.

Dhakal, R. P., Maekawa, K. (2002). “Modeling for Postyield Buckling of Reinforcement,” *Journal of Structural Engineering*, 128(9), 1139-1147.

Gupta A. K., and Maestrini S. R. (1990). “Tension stiffening model for reinforced concrete bars.” *Journal of Structural Engineering*, 116(3), 769-790.

Haskett, M., Oehlers, D.J., Mohamed Ali, M.S., and Sharma, S.K., (2011a) “Evaluating the shear-friction resistance across sliding planes in concrete,” *Engineering Structures*, 33, 1357-1364.

Haskett M., Oehlers DJ., Visintin P., and Mohamed Ali, MS. “The shear-friction material properties of unconfined concrete”, submitted to Cement and Concrete Research 2011b.

Haskett, M., Oehlers, D.J., Mohamed Ali M.S., and Sharma, S. K.. (2010) “The shear-friction aggregate-interlock resistance across sliding planes in concrete”. *Magazine of Concrete Research*, 62(12), 907-924.

Haskett, M., Oehlers, D. J., Mohamed Ali, M. S., and Wu, C. (2009). “Yield penetration hinge rotation in reinforced concrete beams.” *ASCE Structural Journal*, 135(2), 130-138.

Haskett, M., Oehlers, D. J., and Mohamed Ali, M. S. (2008). “Local and global bond characteristics of steel reinforcing bars.” *Engineering Structures*, 30(2), 376-383.

Hofbeck, J. A., Ibrahim, I. O., and Mattock, A.H. (1969), “Shear Transfer in Reinforced Concrete,” *ACI Journal Proceedings*, 66(2), 119-128.

Hognestad, E, Hanson, N. W., and McHenry, D. (1955). “Concrete stress distribution in ultimate strength design.” *Journal of ACI*, 27(4), 455-479.

Kim, J. K., and Yang J.K. (1995). “Buckling behaviour of slender high-strength concrete columns.” *Engineering. Structures*, 17(1), 39–51.

Lucas, W., Oehlers, D. J., and Mohamed Ali, M. S. (2011). “The formulation of a shear resistance mechanism for inclined cracks in RC beams.” Accepted *ASCE Journal of Structural Engineering*.

Mansur, M.A., Vinayagam, T., and Tan, K. H. (2008), “Shear transfer across a crack in reinforced high-strength concrete.” *Journal of Materials in Civil Engineering*, 20(4), 294-302.

Marti, P., Alvarez, M., Kaufmann, W., and Sigrist, V. (1998). “Tension chord model for structural concrete.” *Structural Engineering International*, 8(4), 287-298.

Mohamed Ali, M. S., Oehlers, D. J., and Griffith, M. C. (2010). “The Residual Strength of Confined Concrete.” *Advances in Structural Engineering*, 13(4), 603-618.

Mohamed Ali, M. S., Oehlers, D. J., Griffith, M. C., and Seracino, R. (2008a) “Interfacial stress transfer of near surface mounted FRP-to-concrete joints.” *Engineering Structures*, 30(7), 1861-1868.

Mohamed Ali, M. S., Oehlers, D. J., and Griffith, M. C. (2008b). “Shear transfer across cracks in FRP strengthened RC structures.” *ASCE Journal of Composites in Construction*, 12(4), 416-424.

Muhamad R., Mohamed Ali, M. S., Oehlers, D. J., and Griffith, M. C. (2011). “The tension stiffening mechanism in reinforced concrete prisms.” Submitted to *Advances in Structural Engineering*.

Oehlers, D. J., Mohamed Ali, M. S., Haskett, M., Lucas, W., Muhamad, R. and Visintin, P. (2011). “FRP reinforced concrete beams - a unified approach based on IC theory.” *ASCE Composites for Construction* 1 (1), p. 132.

Oehlers, D. J., Liu, I. S. T., and Seracino, R. (2005). “The gradual formation of hinges throughout reinforced concrete beams.” *Mechanics Based Design of Structures and Machines*, 33(3-4), 375-400.

Panagiotakos, T. B., and Fardis, M. N. (2001). “Deformations of reinforced concrete members at yielding and ultimate.” *ACI Structural Journal*, 98(2), 135-148.

Tasdemir, M.A., Tasdemir, C., Akyuz, S., Jefferson, A.D., Lydon, F.D., and Barr, B.I.G. (1998). “Evaluation of Strains at Peak Stresses in Concrete: A Three-Phase Composite Model Approach”, *Cement and Concrete Composites*, 20 (4): 301-318.

Walraven, J. C., and Reinhardt, H. W. (1981). “Theory and Experiments on mechanical behaviour of cracks in plain and reinforced concrete subjected to shear loading.” *Heron*, 26(1A), 68 pp.

Visintin, P. Oehlers, D.J., Wu, C. and Griffith, M.C. "The Reinforcement Contribution to the Cyclic Behaviour of Reinforced Concrete Beam Hinges" Accepted for publication Earthquake Engineering and Structural Dynamics 2011.

Visintin, P. Oehlers, D.J., Wu, C. and Haskett, M. "A Mechanics Solution for Hinges in RC Beams with Multiple Cracks" Accepted for publication Engineering Structures 2011.

Walraven, J. C., Frenay, J. and Pruijssers, A. (1987). "Influence of Concrete Strength and Load History on the Shear-friction Capacity of Concrete Members." *Prestressed Concrete Institute*, 32(1), 66-85.

Warner, R.,F., Foster. S.J., and Kilpatrick, A.E. (2007) Reinforced Concrete Basics: Analysis and Design of Reinforced Concrete Structures. Pearson Education, Australia.

Wee, T.H., Chin, M.S., and Mansur, M.A. (1996). "Stress-Strain Relationship of High-Strength Concrete in Compression", *Journal of Materials in Civil Engineering*, 8(2): 70-76.

Wu, Z., Yoshikawa, H., and Tanabe, T. (1991). "Tension stiffness model for cracked reinforced concrete." *Journal of Structural Engineering* 117(3), 715-732.

Yuan H, Teng JG, Seracino R, Wu ZS, Yao J. Full-range behavior of FRP-to-concrete bonded joints, *Engineering Structures* 2004; **26** (5): 543-691.

Statement of Authorship

Using shear-friction to simulate concrete softening in reinforced concrete flexural members

Cement and Concrete Research: submitted paper

Haskett, M.

Performed analysis, wrote manuscript and acted as corresponding author.

I hereby certify that the statement of contribution is accurate and I give permission for the inclusion of the paper in the thesis

Signed……..Date……

Oehlers, D.J.

Provided critical evaluation of manuscript and supervised research.

I hereby certify that the statement of contribution is accurate and I give permission for the inclusion of the paper in the thesis

Signed…….Date……

Visintin, P. (candidate)

Performed analysis and evaluated manuscript.

I hereby certify that the statement of contribution is accurate

Signed ……Date……

Mohamed Ali, M.S.

Assisted in manuscript evaluation.

I hereby certify that the statement of contribution is accurate and I give permission for the inclusion of the paper in the thesis

Signed …….Date……

Using shear-friction to simulate concrete softening in reinforced concrete flexural members

Haskett, M., Oehlers, D.J., Visintin, P. and Mohamed Ali M.S.

ABSTRACT

The stress-strain relationships of concrete in compression are of fundamental importance in modelling the behaviour of reinforced concrete members, and can be used confidently whilst modelling the behaviour of members up to peak load. However, the post peak behaviour that requires the softening properties is difficult to quantify as these stress-strain softening properties are both size and shape dependent. In this paper, axial and lateral stress-strain expressions are used to derive the shear-friction properties of unconfined concrete, an approach which has the benefit of allowing for specimen size and shape directly. These mathematical shear friction expressions are then used to back calculate axial stress-strain relationships for various sized concrete cylinders, highlighting the 'size effect' which is difficult to explain empirically. Finally, a practical example of the use of shear friction expressions is presented, where the softening behaviour that occurs in flexural members is simulated using these shear-friction expressions with excellent accuracy.

Keywords: compressive strength; concrete; size effect; stress-strain relationship; material properties; softening, shear friction theory

INTRODUCTION

The ascending branch of the concrete compressive stress-strain relationship is relatively easily determined and has been quantified empirically (e.g. Hognestad 1951, Desayi and Krisnan 1964, Carreira and Chu 1985). However, the ability to accurately model the softening behaviour of concrete has been an ongoing research problem for many years. An example of an axial compressive stress-strain relationship obtained from a concrete cylinder is shown in Figure 1, where the ascending branch O-D-Z is considered to be a material property, and where the strain at the start of softening (ε_{co} or ε_{pk}) can be obtained from empirical expressions (Hognestad 1951, Attard and Settunge 1964). After the peak stress has been achieved, f_{co} at ε_{co} in Figure 1, the cylinder starts to unload but the axial contraction of the cylinder continues to increase. This behaviour is shown as the softening branch Z-A-C-G in Figure 1, where the softening branch Z-A-C-G can be considered to be more of a mechanism rather than a material property (Daniell et al. 2008, Debernardi and Taliano 2001, Mohemed Ali. et at 2010) and is a function of the development of damage within the concrete post peak stress.

The softening branch Z-A-C-G in Figure 1 occurs due to the formation of sliding planes, which create increasing displacement after peak stress. In concrete cylinders, these sliding planes form softening wedges after the peak stress has been achieved and which are inclined at an angle α which depends on the frictional and cohesive properties of the concrete (Mohamed Ali et al 2010) and the restraints at the cylinder ends. This wedge idealisation is shown in Figure 2, where this wedge formation is also supported experimentally from concentrically loaded prism tests (Nurwidayati et al 2011) conducted at the University of Adelaide as in Figure 3 and by other researchers (Ferretti 2004). As softening progresses along Z-A-C-G in Figure 1, these sliding planes displace and separate, shown as Δ and h_{cr} respectively in Figure 2(b), and the ability to transfer forces across these planes reduces (Haskett et al. 2010, Haskett et al. 2011). This reduction in shear transfer capacity across the sliding planes is responsible for the reduction in axial stress along Z-A-C-G in Figure 1. Furthermore, this increasing displacement and crack separation of the sliding planes is responsible for the increasing "strain" along the softening branch Z-A-C-G in Figure 1 and that associated with dilation. The axial strain in Figure 1 is simply the axial contraction of each half of the cylinder, shown as δ_{axial} in Figure 2(b), relative to the gauge length of the halfspecimen, $L_{prism}/2$, where the contraction of the specimen δ_{axial}, is the algebraic sum of the contraction due to the real strain in the cylinder, $L_{prism}\varepsilon_{real}/2$ in Figure 2(b), and the deformation due to sliding (Δ) and crack separation (h_{cr}), shown as $a_{A\text{-}B}$ in Figure 2(b). It can, therefore, be seen that the strains in the ascending branch in Figure 1 are real strains ε_{real} and those in the softening branch are effective strains as the latter are due to both real strains in the concrete and axial contraction due to the formation of sliding planes.

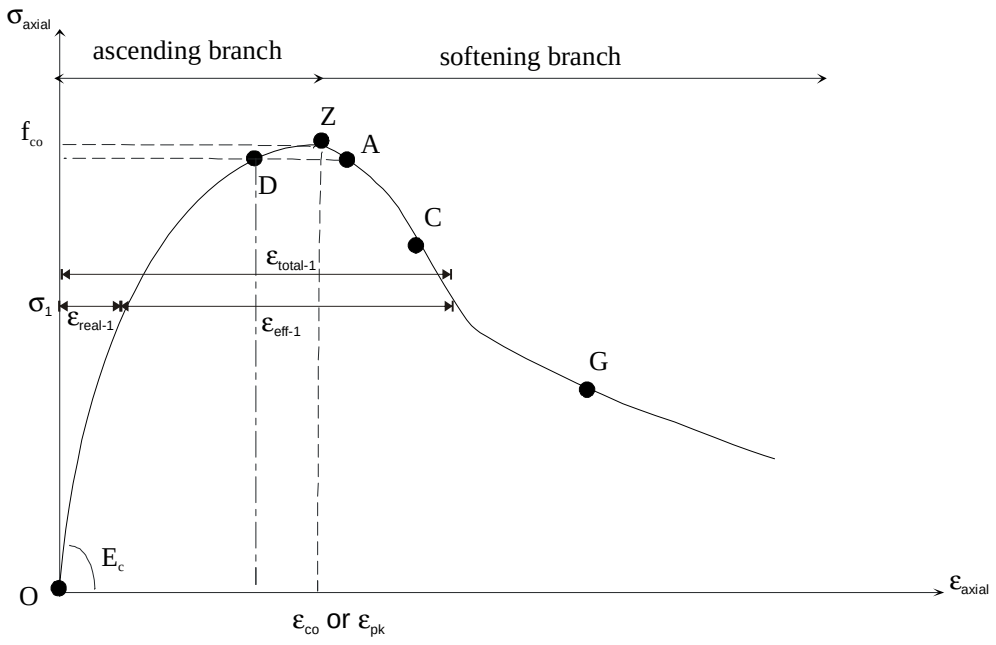

Figure 1: Idealised concrete compressive axial stress-strain relationship

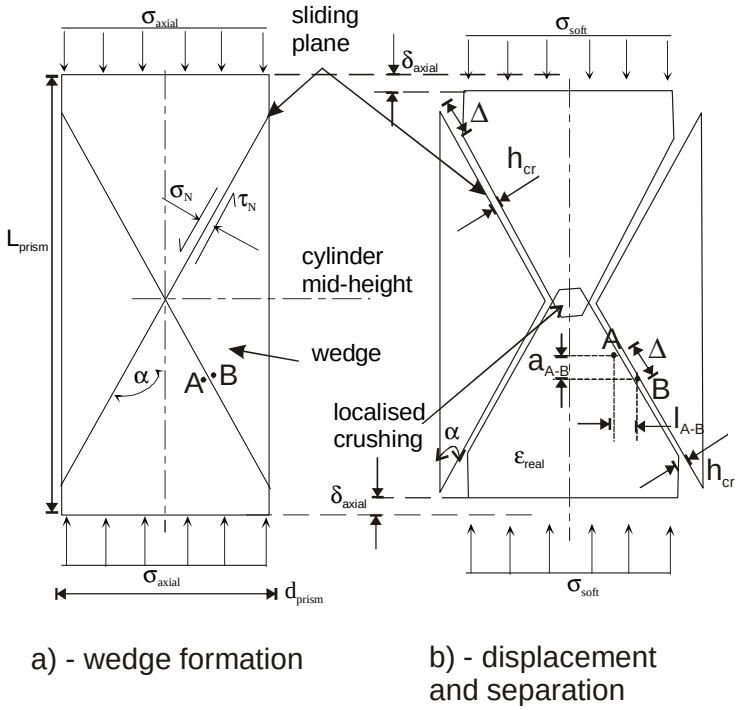

Figure 2: Equilibrium of a wedge and cylinder deformations

Figure 3: Experimental wedge formation in concrete prisms

In this paper, published empirical axial and lateral stress-strain relationships are used to extract the shear-friction properties of initially uncracked unconfined concrete. Mathematical expressions are developed which quantify the shear-friction properties, that is the relationships between the shear stress, τ_N in Fig. 2(a), and crack separation, h_{cr}, in terms of the normal stress σ_N restraining the sliding plane, the displacement of the sliding plane, Δ, and the compressive strength of concrete, f_{co}. These shear-friction properties are then developed in terms of the axial stress σ_{soft} for the analysis of compression zones. An example of the application of these shear friction properties is then presented, where is it shown that the effect of cylinder size on the stress-strain relationship can be explained through the use of shear friction theory. Finally, the softening behaviour of eccentrically loaded unconfined concrete prisms, which behave in the same way as the compression zone of flexural members, is modelled using the shear friction properties of concrete developed in this paper.

EXTRACTING THE SHEAR FRICTION PROPERTIES OF CONCRETE

Shear Friction Mechanics

The shear friction properties can be extracted from empirically derived axial and lateral stress-strain relationships (e.g. Popovics 1973, ACI 1992). For a given axial stress (σ_{soft}), for example point A in Figure 1, the shear stress acting across the sliding plane as in Figure 2(a) can be determined from geometry (Haskett et al. 2011)

$$\tau_N = \sigma_{soft} \sin\alpha \cos\alpha \qquad \text{Equation 1}$$

where α for cylinder tests can be considered constant and approximately equal to 37° (Haskett et al. 2011) in this paper, but is known to be a function of the cohesion and frictional capacity of the concrete (Mohamed Ali et al. 2010). Similarly, the normal stress across the sliding plane is (Haskett et al. 2011)

$$\sigma_N = \sigma_{soft} \sin^2\alpha \qquad \text{Equation 2}$$

Thus, for a given axial stress σ_{soft}, both the shear stress τ_N and normal stress σ_N acting along or across the sliding plane are known. Now let us consider the axial and lateral strains corresponding to this axial stress.

Consider points A and B in Figure 2(a) which are adjacent to each other and on either side of a potential sliding plane. When the wedges move as in Figure 2(b), the adjacent surfaces of the sliding plane move apart by h_{cr} through aggregate interaction and slide relative to each other by Δ as shown. This movement causes an axial contraction $a_{A\text{-}B}$ as shown and consequently an additional effective axial strain, and a lateral expansion $l_{A\text{-}B}$ as shown which provides an additional effective lateral strain. Resolving the displacement and crack

separation in the axial direction according to the angle α that the softening wedge forms, the total axial strain induced in the cylinder is the axial contraction of the cylinder δ_{axial} in Figure 2(b) divided by half the prism length, $L_{prism}/2$, and is given by (Haskett et al. 2011)

$$\varepsilon_{axial} = \frac{2\Delta\cos\alpha}{L_{prism}} + \frac{2h_{cr}\sin\alpha}{L_{prism}} + \varepsilon_{real} \qquad \text{Equation 3}$$

in which the first two components of the strain are effective strains due to sliding and widening across the sliding plane resolved in the axial direction ($a_{A\text{-}B}$ in Figure 2b), and the third component is the real strain the concrete due to the stress σ_{soft}. Consider for example the stress level σ_1 in Figure 1. Whilst on the ascending branch, the strain is the strain in the concrete material shown as $\varepsilon_{real\text{-}1}$. However when on the falling branch where the total strain is $\varepsilon_{total\text{-}1}$, the strain in the concrete material is still $\varepsilon_{real\text{-}1}$ but there is an additional effective strain $\varepsilon_{eff\text{-}1}$ due to Δ and h_{cr}.

A similar approach can also be used to resolve the displacement and crack separation in the lateral direction to find the total lateral strain

$$\varepsilon_{lat} = \frac{2\Delta\sin\alpha}{d_{prism}} + \frac{2h_{cr}}{d_{prism}\cos\alpha} + \nu_c\varepsilon_{real} \qquad \text{Equation 4}$$

where $\nu_c\varepsilon_{real}$ denotes the lateral strain due to the real strain ε_{real} and ν_c is the Poisson ratio prior to concrete softening and can be taken as 0.2, and the remaining components are the effective strains due to Δ and h_{cr} in the lateral direction, shown as $l_{A\text{-}B}$ in Figure 2b.

The relationship between the total axial and total lateral strains in Equations 3 and 4 corresponding to the axial stress σ_{soft} has been determined experimentally through much research. This empirical research can be used in conjunction with Equations 1 to 4 to determine the shear-friction properties of concrete. The following empirical models were used in the derivation of the shear friction properties.

Empirical Softening Relationships

The softening strain ε_{soft} for a given axial softening stress σ_{soft} is given by Popovics (1973) as

$$\frac{\sigma_{soft}}{f_{co}} = \frac{\left(\varepsilon_{soft}/\varepsilon_{co}\right)r}{r-1+\left(\varepsilon_{soft}/\varepsilon_{co}\right)^r} \qquad \text{Equation 5}$$

where the parameter r reflects the brittleness of concrete from Carreira and Chu (1985) and is

$$r = \frac{E_c}{E_c - f_{co}/\varepsilon_{co}} \qquad \text{Equation 6}$$

where E_c is the elastic modulus of concrete and can be taken as (ACI 1993)

$$E_c = 3320\sqrt{f_{co}} + 6900 \qquad \text{Equation 7}$$

The relationship between axial and lateral strain is from Teng et al. (2007)

$$\frac{\varepsilon_{soft}}{\varepsilon_{co}} = 0.85\left\{\left[1 + 0.75\left(\frac{-\varepsilon_{lat}}{\varepsilon_{co}}\right)\right]^{0.7} - \exp\left[-7\left(\frac{-\varepsilon_{lat}}{\varepsilon_{co}}\right)\right]\right\} \qquad \text{Equation 8}$$

and the strain at which softening commences (ε_{co}) can be taken from any empirical expression, for example from the standard stress-strain relationship of Hognestad (1951),

$$\varepsilon_{co} = \frac{2 f_{co}}{E_c} \qquad \text{Equation 9}$$

Thus, for a given softening stress, the shear and normal stress across the sliding plane can be determined from geometry using Equations 1 and 2. The axial and lateral strains for the given axial stress can be determined from empirical stress-strain relationships (Equations 5 and 8), and the displacement and separation of the sliding plane can therefore be determined from Equations 3 and 4. Hence, the shear friction properties of unconfined concrete can be obtained directly from empirical stress-strain expressions. These will be referred to as the *experimental results* throughout this paper

This separation of strains into relative constituents is similar to the compressive damage zone (CDZ) model proposed by Markeset (1993) and summarised in Markeset and Hillerborg (1995), where the strain in a (relatively slender) concrete cylinder is the algebraic sum of the strain in the undamaged portion of the cylinder (ε_{real}), and the strain in the damaged portion of the cylinder due to the formation of longitudinal cracking (which is what we refer to as h_{cr} and Δ). In the following section, the shear friction expressions are developed for various empirical expressions for ε_{co}.

SHEAR STRESS SHEAR-FRICTION PROPERTIES

For concrete strengths in the range 30-70 MPa, varying combinations of compressive strength of concrete and softening axial stress were considered to obtain the *experimental results* from which the shear friction properties were derived. Softening stresses below $50\%f_{co}$ were removed because the empirical expressions used to determine the shear friction

properties of concrete become less accurate at these high levels of softening, possibly reflecting the inaccuracies of these empirical models at very low softening stresses.

Substituting Hognestad's Equation 9 into Equation 6 and solving for the brittleness parameter (r), the brittleness parameter is a constant and equal to 2 for all concrete strengths. The brittleness parameter (r) is the primary mechanism responsible for influencing the shape of the softening stress-strain relationship and therefore, the softening stress-strain relationship is identical for all strengths of concrete when using Hognestad's expression for ε_{co}. This behaviour does not reflect the typical softening response of varying strengths of concrete, where higher strength concrete experiences a more rapid reduction in strength after peak stress than lower strength concrete. This inaccuracy at high strength concrete is also noted by other researchers (Wee et al. 1996). Therefore, in order to accurately simulate the rapid reduction in strength for higher strength concrete, the brittleness parameter r must be a function of the compressive strength of the concrete. Hence, three different empirical expressions for strain at peak stress (Hognestad 1951, Wee et al. 1996, Tasdemir et al. 1998) are considered in this paper and discussed subsequently.

Based on Hognestad's empirical peak strain expression

Experimental results were derived using Hognestad's expression Equation 9 for strain at peak stress. From a statistical analysis of these *experimental results*, the following theoretical shear stress expression as a function of the displacement, normal stress across the sliding plane and the compressive strength of concrete was derived

$$\tau_{N(Theo)} = \left\{\left(-21.78 + 41.91\sigma_N / f_{co}\right)\Delta\right\}\left(\frac{f_{co}}{30}\right)^{0.385} + 0.48 f_{co} \qquad \text{Equation 10}$$

where the units are in Newtons (N) and millimetres (mm). The shear stresses from the *experimental results* $\tau_{N(exp)}$ are compared to the theoretical shear stresses $\tau_{N(Pred)}$ from Equation 10 in Figure 4 for varying displacements, where it can be seen that Equation 10 accurately predicts the experimental shear stresses. The average value of $\tau_{N(Pred)}/\tau_{N(Exp)}$ in Figure 4 is 1.00 with a coefficient of variation of less than 0.4%.

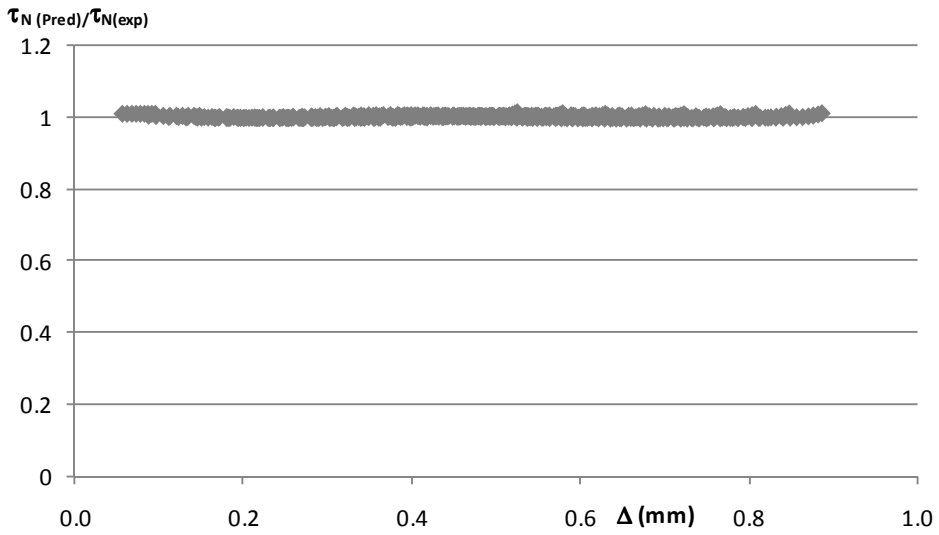

Figure 4: Comparison of shear stresses based on Hognestad's expression for ε_{co}

A more convenient expression for analysis for a specific wedge angle α can be developed in the form of the axial stress in terms of the normal stress σ_N, displacement Δ and compressive strength of concrete f_{co}. Referring back to Figure 2(a), for a given axial softening stress σ_{soft} and wedge angle α, the shear stress τ_N is proportional to the axial softening stress σ_{soft} according to Equation 1. Substituting Equation 10 into Equation 1 for τ_N provides

$$\sigma_{soft} = \tau_N \Big/ \sin\alpha\cos\alpha = \left\{ \frac{\left(-21.78 + 41.91 \sigma_N \Big/ f_{co} \right)}{\sin\alpha\cos\alpha} \Delta \right\} \left(\frac{f_{co}}{30}\right)^{0.385} + f_{co} \qquad \text{Equation 11}$$

Furthermore, the axial stress can also be expressed independently of the normal stress by replacing σ_N in Equation 11 with Equation 2 and rearranging for σ_{soft} yields

$$\sigma_{soft} = \frac{f_{co}\left(-21.78\Delta\left(\frac{f_{co}}{30}\right)^{0.385} + 0.48 f_{co} \right)}{\sin\alpha\cos\alpha\left\{ f_{co} - 41.91\tan\alpha\Delta\left(\frac{f_{co}}{30}\right)^{0.385} \right\}} \qquad \text{Equation 12}$$

Equation 12 shows that the axial stress can be expressed independently of the normal stress and can be expressed solely in terms of the angle of the wedge α, the displacement Δ of the sliding plane and the compressive strength of concrete f_{co} which it will be shown later is convenient for analysis. Continuing this approach and from a statistical analysis of the *experimental results*, the following expression with the same variables can be obtained

$$\sigma_{soft} = (0.105 f_{co} - 46.92)\Delta^2 + (0.026 f_{co} - 4.34)\Delta + f_{co} \qquad \text{Equation 13}$$

where the units are in N and mm, and Δ is the displacement along the sliding plane and which is specific to a wedge with an angle of the sliding plane α of 37° as this was the angle used in deriving the *experimental results*. The predicted axial stress from Equation 13 is compared to the experimental axial stress for varying displacements in Figure 5, where the average value is 1.00 with a coefficient of variation of 1.2%.

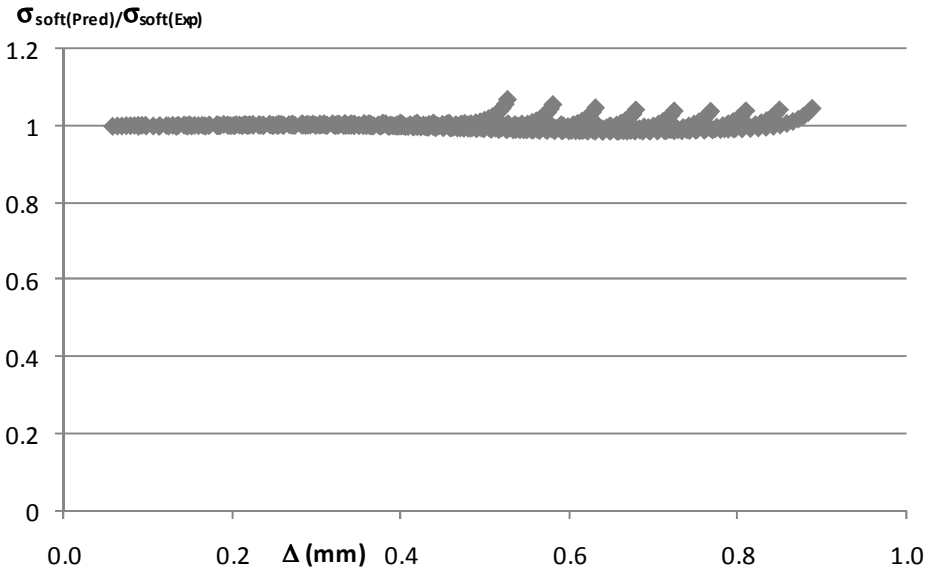

Figure 5: Comparison of axial stresses based on Equation 13 and Hognestad's expression for ε_{co}

From Figure 5, it can be seen that Equation 13 over predicts the axial stress at large values of softening, that is where there are 9 "groups" of data at increasing displacements where $\sigma_{soft(Pred)}/\sigma_{soft(Exp)}$ deviates away from the expected value of 1. These 9 deviations represent varying compressive strengths of concrete (30, 35, 40, 45, 50, 55, 60, 65, and 70MPa) and where the concrete has softened such that the axial stress is less than $55\%f_{co}$. If we only consider softening up to $55\%f_{co}$, then this deviation is not evident and the average value of $\sigma_{soft\ (Pred)}/\sigma_{soft\ (Exp)}$ is 1.00 with a corresponding coefficient of variation of less than 0.6%.

The axial stresses from the *experimental results* $\sigma_{soft(Exp)}$ are compared to the theoretical axial stresses $\sigma_{soft(Pred)}$ from Equation 12 in Figure 6, where it can be seen that Equation 12 very accurately predicts the experimental axial stresses. The average value of $\sigma_{soft\ (Pred)}/\sigma_{soft\ (Exp)}$ in Figure 4 is 1.00 with a coefficient of variation of less than 0.5%. As indicated by comparing Figures 5 and 6, the accuracy of Equation 12 is slightly better than Equation 13, where the

deviation of the results away from the expected value of 1 at increasing displacements is not as noticeable. However, Equation 13 is less complex.

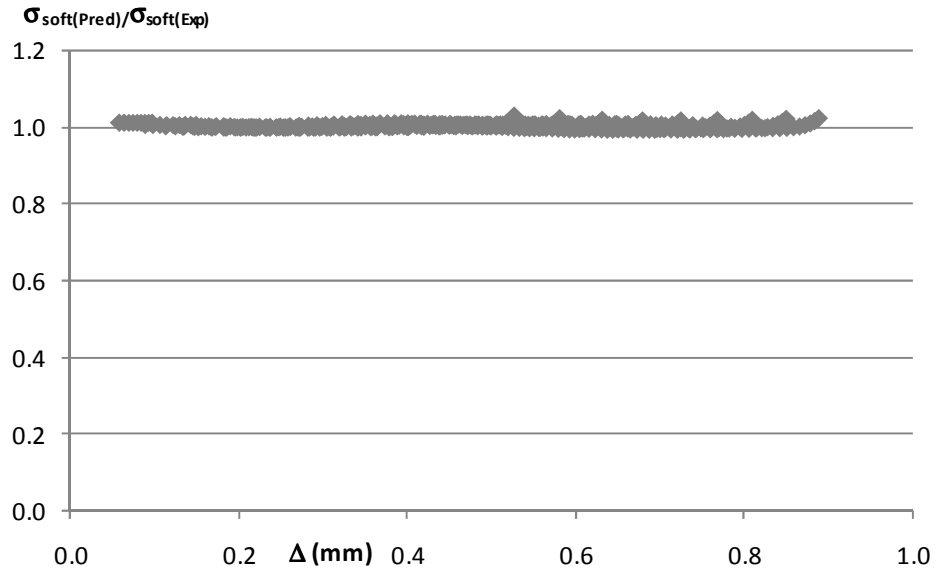

Figure 6: Comparison of axial stresses based on Equation 12 and Hognestad's expression for ε_{co}

In applying Equations 10, 11, 12 and and 13, it should be understood that at zero displacement Δ the concrete has just commenced softening (that is the effective strain is the real strain and equal to ε_{co}) and, therefore, the corresponding axial stress must be equal to f_{co}. This is clear in Equation 13, where at zero displacement the axial stress is f_{co}, but this behaviour is less evident in Equation 10. At zero displacement, Equation 10 predicts a shear stress of $0.48f_{co}$. Assuming that the sliding plane forms at an angle α of 37º in a cylinder test, substituting Equation 10 with Δ=0 into Equation 1 and rearranging for the corresponding axial stress gives

$$\sigma_{soft} = 0.48 f_{co} \Big/ \sin\alpha\cos\alpha = 0.48 f_{co} \Big/ \sin 37^\circ \cos 37^\circ = f_{co} \qquad \text{Equation 14}$$

Hence at zero displacement, a shear stress of $0.48f_{co}$ acting along the sliding plane is geometrically equivalent to an axial stress of f_{co}, which is as expected.

Based on Wee's empirical peak strain expression

Following the same approach as described above but considering the strain at peak stress proposed by Wee et al. (1996)

$$\varepsilon_{co} = 0.00078(f_{co})^{0.25} \qquad \text{Equation 15}$$

where the units are in N and mm, the theoretical shear stress is given by

$$\tau_{N(Theo)} = \left\{\left(-31.39 + 55.89\,\sigma_N \big/ f_{co}\right)\Delta\right\}\left(\frac{f_{co}}{30}\right)^{1.07} + 0.48\,f_{co} \qquad \text{Equation 16}$$

where again the units are in N and mm. The experimental shear stresses when compared to the theoretical shear stresses from Equation 16 in the form shown in Figure 4 give accurate predictions with an average value of 1.00 with a coefficient of variation of less than 0.6%.

In a counterpart to Equation 13, a statistical analysis of the *experimental results* that were based on Wee's peak strain expression gave

$$\sigma_{soft} = (-4.34\,f_{co} + 40.16)\Delta^2 + (-0.10\,f_{co} - 4.34)\Delta + f_{co} \qquad \text{Equation 17}$$

where the units are in N and mm as before. Equation 17 is applicable to a sliding plane α of 37° and when compared with the experimental results has a mean of 1.00 with a coefficient of variation of 0.8%.

Based on Tasdemir's empirical peak strain expression

Repeating the same approach but considering Tasdemir et al's (1998) expression for peak strain

$$\varepsilon_{co} = \left(-0.067(f_{co})^2 + 29.9\,f_{co} + 1053\right)\times 10^{-6} \qquad \text{Equation 18}$$

where the units are in N and mm , the theoretical shear stress is given by

$$\tau_{N(Theo)} = \left\{\left(-30.14 + 51.62\,\sigma_N \big/ f_{co}\right)\Delta\right\}\left(\frac{f_{co}}{30}\right)^{0.60} + 0.48\,f_{co} \qquad \text{Equation 19}$$

where the units are in N and mm. Equation 19 also gives very accurate predictions with a mean of 1.00 and a coefficient of varation of 0.8%. Furthermore from a statistical analysis of the *experimental results* yields

$$\sigma_{soft} = (-0.21\,f_{co} - 89.49)\Delta^2 + (-0.20\,f_{co} + 1.19)\Delta + f_{co} \qquad \text{Equation 20}$$

with units in N and mm. When compared to the experimental results, Equation 20 has a mean of 1.00 and a coefficient of variation of 1%.

It has been shown that shear-friction expressions can be derived using various empirical relationships with very good accuracy. These shear friction expressions are compared in the following section.

Comparison of shear stress expressions

Let us now compare the three shear stress expressions (Equations 10 based on Hognestad, Equation 16 on Wee and Equation 19 on Tasdemir) for various concrete strengths starting with a low concrete strength of 30 MPa in Figure 7. The softening properties in Equation 5 depends on the brittleness parameter r in Equation 6 which itself depends on the strain ε_{co} which is given by Equation 9 (Hognestad), Equation 15 (Wee) and Equation 18 (Tasdemir). These strains ε_{co} and consequently r are reasonably close as shown in Figure 7 so that the variations in the shear stress τ_N in Figure 7 are also reasonably close particularly those based on Wee and Tasdemir, so that the variations in the axial stress from Equations 11(Hognestad), 17 (Wee) and 20 (Tasdemir) will be reasonably close at low concrete strengths.

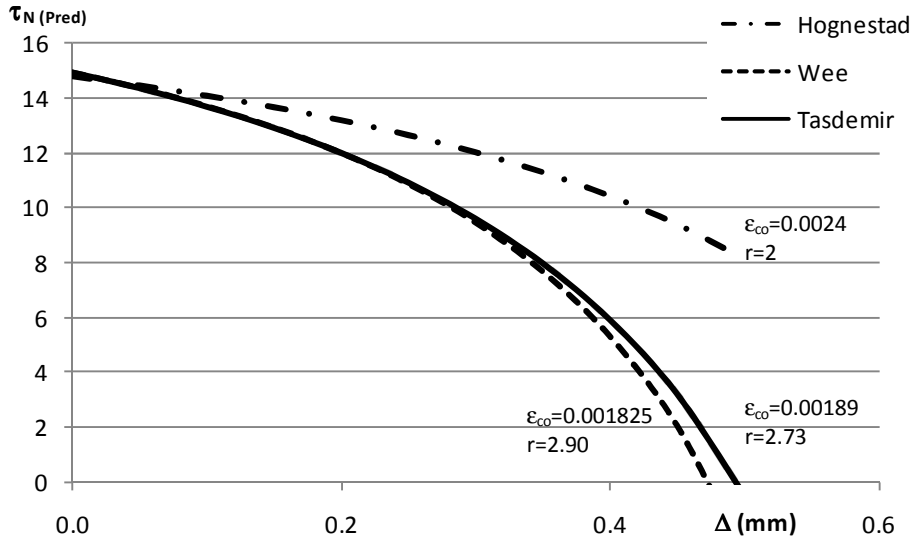

Figure 7: Influence of strain at peak stress (ε_{co}) on shear capacity for f_{co}=30MPa

Considering now 70MPa concrete in Figure 8. As the strain at peak stress (ε_{co}) varies much more between the three expressions, there is a corresponding wide variation in the brittleness parameter r. These properties mean that since Wee's brittleness parameter is largest, Wee will provide a more rapid drop in stress for increasing displacements (and strain) as shown in Figure 8.

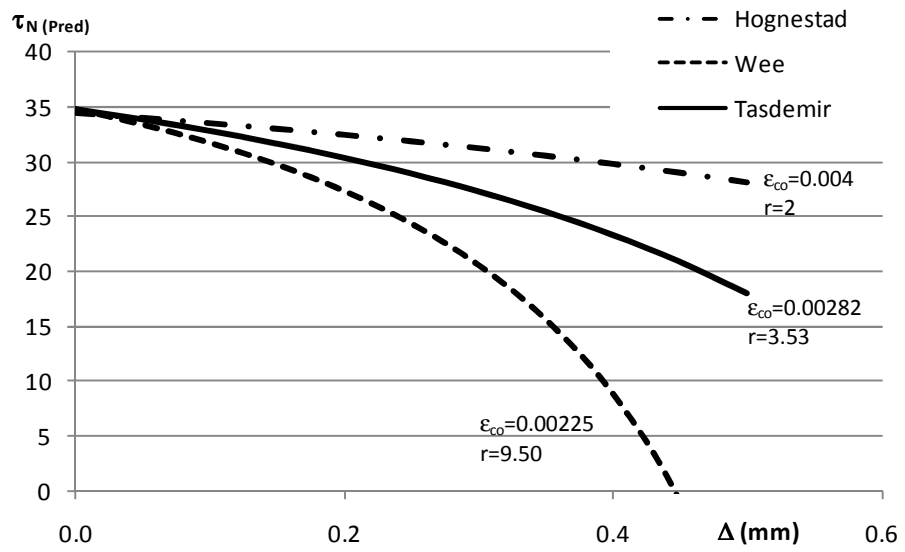

Figure 8: Influence of strain at peak stress (ε_{co}) on shear friction for f_{co}=70MPa

Figures 7 and 8 display the same trends: Hognestad provides a more uniform reduction in shear (and therefore axial) stress for increasing displacements (or strains), while Wee et al. provides the most rapid reduction in shear (and similarly axial) stress for increasing displacements (or strains). It is known that in general weak concrete softens at a slower rate than strong concrete; this is clearly reflected in the results based on Wee and Tasdemir's peak strains but not on Hognestad's where r is independent of the concrete strength and, therefore, the same rate of softening occurs for all concrete. Hence it would be expected that using Wee's and Tasdemir's values for ε_{co} would give better results in the simulations at high concrete strengths as will be confirmed later. These behaviours highlight the sensitivity of the shear friction analysis to the concrete material properties used which can be refined over time if required.

Various expressions have been presented which quantify the shear and axial stress transferred across a concrete interface for a given normal stress, compressive strength of concrete and sliding plane displacement. These expressions have been shown to very accurately model the experimental shear and axial stresses, and can be used with confidence to predict the shear or axial stress for a given displacement, concrete strength and normal confining stress. It was also shown that to accurately simulate the behaviour of higher strength concrete, it is preferable to use peak strain expressions that are independent of E_c. In the following section, an identical approach is used to derive expressions for the crack separation in terms of the same parameters.

CRACK SEPARATION EQUATIONS

Having obtained the shear stress expressions, a similar approach can also be used to quantify the crack separation in terms of similar parameters. As before, excluding the *experimental results* where $\sigma_{soft}/f_{co}<0.5$ and considering Hognestad's expression for strain at peak stress, the crack separation is given by

$$h_{cr} = \left(0.0433 \left(\frac{\tau_N}{f_{co}} \right)^{-2.377} \right) \Delta \qquad \text{Equation 21}$$

The accuracy of Equation 21 in predicting the crack separation is shown in Figure 9 for a range of crack separations. The average value of $h_{cr(Pred)}/h_{cr(Exp)}$ is 1.005 with a coefficient of variation of less than 8% where the majority of the error is at very small crack separations.

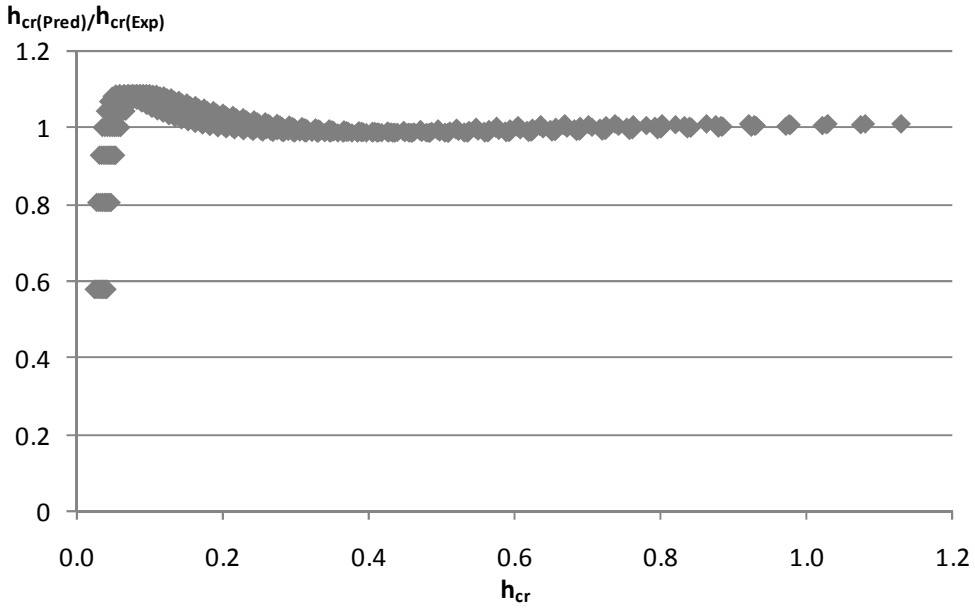

Figure 9: Accuracy of Equation 21 for various displacements

Repeating the same approach but considering Tasdemir et al's (1998) expression for peak strain the theoretical crack separation is given by

$$h_{cr} = \left(0.025 \left(\frac{\tau_N}{f_{co}} \right)^{-2.035} \right) \Delta \left(\frac{f_{co}}{30} \right)^{-1.042} \qquad \text{Equation 22}$$

where the units are in N and mm. Equation 22 also gives accurate predictions with a mean of 0.96 and a coefficient of variation of 20%. Note that Equation 22 is in a different format to

Equation 21 which was less dependent of the compressive strength of concrete. The term $(f_{co}/30)^{-1.042}$ in Equation 22 reflects the presence of a relationship between compressive strength of concrete and the brittleness parameter (r) when using Tasdemir's expression for strain at peak stress.

Repeating the same approach but considering Wee et al's (1996) expression for peak strain the theoretical crack separation is given by

$$h_{cr} = \left(0.021 \left(\frac{\tau_N}{f_{co}} \right)^{-2.024} \right) \Delta \left(\frac{f_{co}}{30} \right)^{-3.040} \qquad \text{Equation 23}$$

where the units are in N and mm. Equation 23 also gives relatively accurate predictions with a mean of 0.99 and a coefficient of variation of 24%.

Having now obtained mathematical expressions for the shear-friction properties, the softening behaviour of concrete in compression can be simulated. As an example, the shear-friction expressions can be used to model the softening stress-strain relationships for concrete cylinders of varying dimensions, and also to simulate the softening behaviour of concrete in an eccentrically loaded prism test.

USING THE SHEAR FRICTION PROPERTIES TO DETERMINE AXIAL STRESS-STRAIN RELATIONSHIPS

The process to obtain the shear friction parameters of concrete from empirical stress-strain relationships has been presented. Conversely, it is possible to use the shear-friction properties of concrete to back-calculate the stress-strain relationships of concrete. As an example of the application of these shear-friction parameters, the influence of cylinder size on the softening behaviour of concrete, Z-A-C-G in Figure 1, can be quantified. This cannot be done using empirical stress-strain relationships because these empirical relationships are only applicable to specific cylinder dimensions from which they were obtained.

The process to obtain the axial stress-strain relationship using the previously derived shear friction expressions is straightforward. For a given softening stress, for example A in Figure 1, the shear stress and normal stress can be determined from Equations 1 and 2. Knowing the normal and shear stresses acting across or along the sliding plane, the corresponding displacement of the sliding plane can be determined by solving a shear stress expression for Δ. For example, rearranging the shear-friction Equation 10, the displacement of the sliding plane for a given shear stress, normal stress and compressive strength of concrete is given by

$$\Delta = \frac{\tau_N - 0.48 f_{co}}{\left(-21.78 + 41.91 \sigma_N / f_{co}\right)\left\{\frac{f_{co}}{30}\right\}^{0.385}} \qquad \text{Equation 24}$$

The separation of the sliding plane h_{cr} for this shear stress and displacement can be determined directly from Equation 21 for example, where Δ in Equation 21 is from Equation 24. Thus, for a given axial stress (and compressive strength of concrete) the displacement and separation of the sliding planes is known. Compatibility of the cylinder shown in Figure 2 is then used to determine the axial and lateral strains in the cylinder corresponding to this displacement and separation. The total axial strain is the sum of the effective axial strain due to Δ and h_{cr} and the real strain in the concrete ε_{real} according to Equation 3. The real strain in the cylinder ε_{real} for a given axial stress can be determined knowing the concrete properties in the ascending branch. For example, Hognestad (1951) modelled the ascending portion of the stress-strain relationship as a parabola.

$$\sigma_{axial} = f_{co}\left[2\left(\frac{\varepsilon_{real}}{\varepsilon_{co}}\right) - \left(\frac{\varepsilon_{real}}{\varepsilon_{co}}\right)^2\right] \qquad \text{Equation 25}$$

Therefore, the real strain for a given axial stress σ_{soft}, can be determined by solving Hognested's stress-strain expression for ε_{real} as

$$\varepsilon_{real} = \varepsilon_{co}\left(\frac{2 f_{co} - \sqrt{4 f_{co}{}^2 - 4 f_{co}\sigma_{soft}}}{2 f_{co}}\right) \qquad \text{Equation 26}$$

Thus, the axial strain for this given softening stress can be determined from Equation 3 since ε_{real}, Δ and h_{cr} are all known. If required, the corresponding lateral strain can also be obtained from Equation 4, where the lateral strain is also a function of the real strain and displacement and separation of the sliding planes. The softening stress is then gradually reduced along Z-A-C-G in Figure 1 to develop the complete axial stress-strain relationship for unconfined concrete for a given compressive strength.

The axial stress-strain relationship obtained from shear-friction theory can be compared to any empirical axial stress-strain expressions previously developed for 200mm high and 100mm diameter concrete cylinders. The theoretical shear friction stress-strain relationship are compared to an empirical stress-strain relationship from Popovics (1973) in Figure 10 for concrete strengths of 30 and 50MPa. As expected, the shear-friction and empirical stress-strain relationships are almost identical. Given the accuracy of Equation 10 in predicting shear stress, the converse is also true: for a given axial stress (and therefore shear stress) the displacement of the sliding plane can be very accurately estimated. Knowing the displacement of the sliding plane, the crack separation can also be accurately estimated.

Hence, the "shear-friction" axial stress-strain relationships shown in Figure 10 are almost identical to the empirical stress-strain relationship.

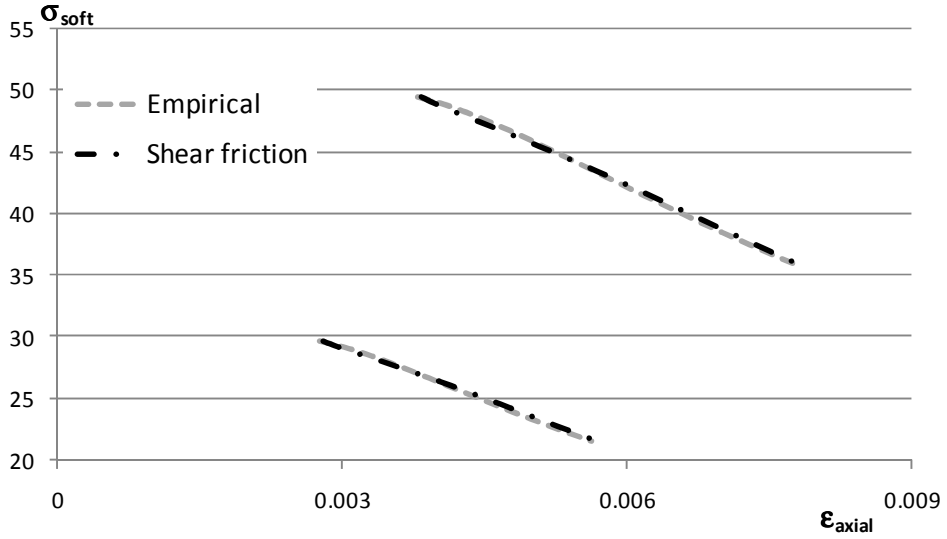

Figure 10: Comparison of empirical and shear-friction stress-strain relationships

The shear-friction expressions in this paper were developed from empirical axial and lateral stress-strain expressions considering 200x100mm concrete cylinders and hence these empirical expressions are only applicable to 200x100mm cylinders. However, the shear-friction expressions are independent of size, since they are a measurement of the instantaneous shear stress able to be transferred across a sliding plane, and the corresponding separation of that sliding plane. Hence, the well known "size effect" (e.g. Yi et al. 2006, Bazant and Xiang 1997, del Viso et al. 2007, Van Mier and Man 2009) can also be investigated through the use of these shear friction expressions.

The influence of cylinder dimensions on the axial stress-strain relationship can be best explained by considering Equation 3, where the total axial strain due to the contraction of the cylinder ε_{axial} is the sum of the real strain in the concrete within the cylinder ε_{real} and the effective strain induced by displacement Δ and crack separation h_{cr}. The dimension of the wedge in Figure 2 is independent of prism dimension. That is, the axial displacement $a_{A\text{-}B}$ in Figure 2 corresponding to an axial stress σ_{soft} is size independent. Hence, the additional strain induced by this axial sliding plane deformation $a_{A\text{-}B}$ in a prism of length $2L_{prism}$ is one half that which would occur in a prism of length L_{prism}. The stress-strain relationships are also dependent on specimen shape, and this occurs when the prism restraints are close enough to influence the angle that the wedge forms, α. For example, for very short prisms, the wedge must be completely contained within the prism length, and therefore the angle at which the wedge develops increases to ensure the wedge is fully contained in a shorter prism length. This change in wedge angle influences the axial and lateral dilations $a_{A\text{-}B}$ and $l_{A\text{-}B}$ in Figure

2b. This influence of the restraint conditions on the failure behaviour of concrete cylinders has also been reported elsewhere (Roddenberry et al. 2011). These behaviours are the well known and commonly referred to as “size effect”, which can now be quantified through the use of the shear friction expressions.

An example of the theoretical axial stress-strain relationship from shear friction expression for various sized concrete cylinders is shown in Figure 11. It is clear that the axial strain for a given softening stress reduces as the cylinder dimensions increase. At the commencement of softening (30MPa in this example) the majority of the axial shortening (δ_{axial} in Figure 2) is from “real” strain in the concrete cylinder. The sliding plane has only just formed and therefore the axial deformation $a_{A\text{-}B}$ in Figure 2(b) tends to zero. As softening progresses (i.e. reducing stresses in Figure 11) the contribution of the individual components to the total strain changes: the axial displacement due crack separation and displacement ($a_{A\text{-}B}$ in Figure 2b) increases, causing an increase in total axial strain, while the real strain in the cylinder reduces in response to the reducing stress. The real strain in the cylinder is not affected by cylinder size, which is as expected because the real strain in the cylinder is obtained from the material behaviour O-D-Z in Figure 1.

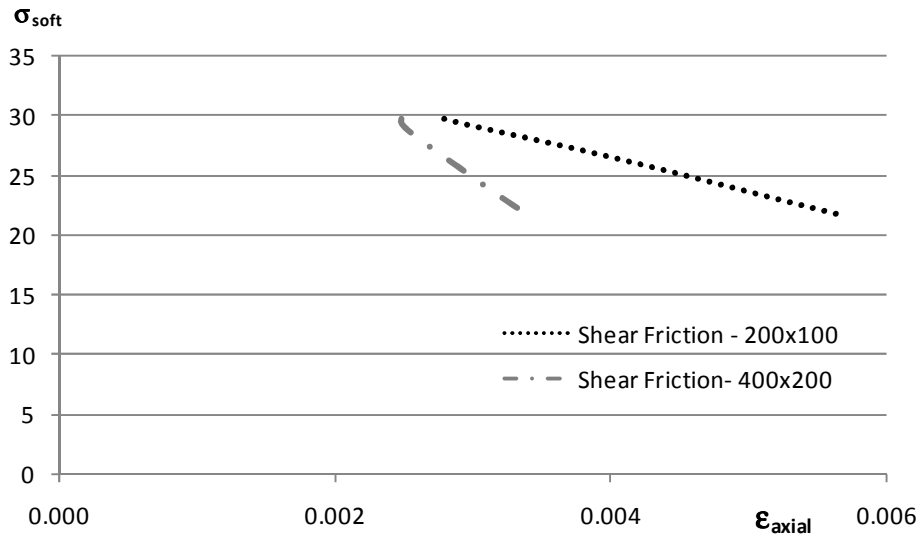

Figure 11: Influence of size on softening

Essentially, irrespective of the cylinder dimension L_{prism} in Figure 2, for a given softening stress, the crack separation h_{cr} and displacement Δ are identical. However, when computing the corresponding axial strain in the prism, these axial deformations $a_{A\text{-}B}$ in Figure 2(b) cause a larger effective strain in a smaller dimensioned specimen which can also be deduced from Equation 3. This is the reason for the size effect and can be explained clearly through the use of shear friction parameters.

USING SHEAR FRICTION THEORY TO SIMULATE ECCENTRICALLY LOADED CONCRETE PRISMS

Shear friction expressions can also be used in a practical sense, for example to simulate concrete softening in a flexural member where there is a gradient in the strain as often simulated in eccentrically loaded concrete prism tests. Consider the concrete prism in Figure 12(a) which is subjected to an applied load (P) at eccentricity (e_{cc}) which causes a deformation as shown by the bold black lines which is also shown in the deformation profile Figure 12(b). The deformation varies linearly over the prism depth d_{prism} from δ_{top} at the top to δ_{bottom} at the base. The effective strain over the prism depth corresponding to this deformation can be determined as in Figure 12(c) where the strain is simply the deformation divided by the length over which it acts, which in this case is $w_{prism}/2$. The corresponding rotation θ for this deformation can be determined from geometry as shown in Figure 12(a). Because of the eccentricity of load, material softening (which we refer to as the formation of a softening wedge) first forms on the loaded side of the prism, and where the depth of softening is a variable and shown as d_{wedge} in Figure 12(a) and forms at an angle α.

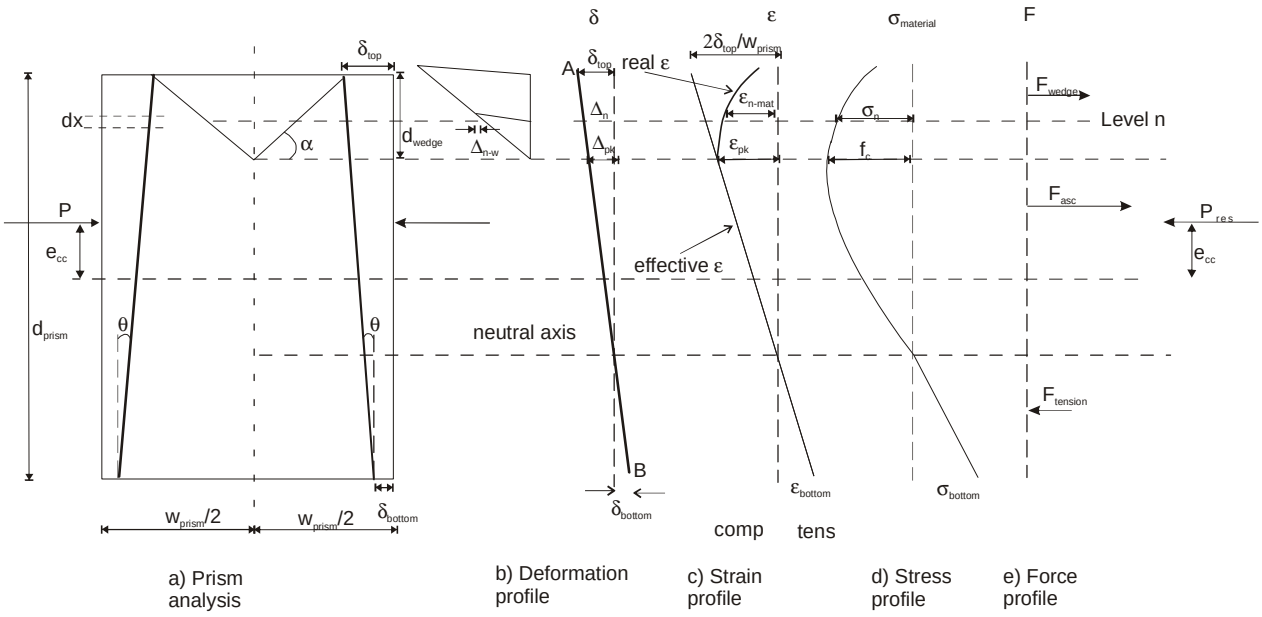

Figure 12: Eccentrically loaded concrete prism analysis technique

According to the deformation profile shown in Figure 12(b), the depth of the softening wedge can be determined as it is known that softening commences when the effective strain exceeds the strain at peak stress, shown as ε_{pk} in Figure 12(c); this occurs at a deformation Δ_{pk} of $\varepsilon_{pk}w_{prism}/2$. The corresponding stress at this position is f_c, as shown in Figure 12(d). Hence, any deformation within the prism that is greater than Δ_{pk} in Figure 12(b), that is over the depth d_{prism}, signifies a region where concrete softening is occurring and, therefore,

requires the use of shear-friction properties to quantify the shear (or axial) stress for a given deformation.

Let us first consider the behaviour below Δ_{pk} in Figure 12(b). The linear deformation produces the effective linear strain distribution shown in Figure 12(c), where depending on the eccentricity (e_{cc}) of the applied load (P), the entire prism may be in compression, or, as shown in Figure 12, a portion of the prism may be in tension. If the strain at the base, δ_{bottom}, is less than the cracking strain of concrete, then a crack has not developed, and the stress distribution in this tensile region can be determined knowing the tensile material properties. The corresponding tensile force, $F_{tension}$ and the location of this force can therefore be determined. If we increase the deformation profile such that the effective strain at the bottom of the prism exceeds the tensile strain capacity of concrete, a crack has formed, and tensile stresses cannot be developed over the region where the strain exceeds this value. Hence, this analysis can also incorporate cracking if it occurs.

Let us now consider the compression behaviour above the neutral axis. Consider level *n*, where the deformation exceeds Δ_{pk} and, therefore, a wedge has formed and the total deformation is Δ_n as shown in the deformation profile. A portion of this deformation (or contraction) is a result of the slip of the wedge, shown as $\tau_{n\text{-}w}$, and the remaining contraction is accommodated by concrete material straining $\varepsilon_{n\text{-}mat}$ as shown in Figure 12(c). The real strain profile over the softening depth is shown in Figure 12(c) as the bold black line, where for increasing deformations the real strain is reducing in response to reducing stresses as shown in Figure 12(d). That is, the deformation due to material straining is given by $\varepsilon_{n\text{-}mat}$ $w_{prism}/2$ and the remaining deformation is due to sliding contraction $\Delta_{n\text{-}w}$ at the wedge interface as shown in Figure 12(a). It is simple a question of finding the stress σ_n in Figure 12(d) such that the material contraction $\varepsilon_{n\text{-}mat}$ $w_{prism}/2$ plus the wedge contraction $\Delta_{n\text{-}w}$, is equal to the total required deformation Δ_n in Figure 12(b), where the stress in the wedge is obtained from shear friction theory. For example, for an assumed wedge slip ($\Delta_{n\text{-}w}$) the corresponding axial stress in the wedge can be determined from Equations 12 or 13. It also should be noted that the deformation $\Delta_{n\text{-}w}$ in Figure 12 must be resolved at an angle α to obtain the displacement of the sliding plane for use in the shear friction equations since the displacement in these equations is measured along the sliding plane. For this axial stress, the material contraction can be determined $\varepsilon_{n\text{-}mat} w_{prism}/2$ and the total deformation must be equal to the total deformation Δ_n. If this is not the case an iterative approach can be used to solve for $\Delta_{n\text{-}w}$ until the sum of the wedge displacement and material contraction is equal to Δ_n. This type of analysis procedure requires the softening region to be sliced into small segments of depth dx, where this procedure is repeated over the entire depth of the wedge to obtain the total force in the softening wedge F_{wedge}.

The forces in the non-softening region, F_{asc}, can be determined from any standard analysis procedure. The position of the resultant force in the prism can now be determined, where the resultant force is required to be in line with the applied external load P. If this is not the case, then the assumed displacement profile A-B is incorrect and the rotation needs to be changed until the resultant internal force is in line with the applied external force. When this occurs a single point on the moment-rotation relationship has been determined and this procedure is subsequently repeated for increasing displacements to obtain the complete moment-rotation relationship.

The theoretical results for this analysis procedure for varying eccentricities (12mm, 24mm, 36,mm and 48mm) and using various shear friction equations (Wee et al. 1996, Hognestad 1951 and Tasdemir et al. 1998) are shown in Figure 13. It is clear that the softening portion of the prism test is accurately modelled using shear friction parameters, and the rate of softening varies according to the shear friction expression considered

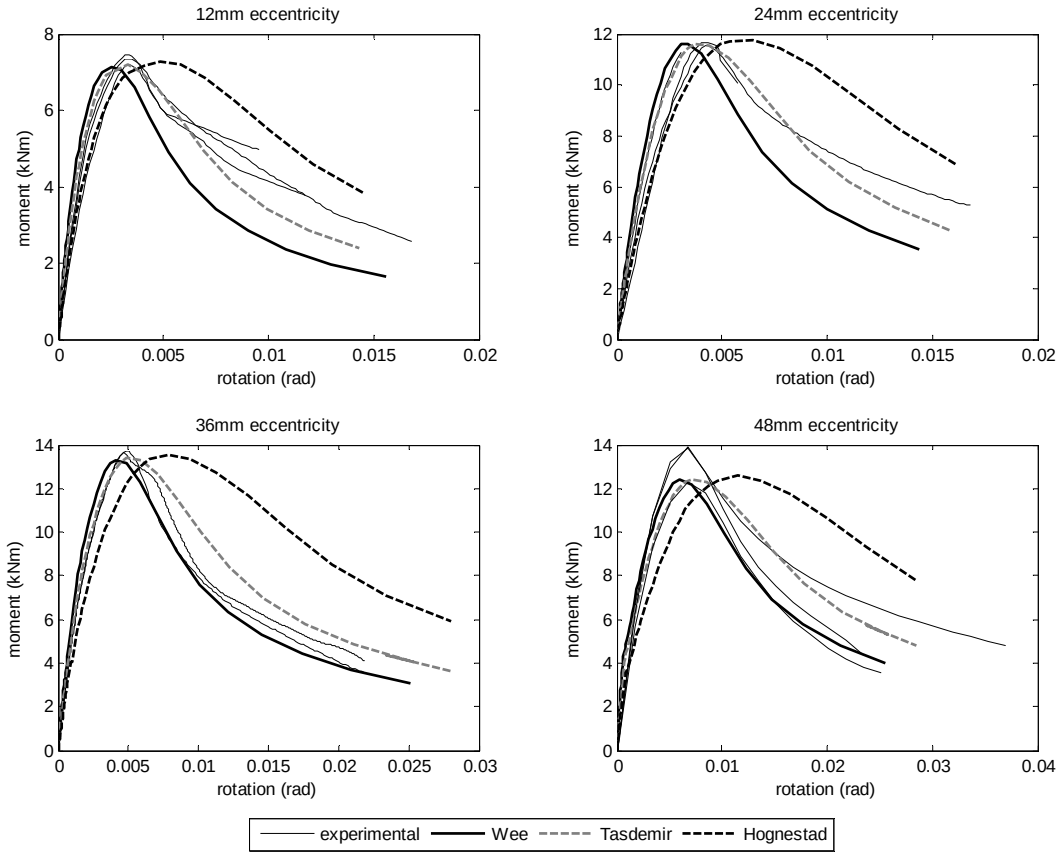

Figure 13: Simulating eccentrically loaded prisms using shear-friction theory

From Figure 13, the different shear friction expressions obtained by using different empirical expressions for strain at peak stress provide differing rates of softening. The use of Wee's

expression for strain at peak stress results in a more rapid reduction in shear (and therefore axial) stress for increasing rotations, while Hognestad's expression for strain at peak stress provides the least rapid reduction. These behaviours are consistent with the responses shown in Figures 7 and 8. Generally it appears that the use of Tasdemir et al's expression for strain at peak stress most accurately simulates the experimental softening response. However, it should be noted, that all three expressions accurately model the softening trend shown in Figure 13, and that any of the shear friction expresssions presented in this paper can be refined through more accurate empirical expressions. The key finding is that shear friction theory can be used to simulate concrete softening that occurs in practice.

CONCLUSION

The shear-friction properties of initially uncracked unconfined concrete have been extracted from standard concrete cylinder tests and developed in a form that can be used to simulate and quantify the behaviour of unconfined concrete under compression. The advantage of this shear-friction approach over existing approaches is that it simulates what is actually seen in practice, that is: the formation of sliding planes in initially uncracked concrete; and the relationship across these sliding planes between the shear stress τ_N, normal stress σ_N, widening h_{cr} and slip Δ. A further advantage is that this shear-friction approach is neither size nor shape dependent. It has been shown how shear-friction theory can be used to simulate the formation of wedges that occur during the softening of concrete under compression in cylinder tests and explains why the axial stress-strain relationship of concrete whilst softening that is extracted from cylinder tests is both size and shape dependent. It has also been shown how the shear-friction approach can be used to simulate the formation of wedges and the rotation that occurs in flexural members giving very good correlation with test results and without the need for empirically derived hinge lengths.

ACKNOWLEDGEMENTS

The financial support of the Australian research Council ARC Discovery project DP0985828 'A unified reinforced concrete model for flexure and shear' is gratefully acknowledged.

REFERENCES

ACI Committee 363 (1992) State of the art report on high strength concrete, ACI Publication 363R-92, American Concrete Institute, Detroit

Attard, M. and Setunge, S. (1964), “Stress strain relationship of confined and unconfined concrete”, *ACI Materials Journal*, Vol 93 No. 5, 432-442

Bažant, Z.P.,Xiang, Y.(1997), “Size effect in compression fracture: Splitting crack band propagation”, *Journal of Engineering Mechanics*, Vol. 123(2),pp. 162-172

Carreira, D.J., and Chu, K.H. (1985), “Stress-strain relationship for plain concrete in compression.” *ACI Journal*, 82(6), 797-804.

Daniell, J., Oehlers, D.J., Griffith, M.C., Mohamed Ali M.S. and Ozbakkaloglu, T. (2008), “The softening rotation of reinforced concrete members”, *Engineering Structures*, Vol. 30, No. 11, 3159-3166.

Debernardi P.G. and Taliano M. (2001), “Softening behaviour of concrete prisms under eccentric compressive forces”, *Magazine of Concrete Research*, Vol. 53, No. 4, 239-249.

del Viso, J.R., Carmona, J.R., Ruiz, G. (2008), “Shape and size effects on the compressive strength of high strength concrete”, Cement and Concrete Research, Vol. 38(3),pp. 386-395

Desayi, P. and Krisnan, S. (1964), “Equation for the stress-strain curve of concrete”, *ACI Journal*, Vol 61 No. 3, 345-350

Ferretti E. (2004) “On Poisson’s ratio and volumetric strain in concrete”, *International Journal of Fracture* Vol 126, 49–55

Haskett M., Oehlers D.J., Mohamed Ali M.S. and Sharma S.K. (2010), “The shear-friction aggregate-interlock resistance across sliding planes in concrete”, *Magazine of Concrete Research*, Vol. 62, No. 12, 907-924

Haskett, M., Oehlers, D.J., Mohamed Ali, M.S., and Sharma, S.K. (2011), “Evaluating the shear-friction resistance across sliding planes in concrete”, Engineering Structures. Vol 33, No. 4, 1357-1364.

Hognestad, E. (1951), “A study of combined bending and axial load in reinforced concrete members” Bulletin No 399, Engineering Experiment Station, University of Illinois

Markeset, G. and Hillerborg, A. (1995), “Softening of concrete in compression – localization and size effects”**,** Cement and Concrete Research, Vol. 25. No. 4, 702-708

Markeset, G. (1993), “Compressive failure of concrete including strain gradients”, PhD thesis 110, Norwegian Institute of Technology, Trondheim

Mohamed Ali MS, Oehlers DJ, and Griffith MC. (2010), “The residual strength of confined concrete”, *Advances in Structural Engineering*; 13 (4), 603-618.

Nurwidayati R., Haskett, M., Oehlers, D.J., Wu, C. (2011) “Wedge based concrete compressive failure in reinforced concrete members”, Submitted to *Strain*, July 2011

Popovics, S. (1973), “Numerical approach to the complete stress-strain relation for concrete.” *Cement and Concrete Research*, 3(5), 583-599

Roddenberry, M., Kampmann, R., Ansley, M.H., Bouchard, N., Ping, W.V. (2011), “Failure behavior of concrete cylinders under different end conditions”, ACI Materials Journal, Vol.108 (1), Pages 79-87

Tasdemir, M.A., Tasdemir, C., Akyuz, S., Jefferson, A.D., Lydon, F.D., and Barr, B.I.G. (1998), “Evaluation of strains at peak stress in concrete: a three phase composite model approach, *Cement and Concrete Composites*, 20, 301-318

Teng J.G., Huang Y.L., Lam L., and Ye L.P., (2007), “Theoretical model for fiber-reinforced polymer confined concrete”, *Journal of Composites for Construction*, 11(2), p 201-210

Van Mier, J.G.M.,Man, H.-K. (2009), “Some notes on microcracking, softening, localization, and size effects” *International Journal of Damage Mechanics*, Vol. 18(3),pp. 283-309.

Wee, T.H., Chin, M.S. and Mansur, M.A. (1996), “Stress-strain relationship of high strength concrete in compression”, *Journal of Materials in Civil Engineering*, 8(2), 70-76

Yi, S.-T.,Yang, E.-I.,Choi, J.-C.(2006), “Effect of specimen sizes, specimen shapes, and placement directions on compressive strength of concrete”, *Nuclear Engineering and Design*, Vol. 236(2),pp. 115-127

Statement of Authorship

The Reinforcement Contribution to the Cyclic Behaviour of Reinforced Concrete Beam Hinges

Earthquake Engineering and Structural Dynamic: Accepted for publication

Visintin, P. (candidate)

Prepared manuscript, performed all analyses, and developed model and theory.

I hereby certify that the statement of contribution is accurate
Signed……..Date……

Oehlers, D.J.

Supervised research, provided critical manuscript evaluation and acted as corresponding author.

I hereby certify that the statement of contribution is accurate and I give permission for the inclusion of the paper in the thesis
Signed…….Date……

Wu, C.

Co-supervised research, provided manuscript evaluation.

I hereby certify that the statement of contribution is accurate and I give permission for the inclusion of the paper in the thesis

Signed …….Date……

Griffith, M.

Co-supervised research, provided manuscript evaluation.

I hereby certify that the statement of contribution is accurate and I give permission for the inclusion of the paper in the thesis

Signed …….Date……

The Reinforcement Contribution to the Cyclic Behaviour of Reinforced Concrete Beam Hinges

Visintin, P., Oehlers, D.J., Wu, C., and Griffith, M.C.

ABSTRACT

The cyclic behaviour of plastic hinges is an essential component in tracking the behaviour of reinforced concrete (RC) frames to failure, not only for monotonically increasing force/pressure loads such as under extreme wind loads but also for dynamic displacement-driven loads such as under earthquake ground motions. In order to describe member deformations at ultimate loading, traditional moment-curvature techniques have required the use of an empirical hinge length to predict rotations, and despite much research a definitive generic expression for this empirical hinge length is yet to be defined. To overcome this problem, a discrete rotation approach, which directly quantifies the rotation between crack faces using mechanics, has been developed for beams and been shown to be accurate under monotonic loading. In this paper, the discrete rotation approach for monotonic loads is extended to cope with cyclic loads for dynamic analyses, and this has led to the development of a new partial interaction numerical simulation capable of allowing for reversals of slip of the reinforcing bars. This numerical tool should be very useful for the nonlinear analysis of reinforced concrete beams and reinforced concrete columns with small axial loads under severe dynamic loads.

Keywords: Reinforced concrete; hinges; ductility; discrete rotation; cyclic loads; and hysteretic behaviour.

INTRODUCTION

The importance of ductility, that is the ability of reinforced concrete members to maintain strength under deflections/rotations beyond their yield point and, thereby, absorb energy inputs such as those from seismic and blast loads, has long been recognised as a key design aspect. Since the early 1960s, a significant amount of experimental and analytical research has been devoted to describing the hysteretic behaviour of reinforced concrete beams and beam column joints under cyclic loading well into the inelastic range. A key feature of the hysteretic response is the loss of stiffness associated with repeated reverse cyclic loading. It is well established [1] that the major causes of this loss of stiffness are: the Baushinger effect which describes the softening behaviour of steel following a reversal of load; concrete cracking and splitting along the reinforcing bars; cyclic deterioration of the bond between the reinforcing bars and the surrounding concrete; and shear sliding and crushing of the concrete.

Early experimental and analytical work in describing the hysteretic behaviour of reinforced concrete sections lead to the proposal of several moment-curvature models [2-5]. These strain-based approaches use standard beam analysis techniques with cyclic material models to describe the cyclic moment curvature response, and, are therefore capable of including the Baushinger effect. However, the moment curvature approach is limited when used to describe member rotation. This is because it is a two-dimensional analysis of a cross-section and, therefore, the hinge length over which the curvature is integrated to derive the rotation has to be determined empirically, as, in theory, it can be shown that the hinge is of zero length [6, 7]. Numerous empirical formulations for determining the hinge length have been suggested in the literature and while they show good accuracy when compared to the data set from which they were derived, when applied to a global data set correlations are poor [8].

Following these early strain-based analyses, and subsequent to the identification of the importance of the influence of bond behaviour in the reduction of member stiffness during cyclic loading, an extensive experimental and analytical effort to describe the mechanics of the bond slip problem was undertaken [9-12]. The development of reliable cyclic bond slip relationships led to several finite element based hysteresis models being developed [13-15]. While these finite element models allow for the influence of the Baushinger effect, include bond slip effects, and are capable of considering the influence of shear [16] they are limited in the same way as the early curvature-based analyses, that is, they need a specified hinge length. This is because the inclusion of concrete material softening in a finite element formulation restricts the softening zone, which is in effect the hinge length, to the length of that element [6].

Recently, a partial-interaction discrete rotation approach has been developed that quantifies the discrete rotation between crack faces by allowing for the relative slip between the reinforcement and the concrete at the crack face, [17-27] and both numerical partial-interaction models [22, 26] and mechanics partial interaction models [21, 29, 25] have been developed. Using these models, the discrete rotation approach has been shown to accurately predict the rotational response of members under monotonic loading. The aim of this paper is to show how the discrete rotation approach for beams can be extended to the cyclic load case.

MOMENT DISCRETE ROTATION APPROACH

Typically, reinforced concrete members can be considered to consist of two distinct regions: (1) the hinge, or disturbed region, characterised by wide flexural cracks and concrete crushing; and (2) the non-hinge, or undisturbed region, where small cracks occur but the concrete does not crush. It is in the hinge region where much of the rotation is concentrated and where the discrete rotation between cracks is applied. The discrete rotation approach treats the undisturbed region and the disturbed hinge regions separately [22, 25, 26, 28, 29].

In the undisturbed region beyond the hinge regions, it is sufficiently accurate to use the Euler-Bernoulli moment curvature approach that assumes full interaction between the reinforcing bars and the surrounding concrete to quantify the deformations, using effective flexural rigidities if necessary to allow for minor cracking. In contrast, in the disturbed hinge region at the location of a wide flexural crack which is associated with hinges at the ultimate limit state, discrete rotation occurs between the crack faces. This rotation is caused by the widening of the tensile crack, which is itself caused by the relative slip between the reinforcing bar and the surrounding concrete, known as partial interaction behaviour. This is a rigid body displacement and as such the curvature approach does not apply as it assumes full interaction. In contrast to this the discrete rotation approach explicitly allows partial interaction and rigid body displacements, and therefore more accurately simulates the physical processes of concrete cracking.

The unified moment discrete rotation approach idealises the plastic hinge as in Figure 1 [26, 28, 29], where each half of the hinge rotates as a rigid body about the apex of the flexural crack. The hinge is considered to have three distinct regions. The compressive zone of the hinge is split into two regions. In the ascending region of depth d_{asc} the concrete is on the rising branch of its stress-strain relationship and standard analysis techniques based on material properties can be applied to determine the force developed (P_{asc}). In the softening wedge of depth d_{soft}, the concrete is strain softening and shear friction theory is used to describe the relative movement between the softening wedge and the ascending region, as well as the stresses acting across the sliding plane and hence the force resisted by the wedge (P_{soft}). Finally, in the partial interaction tensile zone of depth h_{crack}, the load resisted by the reinforcing bars, $P_{reinf\text{-}tens}$, for a given slip, $\Delta_{reinf\text{-}tens}$, is determined using partial interaction theory [21, 24, 25, 28] between the reinforcing bar and surrounding concrete.

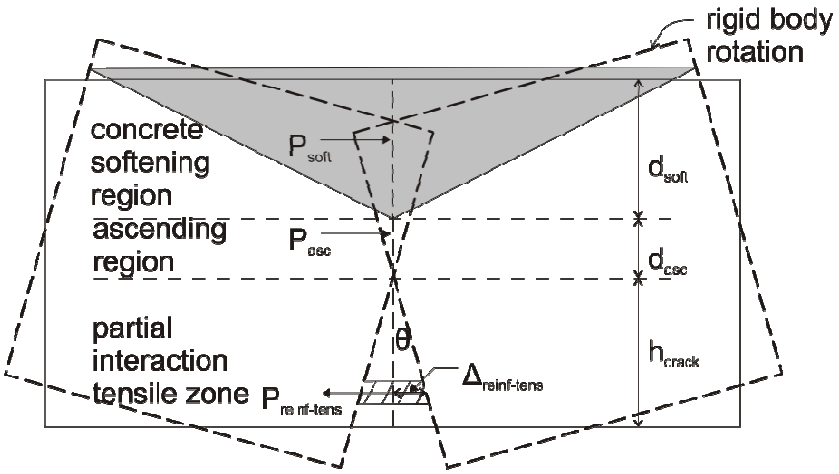

Figure 1: Idealisation of plastic hinge

For analysis, the hinge can be further idealised to consider a single crack face as in Figure 2, where the moment-rotation relationship is derived for increasing depths of the softening wedge, $d_{soft.}$ For a specific value of d_{soft}, which acts as the pivotal point for the analysis, the rigid body displacement profile in Figure2(b) can be rotated through θ radians until longitudinal equilibrium of the forces is achieved, thereby, allowing for the determination of the moment and rotation. The equations for calculating these forces are presented below; however a more detailed derivation of the fundamental principles can be found elsewhere [24, 28, 30]

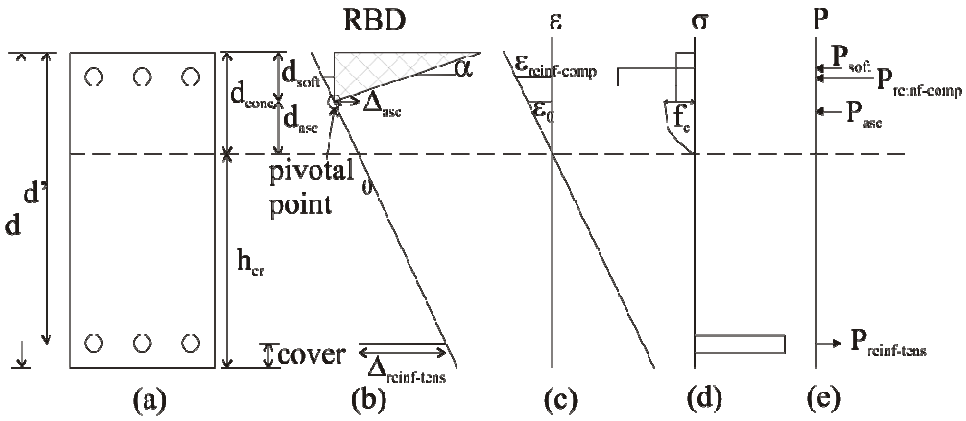

Figure 2: Hinge idealisation for moment rotation analysis

Concrete compression zone

The depth of the softening wedge, d_{soft} in Figure 2 can be determined from the locus of Δ_{asc} as in the following equation where all unknowns are defined in Figure 2.

$$d_{Soft} = \frac{d'\theta - \Delta_{reinf-tens}}{\frac{\varepsilon_0}{tan(\alpha)} + \theta} \qquad \text{Equation 1}$$

The force resisted by the softening wedge, P_{soft}, may then be determined using Equation 2 [31],

$$P_{soft} = w_b d_{soft} \left[\frac{c + \sigma_{lat} cos\alpha (sin\alpha + mcos\alpha)}{sin\alpha (cos\alpha - msin\alpha)}\right] \qquad \text{Equation 2}$$

where, w_b is the width of the cross-section, m and c are the friction and cohesion components of the Mohr-Coulomb failure plane for the concrete which can be derived from material testing [32], σ_{lat} is the lateral confinement provided to the wedge by stirrups and α is the angle at which the wedge forms which is a function of the friction property as given in Equation 3.

$$\alpha = arctan\left(-m + \sqrt{m^2 + 1}\right)$$ Equation 3

In the absence of specific material properties, typical values can be employed in the analysis, with a friction component m of 0.8, a cohesion component c of $0.17f_c$, and an angle of the failure plane, α of 26˚ [31].

Using the rigid body moment-rotation approach, the wedge does not fail when its strength P_{soft} is achieved, but rather has a limit to the slip Δ_{asc} given by Equation 4 where Δ_{slide} is the slip at failure [29].

$$\Delta_{slide} = 2.51\frac{\sigma_{lat}}{f_c} + 0.61$$ Equation 4

For reinforcement located in the softening region, the force developed can be calculated using a strain-based approach, extending a linear strain profile through the known strains at the softening wedge interface and the crack tip as in Figure 2(c).

In the remainder of the concrete in compression, that is, over d_{asc} in Figure 2, the concrete has not softened, and compressive stresses range from zero at the crack tip to the peak compressive strength, $f_{c,}$ at the strain shown as ε_0 in Figure 2(c). While any ascending stress strain relationship may be used, the force developed using Hognestad's parabolic distribution has been typically applied and is given by Equation 5 [33].

$$P_{asc} = \frac{2}{3} f_c w_b d_{asc}$$ Equation 5

For reinforcement located in the ascending regions the strain and consequently force can be calculated using the linear strain profile in Figure 2(c).

Partial interaction (P-Δ) tension region

For reinforcement located in the cracked tension zone, a partial interaction intermediate crack (IC) approach must be used to determine the relationship between the slip of the bar, $\Delta_{reinf\text{-}tens,}$ and the force $P_{reinf\text{-}tens}$ in Figure 2. Again, any appropriate partial interaction model can be applied, and for the monotonic load case closed form structural mechanics solutions are available for a variety of bond stress-slip characteristics [21, 25, 24, 31 34]. However, for the modelling presented, a numerical procedure [24, 35] has been applied as it is necessary to use a nonlinear cyclic bond stress-slip characteristic as outlined below to allow for reversals of load. For the tensile reinforcement, two limits to rotation are imposed; these are fracture and debonding of the bar, both of which can be determined based on the partial interaction model.

The basic numerical shooting procedure [24, 35] is illustrated in Figure 3, where a bar of length L_r measured from the crack face is embedded in concrete of cross-sectional area A_c and is being pulled to a displacement at the crack face of Δ, such that a force $P_r(1)$ is

generated in the reinforcing bar, and $P_c(1)$ is generated in the concrete. To describe the numerical procedure which is required to find the force to develop the given slip, the bar in Figure 3 is sliced into elements of length *dx*, which are much smaller than the overall bar length, and where each element shown has been separated to show the forces acting.

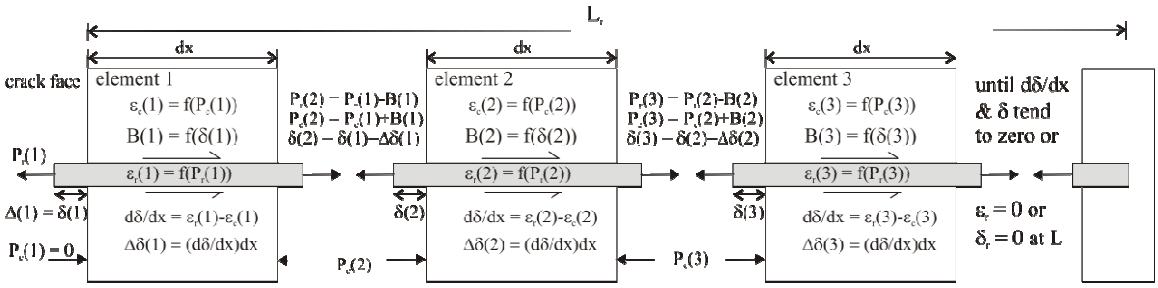

Figure 3: Partial interaction algorithm at an elemental element

The analysis begins by fixing the slip $\Delta(1)$ at the loaded end. It is then a question of finding the load in the reinforcement that induces this slip. This is done by first guessing the reinforcement strain $\varepsilon_r(1)$ and, hence, the force $P_r(1)$ to cause this slip, and iterating to find the correct $P_r(1)$ to induce $\Delta(1)$.

This fixed slip of the bar $\Delta(1)$ is equal to the local slip $\delta(1)$ at the first element and generates a bond stress $\tau(1)$, which is a material property, and can be determined using a bond stress-slip relationship. As the numerical procedure being outlined is generic any bond stress slip distribution can be used, and in the case of the analysis to follow, the cyclic bond stress slip model of Eligehausen et al. [11] has been employed as it can simply describe the loss of strength and stiffness of the bond encountered during cyclic loading, as will be discussed further in the next section.

Knowing the bond stress $\tau(1)$, the bond force, *B*, acting over the element may now be calculated. It is simply the bond stress integrated over the surface area of the bar as in Equation 6, where L_{per} is the circumference of the bar and dx is the length of the segment i.e.

$$B(n) = \tau(n) dx L_{per} \qquad \text{Equation 6}$$

Having determined the bond force acting at a given element, it is possible to determine the load in the reinforcing bar at the end of the element (n), and therefore, at the beginning of the next element (n+1) by equilibrium, as in Equation7.

$$P_r(n+1) = P_r(n) - B(n) \qquad \text{Equation 7}$$

It should also be noted at this point that as a result of cyclic loading the direction of the bond force may change during unloading and reloading because of the influence of friction, and therefore, as will be shown in the results, the force in the bar can build up along the bar length instead of reducing.

The corresponding strain in the reinforcement can then be found using a suitable cyclic stress strain relationship, and in this case the relationship presented by Filippou et al. [13] has been selected based on its simplicity, and will therefore be outlined further in the next section. Similar to the cyclic bond behaviour, it will be shown that the cyclic stress-strain relationship of the reinforcing bar significantly increases the complexity of the partial interaction behaviour, as following strain hardening it is possible for the bar to experience an extending strain while being in compression.

Having determined the strain in the bar, and in order to calculate the change in slip occurring along the element, it is now necessary to determine the strain in the concrete. The force developed in the concrete surrounding the bar can be determined in a similar manner to that of the reinforcing bar; that is, knowing the bond force *B* and that no force is carried by the concrete at the crack face the force in the concrete can be found by equilibrium, as in Equation 8.

$$P_c(n+1) = P_c(n) + B \qquad \text{Equation 8}$$

The concrete strain can then be found simply by assuming a linear tensile stress strain relationship as in Equation 9, where it can be assumed that the concrete remains elastic because it is subjected to only tensile stresses. In order to simplify the analysis, it is also possible to ignore the strain developed in the concrete as the cross-sectional area of concrete is large enough that the strain developed tends to be insignificant compared to those in the reinforcement.

$$\varepsilon_c(n) = \frac{P_c(n)}{E_c A_c} \qquad \text{Equation 9}$$

The difference between the reinforcing bar and concrete strains is the slip strain which can now be found.

$$\frac{d\delta(n)}{dx} = \varepsilon_r(n) - \varepsilon_c(n) \qquad \text{Equation 10}$$

It is this difference in strain which causes the bar to slip, with the change in slip across the element simply being the integration of the slip strain across the element length, as in Equation 11.

$$\Delta\delta(n) = \int \frac{d\delta(n)}{dx}\, dx \qquad \text{Equation 11}$$

Therefore, the slip at the beginning of the next element is:

$$\delta(n) = \delta(n) - \Delta\delta(n) \qquad \text{Equation 12}$$

The numerical procedure is then repeated over the subsequent elements until the following boundary conditions are achieved: $\delta = d\delta/dx = 0$, where the embedment length is sufficient

for full interaction to be achieved, and for short bars, $\varepsilon = 0$ or $\delta = 0$ at the bar end depending on whether the bar end is free or fixed. In the following section the material models used in implementing the cyclic partial interaction model, that is the cyclic bond stress-slip, and steel stress-strain relationships will be outlined in more detail, and then a full description of the mechanics of the cyclic partial interaction model will be explained with the aid of an example.

CYCLIC MATERIAL PROPERTIES

As the partial interaction model is generic, any model to describe the bond stress slip and material stress strain behaviours can be used. Furthermore, as it is the aim of this paper to describe the mechanics of the hinge region under cyclic loading, only a qualitative description of the material properties will be outlined here while references to the original research are provided.

Bond stress-slip relationship

There has been much research on the bond interface shear stress (τ) interface slip (δ) relationship under both monotonic and cyclic loading [9, 10, 11, 13, 36, 37]. The cyclic bond stress-slip relationship seen in Figure 4, developed by Eligehausen et al. [11], has been used in the cyclic partial interaction model described later as it has been shown to adequately, and simply, allow for the degradation of bond stress due to load reversals.

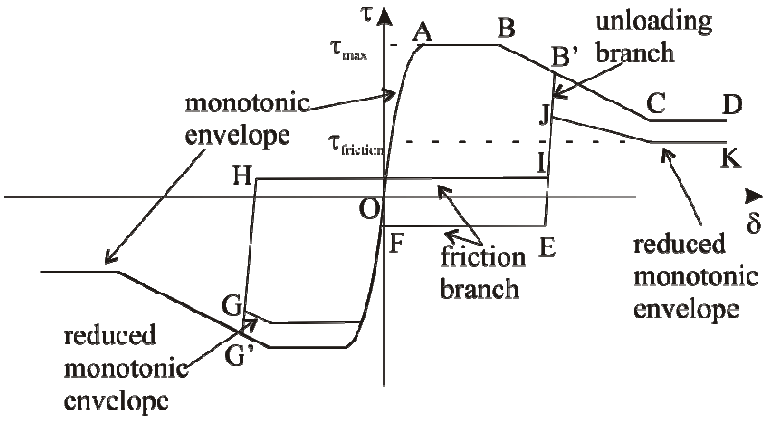

Figure 4: cyclic bond stress slip relationship

Loading – positive monotonic envelope

The key feature of the model is the monotonic envelope, O-A-B-C-D shown in Figure 4 which is followed during initial loading. Upon loading, as the bar begins to slip in region O-A and as shown in Figure 5(a), inclined cracks known as bond cracks which initiate at the tip of the bar ribs form. Moreover, this cracking is accompanied by crushing of the concrete keys which form between the bar ribs as shown in Figure 5(a).

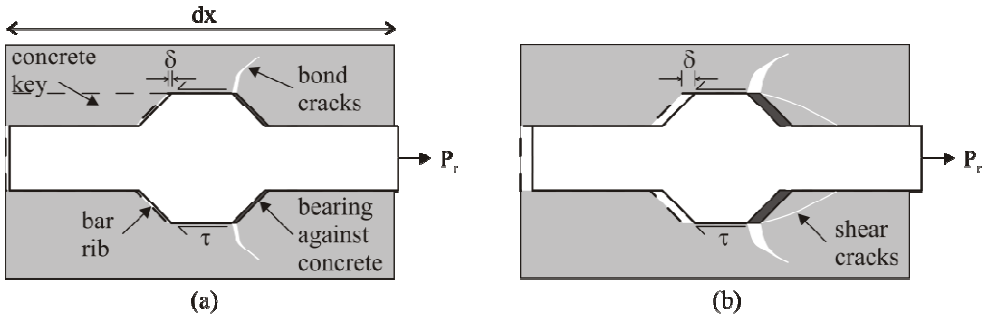

Figure 5: damage of concrete as bar pulled (a) formation of bond cracks, (B) formation of shear cracking

As the bar further slips in region A-B-C on Figure 4, the bond cracks in Figure 5(a) continue to open and shear cracks form in the concrete keys in front of the bar ribs as in Figure 5(b). This behaviour results in the levelling off (region A-B in Figure 4) and eventually a reduction (region B-C) in the bond stress as the concrete keys are sheared off.

For slips exceeding the clear spacing of the bar ribs, that is region C-D in Figure 4, complete crushing and shearing off of the concrete keys has occurred. At this point, the only resistance to the pulling out of the bar is friction, and as such the bond resistance is equal to the frictional resistance $\tau_{friction}$ in Figure 4.

Unloading

Upon unloading, such as at B' on Figure 4, the bond properties follow a very stiff unloading branch B'-E to account for the recoverable elastic deformation. This elastic unloading branch is followed until the frictional branch is reached at E. At this point, the bar can be considered to be slipping in a previously damaged area, as shown in Figure 6, where the only resistance to the slipping of the bar is offered by friction which acts in the opposite direction to the change in slip δ, hence, the negative value of the frictional resistance shown in Figure 4. This frictional resistance strongly influences the partial interaction behaviour and as will be shown later can act to increase the force in the bar P_r as in Figure 6 where the shear stress is acting in the same direction as the applied load.

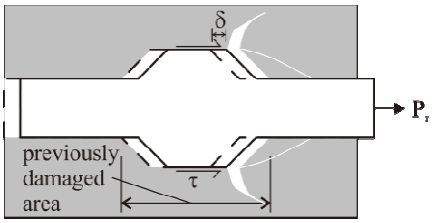

Figure 6: Bar slipping in previously damaged area

Loading – negative monotonic or reduced envelope

Once the slip of the bar has been reduced to a level where it has returned to its original position, point F on Figure 4, the bar ribs are again in contact with the surrounding concrete as in Figure 7. The loading path taken as the slip is further reduced, such that is it now slipping in the opposite direction, now depends on the maximum slip previously reached, point B' on Figure 4. If the maximum slip is less than that to cause shear cracking, that is B' is located within region O-A on Figure 4, any further reduction in slip will result in loading along the negative monotonic envelope F-G', where the old bond cracks close and new bond cracks open as shown in figure 7. However, if the reversal occurs following the formation of shear cracks, that is, B' is located within regions A-B-C-D in Figure 4, loading will occur along the reduced monotonic envelope F-G as the existing bond cracks close.

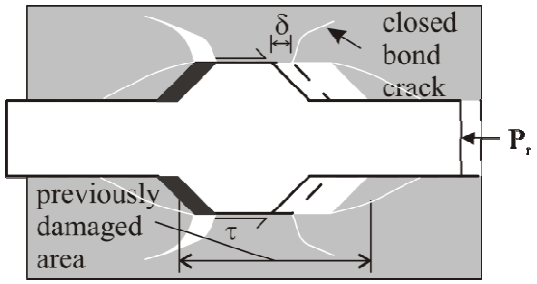

Figure 7: Slipping of bar in opposite direction

The reduced envelope O-G in Figure 4 is obtained by reducing the magnitude of the bond stresses of the monotonic envelope using a damage parameter to account for previous damage. The damage parameter is related to the total energy dissipated during previous loading; full details of which can be found in [11].

Reloading

During reloading, along G'-H on Figure 4, the same process is encountered as during unloading, where to account for the recovery of elastic deformation a stiff curve is followed until the bar's only resistance is due to friction along H-I.

This friction branch is reduced in magnitude compared to that followed during unloading to account for further damage to the concrete. The magnitude of the reduction to the friction branch is also calculated by using a damage factor, where the magnitude of the reduction is related to the total energy dissipated while the bond resistance is due to friction; again full details of which can be found in [11].

Once the bar is again in contact with the concrete at point I in Figure 4, a stiff reloading path is initially followed to allow for any elastic deformation before switching to the reduced monotonic envelope J-K, where the magnitude of the reduction is again based on the total energy dissipated by previous loading.

Steel stress-strain relationship

In addition to a cyclic bond stress-slip relationship, the partial interaction model requires a cyclic stress-strain relationship for the steel reinforcement. While numerous models have been published [38-41], a model which can accurately describe the features of the hysteretic stress strain behaviour, as seen in Figure 8 [40], is required, and as such the model of Filippou et al. [13] has been used in the modelling.

The key features identified and shown in Figure 8 are: the Baushinger effect which is the early departure from the linear elastic response; strain softening which refers to the degradation in the modulus following load reversals; and isotropic strain hardening which causes an increase in strength beyond the initial yield stress. It has been identified that the Baushinger effect is responsible for a significant portion of the loss of stiffness observed at a member level under cyclic loading [1]. This is confirmed in the following cyclic partial interaction model where it is shown that a model capable of describing these behaviours is especially important as the behaviour of the steel strongly influences the partial interaction behaviour.

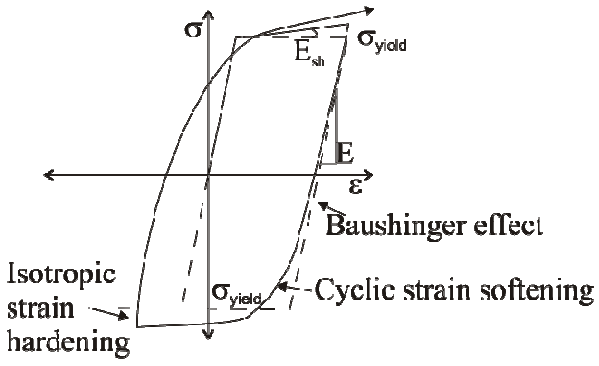

Figure 8: Features of hysteretic steel stress-strain behaviour

CYCLIC PARTIAL INTERACTION MODEL

The monotonic partial-interaction P-Δ model has already been described with the help of Figure 3. A description of the mechanics of adapting this monotonic model for cyclic loads follows. It will be shown that the influence of strain-hardening and that of the friction component of the bond stress-slip relationship are critical in describing the overall load slip relationship at the crack face.

An example of a theoretical cyclic partial interaction load-slip P-Δ curve is presented in Figure 9; the bar is initially loaded to a peak slip of 3mm at point *p*, unloaded to zero slip, and finally reloaded to a slip of 4mm. In addition, a monotonic envelope up to 4mm slip is shown so that the degradation of strength and stiffness that occurs during cyclic loading can be observed. Furthermore, points *a*-*e* in Figure 9 refer to points in the load cycle in which distinct changes in the partial interaction behaviour occur; these will be used as the points of discussion in the following description of the behaviour.

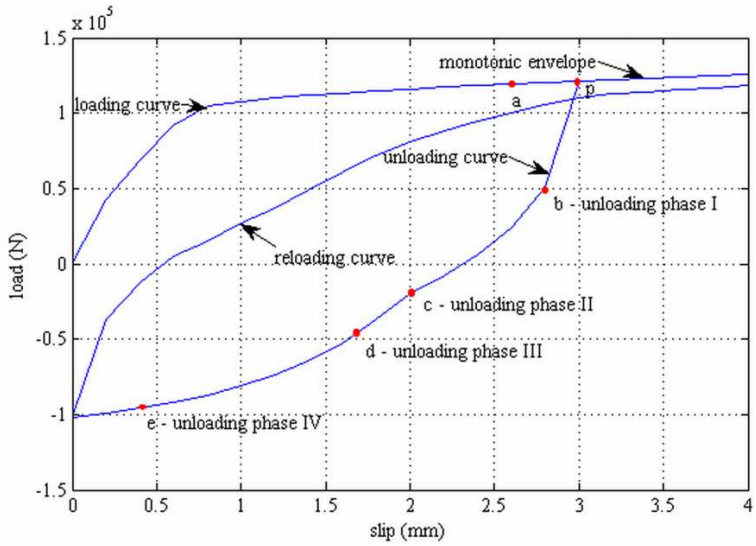

Figure 9: Cyclic load-slip response of an infinitely long bar

Initial loading phase

The discussion begins with the establishment of the most basic behaviour which occurs throughout the initial loading phase and which results in the formation of the initial loading curve and monotonic envelope in Figure 9. The mechanics of the initial loading behaviour can best be described by considering adjacent elements numbered n and n+1 in Figure 10(a). These elements are similar to those in Figure 3, but in this case, to help in the description the strain in the concrete ε_c has been ignored as it tends to zero in comparison to the strain in the reinforcement. Hence, the slip strain is simply the strain in the reinforcing bar ε_r.

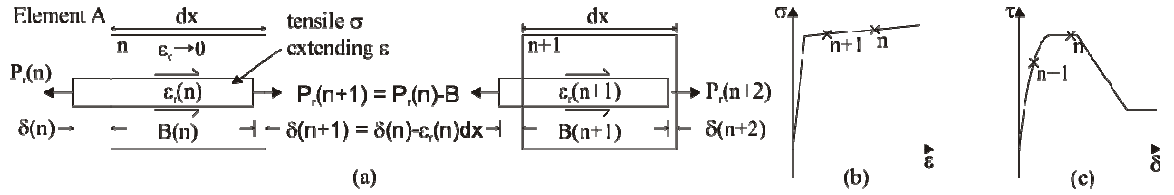

Figure 10: Behaviour of Element A

During the initial stages of loading as shown in Figure 10(a), the bar slips a distance δ(n) relative to the concrete as it is being pulled out with a force $P_r(n)$. This slip causes a bond force B(n) to be developed which resists the pulling out of the bar, and through equilibrium results in a reduction in the force carried by the bar from $P_r(n)$ to $P_r(n+1)$. This corresponds to a reduction in stress and strain from element n to element n+1 as shown in Figure 10(b). Furthermore, as the strain in the bar is extending the bar, the slip is reduced from δ(n) to δ(n+1) as shown in the bond stress-slip relationship in Figure 10(c).

During initial loading, the behaviour of the bar and the bond is confined to the first quadrant of their respective relationships shown in Figures 10(b) and (c). Hence, the behaviour described using the elements in Figure 10(a) is representative of the behaviour anywhere along the bar from the crack face in Figure 3 to the point of full interaction. Figure 11 shows the distributions of the slip, slip strain, stress in the bar and the bond stress from the crack face to the point of full interaction for point *a* on Figure 9. All four distributions reduce as the distance from the crack face increases which is typical of initial loading; where this occurs will be referred to as Zone A. It is worth noting that the force in the bar at the crack face and the slip of the bar at the crack face $P_r(1)$ and Δ(1) in Figure 3 is given in Figure 11 at the distance of zero.

To find a solution to the shooting method illustrated in Figure 3 requires a specific boundary condition to be achieved. For example, for a full-interaction boundary condition which was used in Figure 11, both the slip and slip-strain must converge to zero at the same point, which in this case is at about 750 mm from the crack face as shown. Figure 11 encapsulates all the elemental properties required for the shooting method illustrated in Figure 3 and consequently the conditions required for convergence of the analysis depicted in Figure 3 to find a solution in Figure 11 for Zone A. As will be shown later, these elemental conditions change depending on the quadrant of the bond-slip properties in Figure 4 and the quadrant of the reinforcement material properties in Figure 8 that the analysis is dealing with. All other possible conditions (Figures 13, 15, 16, 18, 20 and 21) will be covered in the following section.

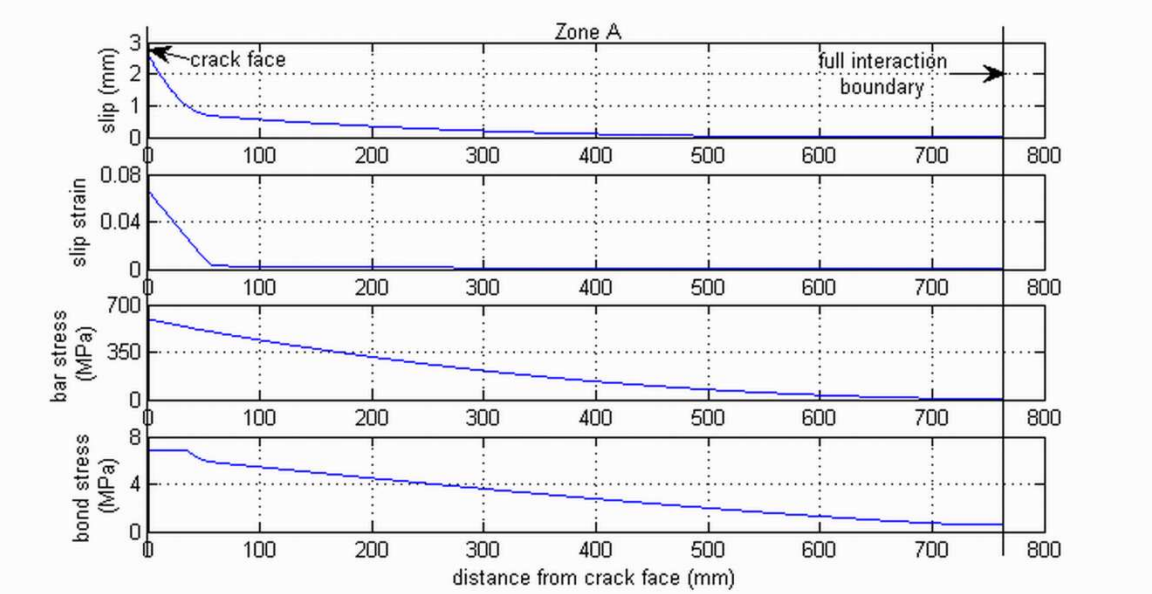

Figure 11: Distribution of slip, slip strain, bar stress and bond stress during loading (point *a*)

Having identified the conditions for convergence for the initial loading case on the elemental level, the behaviour during unloading and reloading of the bar can now be explained through the changes in the stress-strain and bond stress-slip relationships and their resulting changes at the elemental level. It should be noted that throughout the various stages of unloading the behaviour seen along the bar length, as in Figure 11, can be categorised into zones where distinct changes in behaviour occur; each of these zones is accompanied by a description of the behaviour on an elemental level. Where the behaviour along the portion of the bar length, that is zone, is the same as has been described previously, it will not be repeated, but instead, the description of the each phase will focus on the new behaviour and the reader is referred to previous descriptions where the behaviour is common to more than one phase.

Unloading - phase I

Point *b* in Figure 9 is in the first phase of unloading and occurs immediately after the loading is reduced. The behaviour in phase I is characterised by a reduction in slip at the crack face $\Delta(1)$ being accompanied by a reduction in the applied load at the crack face $P_r(1)$. That is, the slip is reduced without the need to push the bar in which is a case considered later.

The initial response of the bar to the reduction in slip must be considered in two distinct stages, because, as shown in Figure 12, the behaviour is initially divergent in zone B, where the bond stress is acting to increase the bar stress before the distributions converge in Zone A to allow full-interaction to be achieved. Zone B is introduced in this unloading phase; Zone A has already been outlined above and will, therefore, not be repeated.

Consider an element in Zone B in Figure 12 as shown in Figure 13(a). The bar is being pulled but with a reduced force compared to that at which the peak slip (point *p* on Figure 10) is achieved. Furthermore, the slip is reduced to a level where the bond stress is located on the negative friction branch as in figure 13(c).

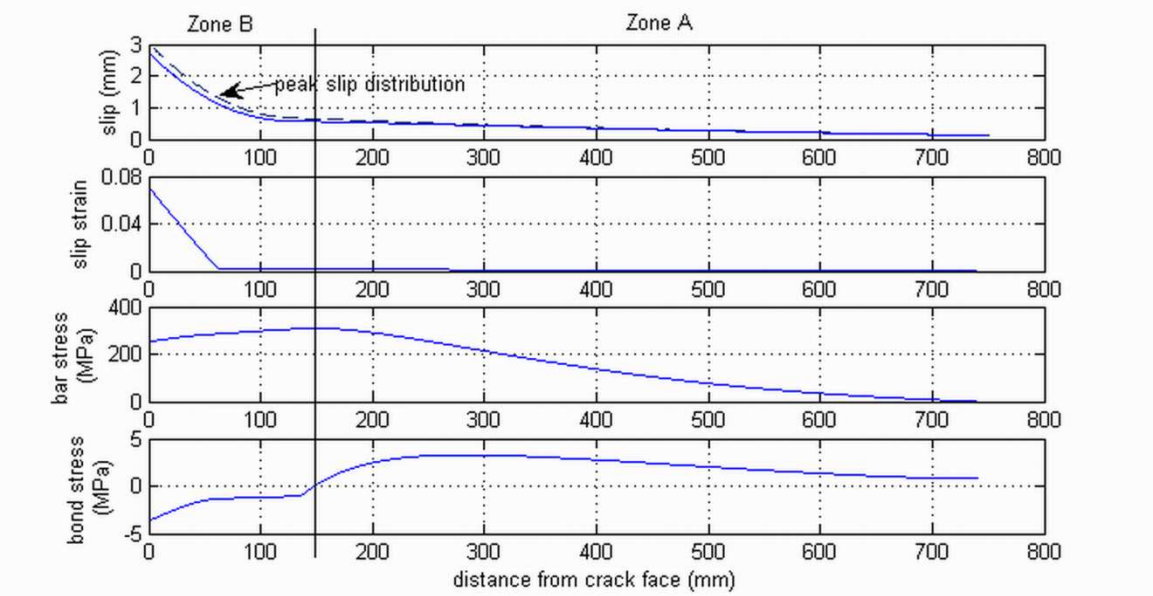

Figure 12: Distribution of slip, slip strain, bar stress and bond stress during unloading phase I (point *b*)

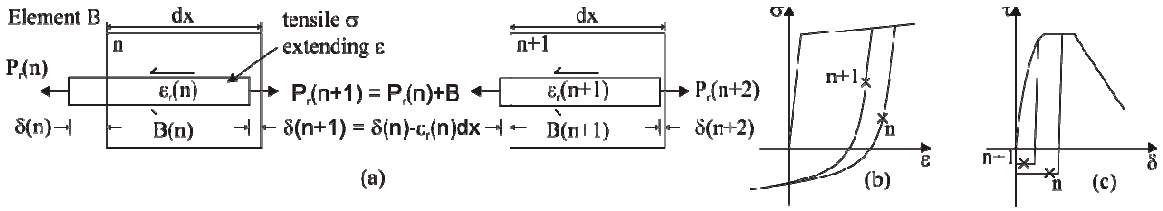

Figure 13: Behaviour of element B

This negative bond stress in Figure 13(c) means that the bond force is acting to increase the force in the bar as shown in Figure 13(a) where the force on the right hand side of each element is greater than that at the left hand side. This increase in force results in an increase in the bar stress but a decrease in strain from n to n+1 in Figure 13(b). This reduction in strain can be explained using Figure 13(b) where it can be seen that each element has its own unloading curve. The shape of these stress-strain relationships is dependent upon the maximum stress achieved during loading, and therefore despite the increasing stress the

strain reduces. Additionally, as the strain in the bar is an extending strain, the slip strain acts to reduce the slip of the bar.

The behaviour outlined above continues from the crack face in Figure 12 until the bond stress is no longer negative. This switch to a positive bond stress can occur in two ways. Firstly, as the slip of the bar approaches the maximum slip previously achieved, shown in Figure 12 as the peak slip distribution which refers to point *p* on Figure 9, the bond stress switches to being on the unloading branch shown in Figure 4. Secondly, as the shape of the stress strain relationship, which controls the rate of reduction of the slip, has changed, it is possible that the slip of the bar at some point exceeds the peak slip. At this point, the bar is slipping further than it has before and as such the monotonic loading bond stress slip relationship is used.

At this point, the bar is being pulled with a tensile force, the strain is an extending strain and the bond stress is positive. These are identical conditions to the initial loading case, that is Zone A, and consequently convergence onto the point of full interaction is achievable.

Unloading – phase II

As unloading continues, the load required at the crack face to reduce the slip of the bar at the crack face further reduces until it is such that the bar must be pushed. This occurs at point *c* on Figure 9, where the distributions along the bar are shown in Figure 14. It can be seen that the bar stress at the crack face and consequently $P_r(1)$ is negative i.e. compressive even though $\Delta(1)$ that is the slip at the crack face is still positive. The additional complexity introduced at the elemental level, now that the bar is in compression, requires that the behaviour be considered in 4 separate zones along the bar length, as shown in Figure 14.

Elements in Zone C in Figure 14 have the properties in Figure 15(a) where the bar has a compressive force applied to it such that the slip of the bar is reduced to $\delta(n)$ where the bond stress is again on the negative friction branch as in Figure 15(c). This negative bond stress yields a bond force which acts to resist the pushing in of the bar thereby reducing the force in the bar as shown in Figure 15(a). As shown in Figure 15(b), this reduction in bar force results in a reduction in compressive stress and a reduction in strain. It can be seen that this behaviour occurs inside the region where the bar has previously strain hardened and, therefore, the bar may experience a compressive stress with an extending strain. During this stage, as the strain is an extending strain, the slip in the bar also continues to reduce and it initially appears that the distributions shown in Zone C of Figure 14 are converging. This behaviour is, however, not convergent due to the short region over which the bar typically strain hardens.

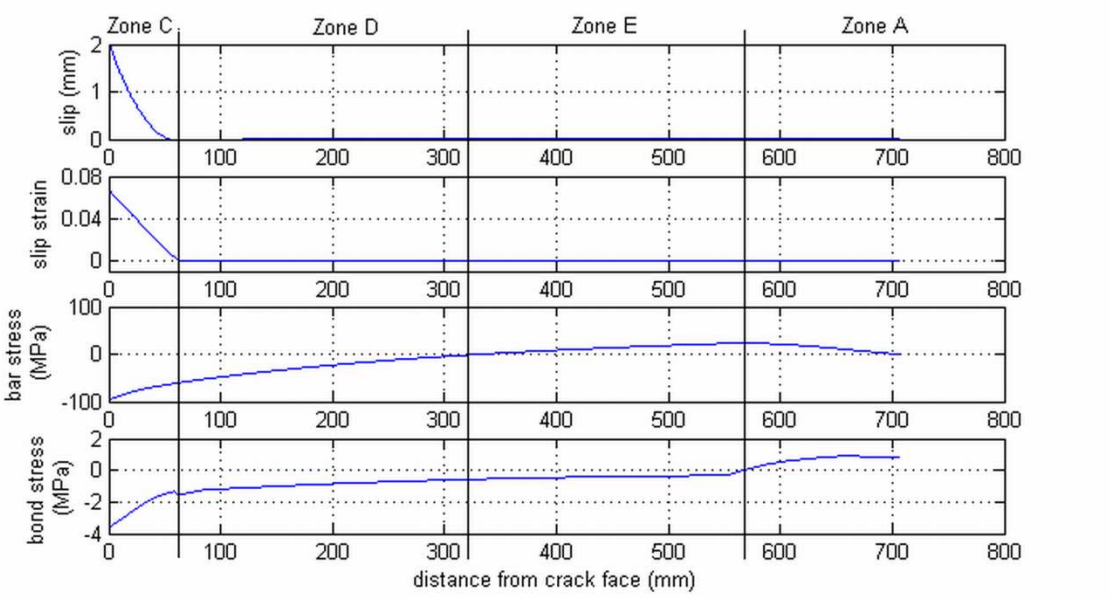

Figure 14: Distribution of slip, slip strain, bar stress and bond stress during unloading phase II (point *c*)

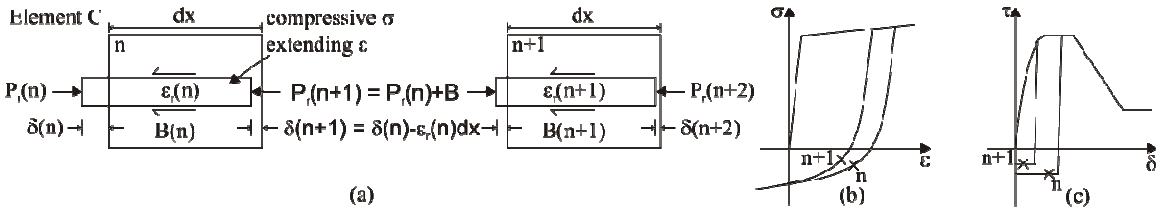

Figure 15: Behaviour of element C

At the end of the region where the bar has undergone strain hardening, the bar may no longer experience a compressive stress and an extending strain. Therefore, the behaviour at an elemental level must now change to that seen in Figure 16 as we are located in Zone D on Figure 14.

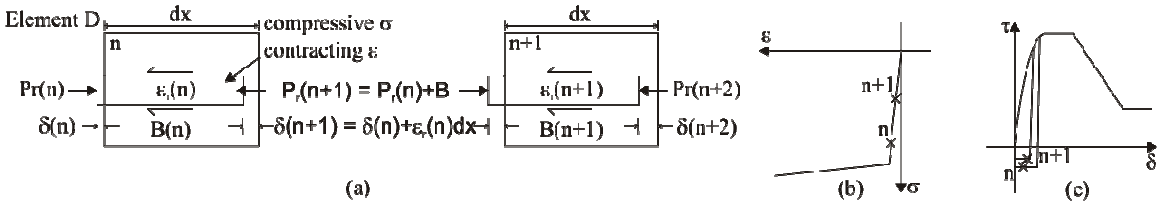

Figure 16: Behaviour of element D

In Zone D, the slip of the bar is still such that the bond stress remains on the friction branch and the bar is still being pushed. Therefore, the stress in the bar is still reducing in compression as shown in Figure 16(b). However and importantly, in this region, as the bar has not previously strain hardened, the strain must be a contracting strain. This contracting strain results in an increase in the slip of the bar as in Figure 16(a) and shown in Zone D of Figure 17 where the distribution of slip strain has been shown on a reduced scale to better show the change in behaviour. Hence, the slip and slip-strain can be seen to be diverging from the point of full interaction.

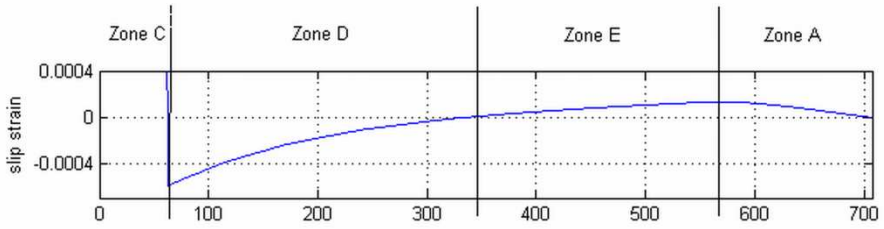

Figure 17: slip strain distribution of point *c*

While the slip of the bar is such that the bond stress is located on the negative friction branch, the force in the bar continues to increase until the bar once again experiences a tensile stress and, since this behaviour is occurring outside the previously strain hardened region, an extending strain. At this point, the behaviour again changes to that seen in Zone E on Figure 14, where the slip of the bar can now be seen to be reducing. The behaviour occurring in this region is outlined using Figure 18, where it can be seen that the bar is again experiencing a tensile stress and extending strain. As the slip is still significantly less than that achieved during previous loading, the bond stress is located on the negative friction branch as in Figure 18(c) and results in a bond force which acts to increase the force in the bar. Importantly, in this region, as the strain is again an extending strain the slip of the bar is reduced across the elements, as seen in Figure 14.

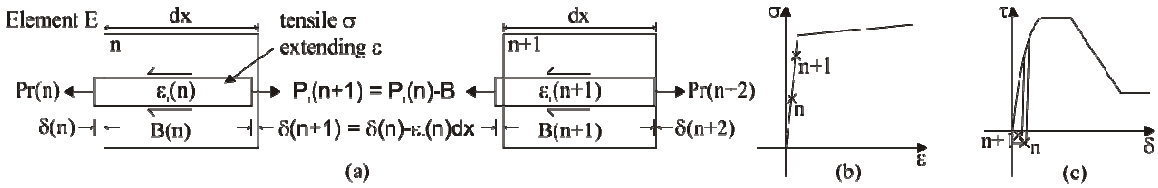

Figure 18: Behaviour of element E

This behaviour continues until the slip of the bar at an element is sufficient that either the bond stress is located on the positive portion of the unloading branch or the slip of the bar at a given element is greater than that experienced during previous loading. At this point, the behaviour is as in Zone A and convergence is achieved.

Unloading – phase III

As unloading continues, such as at Point *d* on Figure 9, the compressive force required to reduce the slip further increases. This changes the overall convergence behaviour as the bar begins to slip in the opposite direction locally, shown as a negative slip on the Figure 19.

As can be seen in Figure 19, the majority of the behaviour seen in phase III is identical to that observed in phase II and it will, therefore, not be outlined in great detail here. Instead, the additional behaviour which occurs in Zones F and G will be focused upon. The behaviour is initially identical to that seen in phase II where in Zone C the bar is pushed with a compressive force which generates an extending strain and the slip is such that the bond stress is on the negative friction branch. Together these conditions act to reduce the slip and slip strain and the behaviour appears to be convergent. However, in phase III the magnitude of the initial slip is low and, therefore, the bar may begin to slip in the opposite direction as shown in Zone F of Figure 19, where a typical element of this region can be seen in Figure 20(a).

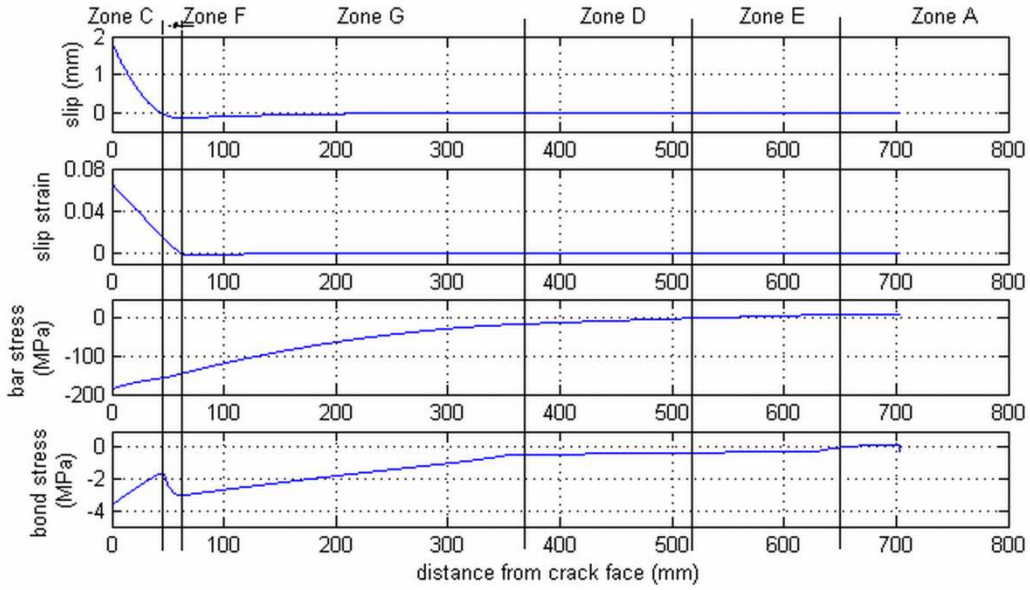

Figure 19: Distribution of slip, slip strain, bar stress and bond stress during unloading (point d)

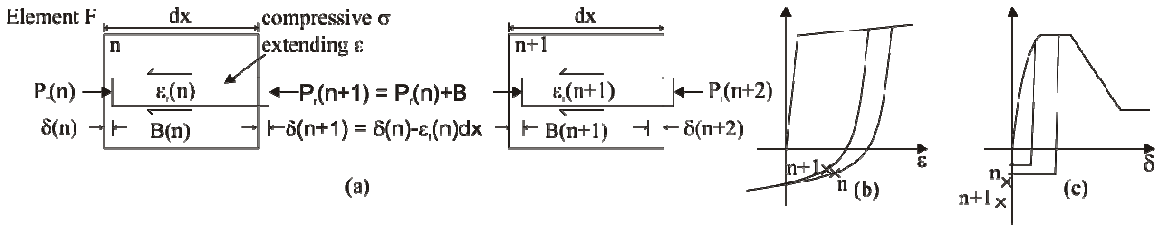

Figure 20: Behaviour of element F

As the bar is now slipping in the opposite direction, as shown in Figure 4, the bond stress is now located on either the negative monotonic envelope or the reduced negative monotonic envelope depending on the previous maximum slip, that is point p on Figure 9. With the force in the bar being in compression, the bond force, by equilibrium, acts to increase the force in the bar. Since Element F is located whin a previously strain hardened portion of the bar, the strain is an extending strain and, therefore, the slip of the bar is further reduced across the element.

This behaviour continues into region G on Figure 19 where the element under consideration, Figure 21(a), is located outside the region which has previously undergone strain hardening. As the force in the bar is compressive, the negative bond force acts to reduce the bar force and, therefore, both the stress and strain across the element as shown in Figure 21(a) and Figure 21(b). Moreover, as the strain is now a contracting strain, the slip of the bar begins to increase as in Figure 19.

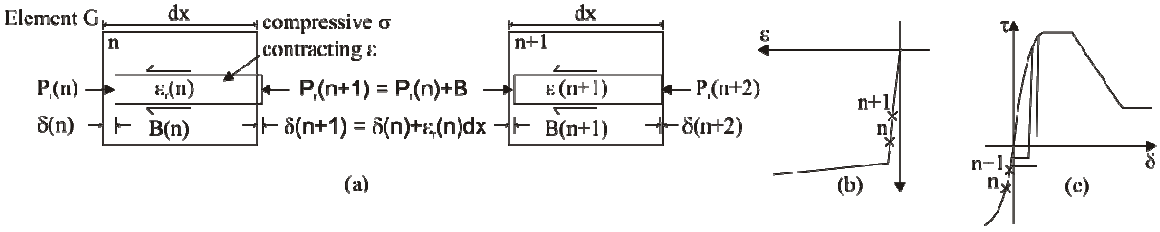

Figure 21: Behaviour of element G

At this point, the slip of the bar is now positive and the stress compressive on the linear elastic portion of the stress strain curve. This behaviour is identical to that seen in Zone D of Phase II and, therefore, the remainder of the behaviour seen in Phase III is identical to that of Zones D, E and F seen in Phase II and will not be described again here.

Unloading – phase IV

The final stage of unloading is characterised by small slips and large compressive forces. A typical distribution of the slip, slip strain, bar stress and bond stress along the bar is shown in Figure 22 which corresponds to point *e* on Figure 9.

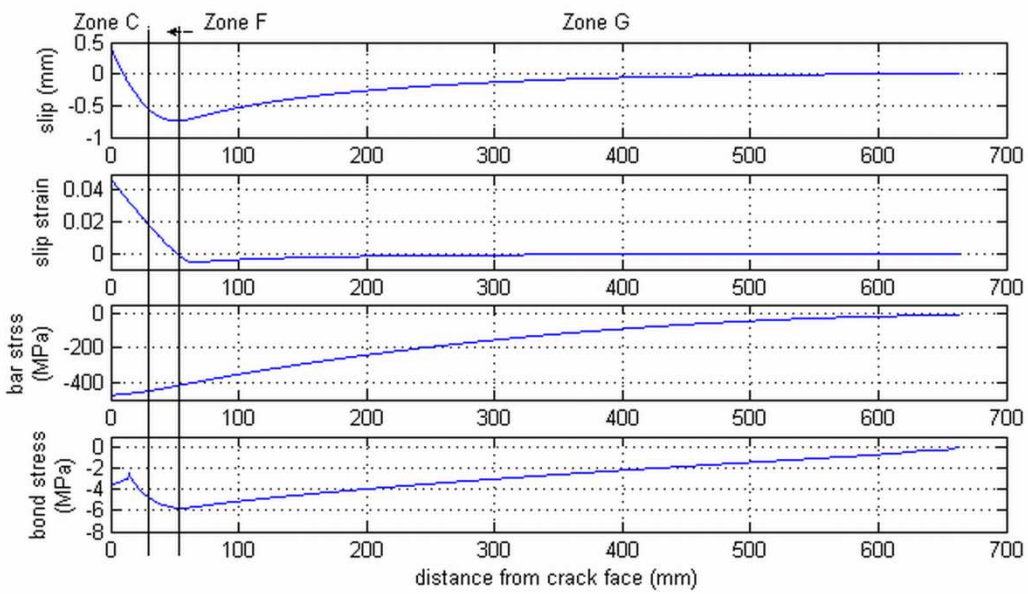

Figure 22: Distribution of slip, slip strain, bar stress and bond stress during unloading (point *e*)

The elemental behaviour for stage IV will not be outlined here as it is identical to that seen at the beginning of phase III (Zones C,F and G). However in this case, as can be seen in Figure 22, full interaction is achieved where the bar is shortening and being pushed in the opposite direction to its initial loading over almost the entire length from the crack face to the point of full interaction.

Reloading phase

During reloading, identified as the reloading curve on Figure 9, the mechanics behind each of the unloading phases also apply. Therefore a detailed description of the behaviour will not be presented. Instead, it should be noted that the reloading branch has been developed by seeking out the same distributions of slip and slip strain as shown in each of the unloading phases but in reverse (from phase IV to phase I).

Comparison of strain hardening and linear elastic material

As much of the mechanics of the load-slip behaviour presented above arises due to strain hardening, a comparison of the behaviour of a linear elastic and a strain hardening reinforcement material is presented in Figure 23. Both materials had initially the same elastic Young's modulus and, hence, initially followed the same path up until the yield point of the strain hardening material, after which they were loaded up to a slip of 3mm, unloaded to a zero slip and then reloaded to a slip of 4mm.

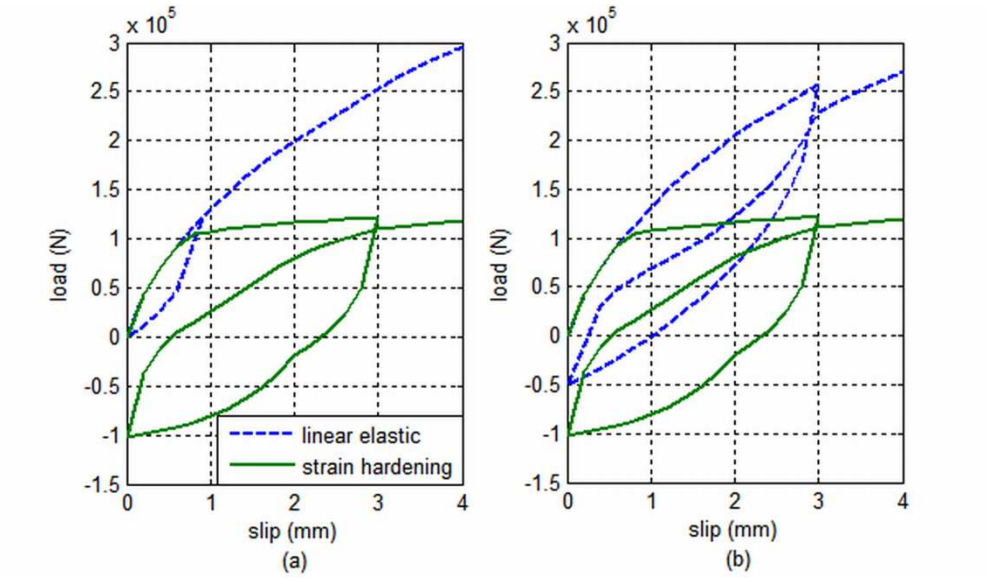

Figure 23: Comparison of load slip relationship for a linear elastic and strain hardening material

The linear elastic curve has been generated by applying the same loading and unloading phases as presented for the strain hardening material but the behaviour is limited to elements where strain hardening played no influence namely Elements A, D and E. A comparison of the behaviour of the linear elastic and the strain hardening curves shows that if the linear elastic material were to be unloaded from the same load level as the strain hardening material, for example after being loaded to 1.2kN, as in Figure 23a, a significant reduction in energy dissipated would occur. However, if allowed to slip to the same amount, that is, up to 3mm before being unloaded as in Figure 23b, the linear elastic material is capable of absorbing a considerable proportion of the energy absorbed by a strain hardening material.

CYCLIC MOMENT-DISCRETE ROTATION APPROACH

The moment discrete rotation approach as illustrated in Figures 1 and 2 has been described previously. Its application depends on the P-Δ relationship of the reinforcement crossing the tensile crack which can be derived from numerical analyses as illustrated in Figure 3 or mechanics solutions [26, 28, 34]. The same analysis can be used for cyclic loads whilst the crack first widens then closes with the P-Δ relations from the cyclic partial interaction model such as that derived in Figure 9.

At some stage of cyclic loading, a full depth crack develops to allow the tension region to go into compression and vice versa as depicted in Figure 24. In order to maintain equilibrium, the uncracked concrete section in Figure 1 must move into tension. This results in a mechanism where the section is cracked through its full depth and only the layers of tension

and compression reinforcing are interacting as in Figure 24. The P-Δ relationship still applies to the originally 'tension' reinforcement which is now in compression as a crack still intercepts this reinforcement and P-Δ still applies until the crack closes that is Δ is zero. The P-Δ relationship now also applies to the originally 'compression' reinforcement as a crack now intercepts this reinforcement allowing the reinforcement to slip relative to the crack face.

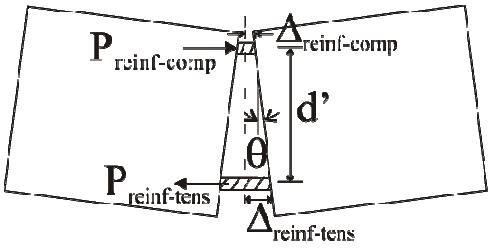

Figure 24: Idealisation of unloading following full depth cracking

For a given slip of the 'tensile' reinforcement, the load carried by the bar is known from the partial interaction P-Δ analysis and since $P_{reinf\text{-}comp} = P_{reinf\text{-}tens}$ in Figure 24 in order to maintain equilibrium, the slip of the 'compression' reinforcement can be determined based on its load-slip relationship. Knowing both the slip of the 'tensile' and 'compressive' reinforcement the rotation can be found using Equation 13, where all unknowns are as defined on Figure 24.

$$\theta = \tan^{-1}\left(\frac{\Delta_{reinf-tens}-\Delta_{reinf-comp}}{d'}\right) \qquad \text{Equation 13}$$

The analysis continues by incrementally reducing the slip of the 'tensile' reinforcement until the slip reduces to zero which implies that the initial tensile crack is closed. With the initial crack in the 'tension' reinforcement region closed, the analysis follows the approach outlined in Figure 1 with the compression and tension regions reversed as the flexural crack is now located on the opposite side of the member. When the 'tension' reinforcement crack closes, the reinforcement is no longer considered to slide relative to the concrete that is it no longer is assumed to have partial interaction behaviour. Instead the reinforcement is assumed to have full interaction behaviour and to have a residual strain of that in the reinforcement when the crack closed.

Figure 25 shows a comparison with an experimental result of Ma et al. (1976) for a cantilever beam loaded under a single large cycle where the behaviour of the hinge is dominated by the behaviour of the reinforcement, thereby allowing for the validation of the cyclic partial interaction model. It can be seen that the results from theoretical procedure outlined are generally in good agreement with the experimental result, and certainly follow the same trend. This would suggest that in cases where the cyclic behaviour of the concrete is not critical, a major component of the cyclic behaviour of reinforced concrete hinges in beams

can be attributed to the cyclic behaviour of the reinforcement and its bond. As a further comparison the test result was also simulated using the well known unloading and reloading rules outlined by Clough (1966) where the initial loading curve has been taken as a bi-linear approximation of the initial loading curve generated using the moment-rotation approach. It can be seen that while the simplified approach certainly follows the same trend as the experimental result it fails to capture the significant reduction in moment capacity brought about by the degradation of the bond and the Baushinger effect.

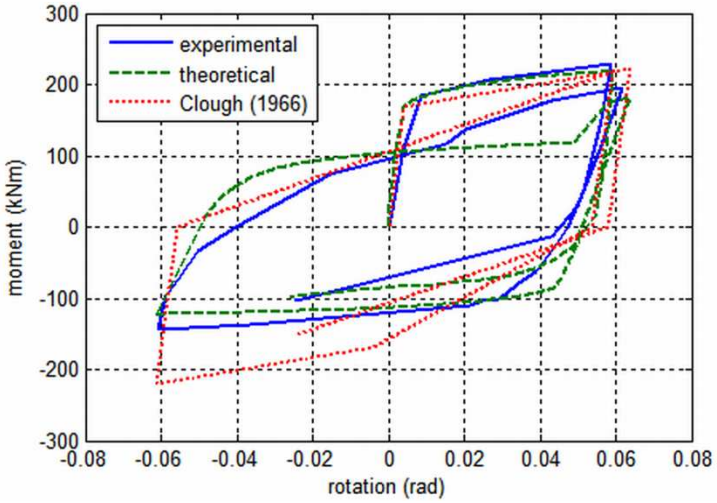

Figure 25: Comparison of theoretical and experimental

CONCLUSION

A generic moment rotation model has been developed for cyclic loads on RC beams. The model allows for the discrete rotation at an individual crack and can, therefore, allow directly for the cyclic bond properties and for the cyclic reinforcement material properties. The model is generic as it can cope with any type of bond and reinforcement properties. The model has been shown to be in good agreement with cyclic test results where the hinge behaviour is dominated by the reinforcement behaviour. The development of a cyclic partial interaction mechanics based model should be useful in the understanding of reinforced concrete seismic behaviour. The model has shown that strain hardening plays an important role in defining the partial interaction behaviour. Furthermore, that a linear elastic reinforcement material with a high strength and strain capacity, through friction at the bond interface, is capable of dissipating a similar amount of energy as a strain hardening reinforcement material.

REFERENCES

[1] Bertero VV, Bresler B. Seismic Behavior of Reinforced Concrete Framed Structures. Proceedings of the Fourth World Conference on Earthquake Engineering, 1969; Chile.

[2] Agrawal GL, Tulin LG, Gersite KH. Response of Doubly Reinforced Concrete Beams to Cyclic Loading. *ACI Journal Proceedings* 1965; **62** (7): 823-836.

[3] Brown RH, Jirsa JO. Reinforced Concrete Beams Under Load Reversals. *ACI Journal Proceedings* 1971; **68** (5): 380-390.

[4] Park R, Kent DC, Sampson RA. Reinforced Concrete Members with Cyclic Loading. *ASCE Journal of the Structural Division* 1972; **98** (ST7): 1341-1360.

[5] Ma SM, Bertero VV, Popov EP. Experimental and analytical studies on the hysteretic behavior of reinforced concrete rectangular and T-beams. *Earthquake Engineering Research Centre* 1976; UCB/EERC76/2.

[6] Oehlers DJ. Ductility of FRP plated flexural members. *Cement and Concrete Composites* 2006; **28** (10): 898-905.

[7] Oehlers DJ, Mohamed Ali MS, Griffith MC, Haskett M, Lucas W. A generic unified reinforced concrete model. Accepted *Proceedings ICE, Structures and Buildings* 2011.

[8] Panagiotakos TB, Fardis MN. Deformation of Reinforced Concrete Members at Yielding and Ultimate. *ACI Structural Journal* 2001; **98** (2): 135-148.

[9] Viwathanatepa S, Popov EP, Bertero VV.Effects of generalized loadings on bond of reinforcing bars embedded in confined concrete. *Earthquake Engineering Research Centre* 1979; UCB/EERC-79/22.

[10] Ciampi V, Eligehausen R, Bertero VV, Popov EP. Analytical model for concrete anchorages of reinforcing bars under generalized excitations. Earthquake Engineering Research Centre 1982; UCB/EERC82/23.

[11] Eligehausen R, Popov EP, Bertero VV. Local bond stress-slip relationship of deformed bars under generalized excitations. *Earthquake Engineering Research Centre* 1982; UCB/EERC83/23.

[12] Monti G, Filippou FC. Finite Element for Anchored Bars Under Cyclic Load Reversals. *ASCE Journal of the Structural Division* 1997; **123** (9): 614-623.

[13] Filippou FC, Popov EP, Bertero VV. Effects of bond deterioration on hysteretic behavior of reinforced concrete joints. *Earthquake Engineering Research Centre* 1983; UCB/EERC-83/19.

[14] Spacone E, Filippou FC, Taucer FF. Fibre Beam-Column Model for Non-Linear Analysis of R/C Frames: Part I. Formulation. *Earthquake Engineering & Structural Dynamics* 1996; **25** (7): 711-725.

[15] Monti, G. and E. Spacone. Reinforced Concrete Fiber Beam Element with Bond-Slip. *Journal of Structural Engineering* 2000; **126** (6): 654-661.

[16] D'Ambrisi A, Filippou FC. Modeling of Cyclic Shear Behavior in RC Members. *Journal of Structural Engineering* 1999; **125** (10): 1143-1150.

[17] Gupta AK, Maestrini SR. "Tension stiffening model for reinforced concrete bars." *Journal of Structural Engineering* 1990; **116** (3): 769-790.

[18] Wu Z, Yoshikawa H, Tanabe T. Tension stiffness model for cracked reinforced concrete. *Journal of Structural Engineering* 1991; **117** (3), 715-732

[19] Choi CK, Cheung SH. Tension stiffening model for planar reinforced concrete members. *Computers & Structures* 1996; **59** (1), 179-190.

[20] Marti P, Alvarez M, Kaufmann W, Sigrist V. Tension chord model for structural concrete. *Structural Engineering International* 1998; **8** (4): 287-298.

[21] Yuan H, Teng JG, Seracino R, Wu ZS, Yao J. Full-range behavior of FRP-to-concrete bonded joints, *Engineering Structures* 2004; **26** (5): 543-691.

[22] Oehlers DJ, Liu IST, Seracino, R. The gradual formation of hinges throughout reinforced concrete beams. *Mechanics Based Design of Structures and Machines* 2005; **33** (3-4): 375-400.

[23] Warner RF, Foster SJ, Kilpatrick AE. Reinforced Concrete Basics: Analysis and Design of Reinforced Concrete Structures. Pearson Education, Australia 2007.

[24] Haskett M, Oehlers DJ, Mohamed Ali MS. Local and global bond characteristics of steel reinforcing bars. *Engineering Structures* 2008; **30** (2): 376-383.

[25] Mohamed Ali, MS, Oehlers DJ, Griffith MC, Seracino R. Interfacial stress transfer of near surface mounted FRP-to-concrete joints. *Engineering Structures* 2008; **30** (7): 1861-1868.

[26] Mohamed Ali MS, Oehlers DJ, Griffith MC. Shear transfer across cracks in FRP strengthened RC structures. *ASCE Journal of Composites in Construction* 2008; **12** (4): 416-424.

[27] Mohamed Ali MS, Oehlers DJ, Haskett M, and Griffith MC. The discrete rotation in reinforced concrete beams. Submitted to *ASCE Journal of Structural Engineering*

[28] Haskett M, Oehlers DJ, Mohamed Ali MS Wu C. Yield penetration hinge rotation in reinforced concrete beams. *ASCE Structural Journal* 2009; **135** (2): 130-138.

[29] Haskett M. Oehlers DJ, Mohamed Ali MS Wu C. Rigid body moment-rotation mechanism for reinforced concrete beam hinges. *Engineering Structures* 2009; **31** (5): 1032-1041.

[30] Oehlers DJ, Mohamed Ali MS, Griffith MC. Concrete component of the rotational ductility of reinforced concrete flexural members. *Advances in Structural Engineering* 2008 **11** (3): 293-303.

[31] Mohamed Ali M S, Oehlers DJ Griffith MC. The Residual Strength of Confined Concrete. *Advances in Structural Engineering* 2010 **13** (4): 603-618.

[32] Mattock, A.H. and Hawkins, N.M., Shear transfer in reinforced concrete recent research, Precast Concrete Institute Journal 1972; (March–April) pp. 55–75.

[33] Hognestad E, Hanson N W, McHenry D. Concrete stress distribution in ultimate strength design. *Journal of ACI* 1955; **27** (4): 455-479.

[34] Muhamad R, Mohamed Ali MS, Oehlers DJ, Sheikh AH. Load-slip relationship of tension reinforcement in reinforced concrete members. *Engineering Structures* 2011; **33** (4): 1098-1106.

[35] Oehlers D J, Mohamed Ali MS, Haskett M, Lucas W, Muhamad R Visintin P. FRP reinforced concrete beams - a unified approach based on IC theory. ASCE Composites for Construction, May/June, 2011, Vol. 15, No. 3, pp293-303.

[36] CEB (1996). Bond between concrete and steel. *RC Elements Under Cyclic Loading State of the Art Report*, 1996 Thomas Telford.

[37] FIB. *Bond of reinforcement in concrete : state-of-art report / prepared by Task Group Bond Models (former CEB Task Group 2.5)Bond of reinforcement in concrete : state-of-art report / prepared by Task Group Bond Models (former CEB Task Group 2.5).* International Federation for Structural Concrete 2000; Lausanne, Switzerland.

[38] Kent DC, Park R. Cyclic load behaviour of reinforcing steel. *Strain* 1973; **9** (3): 98-103.

[39] Park R, Paulay T. strain relationships for concrete and steel. *Reinforced Concrete Structures*. John Wiley & Sons 1975; New York.

[40] CEB. Reinforcing Steel. *RC Elements Under Cyclic Loading State of the Art Report*, 1996; Thomas Telford.

[41] Hoehler MS, Stanton JF. Simple phenomenological model for reinforcing steel under arbitrary load. *Journal of Structural Engineering* 2006; **132** (7): 1061-1069.

[42] Clough RW, Effect of Stiffness Degredation n Earthquake Ductility Requirements. *Structural Engineering and Structural Mechanics Department of Civil Engineering Report No. 66-16*; 1966

Chapter 3 – Member Analysis

Introduction

In this chapter it is shown how the equivalent flexural rigidity which was derived using the segmental PI M/θ approach in Chapter 2 can be used to predict member deflection. This is first shown for both laterally loaded and eccentrically loaded columns loaded to failure in the paper "A moment-rotation approach for analysing the behaviour of RC columns"

The second publication "Simulating the partial-interaction time dependent behaviour of reinforced concrete beams" focuses on the serviceability deflection of beams, specifically the deflections which occur due to concrete creep and shrinkage with time. Significantly, in this paper a new numerical partial-interaction technique, which allows for the prediction of tension stiffening behaviour including time effects is presented, as well as a new mechanics based approach to predicting the time dependent deflection of RC beams.

In the third publication "Partial-interaction short term serviceability deflection of FRP RC beams" closed form solutions are developed for the segmental PI M/θ. These equations can be used to predict the cracked flexural rigidity and deflection of RC beams under serviceability loading, and it is shown that being mechanics based they are equally applicable to members reinforced with ductile steel or brittle FRP bars.

Finally, in "The fundamental mechanisms that govern the flexural ductility of all RC members" the work on the single crack and segmental M/θ approaches is brought together and it is shown how when used in conjunction they provide a mechanics based solution of the analysis of RC members under all load cases.

List of manuscripts

Visintin, P., Oehlers, D.J., Haskett, M., Wu, C and Chen JF., (2012) "A moment-rotation approach for analysing the behaviour of RC columns". Submitted to *Computers and Structures*.

Visintin, P, Oehlers, D.J., Haskett M., (2013) "Partial-interaction time dependent behaviour of reinforced concrete beams". Submitted to *Magazine of Concrete Research*.

Visintin, P., Oehlers, D.J. Muhamad, R. and Wu, C. (2012) "Partial-interaction short term serviceability deflection of FRP RC beams". Submitted to *Engineering Structures.*

Oehlers, D.J., Visintin, P., Haskett, M. and Sebastian, W., (2013) "The fundamental mechanisms that govern the flexural ductility of all RC members". Invited paper for *Construction and Building Materials.*

Statement of Authorship

A moment-rotation approach for analysing the behaviour of RC columns

Computers and Structures: submitted paper

Visintin, P. (candidate)

Prepared manuscript, performed all analyses, and developed model and theory.

I hereby certify that the statement of contribution is accurate

Signed……..Date……

Oehlers, D.J.

Supervised research, provided critical manuscript evaluation and acted as corresponding author.

I hereby certify that the statement of contribution is accurate and I give permission for the inclusion of the paper in the thesis

Signed…….Date……

Haskett, M.

Assisted in manuscript evaluation.

I hereby certify that the statement of contribution is accurate and I give permission for the inclusion of the paper in the thesis

Signed …….Date……

Wu, C

Assisted in manuscript evaluation.

I hereby certify that the statement of contribution is accurate and I give permission for the inclusion of the paper in the thesis

Signed …….Date……

Chen, J.F.

Assisted in manuscript evaluation.

I hereby certify that the statement of contribution is accurate and I give permission for the inclusion of the paper in the thesis

A moment-rotation approach for analysing the behaviour of RC columns

Visintin, P., Oehlers, D.J., Haskett, M., Wu, C. and Chen, J.F.

ABSTRACT

The behaviour of reinforced concrete columns is complex as any errors in simulating the column deformations are compounded by the magnified moments. Hence it is particularly important to simulate the stiffness and ductility of the column accurately which is the subject of this paper. A moment-rotation approach which simulates the formation of cracks, crack widening and crack rotation through slip between the reinforcement and the concrete using partial-interaction mechanics is described. The model also simulates the formation of wedges associated with concrete softening using shear-friction mechanics. The moment-rotation model shows good correlation with tests results at all stages of loading.

Keywords: reinforced concrete columns; serviceability; ultimate; collapse.

INTRODUCTION

The Euler-Bernoulli principal of plane sections remaining plane and in particular its corollary of a linear strain profile and the associated moment-curvature (M/χ) analysis and consequential flexural rigidity (EI) are commonly used to simulate the behaviour of reinforced concrete columns [1-3]. A difficulty in using this approach is to decide on an appropriate effective flexural rigidity (EI_{eff}) to allow for the tension stiffening effects that occur in the vicinity of a flexural crack, and which are generally determined empirically [4,5]. A further difficulty is deciding on a hinge length over which the curvature at the ultimate limit can be integrated to quantify the rotation, this too is generally determined empirically [3, 6-9]

In this paper, a moment-rotation (M/θ) approach is developed that is based on the Euler-Bernoulli principal of plane sections remaining plane [10]. This M/θ approach uses the established mechanics of partial-interaction theory [11-24], which considers the slip between the reinforcement and the concrete, to allow for the discrete rotation at cracks first proposed by Bachman [25]. It also uses the established mechanics of shear-friction theory [26-30] to allow for the softening of concrete that is associated with the formation of wedges. Hence the mechanics of the M/θ approach [31] can quantify the rotation at all stages of loading that is at serviceability, ultimate and failure without the need for empirical components of the model such as effective flexural rigidities (EI_{eff}) and hinge lengths. Consequently, the moment-rotations from the M/θ approach can be converted to moment-curvatures and their equivalent flexural rigidities (EI_{equ}) at all stages of loading so that the M/θ approach can be considered as extending and refining the M/χ approach.

Prior to cracking or softening, the M/θ approach and the M/χ approach give exactly the same results and consequently exactly the same flexural rigidities (EI). After cracking, the equivalent flexural rigidities (EI_{equ}) derived directly from the M/θ approach replace the need for empirically derived effective flexural rigidities (EI_{eff}) as required in the M/χ approach. Furthermore at the commencement of softening, the M/θ approach directly provides the rotation without the need for empirical hinge lengths associated with the M/χ approach. Hence the M/θ approach can be used to replace the empirical components of the M/χ approach and lead to its wider application.

The moment-rotation of a segment of a reinforced concrete column is first developed and the reader is referred to several papers on the development of the M/θ approach for further discussion of the subject [22, 31, 32]. Columns are then divided into segments and the behaviour of a column is then derived from that of the individual segments. The moment-rotation analysis is then compared with test results where it is shown that all stages of loading can be simulated, and the variation of the flexural rigidity along the length of the column determined.

MOMENT-ROTATION OF A SEGMENT

Consider the column in Figure 1, which has an applied axial load P and moment M such that both concrete cracking and concrete softening is occurring. To determine member deformation, the column is divided into small segments of length L_{def} over which the moment is assumed to be constant. The moment-rotation relationship for each segment can then be determined for each stage of loading as follows.

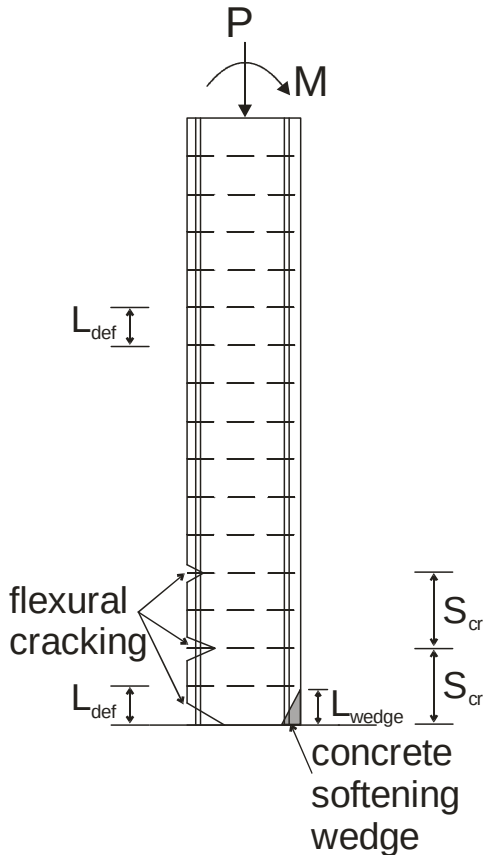

Figure 1: Column idealisation

Prior to softening and cracking

Let us firstly consider a loading of the column in Figure 1 where the combination of the applied axial load P_{seg} and moment M_{seg} on the segment is not yet significant enough to cause either concrete cracking or concrete softening. A segment taken from the column is shown in Figure 2(a) where the application of an axial load and moment causes a shortening and relative rotation between the segment ends θ from A-A to B-B.

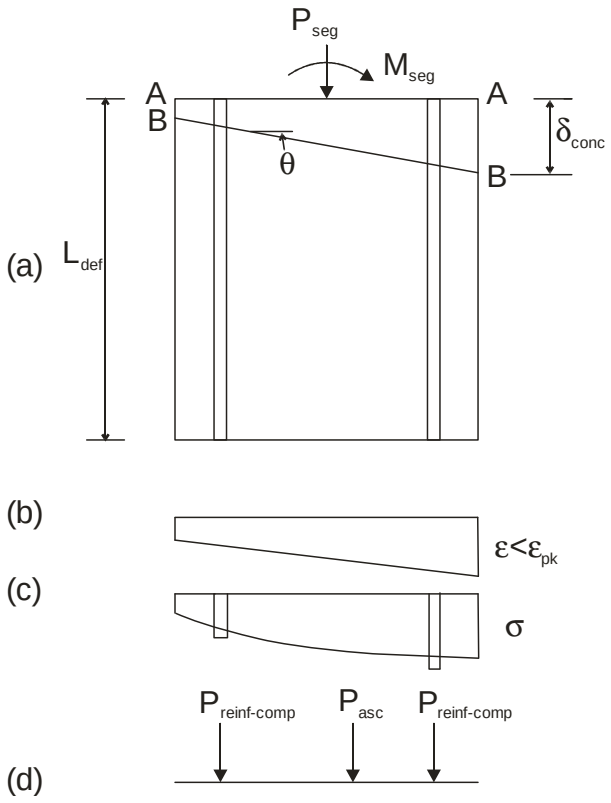

Figure 2: Uncracked segment behaviour

The deformation profile B-B in Figure 2(a) can be converted to a strain as in Figure 2(b) by dividing the deformation from A-A to B-B by the length L_{def}. These are real strains, that is, these are the strains the material is accommodating and as such would be measured by strain gauges. Having obtained the distribution of strain in Figure 2(b), and because the strains are real strains, the distribution of stress can be determined using material stress-strain relationships, yielding the stress profile in Figure 2(c) and, hence, the internal forces shown in Figure 2(d). Knowing the internal forces the maximum displacement in the concrete δ_{conc} can be varied, thereby adjusting the neutral axis depth until internal equilibrium is achieved for the given rotation θ. This analysis yields a single point on the moment-rotation relationship such as point A in Figure 3(a) and can be repeated for increasing rotations until: either the section cracks when the maximum tensile strain exceeds the concrete cracking strain ε_t and the crack tip reaches a layer of reinforcement; or until the maximum compressive strain exceeds the peak strain of the concrete ε_{pk} that is the strain prior to softening.

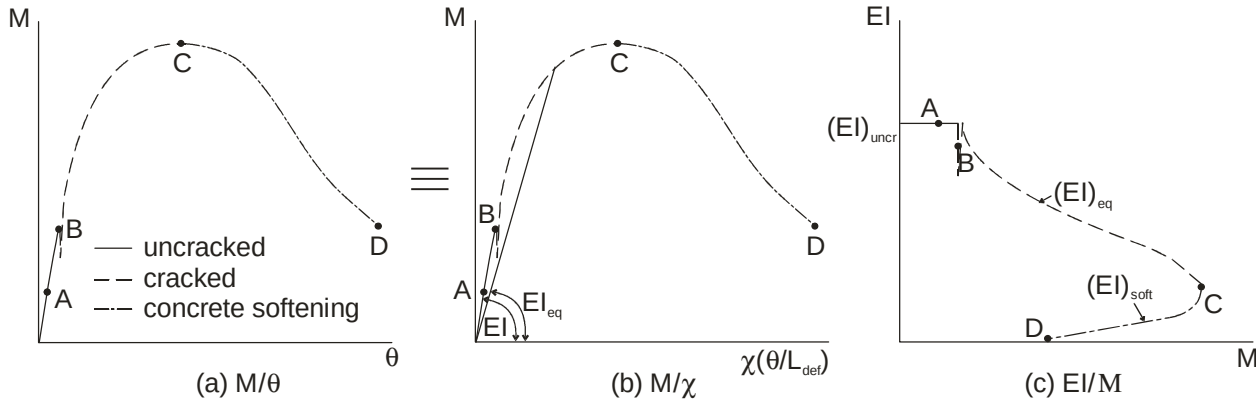

Figure 3: Moment-rotation of segment

It is also important to note that, as shown in Figure 3(b), the moment-rotation relationship can be converted into a moment-curvature relationship by dividing the rotation by the deformation length L_{def}. At the uncracked stage, the relationship obtained from a moment-rotation analysis and that obtained form a traditional moment-curvature analysis are identical and, hence, so too are the uncracked flexural rigidities $(EI)_{uncr}$ shown in Figure 3(c). This is important as in the uncracked case the moment-curvature analysis technique is a mechanically correct approach, that is, no empirically derived factors are required in order to determine member deflection. This also means that at this stage the deformation length L_{def} can be any length.

It can be seen that as at this stage the M/θ analysis yields exactly the same results as the traditional M/χ analysis the length L_{def} used in the analysis depicted in Figure 3 is irrelevant as any length gives the same M/χ. It is also worth noting that prior to cracking and whilst the material stays elastic the flexural rigidity is that of the uncracked section EI_{uncr} as obtained from elementary transformed section and shown in Figure 3(c). Furthermore, this analysis still applies after the start of cracking but until the crack tip reaches a layer of reinforcement shown as point B in Figure 3. After the crack tip has reached a layer of reinforcement, partial-interaction theory has to be used to determine the force in the tension reinforcement as explained in the following section.

Accommodation of cracking

Let us now consider what happens when cracking occurs, that is when the tensile strain exceeds ε_t and the crack intercepts the reinforcement as in Figure 4(a). The force in the reinforcing bar now depends on the slip of the reinforcing bar at the crack face Δ_{reinf} which depends on the bond-slip (τ/δ) property between the reinforcing bar and the concrete encasing it. The relationship between the reinforcement force at the crack face $P_{reinf\text{-}tens}$ and the slip Δ_{reinf} can be determined through the partial-interaction analysis of a reinforcing bar of area A_r encased in a prism of area A_c and depth d_{prism} in Figure 4(a) as illustrated in Figure 5 [10].

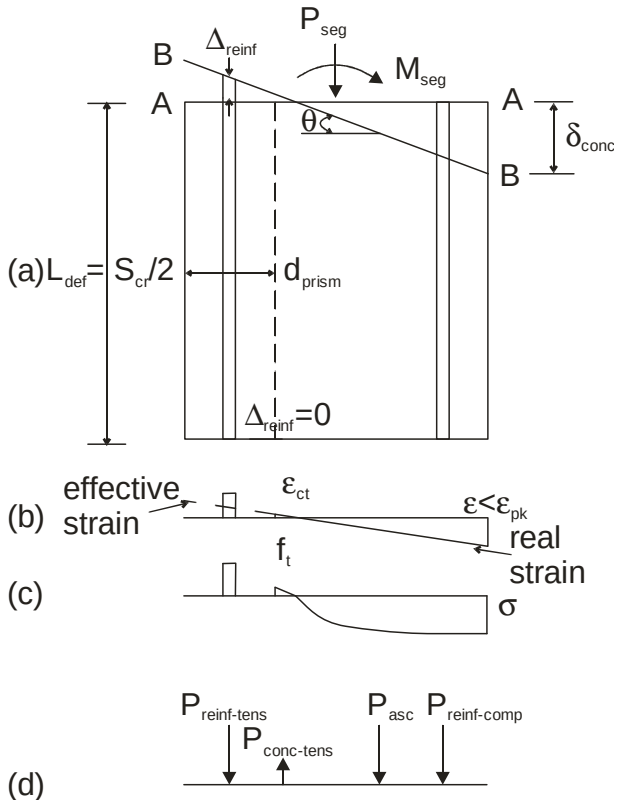

Figure 4: Cracked element idealisation

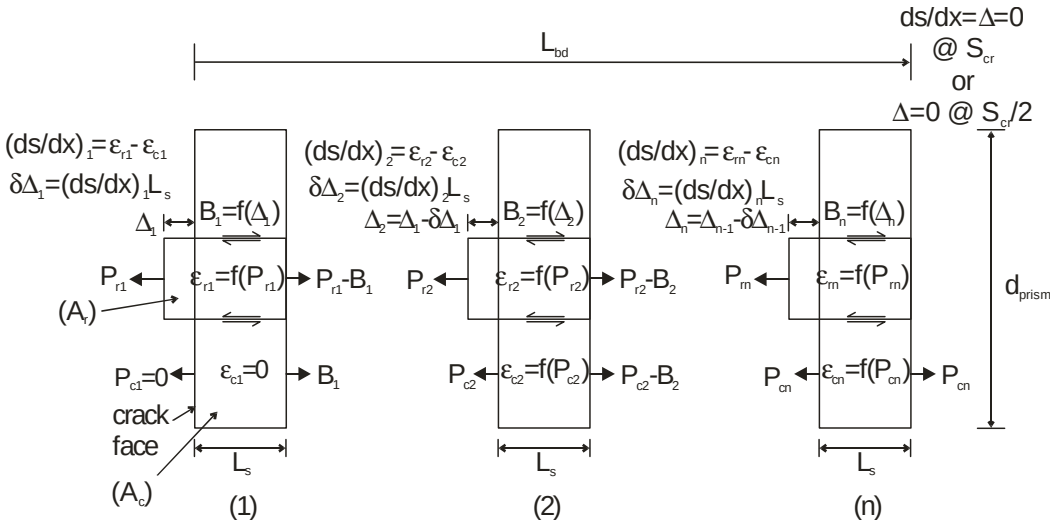

Figure 5: Partial-interaction numerical procedure

The prism of length L_{bd} in Figure 5 is sub-divided into elements of length $L_{s,}$ which are much smaller than L_{bd}, and a displacement of the bar Δ_1 representing a slip of the bar at the crack face is set. It is now a matter of determining the force P_{r1} that induces the imposed slip at the

crack face. From the known bond slip (τ-δ) properties [32] and for the given displacement Δ_1, the bond force in the first element B_1 is determined. Making an initial guess for P_{r1}, the stress, and therefore the accompanying strain in the bar ε_{r1} is known. At the crack face the strain in the concrete is zero, and since the element length has been chosen to be very small the strain in the concrete for the first element can be taken to be zero. The slip-strain (ds/dx) is the algebraic difference in strain between the reinforcement and the concrete ε_{r1}-ε_{c1}, and the change in slip over element 1, $\delta\Delta_1$, is the integration of the slip-strain over L_s. Hence, both the slip and slip-strain in element 1 are known. The analysis is then repeated for element 2 in which the force in the reinforcing bar P_{r2} by equilibrium is P_{r1}-B_1 and the force in the prism P_{c2} is B_1. The slip of the reinforcement Δ_2 is then Δ_1-$\delta\Delta_1$, from which the bond force B_2 can be derived. The analysis can then be repeated over subsequent elements to give the variation in slip Δ and slip strain ds/dx, and the initial guess for P_{r1} adjusted until a known boundary condition is achieved.

The analysis depicted in Figure 5 can be used to determine the crack spacing of primary cracks as this occurs where the full-interaction boundary condition is achieved that is where both the slip-strain (ds/dx) and the slip Δ tend to zero at the same position. This position L_{bd} in Figure 5 is, therefore, the crack spacing S_{cr} of the primary cracks in Figure 1. Hence it can be seen that L_{def} is half S_{cr} as shown in Figure 4 that is the length of the segment in this part of the analysis has to be half the crack spacing. It is also worth noting that as the crack spacing S_{cr} may be one or two orders of magnitude smaller than the length of the column, the moment may therefore be considered to be constant over this length, thus by symmetry the reinforcement slip mid-way between cracks is zero. Hence the slip Δ at the base of the prism in Figure 4 at $L_{def} = S_{cr}/2$ from the crack face is zero as shown. This new boundary condition can be used in the analysis in Figure 5 to determine the P/Δ relationship that is required for the analysis in Figure 4. This analysis can also be used to determine the reinforcement force to cause cracking at L_{def} that is to cause secondary cracks and also the P/Δ should secondary cracks occur.

The analysis procedure for the cracked segment in Figure 4(a) can now proceed using the same approach as for the uncracked segment. The combination of the applied axial load and moment cause a change in deformation from A-A to B-B with a rotation of θ, and this deformation is used to determine the strain profile given in Figure 4(b), by dividing by the deformation length $L_{def.}$ In the compressive and uncracked tension regions, this strain is a real strain and, hence, material stress strain relationships can be used to determine the stress and forces developed as in Figure 4(c) and Figure 4(d). For the cracked tension region, the slip of the reinforcement from the crack face Δ_{reinf} can be determined from simple geometry, and for the given slip, the load developed can be found using the tension stiffening partial-interaction model in Figure 5. Having determined the internal forces, the maximum deformation in the concrete δ_{conc} can again be adjusted until equilibrium is achieved. The rotation in Figure 4

can be gradually increased to derive the moment-rotation relationship from B to C in Figure 3(a) at which point softening commences which is dealt with in the following section.

Using the partial-interaction theory, the M/θ approach in Figure 4 represents a structural mechanics based solution to concrete cracking, as it simulates the crack spacing and crack widening as the reinforcement slips relative to the concrete. Furthermore if the strain profile in Figure 4(b) is examined, it can be seen that the M/θ approach simulates what is seen in practice, that is, the real strain profile is linear only in the uncracked tension and compression region. In the cracked tension region, the real strain is zero at the crack face, and increases until the midpoint between the cracks following the partial-interaction theory. This is in contrast to a full-interaction M/χ approach which smears the cracking deformation to produce a single linear effective strain profile shown as the dashed line in Figure 4(b).

Once again, the moment-rotation relationship from B to C in Figure 3(a) can be converted into an equivalent moment-curvature relationship as in Figure 3(b) by dividing by $L_{def.}$ In this case, the relationship derived from a M/θ analysis and that derived from a traditional M/χ approach will not be the same for the reasons described above. The M/θ analysis can also be used to define an equivalent flexural rigidity (EI_{equ}) in Figure 3(c) for use in analysis, this equivalent flexural rigidity (EI_{equ}) is different from the effective flexural rigidity (EI_{eff}) found using typical approaches such as Branson's equation as it uses structural mechanics to account for concrete cracking rather than being empirically based. It may also be worth noting that even though the M/θ analysis is based on a segment of length $S_{cr}/2$ in Figure 4 and on a segment subjected to a constant moment, it can be conveniently converted to a moment-curvature with continuously varying flexural rigidity from B to C in Figure 3 which may be much more convenient for analysis in a column with a continuously varying moment.

Accommodation of softening

An idealised stress strain relationship for concrete is shown in Figure 6(a). The deformation in the ascending branch O-C, that is, up to the strain ε_{pk} at the peak stress f_c can be assumed to be accommodated directly by the material deformation. In the descending branch C-D, the concrete material is still governed by O-C so that any additional deformation can only be accommodated by sliding of the wedges associated with softening [10]. Hence, the strain along C-D such as $(\varepsilon_2)_{eff}$ is an effective strain which allows for the reduction in strain due to sliding of the wedges. To impose a rotation beyond point C in Figure 3 requires a deformation in the segment in Figure 4(a) in the concrete in the compression zone that exceeds $\varepsilon_{pk}L_{def}$, that is a deformation that exceeds that which can be accommodated by the peak material strain capacity ε_{pk}. This can only be accommodated by the formation of a wedge as shown in Figure 7(a) which is associated with concrete softening. This wedge has a depth of d_{wdg} and length L_{wdg} and forms at an angle of α which is dependent upon the cohesive and frictional properties of the concrete [33].

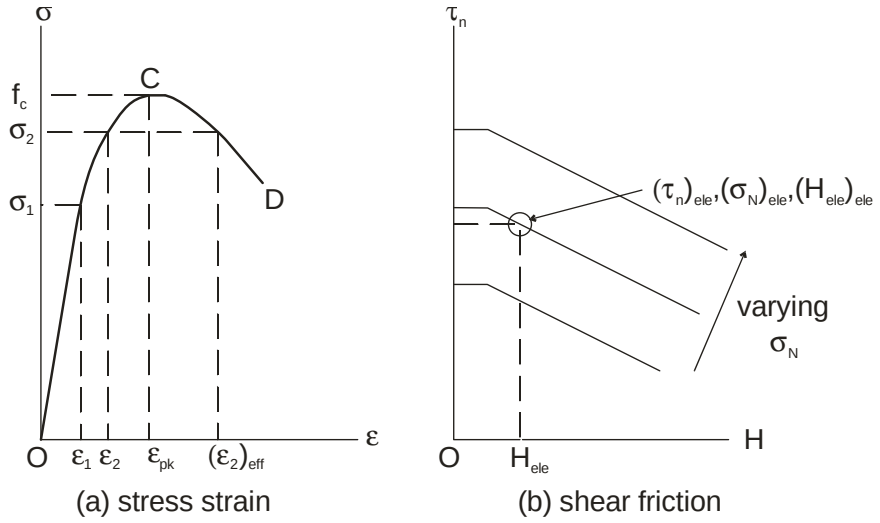

Figure 6: Concrete stress-strain and shear friction material properties

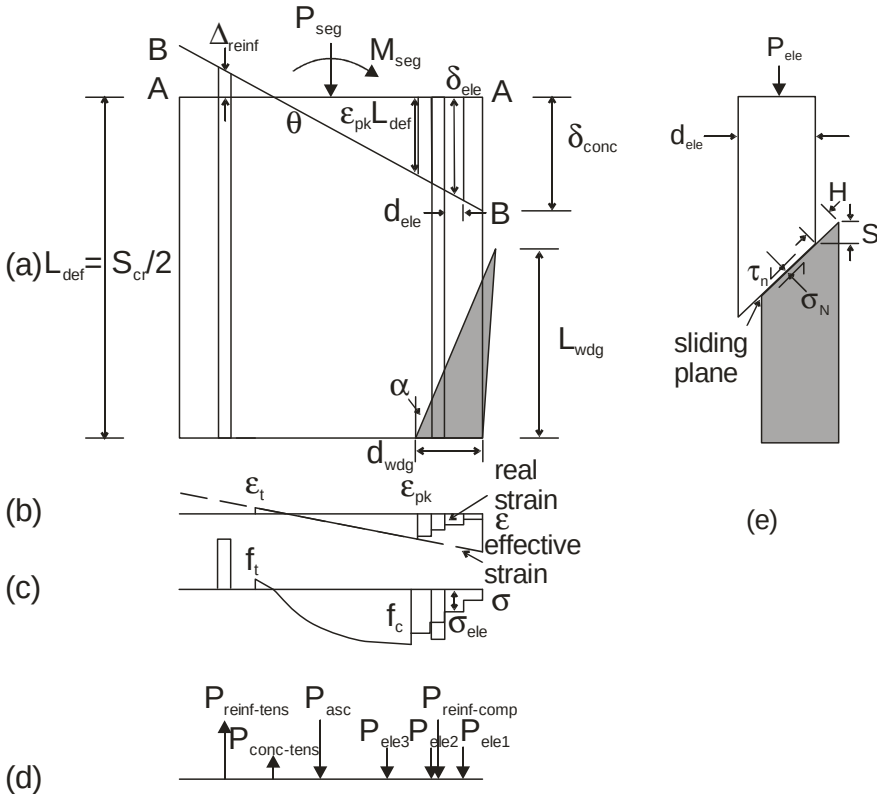

Figure 7: Softening and cracked element idealisation

The concrete contained within the softening zone in Figure 7(a) is traditionally simulated within a M/χ analysis indirectly through the use of both an empirically derived softening branch of the compressive stress-strain relationship and an empirically derived hinge length. However using the moment-rotation relationship, it can be directly simulated using the well established shear friction theory [26-30].

To understand the shear-friction mechanism, let us consider an element from Figure 7(a) within the depth of the wedge d_{wdg} which itself has a depth of $d_{ele.}$ As has been shown in the previous two load cases in Figures 2 and 4, prior to softening the deformation taking place over this element, δ_{ele} in Figure 7(a), can be divided by the deformation length L_{def} to give the corresponding real strain ε_1 in Figure 6(a). Since this deformation can be accommodated for entirely by the material, a stress-strain relationship such as in Figure 6(a) can be used to determine the stress σ_1 developed. This behaviour continues until the peak strain ε_{pk} corresponding to the peak stress f_c in Figure 6(a) is attained. At this point no further increase in material deformation is possible and a softening wedge must form to accommodate the additional deformation required. The gradual formation and failure of this softening wedge, which is seen in practice, allows for non-material deformation to take place.

This non-material deformation, shown for the element in question in Figure 7(e), takes place in the form of sliding along the shear friction plane a distance of H such that an additional vertical deformation S occurs. This non-material deformation allows the strain in the material to drop below ε_{pk} such that the stress developed decreases to σ_2 in Figure 6(a). Hence the total deformation δ_{ele} consists of a material deformation $\varepsilon_2 L_{def}$ plus that due to wedge sliding S giving a total effective strain in the concrete of $\varepsilon_{2eff} = \varepsilon_2 + S/L_{def}$. The magnitude of the stress developed for a given slip can be determined using well defined the shear-friction theory illustrated in Figure 6(b) [10,26-30]. Figure 6(b) quantifies the shear-friction properties required for the analysis depicted in Figure 7(e), which provides a relationship between the displacement H along the sliding plane and the shear stress τ_n and normal stress σ_N transferable across the cracked plane. It may be worth noting that the sliding plane in Figure 7(e) also opens up through aggregate interlock but the effect of this movement on the overall longitudinal effective strain is at least one order of magnitude less than that due to the slip S and consequently can be ignored [29,30].

An example of the analysis using this shear friction theory is as follows. Let us guess that a stress of $(\sigma_{ele})_{guess}$ occurs in the element of width d_{ele} of Figure 7(a), now shown in Figure 7(e), which is required to induce the displacement δ_{ele}. From the material stress strain relationship in Figure 6(a), the strain to cause this stress is known to be $(\varepsilon_{ele})_{guess}$. Hence, the material deformation is known to be $(\varepsilon_e)_{guess} L_{def}$, and, consequently, the deformation required by sliding $S = \delta_{ele} - (\varepsilon_{ele})_{guess} L_{def}$. Knowing the angle of formation of the wedge α [33] in Figures 7(a) and 7(e) and S, the sliding displacement H can be determined from simple geometry. It is then simply a matter of finding a combination of τ_n and σ_N which gives the vertical component P_{ele} in Figure 7(e) and iterating until the stress σ_{ele} is equal to $(\sigma_{ele})_{guess}$. This solution has also been defined in a closed form by Haskett et al. [30].

Having established how shear friction theory can be used to describe the softening behaviour of a single element of the softening wedge, we can again consider the whole segment. The

applied combination of axial load and moment again cause a change in displacement from A-A to B-B in Figure 7(a) causing both concrete cracking and softening. In the non-softening compression region and the uncracked tension region, the strain developed can again simply be determined by dividing the deformation by L_{def} to give a real strain as in Figure 7(b) which are used in a material stress strain relationship to give the stress profile in Figure 7(c). Similarly the force developed in the tensile reinforcement can be determined as previously shown through the application of partial interaction theory by determining the slip of the reinforcement Δ_{reinf} based on the deformation profile B-B. Finally in the softening region, the wedge is split into a number of slices and for each slice the slip of the wedge H determined so that the shear friction theory described can be applied. Again for the analysis of the segment, it is then simply a matter of adjusting the maximum displacement in the concrete δ_{conc} until equilibrium of the forces shown in Figure 7(d) is achieved.

Depending on the magnitude of the axial load, softening can occur prior to or post concrete cracking, and this in turn affects the deformation length L_{def}. For the case when softening occurs after cracking, the wedge must be entirely contained within the deformation length. Hence if L_{wdg} it is greater than L_{def} in Figure 7(b), the deformation length L_{def} must be incrementally increased [10], that is L_{wdg} must be less than n times L_{def}. When softening occurs prior to cracking, L_{def} must be chosen so that it is greater than the L_{wdg}. In this case, it may be easier to choose a multiple of the crack spacing so that the length does not need to change once cracking does occur after softening.

Similar to the cracked case in Figure 4, it can be seen that the moment rotation approach in Figure 7 simulates what is actually seen in practice, that is, the formation and failure of the softening wedge. Considering the strain profile in Figure 7(b), the strain in the concrete within the softening region is given by the real strain which can be seen to be reducing, until it eventually drops to zero as the slip increases, this is what is measured in practice. In a traditional moment-curvature analysis, the strain considered is the effective strain given by the dashed line which is a combination of the material and non-material deformations and, hence, an empirically derived hinge length is required to determine member deflection. Similar to the previous load cases, the moment-rotation result can be converted to an equivalent moment-curvature relationship, and in this case provides an equivalent flexural rigidity as in Figure 3(c) from C to D. However as we are now dealing with softening, that is C to D in Figure 6(a) and C to D in Figures 3(a) and (b), the region over which this occurs that is L_{def} in the column must be specifically defined. That is, within this softening region C-D in Figure 3(c) applies, whilst outside this region, where the moments may be the same, A-C applies. The length L_{def} once softening has occurred is in effect a hinge length, but it only occurs in regions where softening is taking place, and in this case is derived from the shear-friction theory as opposed to the empirical hinge lengths required in the M/χ approach.

With the three stages of the analysis presented, it is now possible to produce moment M flexural rigidity ($EI_{equ)}$ relationships for a segment, as shown in Figure 3(c), which accounts for concrete cracking and softening using structural mechanics and which applies to all of the segments in the column in Figure 1. This M-EI_{equ} variation can be used in a traditional manner to determine member deflection without the need of an empirically derived flexural rigidity EI_{eff} or hinge length and shows the potential of the moment-rotation approach to be used to improve traditional analysis techniques which are based on the Euler-Bernoulli assumption of plane sections remaining plane.

MOMENT ROTATION ANALYSIS OF A COLUMN

Having now described the moment-rotation procedure for a segment, it will now be shown how the approach can be applied to describe the load deflection behaviour of laterally and eccentrically loaded columns, including those with significant second order effects. The column shown in Figure 8(a) of height L, which has been divided into segments of length L_{def}, represents either a laterally loaded cantilever column with a fixed base or half of an eccentrically loaded column with hinged ends, where the maximum deflection corresponds to the deflection at mid-height.

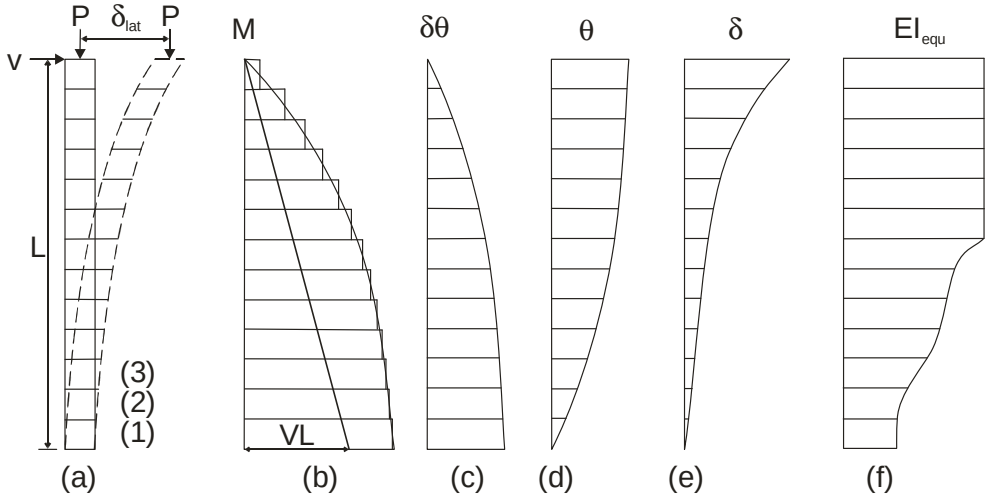

Figure 8: Numerical procedure for analysing member deflection

The first step of the analysis is to generate a M/θ relationship which can be used to determine the change in rotation of each segment as described previously. For the case of the laterally loaded column, the analysis proceeds by setting the tip deflection of the column δ_{lat} as in Figure 8(a) and guessing the lateral load V. The magnified moment M_1 in Figure 8(b) in the first element (1) at the base of Figure 8(a) is $VL+P\delta_{lat}$. Hence from the moment-rotation relationship and for this moment can be determined the change in rotation $\delta\theta_1$ for this element in Figure 8(c). With the boundary condition that at the base of the column the rotation is zero, the change in rotation $\delta\theta_1$ in Figure 8(c) for the first element is also the total

rotation θ_1 in Figure 8(d). The integration of this rotation over the element length L_{def} gives the lateral displacement δ_1. Hence in element (2), the component of the moment due to the axial load is now $P(\delta_{lat}-\delta_1)$ so that the magnified moment M_2 in Figure 8(b) can be determined, consequently from the moment-rotation analysis $\delta\theta_2$ in Figure 8(c) and so on up the column until the tip deflection is found, and if it is not equal to that which was initially set the lateral load V must be changed until it is.

The analysis for an eccentrically loaded column with a varying axial load follows a similar procedure. A mid-height deflection δ_{lat} is set and an axial load P to give this deflection is guessed. For this axial load P, a segmental moment rotation relationship is developed and as above the deflection is determined, this time with the boundary condition that at mid-height the rotation is zero and knowing that at the end of the column the deflection should be zero; if not the analysis is repeated for a new guess of P.

It is also important to note that it is possible to determine the deflection of the member using a moment-curvature analysis, where, instead of determining the change in rotation of each element the curvature is found. It is then simply a matter of integrating the curvature to get the deflection as in a traditional analysis. When using this approach it is, however, required that the element at which softening takes place be of equal length to that which was used to derive the moment rotation relationship. An alternative moment-curvature approach is to use a standard analysis package where the flexural rigidity can be varied along the length of the column as in Figure 8(f) and the same boundary conditions used to iterate towards a solution. It may also be worth noting that this approach can be incorporated into finite difference analysis where each segment is allocated a flexural rigidity as in Figure 3(c).

APPLICATION TO TEST SPECIMENS

The moment-rotation approach has been used determine the load deflection response of both laterally loaded columns, as tested by Atalay and Penzien [34], and eccentrically loaded slender columns, as tested by Kim and Yang [5].

Throughout the previous explanation only a qualitative description of the moment-rotation approach has been described. In order to develop a M/θ relationship, an example of which is shown in Figure 9(a) along with a corresponding moment-EI_{equ} relationship (M/EI_{equ}) in Figure 9(b), several material models are required. It is important to note that these are not critical to the application of the moment-rotation approach, any material model can be used and as these are refined better results can be expected.

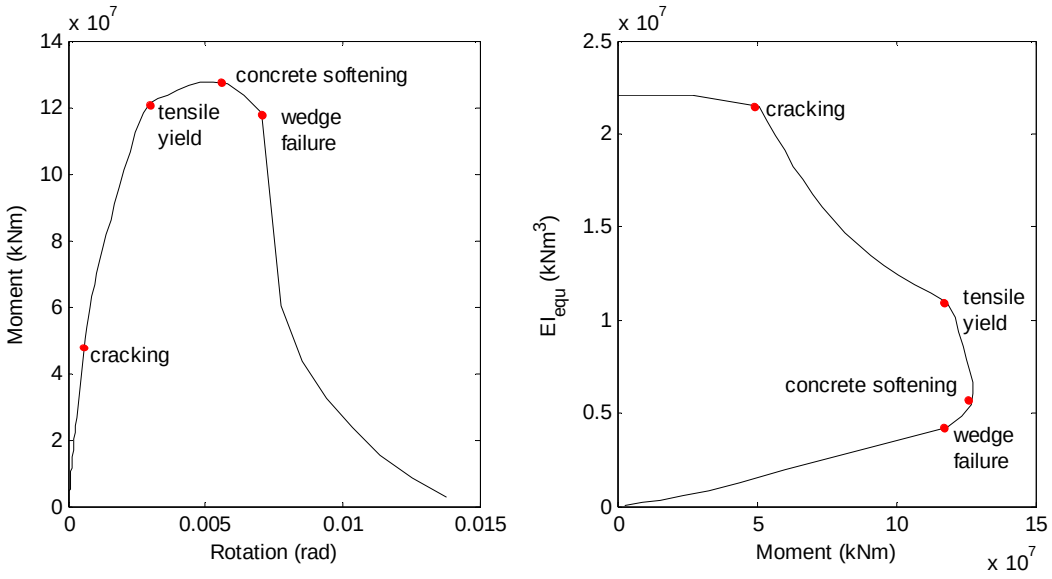

Figure 9: Typical moment-rotation response

Material properties

Prior to cracking, a linear elastic tensile stress (σ) strain (ε) relationship has been assumed for concrete in tension, and in compression that of Hognestad [35] as in Eq. 1 has been used

$$\sigma = \left[\frac{2\varepsilon}{\varepsilon_{pk}} - \left(\frac{\varepsilon}{\varepsilon_{pk}}\right)^2\right] \tag{1}$$

where the strain ε_{pk} corresponding to the onset of concrete softening at f_c in Figure 6(a) and the formation of a softening wedge has been determined using the empirical model of Tasdamir [36] as in Eq. 2, where f_c is the peak concrete strength in MPa. This has replaced that suggested by Hognestad [35] as it was derived over a wider range of concrete strengths.

$$\varepsilon_{pk} = (-0.067f_c + 29.9f_c + 1053)10^{-6} \tag{2}$$

Once the concrete has cracked, the partial interaction analysis requires the definition of a bond stress slip (τ/δ) relationship. The model used in the present analysis is that suggested by the CEB for deformed bars [32] and given by Eq. 3-6.

$$\tau = \tau_{max}\left(\frac{\delta}{\delta_1}\right)^{0.4} \quad \delta \le \delta_1 \tag{3}$$

$$\tau = \tau_{max} \quad \delta_1 < \delta \le \delta_2 \tag{4}$$

$$\tau = \tau_{max} - \left(\tau_{max} - \tau_f\right)\left(\frac{\delta - \delta_2}{\delta_3 - \delta_2}\right) \quad \delta_2 < \delta \le \delta_3 \tag{5}$$

$$\tau = \tau_f \quad \delta > \delta_3 \tag{6}$$

Where δ_1=1, δ_2=3, δ_3 is the clear spacing between ribs, which can be taken as 10.5 if unknown, $\tau_{max} = 2.5\sqrt{f_c}$ MPa and $\tau_f = 0.4\tau_{max}$ MPa.

For concrete softening, the closed form solution given by Eq. 7, which was derived by Haskett et al. [30], gives the relationship between the total material and non material deformation, δ_{ele} in Figure 7(a) and stress developed σ_{ele} in Figure 7(c). For the present analysis the angle at which the wedge forms (α) has been taken as 30°.

$$\Delta = \left(\varepsilon_{pk} - \frac{\sqrt{f_c^2 - \sigma}}{f_c}\varepsilon_{pk}\right) L_{def} + \frac{(\sigma - f_c) f_c \cos\alpha \sin\alpha}{\left[\left(\frac{f_c}{30}\right)^{0.6011} (-30.142 f_c + 51.623\sigma \sin^2\alpha)\cos\alpha\right]} \tag{7}$$

Finally when the depth of the softening wedge d_{wdg} in Figure 7(a) exceeds the cover to the compression reinforcement, it is assumed that the bars are unrestrained and can therefore buckle once they have yielded. To allow for buckling the empirically derived stress σ strain ε relationship of Dhakal and Maekawa [37] is used. This model requires that an intermediate point (ε*,σ*) be determined using Eq. 8 and Eq. 9.

$$\frac{\varepsilon^*}{\varepsilon_y} = 55 - 2.3\sqrt{\frac{f_y}{100}}\frac{L}{D};\ \frac{\varepsilon^*}{\varepsilon_y} \geq 7 \tag{8}$$

$$\frac{\sigma^*}{\sigma_l^*} = \left(1.1 - 0.016\sqrt{\frac{f_y}{100}}\frac{L}{D}\right) \quad ;\ \sigma^* \geq 0.2 f_y \tag{9}$$

where ε_y is the yield strain of the bar, f_y is the yield stress, L is the spacing between stirrups, D is the diameter of the longitudinal reinforcement and σ_l^* is the stress corresponding to the strain ε* if buckling is ignored.

For strains ε less than ε*, the stress σ including the effects of buckling, can be determined using Eq.10, where σ_l is the stress developed in the bar for the strain ε if buckling is ignored.

$$\frac{\sigma}{\sigma_l} = 1 - \left(1 - \frac{\sigma^*}{\sigma_l^*}\right)\left(\frac{\varepsilon - \varepsilon_y}{\varepsilon^* - \varepsilon_y}\right);\ \text{for}\ \varepsilon_y < \varepsilon \leq \varepsilon^* \tag{10}$$

Once the intermediate point is reached the stress in the bar is determined using Eq. 11, where E_r is the elastic modulus of the bar and the additional constrain that $\sigma \geq 0.2 f_y$ is applied.

$$\sigma = \sigma^* - 0.02 E_r(\varepsilon - \varepsilon^*);\ \text{for}\ \varepsilon \geq \varepsilon^* \tag{11}$$

Examining the M/θ and M/EI_{equ} relationships in Figure 9, the points at which concrete cracking, yield of the tensile reinforcement, commencement of concrete softening and wedge failure can be clearly seen. It may be of interest to note that the point at which concrete softening commences does not necessarily correspond to the peak moment, but rather the moment continues to increase following the commencement of concrete softening. This occurs because initially the slip of the wedge is small, and hence, it is possible that the average stress in the softening wedge may remain close to f_c. The ability of the section to maintain this increase in moment following the commencement of concrete softening is highly dependent upon the behaviour of the compression reinforcement. Without compression reinforcement, a falling moment rotation relationship is seen immediately after the commencement of concrete softening as show in. When heavily reinforced in the compression region, or when the reinforcement has a large strain hardening modulus, a greater proportion of the total compressive force is taken by the reinforcement and, hence, both the depth and slip of the wedge are reduced leading to a more significant rising branch post concrete softening

A further significant feature of the analysis shown in Figure 9 is the failure of the wedge. Wedge failure occurs as beyond a certain slip, which can be determined using Eq 3, the elements of the wedge can no longer sustain any load. It therefore follows that as rotations increase, portions of the wedge, as in Figure 7(a), gradually reach this limit and stop contributing to the resistance of the applied actions. Again depending on the amount and properties of the compression reinforcement, the failure of a small portion of the wedge can lead to a rapid increase in wedge depth and therefore a sudden drop in moment capacity as seen in Figure 9(a).

Laterally loaded columns

Figure 10 shows the application of the above technique to the three columns tested by Atalay and Penzien [34], where each column had a height of 1676mm and cross section of 305mmx305mm and was reinforced longitudinally with 4 No. 22mm bars and transversely with stirrups at 127mm centres and the axial load ranged from 262 to 801kN.

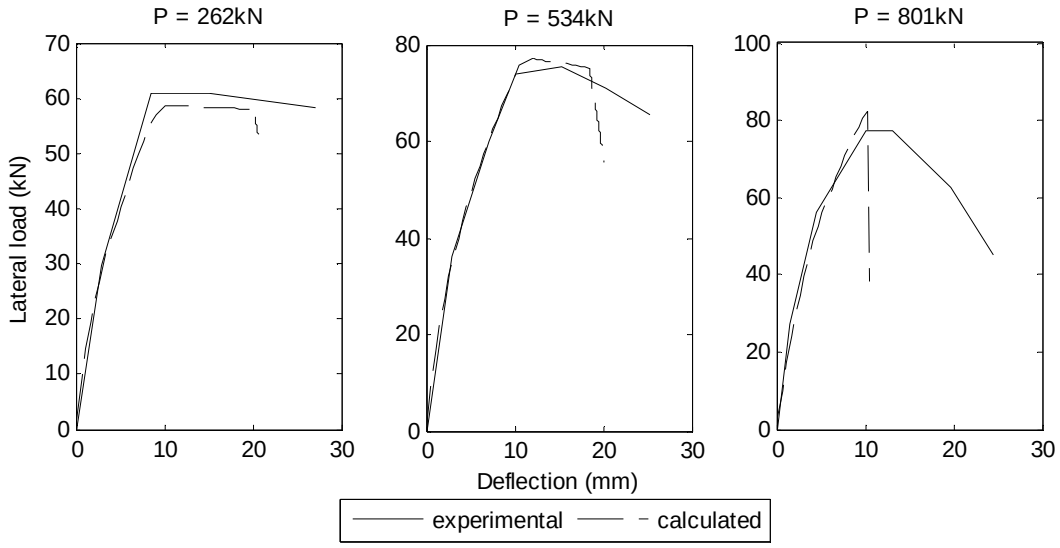

Figure 10: Comparison of experimental and simulated results for laterally loaded columns tested by Atalay and Penzien [34]

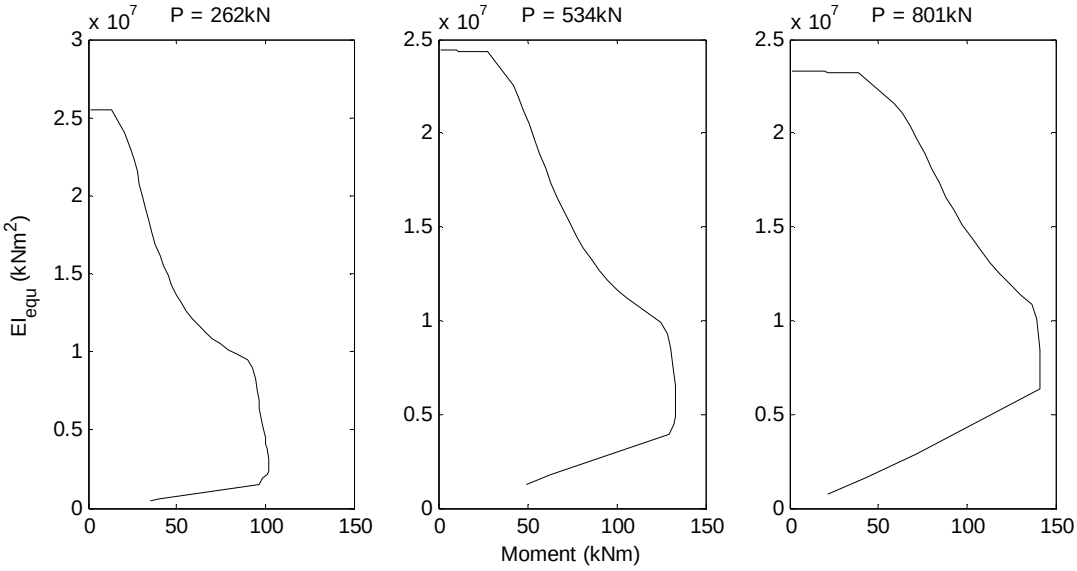

Figure 11: Moment-EI_{equ} relationships for columns tested by Atalay and Penzien [34]

It can be seen from the comparison of the experimental and theoretical results in Figure 10 that the moment rotation approach is capable of accurately predicting the response of the columns both in terms of shape and magnitude on the rising branch and under low axial loads up until the ultimate limit. The simulation under higher axial loads, however, predicts a far more rapid loss of strength than seen in practice. This may be attributed to the fact that the influence of stirrups has not been included in the present analysis, that is the confining effect of stirrups has not been included in Eq. 3 which was derived from laterally unconfined

concrete [16]. If stirrups were included it could be expected that a more gradual failure of the wedge would occur as stirrups would act to reduce wedge slip through their confining action.

Also shown in Figure 11 is the M/EI_{equ} relationship for a segment of each column. It can be seen that with increasing axial loads the section cracks later and initially shows a more gradual reduction in flexural rigidity; this is an example of how the M/θ approach automatically allows for the effects of tension stiffening at all stages of loading and for any axial load. Once the reinforcement begins to yield there is a rapid deterioration in the flexural rigidity. In the case of the tree columns tested, because the compression reinforcement has yielded and the bars have a low strain hardening modulus meaning that as the section continues to rotate a larger proportion of the compressive force must be carried by the concrete, which in turn leads to the peak strain being reached at lower rotations. The earlier commencement of concrete softening also means that the wedge begins to fail at lower rotations and so the rapid reduction in flexural rigidity, indicating wedge failure, occurs earlier.

Eccentrically loaded columns

This analysis technique has also been applied to the columns tested by Kim and Yang [5], which had heights of either 1440mm or 2400mm and cross sections of 80mm x 80mm. The columns were reinforced with either four 6.4mm bars to give a reinforcing ratio of 1.98%, or eight 6.4mm bars to give a reinforcing ratio of 3.95% and had stirrups at 60mm spacing. The columns had concrete strengths of either 25.5MPa or 63.5MPa.

From the load deflection results presented in Figure 12, it can be seen that the present approach accurately predicts both the general behaviour and the magnitude of these test results. It is, however, expected that both the results for the laterally loaded columns, as well as the results for the eccentrically loaded columns can be improved with time as the shear friction properties are developed such that stirrups can be considered. It can also be seen from the first test results in Figure 12 that the moment rotation approach used is capable of predicting behaviour up until a complete loss of strength is observed that is it can follow the collapse.

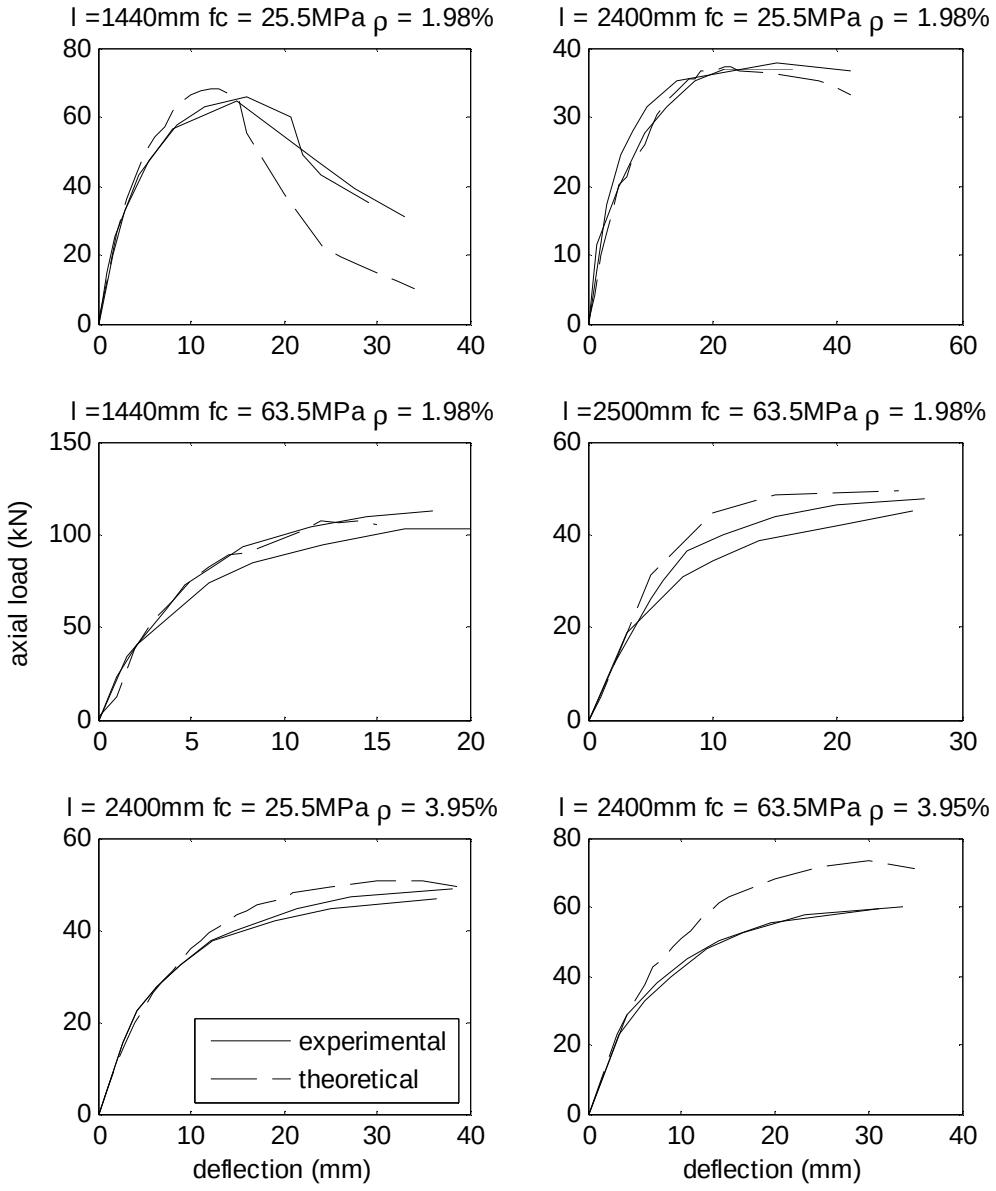

Figure 13: Application of moment-rotation analysis to columns tested by Kim and Yang [5]

In the analysis of eccentrically loaded columns, it was necessary to generate a family of M/θ responses with varying axial loads. Some of the results in terms of M/EI_{equ} are shown in Figure 14. Once again it can be seen that this approach automatically allows for tension-stiffening and concrete softening on the flexural rigidity without the need for empirically derived components for the model such as hinge lengths and effective flexural rigidities. In the case of these eccentrically loaded columns, unstable sliding of wedge does not occur. Wedge failure is prevented as the sections have a higher reinforcement ratio than those of

Atalay and Penzien. Consequently, as in Figure 14, even under higher axial loads the flexural rigidity gradually approaches zero. It may be noted that for both laterally loaded and eccentrically loaded columns failure of the wedge could be delayed by the addition of stirrups.

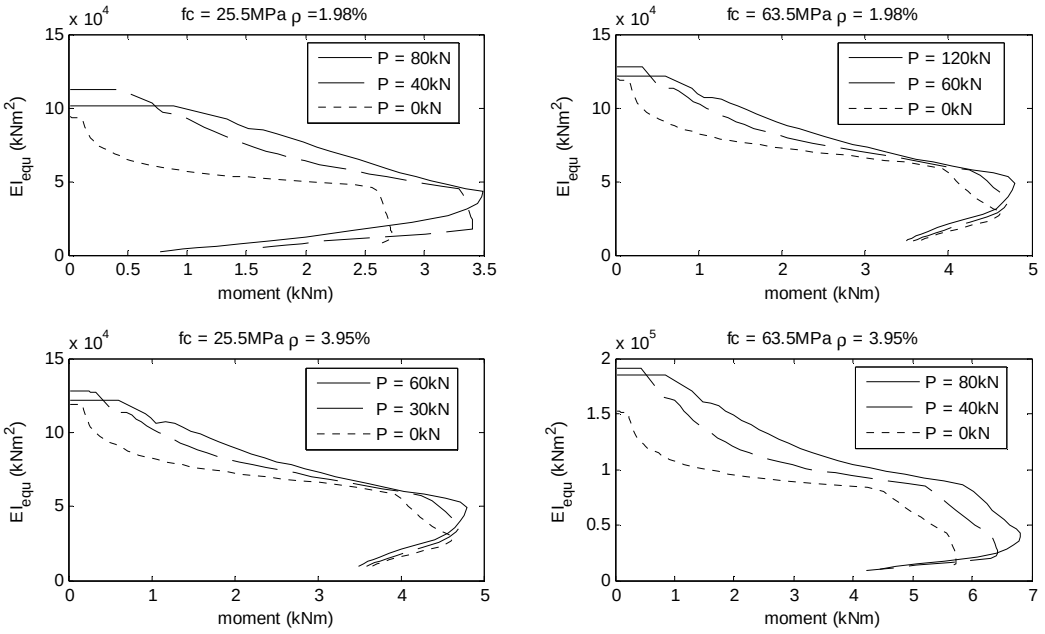

Figure 14: Moment-EI_{equ} relationships for varying axial loads

CONCLUSIONS

In this paper, a M/θ approach has been developed for the analysis of reinforced concrete columns and has been validated by comparison with both laterally and eccentrically loaded column tests. This M/θ approach uses the established mechanics of partial-interaction theory and shear-friction theory to allow for cracking and softening of concrete and for tension-stiffening. Hence the M/θ approach can quantify the rotation at all stages of loading, that is, at serviceability, ultimate and failure without the need for empirical components such as effective flexural rigidities and hinge lengths. Furthermore, the moment-rotations from the M/θ approach can be converted to moment-curvatures and equivalent flexural rigidities at all stages of loading so that the M/θ approach can be considered as extending the M/χ approach by automatically allowing for tension-stiffening and concrete softening on the flexural rigidity of a member.

ACKNOWLEDGEMENTS
The financial support of the Australian research Council ARC Linkage Project LP 0883451 "Blast resistance of flexural high performance concrete members' and ARC Discovery project DP0985828 'A unified reinforced concrete model for flexure and shear' are gratefully acknowledged.

REFERENCES

[1] Park, R., Paulay, R, Reinforced Concrete Structures, Wiley Interscience, New York, 1975

[2] Yalcin, C., Saatcioglu, M, Inelastic analysis of reinforced concrete columns, Computers and Structures, 77 (2000) 539-555.

[3] Bae, S., Bayrak, O., Plastic Hinge Length of Reinforced Concrete Columns, ACI Structural Journal 105(3) (2008) 290-300.

[4] Zeng, J.M., Duan, L., Wang, F.M., Chen, W.F., Flexural Rigidity of Reinforced Concrete Columns, ACI Structural Journal, 89(2) (1992) 150-158.

[5] Kim, J. K., and Yang J.K., Buckling behaviour of slender high-strength concrete columns, Engineering Structures, 17(1) (1995) 39–51.

[6]Park, R., Priestly, M.J.N., Gill, W.D., Ductility of Square Confined Concrete Columns, ASCE Journal of the Structural Division, 108 ST4 (1982) 929-950.

[7] Sakai, K., Sheikh, S.A., What Do We Know about Confinement in Reinforced Concrete Columns? (A Critical Review of Previous Work and Code Provisions), ACI Structural Journal, 86(2) (1989) 192-207.

[8] Sheikh, S.A., Khoury, S.S., Confined Concrete Columns with Stubs, ACI Structural Journal, 90(4) (1993) 414-431.

[9] Panagiotakos, T. B., and Fardis, M. N., Deformations of reinforced concrete members at yielding and ultimate, *ACI Structural Journal*, 98(2) (2001) 135-148.

[10] Visintin, P., Oehlers, D. J., Haskett, M., Wu, C., A Mechanics Based Hinge Analysis for Reinforced Concrete Columns, Submitted to ASCE Journal of Structural Engineering 2011.

[11] Marti, P., Alvarez, M., Kaufmann, W., Sigrist, V., Tension chord model for structural concrete. Structural Engineering International 8(4) (1998) 287-298.

[12]Gupta, A.K., Maestrini, S.R., Tension stiffening model for reinforced concrete bars, Journal of Structural Engineering, 116 (3) (1990) 769-790.

[13] Wu, Z., Yoshikawa H., Tanabe T., Tension stiffness model for cracked reinforced concrete, Journal of Structural Engineering, 117(3) (1991) 715-732

[14] Choi, C.K., Cheung, S.H., Tension stiffening model for planar reinforced concrete members, Computers & Structures, 59 (1) (1996) 179-190.

[15] Yuan, H., Teng, J.G., Seracino, R., Wu, Z.S., Yao J. Full-range behavior of FRP-to-concrete bonded joints, Engineering Structures 26 (5) (2004) 543-691.

[16] Oehlers, D.J., Liu, I.S.T., Seracino, R., The gradual formation of hinges throughout reinforced concrete beams, Mechanics Based Design of Structures and Machines 33 (3-4) (2005) 375-400.

[17] Warner, R.F., Foster, S.J., Kilpatrick, A.E., Reinforced Concrete Basics: Analysis and Design of Reinforced Concrete Structures, Pearson Education, Australia 2007.

[18] Haskett, M., Oehlers, D.J., Mohamed Ali, M.S., Local and global bond characteristics of steel reinforcing bars, Engineering Structures 30(2) (2008) 376-383.

[19] Mohamed Ali MS, Oehlers DJ, Griffith MC, Seracino R. Interfacial stress transfer of near surface mounted FRP-to-concrete joints, Engineering Structures 30(7) (2008) 1861-1868.

[20] Mohamed Ali, M.S., Oehlers, D.J., Griffith, M.C., Shear transfer across cracks in FRP strengthened RC structures, ASCE Journal of Composites in Construction 12(4) (2008) 416-424.

[21] Yankelevsky, D.Z., Jabareen, M., and Abutbul, A.D., One-dimensional analysis of tension stiffening in reinforced concrete with discrete cracks, *Engineering Struct*ures 30 (2008) 206-217.

[22] Haskett, M., Oehlers, D.J., Mohamed Ali, M.S., and Wu, C., (2009) “Rigid body moment-rotation mechanism for reinforced concrete beam hinges” Engineering Structures, 31 (2009) 1032-1041.

[23] Haskett, M., Oehlers, D.J., Mohamed Ali and Wu, C. (2009) “Yield penetration hinge rotation in reinforced concrete beams”. *ASCE Structural Journal*, Vol. 135, Issue 2, Feb., 130-138.

[24] Haskett, M., Mohamed Ali M.S., Oehlers D.J., and Wu, C., (2009) "Influence of bond on the hinge rotation of FRP plated beams", special edition of *Advances in Structural Engineering*, Vol. 12, No. 6, pp 833-843.

[25] Bachmann, H., Influence of shear and bond on rotational capacity of reinforced concrete beams, Publications IABSE Zurich, Vol. 30 Part II (1970) 11-28.

[26] Walraven J.C., Reinhardt H.W., Theory and Experiments on mechanical behaviour of cracks in plain and reinforced concrete subjected to shear loading, Heron 26 (1A) (1981) 68 pp.

[27] Walraven J.C., Frenay J., Pruijssers A., Influence of Concrete Strength and Load History on the Shear-friction Capacity of Concrete Members, Prestressed Concrete Institute 32(1) (1987) 66-85.

[28] Haskett, M., Oehlers, D.J., Mohamed Ali, M.S., and Sharma, S.K., The shear-friction aggregate-interlock resistance across sliding planes in concrete, Magazine of Concrete Research, 62(12) (2010) 907-924.

[29] Haskett, M., Oehlers, D.J., Mohamed Ali, M.S., and Sharma, S.K., Evaluating the shear-friction resistance across sliding planes in concrete, Engineering Structures 33 (2011) 1357-1364.

[30] Haskett, M., Oehlers, D.J., Visintin, P., and Mohamed Ali, M.S., The shear-friction material properties of unconfined concrete, submitted to Cement and Concrete Research 2011.

[31] Oehlers, D.J., Mohamed Ali, M.S., Haskett, M., Lucas, W., Muhamad, R. Visintin, P., FRP reinforced concrete beams - a unified approach based on IC theory, ASCE Composites for Construction 2011 15(3) (2011) 293-303.

[32] CEB, CEB-FIP Model Code 90, London, 1992.

[33] Mohamed Ali, M.S., Oehlers, D.J., Griffith, M.C., The residual strength of confined concrete, Advances in Structural Engineering 13(4) (2010) 603-618.

[34] Atalay, M.B., Penzien, J., The Seismic Behavior of Critical Regions of Reinforced Concrete Components as Influenced by Moment, Shear and Axial Force" Report No. EERC 75-19, University of California, Berkeley, December 1975, 226 pages.

[35] Hognestad ,E., Hanson, N.W., McHenry, D., Concrete stress distribution in ultimate strength design, Journal of ACI 27(4) (1955) 455-479.

[36] Tasdemir, M.A., Tasdemir, C., Akyuz, S., Jefferson, A.D., Lydon, F.D., and Barr, B.I.G., Evaluation of Strains at Peak Stresses in Concrete: A Three-Phase Composite Model Approach", *Cement and Concrete Composites*, 20 (4) (1998) 301-318.

[37] Dhakal, R. P., Maekawa, K., Modeling for Postyield Buckling of Reinforcement, *Journal of Structural Engineering*, 128(9) (2002) 1139-1147.

Statement of Authorship

Partial-interaction time dependent behaviour of reinforced concrete beams
Magazine of Concrete Research: submitted paper

Visintin, P. (candidate)

Prepared manuscript, performed all analyses, and developed model and theory.

I hereby certify that the statement of contribution is accurate

Signed……..Date……

Oehlers, D.J.

Supervised research, provided critical manuscript evaluation and acted as corresponding author.

I hereby certify that the statement of contribution is accurate and I give permission for the inclusion of the paper in the thesis

Signed…….Date……

Haskett, M.

Assisted in manuscript evaluation.

I hereby certify that the statement of contribution is accurate and I give permission for the inclusion of the paper in the thesis

Signed …….Date……

Partial-interaction time dependent behaviour of reinforced concrete beams

Visintin P., Oehlers D.J. and Haskett M.

ABSTRACT

When a concrete member is subjected to a load its response is both instantaneous and time dependent. The influence of time dependent deformation is particularly import because it may lead to serviceability failures in structural members where deflections or crack widths are excessive. Current analysis techniques for reinforced concrete members are built around a moment-curvature (M/χ) approach that is based on the assumption of full-interaction (FI), that is, the reinforcement does not slip relative to the concrete which encases it and, consequently, the widening of cracks and their effect on deflection cannot be simulated directly. Hence in order to determine member deflection, empirically derived expressions for the flexural rigidity of a member (EI_{emp}) are required to allow for the tension stiffening associated with cracking. In contrast to this FI M/χ approach, a moment-rotation (M/θ) approach has been developed which allows for slip between the reinforcement and concrete, that is partial-interaction (PI) and which, consequently, obviates the need for the empirically derived flexural rigidities (EI_{emp}). The PI M/θ approach simulates directly, through partial-interaction structural mechanics, the formation and widening of cracks as the reinforcement pulls from the concrete at crack faces and, consequently, automatically allows for tension stiffening. Hence the PI M/θ approach is a useful improvement of the current FI M/χ approach as it quantifies the flexural rigidities associated with tension stiffening which can then be used in standard analysis techniques. It is also shown in this paper that the moment rotation approach can be used to derive flexural rigidities that account for the long term effects of creep and shrinkage as well as predicting the effects of creep and shrinkage on cracks widths and spacings.

Keywords: reinforced concrete beams; creep; shrinkage; deflection; serviceability; partial interaction theory

SYMBOLS

A_r – Area of tensile reinforcement
B – Bond force
E_c – Elastic modulus of concrete
E_r – Elastic modulus of reinforcing
EI – Flexural rigidity
EI_{emp} – Empirically derived effective EI
EI_{equ} – Equivalent EI
EI_{uncr} – Uncracked EI
L_{bd} - Length of concrete prism to FI boundary condition
L_{def} - Deformation length

L_p – Perimeter of all reinforcing bars
L_T - Total length of reinforcing bar to FI boundary condition
L_s - Segment length for numerical PI analysis
M - Moment
M_{seg} –Moment applied to a segment
P_{conc} – Force developed in the concrete in compression
$P_{conc\text{-}tens}$ - Force developed in the concrete in tension
P_r – Force in the reinforcing bar in the PI model
P_{reinf} - Force developed in reinforcing bar at crack face
$P_{reinf\text{-}tens}$ - Force developed in the tension reinforcement
$P_{reinf\text{-}comp}$ Force developed in the compression reinforcement

ds/dx – Slip strain
(ds/dx)FI – Full interaction slip strain
f_c – Peak concrete stress
t – Time
t_0 – Time at which load is first applied

Δ – Slip of reinforcing bar in a segment from the numerical PI model
Δ_{reinf} –Slip of the reinforcement form the crack face

δ - Slip of the reinforcement in the numerical PI model
δ_1, δ_2, δ_3 – slip of the reinforcement which define the (τ/δ) characteristic
δ_c – Extension of the concrete from the base line
$\delta\Delta$ – Change in slip of the reinforcement over a segment
δ_r - Contraction of the reinforcement from the base line
δ_{top} – Deformation of concrete at the top fiber
χ - Curvature
χ_{sh} – Curvature due to shrinkage alone
$(\varepsilon_r)_{FI}$ – Full interaction strain in the reinforcing bar
$(\varepsilon_c)_{FI}$ – Full interaction strain in the concrete
ε_{sh} – Shrinkage strain
ε_{pk} –Strain corresponding to the peak stress f_c
ϕ – Creep coefficient
θ - Rotation
θ_{sh} – Rotation due to shrinkage alone
τ – Bond stress
τ_{max} –Maximum bond stress
τ_f – Frictional bond stress

INTRODUCTION

When concrete is subjected to a sustained load, time dependent strains due to creep and shrinkage develop. These creep and shrinkage strains have considerable impact on the performance of structural members, causing increased crack widths and deflections which may result in serviceability failure. The unfavourable nature of time effects on reinforced concrete means it has been an area of research interest for more than 80 years, with much effort devoted to the development of models to predict the changes in concrete material behaviour with time (Bazant and Panula 1979a-c; Neville et al. 1983; Eurocode 2; ACI 1982; CEB-FIP 1994; RELIM 1995a,b Gardner and Lockman 2001; Standards Australia 2009) and to methods of incorporating these changes into sectional analyses (Faber 1927; Whitney 1932; Bresler and Selna 1964; Ghali 1967; Bazant 1972; Branson 1977; Neville 1983; Gilbert 1988; Westerberg 2008; Gilbert 2011). These cited approaches utilise methods of varying complexity to determine the change in concrete material properties with time and, hence, cross sectional behaviour. However in mechanics terms, all of these approaches are based on a moment-curvature (M/χ) analysis technique: in which there is a linear strain profile; and in which there is full interaction (FI), that is, the reinforcement does not slip relative to the concrete so that there is a uni-linear strain profile. These assumptions mean that the techniques are unable to describe crack spacing or widening directly and, therefore, must resort to empirically derived approaches to do so. Thus these approaches ultimately rely on the definition of an effective flexural rigidity (EI_{emp}), which must be defined empirically, to determine member deflection.

In contrast to the FI M/χ approach, a partial interaction (PI) moment-rotation (M/θ) approach for simulating reinforced concrete behaviour under instantaneous loading has been developed by the authors (Oehlers et al. 2011; and Visintin et al. 2012a,b); this approach directly simulates what is seen in practice, that is, the formation and widening of cracks using partial-interaction theory (Bachmann 1970; Yuan et al. 2004; Oehlers et al. 2005; Mohamed Ali et al. 2008a,b; Haskett et al 2008; Muhamad et al. 2011). In the following paper, the PI M/θ approach is extended to account for the influence of creep and shrinkage. It is first shown how the PI M/θ approach can be applied to a segment of a member to derive the equivalent flexural rigidity of a cross section (EI_{equ}) to allow for tension-stiffening, creep and shrinkage; these equivalent flexural rigidities (EI_{equ}) are a replacement of the empirically derived effective flexural rigidities (EI_{emp}) used in the FI M/χ approach. The equivalent flexural rigidity of a cross section is then used to describe the load deflection behaviour of an entire member through the application of standard analysis techniques. Finally, the approach is used to predict the behaviour of beams tested by Gilbert and Nejadi (2008) under a sustained load and FRP reinforced beams tested by Barris et al. (2009) under instantaneous loads, where the PI M/θ approach is used to predict the additional deflections which take place due to shrinkage.

MOMENT-ROTATION ANALYSIS OF A SEGMENT

The PI M/θ analysis is illustrated in Figure 1(b) for a segment of a beam of outline A-A-A-A, of length $2L_{def}$ and of the cross section in Figure 1(a). The segment is symmetrical and symmetrically loaded about E-E so that all deformations can be measured relative to E-E which in effect remains stationary. Prior to any deformations taking place, either as a result of shrinkage or the application of an external load, both the concrete and the reinforcement are of length $2L_{def.}$ If a shrinkage strain ε_{sh} is allowed to take place and the concrete were free of any restraint from the reinforcement, a deformation of the concrete of magnitude $\varepsilon_{sh}L_{def}$ from A-A to B-B would take place over each half of the segment A-E. However, due to the presence of internal reinforcement, which in this case is non-symmetrically placed, the concrete is restrained and, hence, the actual deformation of the concrete is from A-A to C-C causing a rotation θ_{sh}. If a constant moment M_{seg} is now applied over the segment, a further rotation takes place such that the total rotation is θ and the deformation is to D-D. By symmetry, the deformations at each end of the segment shown shaded are equal, so that relative to E-E at the mid-length of the segment they produce the same strains or effective strains. Hence it is only necessary to consider one half of the segment which is of length L_{def} in the following analyses. Let us first consider the behaviour of the segment prior to cracking, beginning with the case where the applied moment M_{seg} is zero and, hence, all deformations are the result of shrinkage alone.

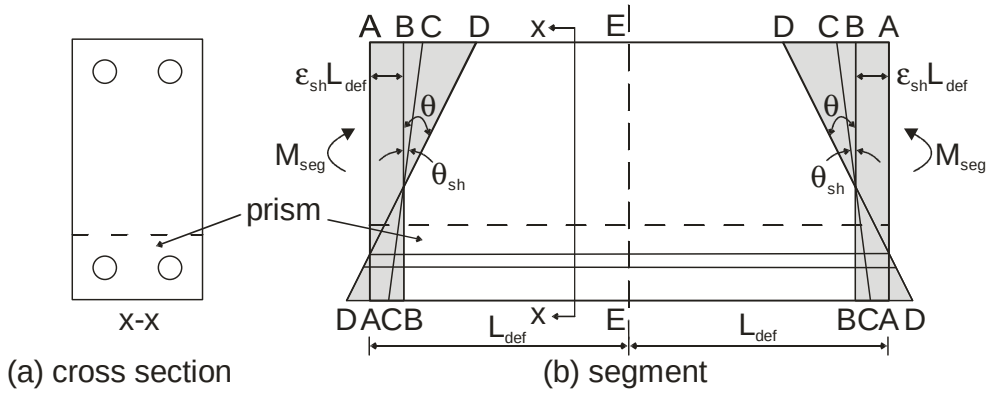

Figure 1: Segmental M/θ

SEGMENTAL ANALYSIS PRIOR TO CRACKING

The left hand side of the segment in Figure 1(b) is shown in Figure 2(a). The segment has an original length L_{def}; hence prior to any deformation, both the reinforcement and the concrete are of this length. Since any deformation of the reinforcement from this initial length causes a stress to be induced, A-A becomes the baseline for deformations which induce a stress in the reinforcement. Similarly if the concrete were free to shrink without restraint, then it would reduce in length $\varepsilon_{sh}L_{def}$ from A-A to B-B. This shortening would not induce a stress. Hence any deformation of the concrete away from B-B induces a stress in the concrete and,

therefore, B-B becomes the baseline for concrete deformations which induce a stress in the concrete.

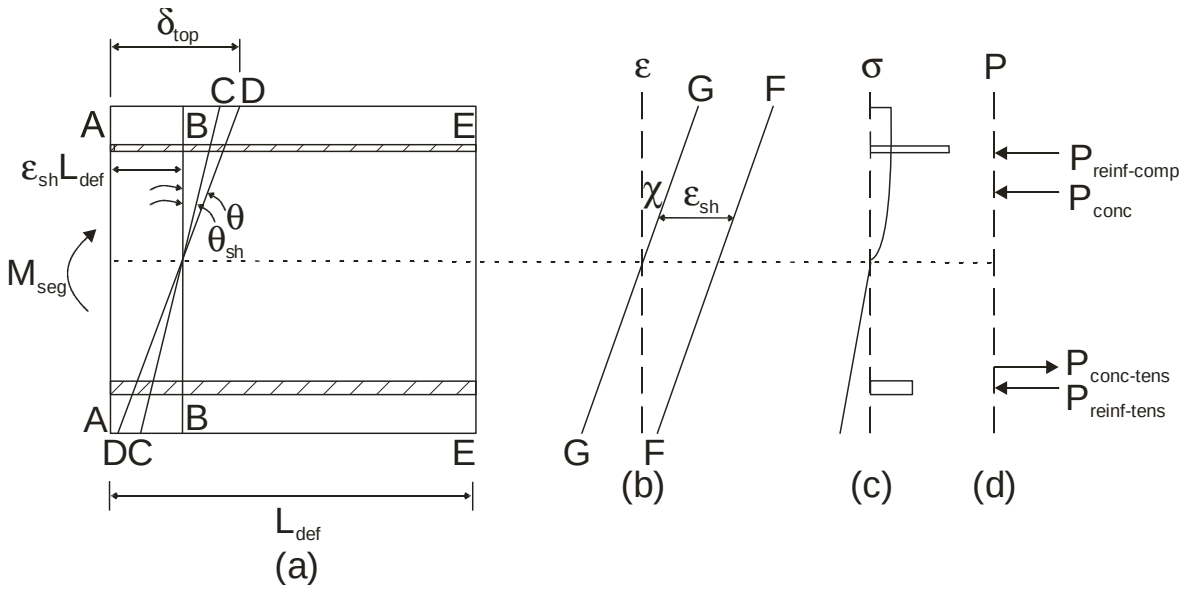

Figure 2: Analysis of an uncracked segment

Prior to the application of any external loads, it is therefore a question of finding a deformation C-C in Figure 2(a), which has a rotation of $\theta_{sh,}$ such that for longitudinal equilibrium the moment M_{seg} is zero. To do this, an iterative process is required. The procedure begins by fixing θ_{sh} and guessing the location δ_{top}, thereby, fixing the position of the deformation profile C-C in Figure 2(a). Since the section is uncracked, the deformations can be divided by the deformation length L_{def} to give the strain profiles in Figure 2(b). It needs to be stressed, however, that two strain profiles exist, one for the reinforcement and one for the concrete. Since it has been established that any deformation away from A-A results in a strain to cause a stress in the reinforcement, the deformation from A-A to C-C divided by L_{def} gives the strain profile for the reinforcement, that is, F-F in Figure 2(b). Similarly, since any deformation away from B-B results in a strain to cause a stress in the concrete, the deformation from B-B to C-C divided by L_{def} gives the strain profile G-G in Figure 2(b). It can also be seen in Figure 2(b) that these profiles are parallel and located ε_{sh} apart. As the section is uncracked, these strains are real material strains, that is, they would be measured by strain gauges placed on the member. Knowing the distribution of strain in the segment, and because all the strains are real strains, the distribution of stress in Figure 2(c) can be determined using any conventional material stress-strain relationship and, hence, the internal forces in Figure 2(d) can be determined. If the algebraic sum of these forces is not equal to zero, then the maximum deformation at the top face δ_{top} can be adjusted, thereby shifting the depth of the neutral axis, until equilibrium of the internal forces is achieved that is they sum to zero. If at this point of longitudinal equilibrium the moment is not zero then θ_{sh} must be adjusted and the analysis repeated until it does so. Hence both longitudinal and

rotational equilibrium have to be achieved to find the deformation C-C, and in this case both stress resultants are zero.

The analysis above provides the initial rotation of the segment due to shrinkage alone, that is θ_{sh} at point O in Figure 3(a), and is applicable when the shrinkage strain is insufficient to cause concrete cracking. The shrinkage rotation θ_{sh} in figure 3(a) can be converted into a shrinkage curvature χ_{sh} in figure 3(b) by dividing by the deformation length L_{def} in Figure 2(a). As the section is uncracked, this initial curvature is the same as that which could be derived using a standard full interaction analysis. Hence the deformation length L_{def} used in the analysis in Figure 2 is irrelevant as any deformation length will provide the same initial curvature.

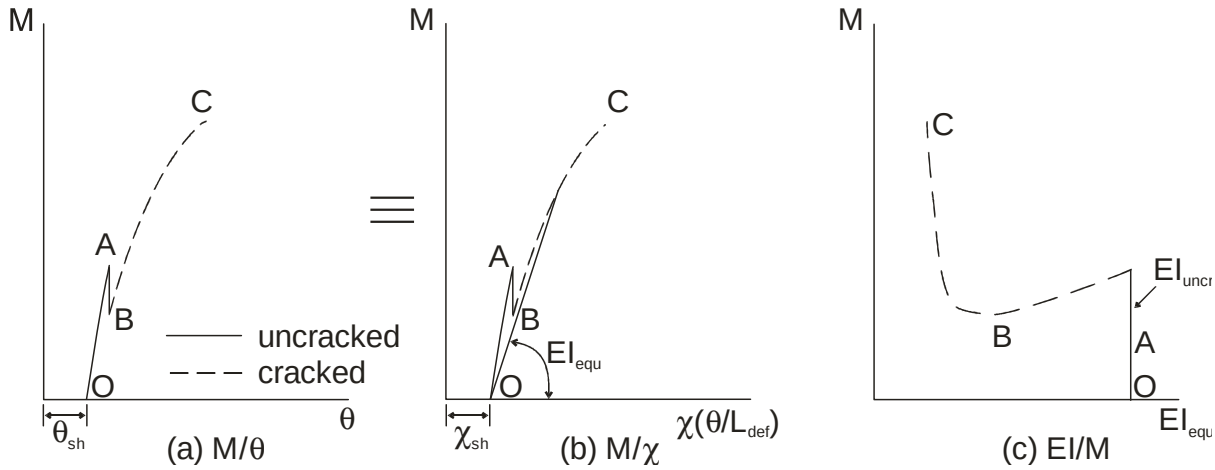

Figure 3: Variation of rotation, curvature and EI

Let us now consider what happens when a moment M_{seg} is applied to the segment in Figure 2(a) and sustained for some period of time *t*. The combination of shrinkage and the applied moment causes a total rotation θ in Figure 2(a), such that the total deformation of the segment face is now from A-A to D-D. The same analysis as outlined for the case of shrinkage alone can now be applied. However in this case θ is varied until the resulting moment is now M_{seg}. Hence the longitudinal equilibrium requirement remains at zero whilst rotational equilibrium requires a moment of M_{seg}; an alternative approach would be to fix θ and vary δ_{top} until there was longitudinal equilibrium after which the moment could be taken for that fixed or imposed θ. Therefore by repeating the analysis for increasing rotations, the moment-rotation relationship O-A in Figure 3(a) is established. It should also be noted, that in order to allow for creep, when determining the stress in the concrete, a reduced elastic modulus must be used where the magnitude of this reduction is determined by any convenient method.

Again, as shown in Figure 3(b), the M/θ relationship O-A in Figure 3(a) can be converted into an equivalent M/χ relationship by dividing the rotations by the deformation length $L_{def.}$ At the uncracked stage, the result obtained from the M/θ analysis and a traditional FI M/χ analysis are identical as both are FI analyses. The deformation length L_{def} used in the analysis from O to A is, therefore, irrelevant as any length will give the same M/χ. Furthermore, as both approaches are identical so too are the uncracked flexural rigidities (EI_{uncr}) as shown in Figure 3(c), these could therefore also be obtained from the traditional FI M/χ analysis. It is important to emphasise that both approaches are identical for uncracked segments, because, at the uncracked stage, a traditional FI M/χ analysis does not rely on empirically derived factors such as those required to determine deflections in particular EI_{emp}. Hence, a M/θ analysis carried out on a segment subjected to a constant moment, can be used to determine the variation in the local flexural rigidity of the cross section with moment, which can in turn can be used to determine the deflection of the member for any moment distribution. Bearing in mind of course that that the member is already subjected to a shrinkage curvature χ_{sh} along its length that induces deflection.

The analysis in Figure 2 is applicable following cracking, but only to the point at which the crack tip just crosses the tensile reinforcement. After this point, partial-interaction theory must be used to determine the force developed in the tension reinforcement. The use of partial-interaction theory allows for slip of the reinforcement relative to the surrounding concrete which in practice is what allows cracks to open.

ACCOMMODATION OF CRACKING WITHIN SEGMENTAL ANALYSIS

Again consider the left hand side of the beam segment in Figure 1(b), now shown in Figure 4(a), which is cracked to a level above the reinforcing bar. Partial interaction theory must now be used to describe the behaviour of the tensile reinforcement. This is because the load developed in the reinforcement is now dependent on the slip of the bar at the crack face, Δ_{reinf} in Figure 4(a), which in turn depends on the bond slip (τ/δ) properties between the bar and the concrete surrounding it.

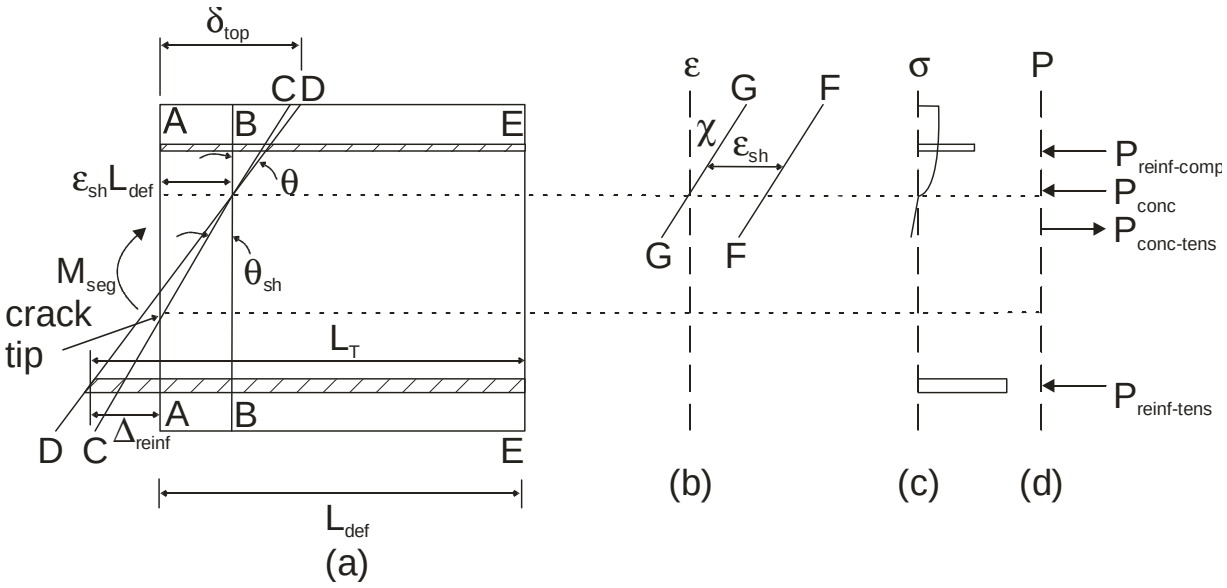

Figure 4: Cracked segment analysis

Tension stiffening model

Full-interaction boundary condition

The partial interaction load-slip behaviour allowing for the influence of both creep and shrinkage can be determined through the adaptation of a well established numerical technique (Haskett et al. 2008; and Oehlers et al. 2011). To make this adaptation and in order to establish boundary conditions which differentiate the partial interaction and full interaction regions, we must first consider the case of full interaction. Consider a reinforcement bar of axial rigidity E_rA_r embedded in a prism of axial rigidity E_cA_c as in Figure 5(a). We will assume that the stiffness of the bond is infinite so that the build up of stress is over zero length; the gradual build up of stress to reach a full-interaction position is dealt with in the next section.

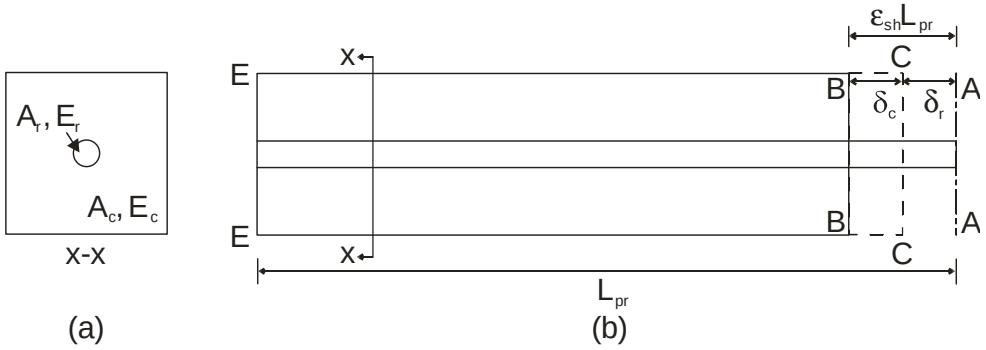

Figure 5: Full interaction boundary condition

Prior to shrinkage, the concrete and reinforcement in Figure 5 are of length $L_{pr.}$ If no bond were present and if a shrinkage strain of ε_{sh} were to develop, the end of the reinforcement at A-A would remain stationary while the concrete would shorten by $\varepsilon_{sh}L_{pr}$ to B-B relative to a fixed boundary E-E. Through bond however, the contraction of the concrete is resisted by the reinforcing bar which goes into compression, and hence it only shortens to C-C. Moreover, as we are dealing with full interaction, that is an infinitely stiff bond exists, the concrete must go into tension, extending from B-B to C-C. Hence the reinforcing bar has contracted by δ_r from its base line position A-A and the concrete has extended by δ_c from its base line position B-B. Hence by compatibility at E-E, the force in the reinforcement P_r and the force in the concrete P_c are

$$P_r = \frac{\delta_r}{L_{pr}} E_r A_r \tag{1}$$

$$P_c = \frac{\delta_c}{L_{pr}} E_c A_c \tag{2}$$

where all unknowns are as defined in Figure 5. From equilibrium $P_r = P_c$, hence equating Eqs. 1 and 2 gives the contraction of the reinforcement δ_r and the extension of the concrete δ_c as

$$\delta_r = \frac{\delta_c E_c A_c}{E_r A_r} \tag{3}$$

$$\delta_c = \frac{\delta_r E_r A_r}{E_c A_c} \tag{4}$$

From Figure 5(b), it can also be seen that

$$\varepsilon_{sh} L_{pr} = \delta_c + \delta_r \tag{5}$$

Substituting for δ_r from Eq. 3 yields the strain in the concrete at full interaction $(\varepsilon_c)_{FI}$

$$\frac{\delta_c}{L_{pr}} = (\varepsilon_c)_{FI} = \frac{\varepsilon_{sh}}{1+\frac{E_c A_c}{E_r A_r}} \tag{6}$$

Similarly, substituting for δ_c into Eq. 5 yields the full interaction strain in the reinforcement $(\varepsilon_r)_{FI}$

$$\frac{\delta_r}{L_{pr}} = (\varepsilon_r)_{FI} = \frac{\varepsilon_{sh}}{1+\frac{E_r A_r}{E_c A_c}} \tag{7}$$

The full interaction slip strain $(ds/dx)_{FI}$ is the difference between the strain in the reinforcement and the adjacent concrete and is, therefore, equal to

$$\left(\frac{ds}{dx}\right)_{FI} = (\varepsilon_r)_{FI} - (\varepsilon_c)_{FI} \tag{8}$$

As we are dealing with a full-interaction analysis, that is an infinitely stiff bond, the slip of the reinforcement relative to the concrete is also known to be zero, that is $\Delta=0$.

Let us now consider the prism in Figure 6(a) in which the bond stiffness is no longer infinite. Hence a finite length of prism L_{bd} is required for the stresses to stabilise from where the reinforcement load P_r is applied to E-E beyond which the stresses and deformations remain unchanged. This is the full-interaction region where the slip $\Delta=0$ and the slip strain is given by Eq. 8. The analysis of the partial-interaction region which is given in the following section requires this full-interaction boundary condition.

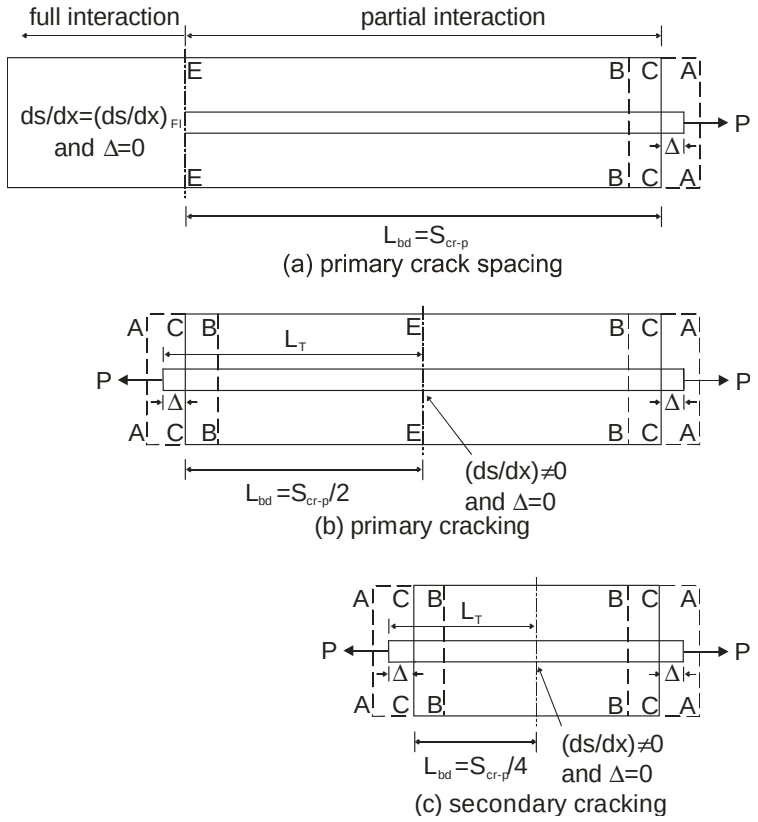

Figure 6: Tension stiffening behaviour

Partial-interaction tension-stiffening model

Let us now consider the behaviour in the partial interaction region in Figure 6(a) which is shown divided into elements of length L_s in Figure 7 which are small enough so that the slip can be considered to be constant over each element. It is now a question of finding the

relationship between the slip of the reinforcement at the crack face, Δ_1, and the load P_{r1} for use in the segmental analysis in Figure 4.

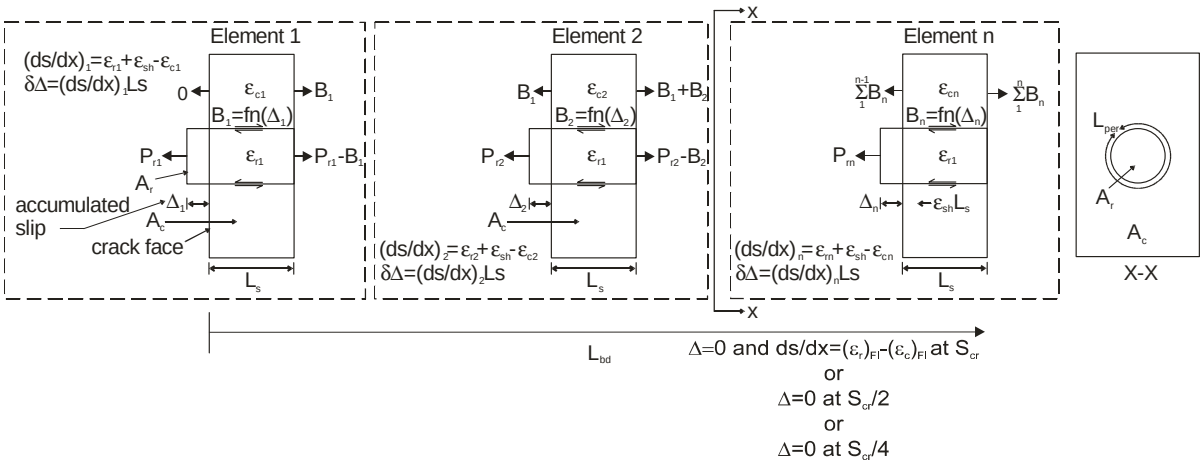

Figure 7: Partial-interaction numerical procedure

As with the M/θ analyses in Figures 2 and 4, for each element of the prism in Figure 7 a base line needs to be established for deformations which cause a stress in the reinforcement and a stress in the concrete. This can be done by considering the localised deformations that occur within a single element, that is, the deformations due to the stresses and strains within that element, as shown in Figure 8. As in Figures 2 and 4, the deformations are measured relative to E-E. Prior to any applied loads or shrinkage, both the reinforcing bar and the concrete are of length L_s, so that their left faces relative to E-E are at A-A. Hence, any deformation relative to A-A would cause stresses to develop. Let us now apply a shrinkage strain of ε_{sh}. If there is no restraint between the concrete and the reinforcement, that is the bond force B_x is zero, then the concrete face at A-A would move $\varepsilon_{sh}L_s$ to B-B. Therefore A-A is the base line to measure deformations to cause stress in the reinforcement and B-B is the base line to cause stress in the concrete. The average of the concrete forces on the left and right of the element causes a strain ε_{cr}. This strain, if tensile, causes the concrete face to extend $\varepsilon_{cx}L_s$ as shown. Similarly the average of the reinforcement forces on the left and right cause a strain ε_{rx} and if this strain is tensile it would cause the reinforcement face to extend $\varepsilon_{rx}L_s$. The distance between the reinforcement face and the concrete face shown as $\delta\Delta_x$ is the slip induced within an element. This is equal to $(\varepsilon_{sh}+\varepsilon_{rx}-\varepsilon_{cx})L_s$ where the term $(\varepsilon_{sh}+\varepsilon_{rx}-\varepsilon_{cx})$ is the slip-strain (ds/dx).

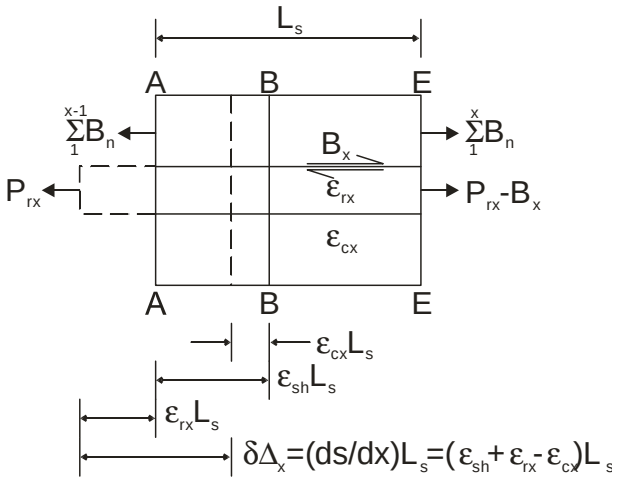

Figure 8: Element localised deformations

The analysis of the prism in Figure 7 now begins by setting a displacement of the bar Δ_1 at the crack face and guessing the force in the reinforcement P_{r1} to cause this crack face slip; Δ_1 is not the increase in slip within an element shown as $\delta\Delta$ in Figure 8 but is the accumulation of slip of all the elements to the right in Figure 7. As the displacement of the bar at the first element is known to be Δ_1, the bond force in the first element B_1 can be determined from the known bond slip (τ/δ) properties, which as an example have been defined for steel reinforcement in CEB (1994); that is B_1 is $L_s L_{per} \tau_1$ where L_{per} is the perimeter length of the reinforcement as in Figure 7 and τ_1 is the shear stress for a slip of Δ_1 which can be obtained from the bond-slip properties. The force in the reinforcement in Element 1, therefore, varies from P_{r1} to P_{r1}-B_1 such that the mean stress and, hence, strain ε_{r1} can be determined. Moreover, the force in the concrete at the crack face is zero and at the right hand side of Element 1 it is B_1. Hence the mean stress and consequently strain ε_{c1} can be determined as in Figure 8. The slip strain in Element 1 $(ds/dx)_1$ is the difference between the strain in the reinforcement and the total strain in the concrete, that is, $\varepsilon_{r1}+\varepsilon_{sh}-\varepsilon c1$ as shown in Figure 8 and the change in slip over the first element $\delta\Delta_1$ is the slip strain integrated over L_s also shown in Figure 8. The slip and the slip strain are therefore both known for the first element. The procedure can be repeated for Element 2, in which it is known that the force in the reinforcing bar P_{r2} is P_{r1}-B_1 and the force in the prism P_{c2} is B_1. It is also known that the slip of the reinforcement Δ_2 is Δ_1- $\delta\Delta_1$ from which the bond force B_2 can be determined. The analysis can then be repeated over subsequent elements to give the variation in slip Δ and slip strain ds/dx, and the initial guess for P_{r1} adjusted until a known boundary condition is reached as outlined below.

The partial interaction analysis outlined in Figure 7 can be used to determine the primary crack spacing $S_{cr\text{-}p.}$ The stresses in the concrete build up from zero at the crack face C-C in Figure 6(a) to a maximum value where full-interaction boundary condition is achieved at E-E. Hence a crack can occur anywhere beyond E-E. The same analysis can also be used to

determine the force in the reinforcement to cause cracking which in this case is the force to cause primary cracking when the strain in the concrete at E-E exceeds the tensile rupture strain. It is important to stress that the partial interaction approach in Figure 7 produces the minimum crack spacing because a crack can form anywhere in the full interaction region shown in Figure 6(a). In beams subjected to a constant moment this leads to the random nature of cracking. However in beams subjected to a varying moment, cracks tend to occur in the full-interaction region where the moment is maximum and, hence, will tend to occur at L_{bd}. The implications of the random nature of cracking have been further investigated in Visintin et al. (2012b).

Once a crack has formed at $L_{bd} = S_{cr-p}$ in Figure 6(a), a prism of length equal to the crack spacing, as shown in Figure 6(b), now applies. The analysis of this prism in Figure 6(b) is identical to that in Figure 6(a) except that the boundary conditions changes to $\Delta = 0$ at $S_{cr-p}/2$. Hence, the tension stiffening behaviour of the prism in Figure 6(b) can be determined using the partial-interaction analysis in Figure 7 as it is known that if the reinforcement is pulled from each crack face with an equal force P, and by symmetry, the slip of the reinforcement at $S_{cr-p}/2$ must be zero. Hence, the analysis now provides the relationship between the total length of the reinforcing bar T_L and the load developed P_{reinf} required for the M/θ analysis in Figure 4(a), as the total length of the bar can be determined from the known ε_r distribution obtained from the PI analysis. Similarly, when the strain in the concrete to cause a stress ε_c exceeds the tensile cracking strain at the mid point of the prism, that is at $S_{cr-p}/2$ a secondary crack will form. The analysis can be applied to determine the tension stiffening behaviour as it is known that a point of full interaction where $\Delta = 0$ must exist at $S_{cr-p}/4$ as shown in Figure 6(c).

M/θ analysis of a cracked section

Having defined the tension stiffening behaviour above using PI theory, the M/θ analysis can be applied to the cracked section in Figure 4 bearing in mind that L_{def} in Figure 4(a) is equal to $S_{cr-p}/2$ in regions where only primary cracks occur and is equal to $S_{cr-p}/4$ in regions where secondary cracks occur. For a given rotation θ, the analysis in the uncracked portion of the beam is identical to that presented for the uncracked beam in Figure 2. In the cracked tension region however, the load developed in the reinforcing bar P_{reinf} in Figure 4(d) is based on the total length of the reinforcement T_L and must be determined using the partial interaction theory described above and where L_T in Figure 4(a) can be determined from simple geometry. Hence, the analysis in Figure 4(a) can be applied for increasing rotations θ to determine the moment rotation relationship for the cracked section from B-C in Figure 3(a).

The same analysis can also be applied to the case where shrinkage alone causes the member to crack. When this occurs, it is simply a matter of iterating the analysis to determine the

rotation θ_{sh} in Figure 4(a) where at the point of longitudinal equilibrium the moment developed is zero as was described for the uncracked.

Again the M/θ relationship obtained from this analysis can be converted to an equivalent M/χ relationship, as in Figure 3(b), by dividing by the deformation length L_{def}; and the results in Figure 3(b) used to derive the variation of the equivalent flexural rigidity EI_{equ} with moment. Importantly, the variation of these flexural rigidities (EI_{equ}) derived from this PI M/θ analysis are not the same as those obtained through a standard FI M/χ analysis. This is because when cracked, the M/θ approach uses partial-interaction theory that incorporates the effects of shrinkage to allow for crack formation and widening and, hence, represents a mechanics based solution to describing the behaviour of cracked concrete that includes time effects.

PARAMETRIC STUDY OF TIME DEPENDENT BEHAVIOUR

Material properties

In order to apply the M/θ analysis several material models must be defined, these material models are not a critical component of the M/θ approach and any desired material models may be substituted to achieve greater accuracy. The following have been used in the ensuing parametric study to illustrated the time dependent behaviour of cracked reinforced concrete.

The elastic modulus of concrete at any point in time $E_c(t,t_0)$ has been defined using an effective modulus method where at some time *t* the elastic modulus of the concrete is given by

$$E_c(t,t_0) = \frac{E_c(t_0)}{1+\phi(t,t_0)} \tag{9}$$

in which t_0 is the time at first loading and ϕ is the creep coefficient at time *t* for concrete first loaded at time t_0.

The change in elastic modulus due to creep has been applied to both concrete in compression and in tension as suggested by Gilbert and Ranzi (2011). For concrete in tension, a linear elastic stress-strain relationship has been assumed, and in compression the following parabolic distribution of Hognestad (1955) employed

$$\sigma = \left[\frac{2\varepsilon}{\varepsilon_{pk}} - \left(\frac{\varepsilon}{\varepsilon_{pk}}\right)^2\right] \tag{10}$$

where ε is the strain in the concrete which causes a stress and ε_{pk} is the strain which corresponds to the peaks stress f_c, and has been taken as that defined by Tasdamir (1998) for instantaneous loading

$$\varepsilon_{pk} = (-0.067f_c + 29.9f_c + 1053)10^{-6} \tag{11}$$

In Eq. 11 f_c is in MPa and the strain ε_{pk} must be increased according to the decrease in elastic modulus as defined by Eq. 9.

Once cracking has occurred, the partial interaction analysis requires a bond stress slip (τ/δ) property. These have been taken as that defined by CEB (1994) for deformed steel bars, that is,

$$\tau = \tau_{max}\left(\frac{\delta}{\delta_1}\right)^{0.4} \quad \delta \leq \delta_1 \tag{12}$$

$$\tau = \tau_{max} \quad \delta_1 < \delta \leq \delta_2 \tag{13}$$

$$\tau = \tau_{max} - \left(\tau_{max} - \tau_f\right)\left(\frac{\delta - \delta_2}{\delta_3 - \delta_2}\right) \quad \delta_2 < \delta \leq \delta_3 \tag{14}$$

$$\tau = \tau_f \quad \delta > \delta_3 \tag{15}$$

where, δ_1=1 mm, δ_2=3 mm, δ_3 is the clear spacing between ribs which can be taken as 10.5 mm if unknown, the maximum bond stress $\tau_{max} = \sqrt{f_c}$ MPa and the frictional component of the bond stress $\tau_f = 0.4\tau_{max}$ MPa.

Tension stiffening analysis

Let us firstly investigate the influence of shrinkage and creep individually on the tension stiffening analysis by considering the example of a 16 mm steel reinforcing bar embedded in concrete prism of area 6666 mm^2 which has a concrete strength of 30 MPa. The variation in the primary crack spacing ($S_{cr\text{-}p}$) with shrinkage strain can be seen in Figure 9(a) and the corresponding load in the reinforcing bar to cause cracking in Figure 9(b).

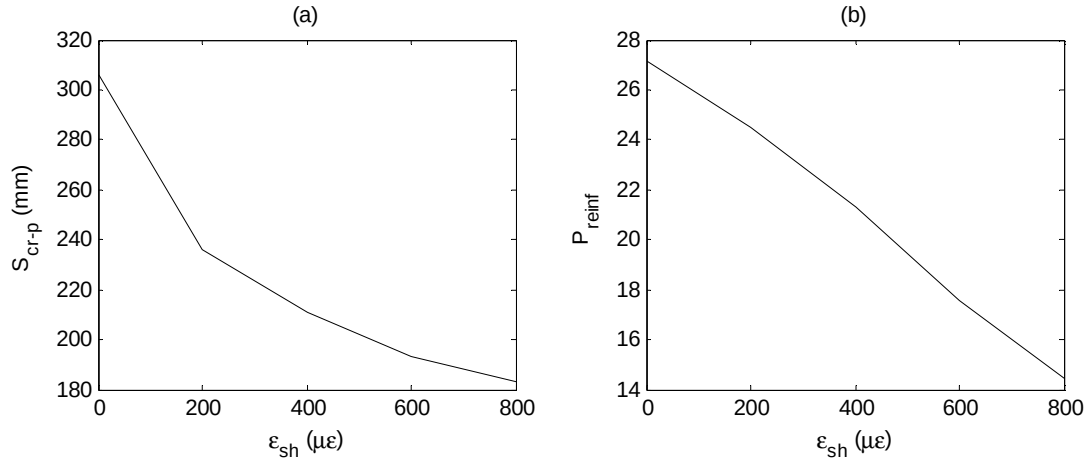

Figure 9: Influence of shrinkage strain on $S_{cr\text{-}p}$

It can be observed in Figure 9 that for increasing shrinkage strains both the crack spacing and the load to cause primary cracking reduces as would be expected. It can be seen in Figure 8

that the change in slip within an element $\delta\Delta_x$ increases with ε_{sh} which means that the rate of change of slip in Figure 6(a) is greater and, therefore, the partial-interaction length which is also the crack spacing $S_{cr\text{-}p}$ is shorter. The reason for the reduced load to cause cracking is that cracking occurs in the full-interaction region as illustrated in Figure 5; this analysis has already shown that δ_c increases with ε_{sh}, that is there is a residual tensile strain and consequently tensile stress prior to the reinforcement being loaded so that the force to cause the reinforcement to increase the stress to the tensile fracture stress is reduced.

The half total length L_T in Figure 6(b) is required in the segmental analysis in Figure 4 and consequently the effect of shrinkage on the total length is important. Shrinkage affects the crack spacing, so to illustrate the effect of shrinkage by itself on the total length let us use the half crack spacing of 153 mm which would occur if there were no shrinkage. Using the tension stiffening analysis for a section with primary cracks as in Figure 6(b) the relationship between the reinforcement force and total length L_T for varying shrinkage strains can be obtained as in Figure 10.

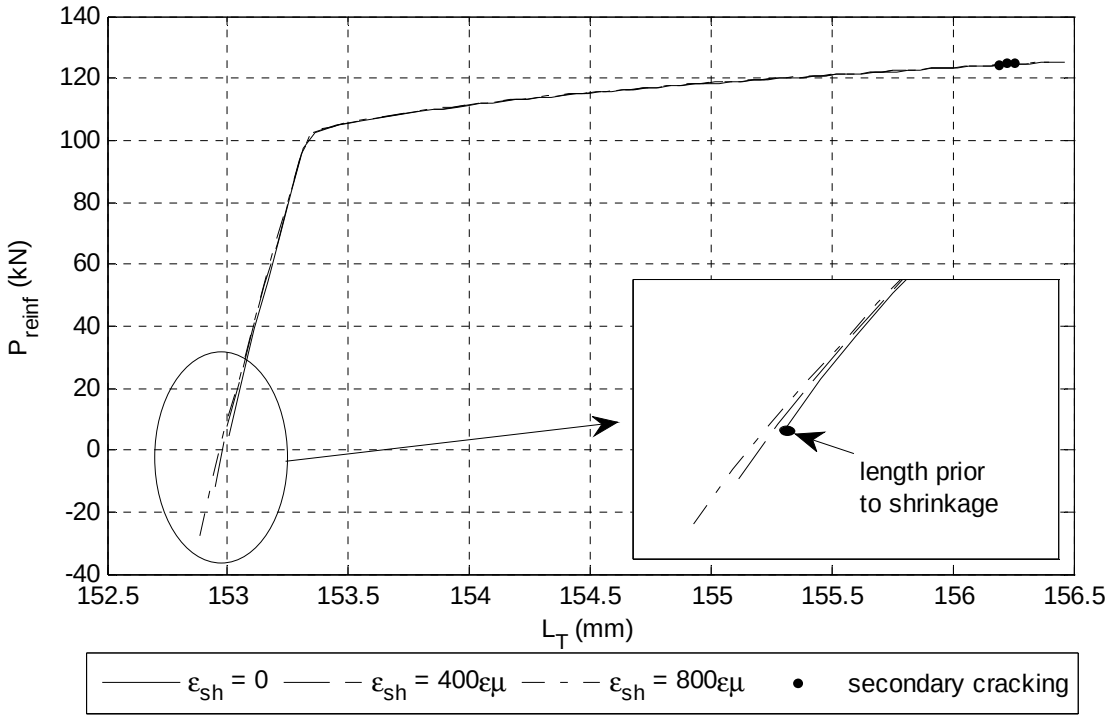

Figure 10: Influence of concrete shrinkage on tension stiffening

It can be seen in Figure 10 that prior to shrinkage, that is, for a shrinkage strain $\varepsilon_{sh} = 0$ the total length of the bar when no load is applied corresponds to half the crack spacing, which in this case is 153mm. For all shrinkage strains, the bar initially shortens as the concrete surrounding it contracts due to shrinkage, and hence, for any shrinkage strain above zero, the reinforcing bar is initially subjected to a contracting strain and a compressive stress. When the bar begins to be pulled at the crack face in Figure 6(b), the average strain over L_T in the

bar remains contracting and the force is compressive. This occurs as initially the load required to induce a small slip Δ in the opposite direction to the contraction due to shrinkage is small, and so the applied load P acts only to reduce the compressive load induced by shrinkage. If the slip Δ is increased, the applied tensile load P must also increase such that it may be tensile. This however does not necessarily mean that the bar is immediately extending, because, although the bar may be extending at the loaded end, the strain induced by the load P reduces over the bars length while the contraction due to shrinkage remains constant, therefore the average strain may be contracting despite a tensile load developing at the loaded end. As the slip Δ is further increased the load P must eventually increase to a level such that the net strain in the reinforcing over the bar length is extending and at this point L_T must be extending, that is L_T is greater than 153 mm in Figure 10. It can be seen that tension-stiffening can be simulated at all stages of loading and even when there is only shrinkage.

The load at which secondary cracking occurs can be determined from the analysis in Figure 6(b). The effect of shrinkage on this load is very small as can be seen in Figure 10. This is because for the large loads at which secondary cracking occurs the L_T/P_{reinf} relationship is essentially independent of the shrinkage strain because the strain in the reinforcement is typically two orders of magnitude larger than the total strain in the concrete.

The effect of concrete creep is illustrated in Figure 11 where ϕ is the creep coefficient in Eq. 9. It can be seen that similar to shrinkage, concrete creep leads to a reduction in both the crack spacing and the load to cause cracking.

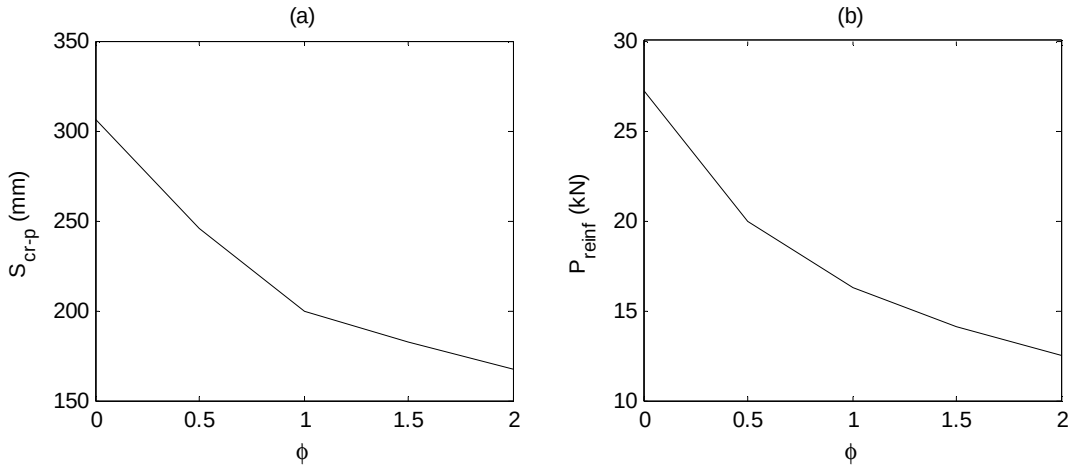

Figure 11: Influence of concrete creep on crack spacing

Although concrete creep influences the crack spacing, if the crack spacing is fixed and the creep coefficient varied, as was done previously for varying shrinkage strains, as shown in Figure 12 the change to the L_T/P_{reinf} relationship is negligible. This is because the strains in

the reinforcement are generally an order of magnitude larger than the strains in the concrete, even in the serviceability range, hence any change to the strain in the concrete due to creep has little influence on the slip strain and hence slip.

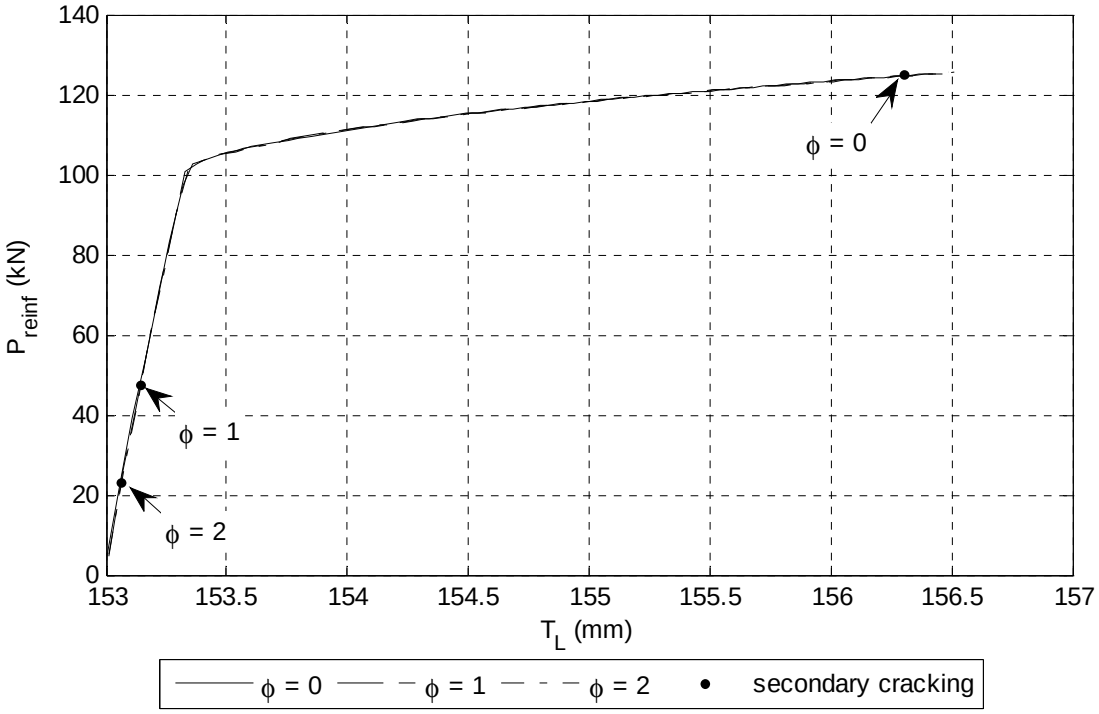

Figure 12: Influence of concrete creep and secondary cracking

Concrete creep does, however, have a significant influence on the secondary cracking behaviour, causing a large reduction in the load to cause secondary cracking as well as the slip at which secondary cracking occurs as shown in Figure 12. This is because the reduction in elastic modulus means the concrete strain to cause a stress builds more rapidly and, hence, the concrete strain exceeds the tensile rupture strain at a lesser load in the reinforcement P and slip Δ in Figure 6(b). Hence creep can increase deflections not just through material flexibility but also through additional cracking.

Sectional properties

Now let us look at the effect of shrinkage and creep individually on the M/θ behaviour of a segment. Figure 13 shows the change in the M/θ, M/χ and M/EI relationships for increasing shrinkage strains where the analysis has been carried out on a beam of concrete strength 30MPa with a width of 250 mm, depth 350 mm and reinforced with 3No. 16 mm steel bars. Firstly consider Figure 13(a) which shows the M/θ relationships. It can be seen that for increasing shrinkage strains the shrinkage rotation θ_{sh}, that is the rotation at zero moment, increases. Prior to cracking, all M/θ relationships have the same slope. Following cracking it can be seen that there is a rapid loss of moment which represents instability of the crack. This

occurs because, as shown in Figure 10, immediately following cracking the reinforcing bar is in compression and the bar is contracting in length. During this period, the total compressive force in the reinforcement must be balanced by tensile forces in the concrete and so large changes in the neutral axis depth and, hence, the location of the tensile lever arm may occur resulting overall in a reduction in moment. Upon further increases in rotation, the crack stabilises as the load in the reinforcing bar becomes tensile and it can be seen that for all shrinkage strains the M/θ relationships are generally parallel to each other. It is also important to note the case of higher shrinkage strains, such as ε_{sh} = 800με in Figure 13(a), that the shrinkage strain is significant enough that shrinkage alone causes the cross section to crack and, hence, the entire M/θ relationship is for a cracked section.

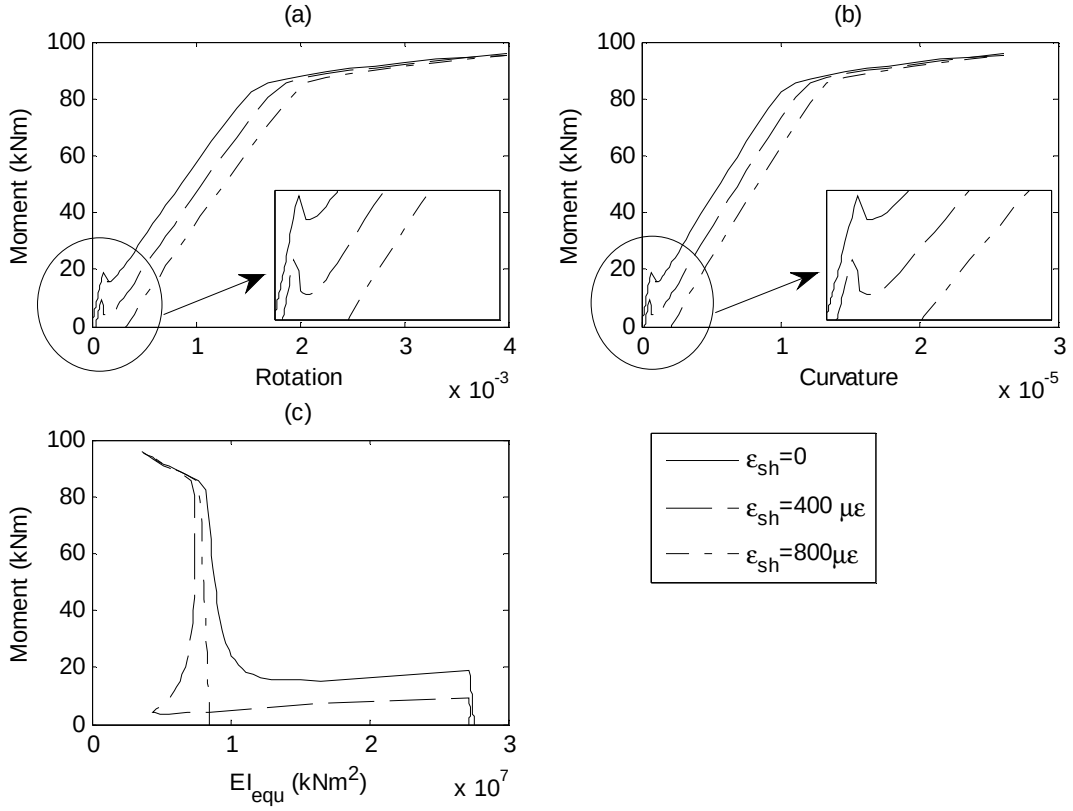

Figure 13: Variation in M/θ, M/χ and M/EI with shrinkage strain

As explained previously, the moment-rotation in Figure 13(a) can be converted to a moment-curvature in Figure 13(b) by dividing by the segment half length which in turn can be converted to equivalent flexural rigidities in Figure 13(c). These are flexural rigidities which give the correct deformational allowing for tensions stiffening and time effects for use in member analyses. Hence the segmental analysis gives the residual curvature χ_{sh} and equivalent flexural rigidity EI_{equ} at a section for a member analysis. The effects of creep are shown in Figure 14 and as can be seen the results can be converted to EI_{equ} for member

analysis. In practice, creep and shrinkage will be applied simultaneously to derive χ_{sh} and EI_{equ} for member analysis

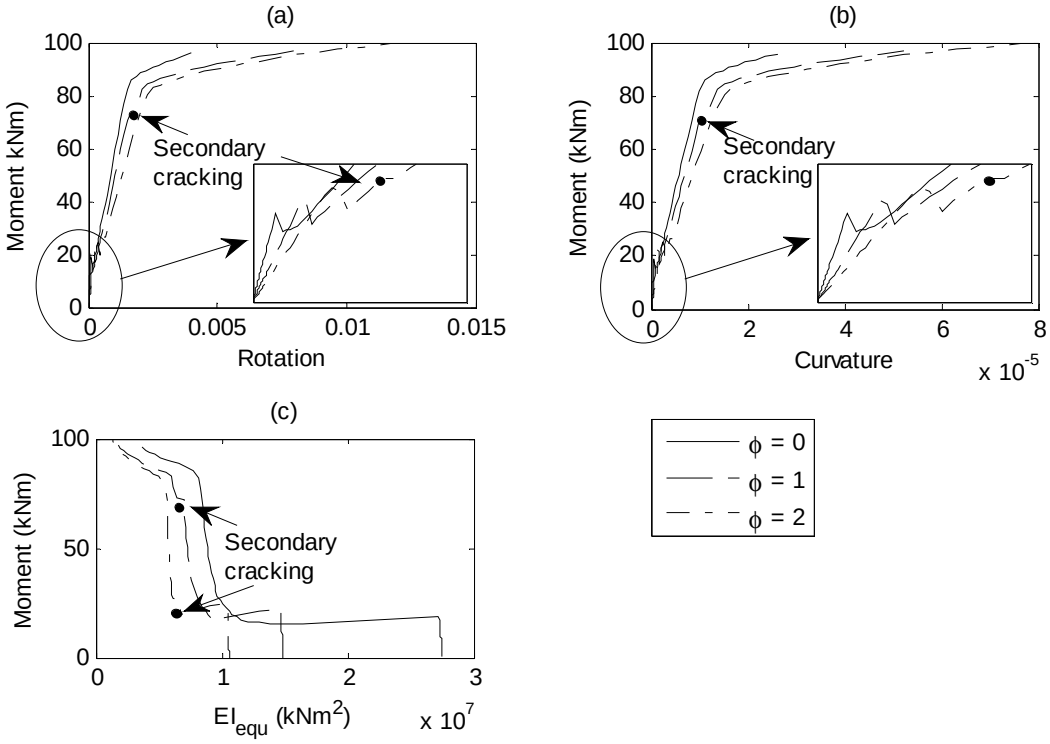

Figure 14: Variation in M/θ, M/χ and M/EI with concrete creep

Beam analysis

Having determined the variation in EI_{equ} with moment as well as the equivalent curvature of the section due to shrinkage alone χ_{sh}, it is now a straightforward procedure to determine member deflection. Consider the simply supported member in Figure 9(a). Prior to the application of any load and due to concrete shrinkage alone, a uniform curvature χ_{sh} as in Figure 15(d) is developed. Upon the application of a sustained point load P in Figure 15(a) the moment distribution in Figure 15(b) is developed and, hence, from the M/EI_{equ} relationship the distribution of EI in Figure 15(c) is also known. Dividing the flexural rigidities in Figure 15(c) by the moments in Figure 15(b) gives the variation in curvature, which must be added to χ_{sh} to give the total curvature profile in Figure 15(d). The variation in curvature can then be integrated to give the member deflection at some point in time and the analysis repeated with a new M/EI_{equ} relationship for each desired point in time. The alternative is to use a finite element package that can cope with variations in EI.

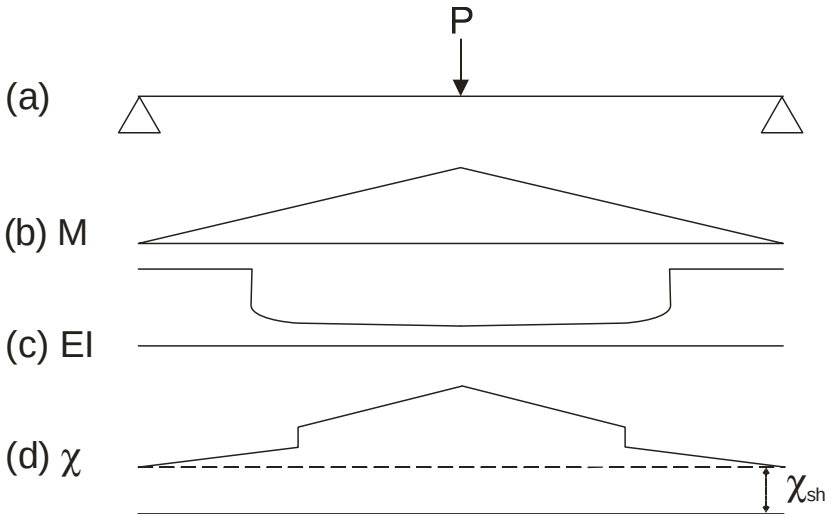

Figure 15: Numerical analysis of beam deflection

The section properties derived above will now be used to show the influence of shrinkage and creep on member deflection up to concrete softening. A beam with a span of 4 m and a single point load that is applied rapidly at mid span has been considered. Significantly, Figure 16 shows considerable increases in member deflection due to concrete shrinkage, particularly in the case of the section subjected to a shrinkage strain of 800με, which is fully cracked occurs prior to the addition of any load.

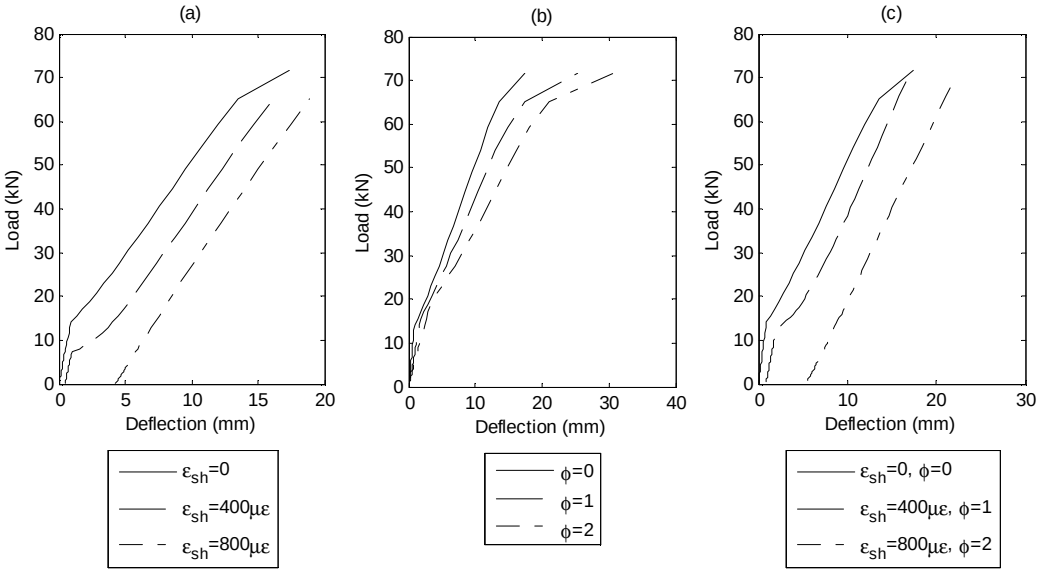

Figure 16: influence of creep and shrinkage on member deflection

It can also be seen in Figure (b) that the additional deflection due to creep increases with applied load. This is in contrast to the case of shrinkage in Figure 16(a) where the increase in deflection was relatively constant over the entire loading range. The deflection due to a combination of creep and shrinkage is also shown in Figure 16(c)

COMPARISON WITH TEST RESULTS

For validation of the M/θ approach on beams, the method has been applied to a series of six beams tested by Gilbert and Nejadi (2008). These beams were simply supported over a span of 3500mm and loaded at the third points for a period of 394 days. Beams B1a and B1b were reinforced with 2No. 16 mm bars with 48 mm cover, beams B2a and B2b were reinforced with 2No. 16 mm bars with 33mm cover and beams B3a and B3B were reinforced with 3No. 16mm bars with 33mm cover. All were all loaded at an age of 14 days when the concrete strength was 18.3MPa which increased to 28MPa by day 28. Specimens B1a and B2a were loaded with 2 point loads of 18.6kN, B2a and B2b with point loads of 11.8kN, beam B3a with point loads of 27.0kN and beam B3b with point loads of 15.2kN. Creep coefficients and shrinkage strains were also determined periodically by testing and can be found in Gilbert and Nejadi (2008).

The PI M/θ approach was used to determine the variations in M/χ and M/EI_{equ} for each cross section in Figure 17 which were used to predict the deflections of the beams in Figure 18. In general it can be seen in Figure 18 that the PI M/θ approach is able to reasonably predict the deflection of the beams over time. Of interest, it can be seen in Figure 18 that the major disparity between the predicted and recorded results come following secondary cracking. It has been shown in Visintin et al. (2012b) that, due to the random nature of cracking, the crack spacing my be greater than the minimum predicted using the partial interaction approach, particularly for members with a constant moment region such as those simulated. In this case, secondary cracking occurs at a reduced moment but the stiffness of the cross section increases, this may mean that in sustained loading analyses as presented here, the deflection may be reduced due to the random nature of crack formation.

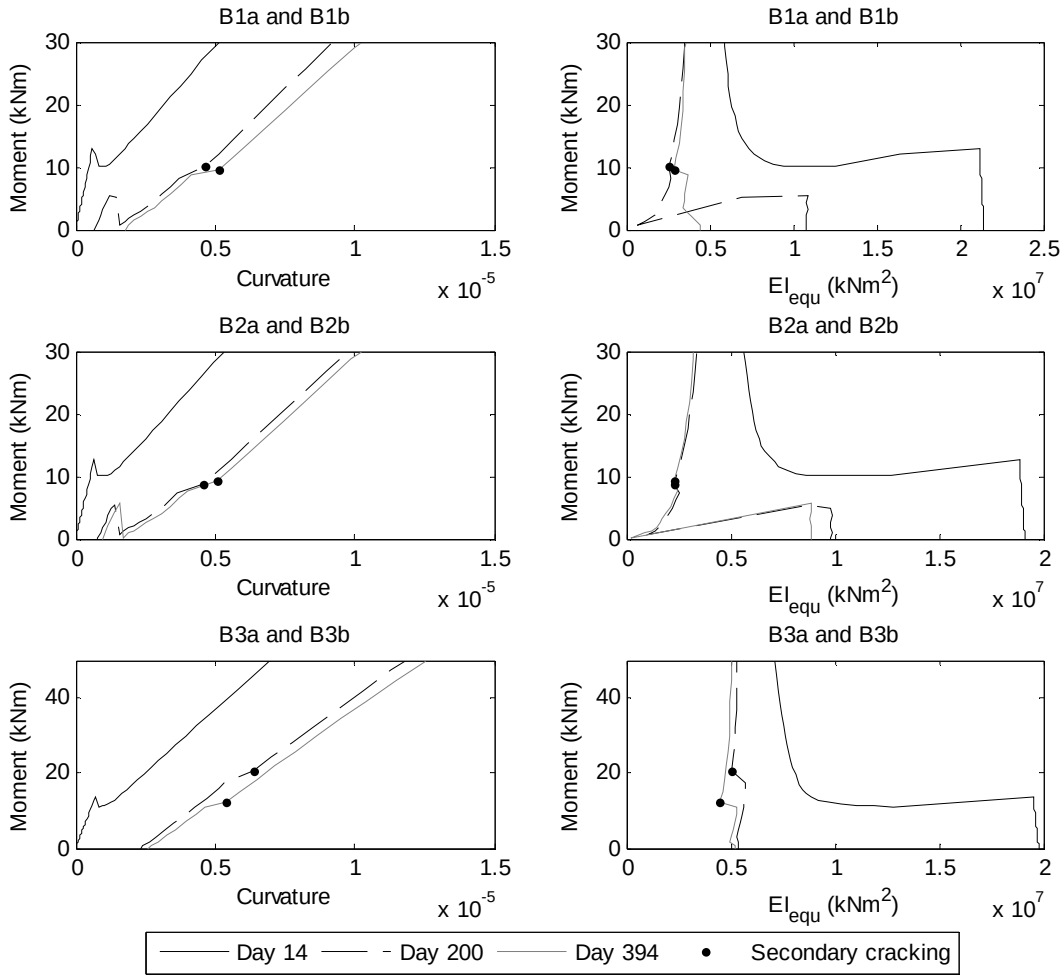

Figure 17: M/χ and M/EI relationships for beams tested by Gilbert and Nejadi (2008)

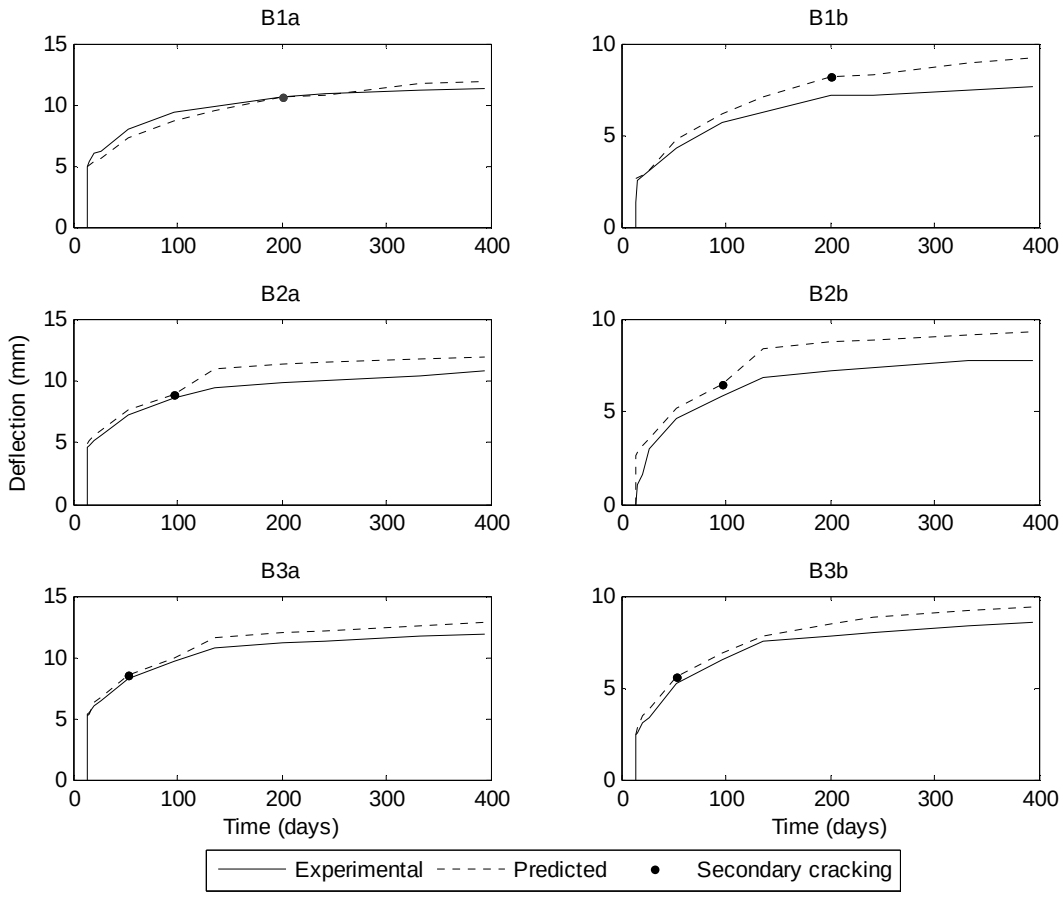

Figure 18: Predicted deflection of beams tested by Gilbert and Nejadi (2008)

Finally and in order to show the influence of concrete shrinkage for a beam subjected to instantaneous loading, the M/θ approach has been compared to a pair of tests carried out by Barris et al. (2009) on FRP reinforced beams under 4 point bending where the loads were applied at 300mm from the centre point. These beams had a span of 1800mm, a depth of 190mm, and were reinforced with 2No. 16mm ribbed GFRP bars with an elastic modulus of 64,153MPa. Beam C-216-D1 had a concrete strength of 56.3MPa, a width of 140mm and cover to the reinforcing of 20mm while beam C-216-D2 had a concrete strength of 61.7MPa a width of 160mm and cover to the reinforcing of 40mm. For each case, the shrinkage strain has been determined according to AS 3600-2009 (Standards Australia 2009) where it has been assumed that the member was loaded to failure on day 28. Figure 19 shows that allowing for shrinkage, member deflection is significantly increased, particularly following cracking, and more closely matches the experimental behaviour.

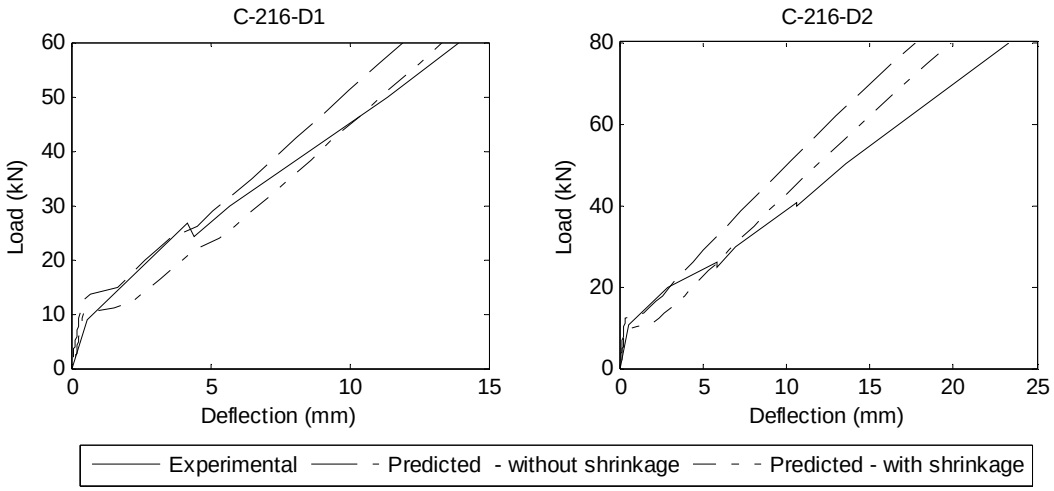

Figure 19: Variation in deflection of instantaneously loaded beams with shrinkage

CONCLUSIONS

A numerical partial-interaction (PI) moment-rotation (M/θ) approach has been developed to quantify the short and long term flexural rigidities (EI_{equ}) of a reinforced concrete beam through mechanics. This PI M/θ approach is versatile as it can cope with cracked and uncracked sections and with the time effects of shrinkage and creep. Prior to cracking this PI M/θ approach gives exactly the same flexural rigidities as a conventional full-interaction (FI) moment-curvature (M/χ) approach. However its strength is in the fact that it can quantify, through the derivation of equivalent flexural rigidities EI_{equ}, the effects of cracking and, in particular, the effects of creep and shrinkage on cracked sections. This is in contrast to the conventional FI M/χ approach which relies on empirically derived flexural rigidities EI_{emp} to allow for cracking and the effects of creep and shrinkage on cracking. In effect the PI M/θ approach replaces the FI M/χ EI_{emp} with mechanics derived EI_{equ}. Hence this PI M/θ approach can be considered to enhance the existing FI M/χ by providing better estimates of the cracked flexural rigidities with creep and shrinkage. This enhancement can be seen by the fact that once the equivalent flexural rigidities have been determined, the analysis procedure of the member is exactly the same as in a conventional FI M/χ approach.

ACKNOWLEDGEMENTS

The financial support of the Australian research Council ARC Linkage Project LP 0883451 “Blast resistance of flexural high performance concrete members’ and ARC Discovery project DP0985828 ‘A unified reinforced concrete model for flexure and shear’ are gratefully acknowledged.

REFERENCES

American Concrete Institute (ACI). (1982). “Prediction of creep, shrinkage and temperature effects in concrete structures.” ACI-209R-82, ACI Committee 209, Detroit.

Bachmann, H. (1970). “Influence of shear and bond on rotational capacity of reinforced concrete beams.” Publications, IABSE, Zurich,: Vol. 30, Part II, 11-28.

Bazant, Z.P. (1972). “Prediction of Concrete Creep Effects using Age-Adjusted Effective Modulus Method”, ACI Journal, 69, April 1972, pp323-217.

Bazant, Z.P., and Panula, L. (1979). “Practical prediction of time-dependent deformations of concrte. Part I. Materials and Structures. 11, 307-316.

Bazant, Z.P., and Panula, L. (1979). “Practical prediction of time-dependent deformations of concrte. Part II. Materials and Structures. 11, 317-328.

Bazant, Z.P., and Panula, L. (1979). “Practical prediction of time-dependent deformations of concrte. Part III. Materials and Structures. 11, 425-434.

Birkeland PW and Birkeland HW. Connections in Precast Concrete Construction, ACI Journal Proceedings 1966; 63 (3): 345-368.

Branson, D.E. (1977). Deformation of Concrete Structures. McGraw Hill.

Bresler, B and Selna, L. (1964). “Analysis of Time Dependent Behaviour of Reinforced Concrete Structures”, Symposium of Creep in Concrete, ACI Special Publication SP-9, No.5, pp115-128.

CEB-FIP. (1994) CEB-FIP model code 1990: Design code 1994, Thomas Telford, London.

Eurocode 2, Design of concrete structures – Part 1-1: General rules and rules for buildings. CEN, European Committee for Standardization, EN 1992-1-1:2004

Faber, O. (1927). “Plastic Yield, Shrinkage and Other Problems of Concrete and their Effects on Design.” Minutes of the Proceedings of the Institute of Civil Engineers, 225, Part I, pp 27-73. London.

Gardner, N. J., and Lockman M. J. (2001). “Design Provisions for drying shrinkage and creep of normal-strength concrete.” ACI Materials Journal, 98(2), 159-167.

Ghali, A., Nevile, A.M. and Jha, P.C., “Effect of Elastic and Creep Recoveries of Concrete on Loss of Pretress”, ACI Journal, 64, 1967 pp802-810.

Gilbert, R.I. (1988). “Time Effects in Concrete Structures”, Elsevier Science Publishers B.V., The Netherlands.

Gilbert, R.I., and Nejadi, S. “An experimental study of flexural cracking in reinforced concrete” Australasian Structural Engineering conference June 2008, Melbourne Australia.

Gilbert R.I., Ranzi, G. (2011). “Time-dependent behaviour of concrete structures” Spoon Press.

Goel, R., Kumar, R., Paul, D.K. (2007) “Comparative Study of Various Creep and Shrinkage Prediction Models for Concrete”, ASCE Journal of Materials in Civil Engineering 19(3) pp249-260.

Hognestad ,E., Hanson, N.W., McHenry, D., Concrete stress distribution in ultimate strength design, Journal of ACI 27(4) (1955) 455-479.

Haskett M, Oehlers DJ, Mohamed Ali MS. Local and global bond characteristics of steel reinforcing bars. *Engineering Structures* 2008; 30 (2): 376-383.

Haskett M, Oehlers DJ, Mohamed Ali MS, and Sharma SK. The shear-friction aggregate interlock resistance across sliding planes in concrete”, Magazine of Concrete Research 2010; 62
(12): 907-924.

Haskett M, Oehlers DJ, Mohamed Ali MS, and Sharma SK. Evaluating the shear-friction resistance across sliding planes in concrete”, Engineering Structures 2011; 33:1357-1364.

Hofbeck JA, Ibrahim IO, and Mattock AH. Shear Transfer in Reinforced Concrete, ACI Journal Proceedings 1969; 66 (2): 119-128.

Mansur MA, Vinayagam T, and Tan KH. Shear transfer across a crack in reinforced high strength concrete”, Journal of Materials in Civil Engineering 2008; 20 (4): 294-302.

Mohamed Ali, M. S., Oehlers, D. J., Griffith, M. C., and Seracino, R. (2008a) “Interfacial stress transfer of near surface mounted FRP-to-concrete joints.” *Engineering Structures*, 30(7), 1861-1868.

Mohamed Ali, M.S., Oehlers, D.J., Griffith, M.C. (2008b) “Shear transfer across cracks in FRP strengthened RC structures”, ASCE Journal of Composites in Construction 12(4) 416-424.

Muhamad R., Mohamed Ali, M. S., Oehlers, D. J., and Griffith, M. C. (2011). “The tension stiffening mechanism in reinforced concrete prisms.” Accepted *Advances in Structural Engineering*.

Neville, A.M., Dilger, W.H. and Brooks, J.J. (1983) “Creep of Plane and Structural Concrete Structures”, Construction Press Longman Group Ltd.

Oehlers, D. J., Liu, I. S. T., and Seracino, R. (2005). “The gradual formation of hinges throughout reinforced concrete beams.” *Mechanics Based Design of Structures and Machines*, 33(3-4), 375-400.

Oehlers, D.J., Mohamed Ali, M.S., Haskett, M., Lucas, W., Muhamad, R. Visintin, P., (2011). “FRP reinforced concrete beams - a unified approach based on IC theory”, ASCE Composites for Construction 2011 15(3) 293-303.

RELIM TC-107GCS. (1995a) “Creep and shrinkage prediction models for analysis and design of concrete structures – Model B3.” Materials and Structures, 28, 357-365.

RELIM TC-107GCS. (1995b) “Errata: Creep and shrinkage prediction models for analysis and design of concrete structures – Model B3.” Materials and Structures, 29, 126.

Standards Australia (2009). “AS 3600-2009 Concrete Structures”

Tasdemir, M.A., Tasdemir, C., Akyuz, S., Jefferson, A.D., Lydon, F.D., and Barr, B.I.G., Evaluation of Strains at Peak Stresses in Concrete: A Three-Phase Composite Model Approach”, *Cement and Concrete Composites*, 20 (4) (1998) 301-318.

Yuan H, Teng JG, Seracino R, Wu ZS, Yao J. Full-range behavior of FRP-to-concrete bonded joints, *Engineering Structures* 2004; 26 (5): 543-691.

Westerberg, B. (2008) “Time-dependent effects in the analysis and design of slender concrete compression members” Doctoral Thesis.

Whitney, C.S. (1932). “Plain and Reinforced Concrete Arches”, ACI Journal, 28, pp479-519.

Visintin, P. Oehlers, D.J., Wu, C. and Haskett, M. (2012a) “A Mechanics Solution for Hinges in RC Beams with Multiple Cracks” *Engineering Structures*, 36 March, 61-69.

Visintin, P., Oehlers, D.J. Muhamad, R. and Wu, C. (2012b) “Partial-interaction short term serviceability deflection of FRP RC beams” Submitted to *Engineering Structures*.

Statement of Authorship

Partial-interaction short term serviceability deflection of FRP RC beams
Engineering Structures: submitted paper

Visintin, P. (candidate)

Prepared manuscript, performed all analyses, and developed model and theory.

I hereby certify that the statement of contribution is accurate
Signed……..Date……

Oehlers, D.J.

Supervised research, provided critical manuscript evaluation and acted as corresponding author.

I hereby certify that the statement of contribution is accurate and I give permission for the inclusion of the paper in the thesis
Signed…….Date……

Muhamad, R.

Assisted in manuscript evaluation.

I hereby certify that the statement of contribution is accurate and I give permission for the inclusion of the paper in the thesis

Signed… ……..Date……..

Wu, C.

Assisted in manuscript evaluation.

I hereby certify that the statement of contribution is accurate and I give permission for the inclusion of the paper in the thesis

Signed …….Date……

Partial-interaction short term serviceability deflection of FRP RC beams

Visintin, P., Oehlers, D.J. Muhamad, R. and Wu, C.

ABSTRACT

A widely accepted approach for quantifying the serviceability short term deflection of RC beams is to use some combination of the flexural rigidities of the uncracked ($EI_{fi\text{-}uncr}$) and cracked ($EI_{fi\text{-}cr}$) sections that are obtained from a full-interaction analysis of transformed sections; a full-interaction analysis implies that there is no slip between the reinforcement and concrete. The combination of $EI_{fi\text{-}uncr}$ and $EI_{fi\text{-}cr,}$ that is the effective flexural rigidity (EI_{eff}) to be used for calculating the deflection, has to be determined purely from testing. In this paper partial-interaction theory, which allows for slip between the reinforcement and concrete and consequently the bond-slip characteristics, is used to determine the partial-interaction flexural rigidity of a cracked section ($EI_{pi\text{-}cr}$). It is shown that: by replacing the cracked section $EI_{fi\text{-}cr}$ with $EI_{pi\text{-}cr}$ obviates the need to determine EI_{eff} directly from testing; the replacement of $EI_{fi\text{-}cr}$ by $EI_{pi\text{-}cr}$ allows closed form solutions to be derived for EI_{eff} and also allows for the distinction between the formation of primary and secondary cracks. The partial interaction approach also provides a way of determining, through mechanics, the minimum crack spacing and hence can be used to study the random component of cracking and its influence on member deflection. The partial-interaction flexural rigidity should be a convenient tool for not only refining existing deflection procedures but also for quantifying the deflection of RC beams with new types of reinforcement and new types of bond, in particular those associated with FRP reinforced members.

LIST OF SYMBOLS

a – Distance from support to the location of a point load
A_c – Area of concrete which interacts with reinforcement in a PI analysis
A_r – Total area of reinforcement in the tension region
B – Bond force
b – Width of the section
c – Cover to the centre of reinforcement
d – Depth of the section
$d_{cr\text{-}p}$ – Primary crack height
$d_{cr\text{-}s}$ –Secondary crack height
ds/dx – Slip strain
E_c – Elastic modulus of concrete
EI – Flexural rigidity
EI_{cr} – Cracked EI
EI_{eff} – Effective EI for a member
$EI_{fi\text{-}uncr}$ – Uncracked EI from a FI analysis

$EI_{fi\text{-}cr}$ – Cracked EI derived from a FI analysis
$EI_{pi\text{-}cr}$ – Cracked EI from a PI analysis
$EI_{pi\text{-}p}$– Cracked EI from a PI analysis for primary cracking
$EI_{pi\text{-}s}$– Cracked EI from a PI analysis for secondary cracking
E_r – Elastic modulus of reinforcement
f_c –Peak concrete stress
FI – Full interaction
$I_{fi\text{-}cr}$ - Cracked moment of inertia from a FI analysis
$I_{fi\text{-}uncr}$ – Uncracked moment of inertia from a FI analysis
K_e – Bond stiffness
L_{bd} – Length of concrete prism to FI boundary condition
L_{def} – Deformation length
L_p – Total perimeter of all reinforcing bars
L_s - Segment length for numerical PI analysis
M – Applied moment
M_{cr} – Moment to cause, taken as the minimum of that from a FI or PI analysis
$M_{cr\text{-}p}$ – Primary cracking moment from PI analysis
$M_{cr\text{-}s}$ –Secondary cracking moment from PI analysis
$M_{fi\text{-}cr}$ –FI cracking moment
M_{seg} – Moment applied to a segment of a member
P – Applied load
P_{conc} – Force developed in the concrete in compression
$P_{conc\text{-}tens}$ – Force developed in the concrete in tension
PI – Partial interaction
P_r – Force in the reinforcing bar in the numerical PI model
P_{reinf} - Force developed in reinforcing bar at crack face
$P_{reinf\text{-}cr\text{-}p}$ – Force in reinforcement to cause primary cracking
$P_{reinf\text{-}cr\text{-}s}$ – Force in reinforcement to cause secondary cracking
x_{uncr} – Uncracked length of member
$x_{cr\text{-}p}$ – Length of member with primary cracks
$x_{cr\text{-}s}$ – Length of member with primary and secondary cracks
y – Member deflection
y_{uncr} - Deflection of uncracked member
$y_{pi\text{-}p}$ - Deflection of member with primary cracks
$y_{pi\text{-}s}$ - Deflection of member with primary and secondary cracks
$S_{cr\text{-}p}$ – Primary crack spacing

β – Geometric constant
$\chi_{pi\text{-}p}$ – Curvature from PI analysis following primary cracking
$\chi_{pi\text{-}s}$ – Curvature from PI analysis following secondary cracking

Δ – Slip of reinforcing bar in a segment from the numerical PI model
Δ_{reinf} –slip of the reinforcement form the crack face
$\delta\Delta$ – Change in slip of the reinforcement over a segment
δ_{conc} –Deformation of concrete
δ – Local interface slip
δ_1 – interface slip at τ_{max}
ε_c – Concrete strain
ε_{pk} – Strain at f_c
ε_r – Reinforcement strain
λ – Bond stiffness constant
τ – Bond stress
τ_{max} – Maximum bond stress
θ – Rotation
$\theta_{pi\text{-}p}$ – Rotation from PI analysis following primary cracking
$\theta_{pi\text{-}s}$ – Rotation from PI analysis following secondary cracking

INTRODUCTION

The design of members for serviceability deflections has become increasingly important in recent years as the use of new higher strength materials has led to a decrease in both member depth and reinforcement ratio. Traditional analysis techniques for determining the short term deflection of steel reinforced members can be split into two categories: those in which an effective flexural rigidity (EI_{eff}) is used in conjunction with an elastic deflection equation [1-10]; and those in which the curvature is integrated to determine the distribution of deflection along a member's length [11-14]. Most design codes currently use the following effective moment of inertia originally proposed by [1]

$$I_{eff} = I_{uncr-fi}\left(\frac{M_{cr}}{M}\right)^3 + I_{fi-cr}\left[1-\left(\frac{M_{cr}}{M}\right)^3\right];\ \ I_{eff} \le I_{uncr-fi} \tag{1}$$

which was calibrated empirically and represents the transition from the transformed uncracked moment of inertia ($I_{fi\text{-}uncr}$) to the transformed cracked moment of inertia ($I_{fi\text{-}cr}$) for the applied moment M following cracking which takes place at $M_{cr.}$

Branson's equation typically provides a reasonable estimate of deflection when used within the bounds of the experimental results from which it was calibrated. However outside this range its application can lead to significant discrepancies between the predicted deflection and that seen in practice. Branson's equation tends to under predict deflections for low reinforcement ratios because tension stiffening is overestimated and, therefore, so too is EI_{eff}. The problem of over prediction of tension stiffening becomes particularly apparent when Branson's equation is applied to FRP reinforced members which, due to the high strength of

the bars, are generally lightly reinforced, and because of the low elasticity of the bars have low member stiffness [2].

Much research, most recently by the FRP community, has been devoted to developing a new approach to determining service deflections by either adapting or replacing Branson's equation [2-10] or by proposing methods to simply integrate member curvature [11-14]. These approaches have had varied success and typically are not applicable to a wide range of member type and reinforcement ratio, and the vast majority cannot be applied to both steel and FRP reinforced members.

In this paper, a partial-interaction (PI) moment-rotation (M/θ) approach is outlined which is based on the Euler-Bernoulli principal of plane sections remaining plane, but not directly on the corollary of a linear strain profile [15]. This M/θ approach uses the well defined mechanics of partial-interaction theory [16-28] to simulate the slip between the reinforcement and the surrounding concrete and hence, through mechanics, allows for the formation and widening of primary and secondary cracks. This approach can, therefore, quantify serviceability behaviour without the need for empirically derived effective flexural rigidities EI_{eff}. Moreover, this approach is applicable to any type of member, with any type of reinforcement and with any type of bond-slip characteristic and, consequently, is ideally suited for FRP reinforcement where these characteristics can vary widely.

In the following, the PI M/θ approach is firstly developed numerically for a segment of a beam and it is shown how this M/θ relationship can be used to give a mechanics based flexural rigidities which account for the partial interaction behaviour of the reinforcement ($EI_{pi\text{-}cr}$). It will then be shown that the numerical approach can be simplified into closed form solutions to give the cracked flexural rigidity of a segment for both primary ($EI_{pi\text{-}p}$) and secondary ($EI_{pi\text{-}s}$) cracking. The flexural rigidities of the uncracked ($EI_{fi\text{-}uncr}$) and cracked ($EI_{pi\text{-}cr}$) segments are then used to derive the deflection of an entire member. The deflections predicted using the closed form solutions are finally compared to experimental results for both FRP and steel reinforced sections. It should be noted that the influence of creep and shrinkage is not considered here, but can be included in the numerical approach as in Visintin et al [29].

SEGMENTAL M/θ NUMERICAL ANALYSIS

The PI M/θ analysis [15] is illustrated in Fig. 1(b), for a beam with the cross-section in Fig. 1(a). For analysis, a segment of the beam of length $2L_{def}$, is subjected to a constant moment M_{seg} which causes the ends of the segment to rotate by θ from A-A to B-B. By symmetry, C-C at mid-way can be considered to be stationary, such that imposed deformations shown shaded are measured relative to C-C. As the behaviour to the left of C-C is identical to that to

the right it is only necessary to consider one half of the segment of length L_{def}. Let us first consider the behaviour prior to concrete cracking.

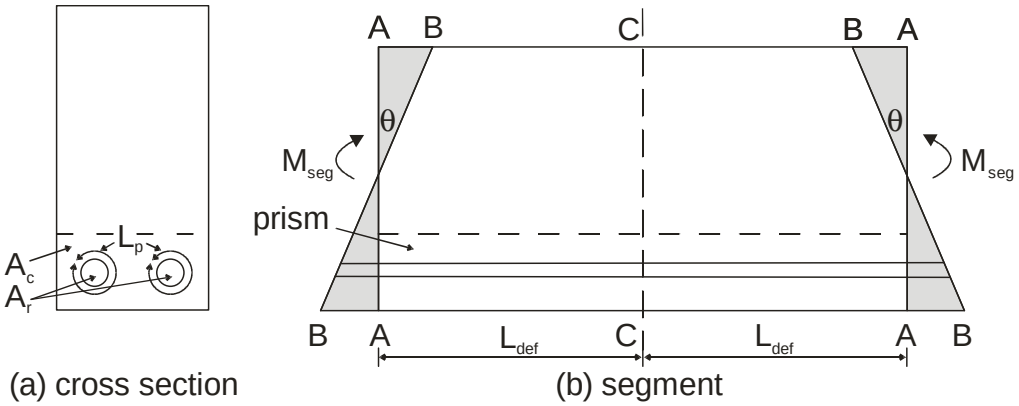

Figure 1: M/θ analysis

Prior to cracking

The left half of the segment in Fig. 1(b) is shown in Fig. 2(a). The segment end A-A is rotated by θ to B-B. The deformation B-B, such as δ_{conc}, can be converted into a strain profile, shown in Fig. 2(b), by dividing by the deformation length L_{def}. Since the section is uncracked these strain are real strains, that is, they would be measured by strain gauges placed on the member. Knowing the distribution of strain in the segment, and because all the strains are real strains, the distribution of stress in Fig. 2(c) can be determined using any conventional material stress-strain relationship giving the internal forces in Fig. 2(d).

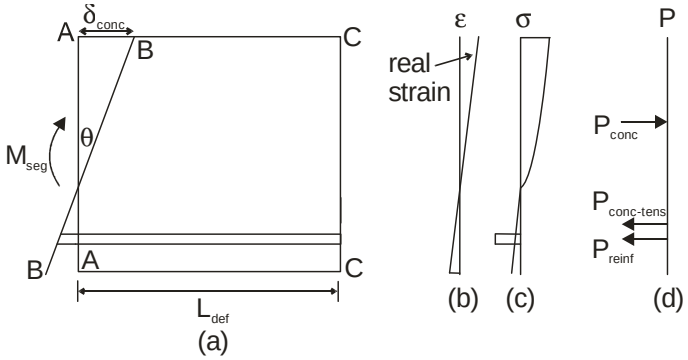

Figure 2: Uncracked segment for M/θ analysis

Having determined the internal forces in Fig. 2(d), the maximum displacement of the concrete δ_{conc} can be varied for a fixed value of θ, effectively adjusting the neutral axis depth until internal equilibrium is achieved. This analysis gives a single point on the M/θ relationship, between O and A in Fig. 3(a) and is repeated for increasing rotations until a

crack develops when the maximum tensile strain in the concrete reaches the tensile cracking strain, and the crack tip reaches the tensile reinforcement.

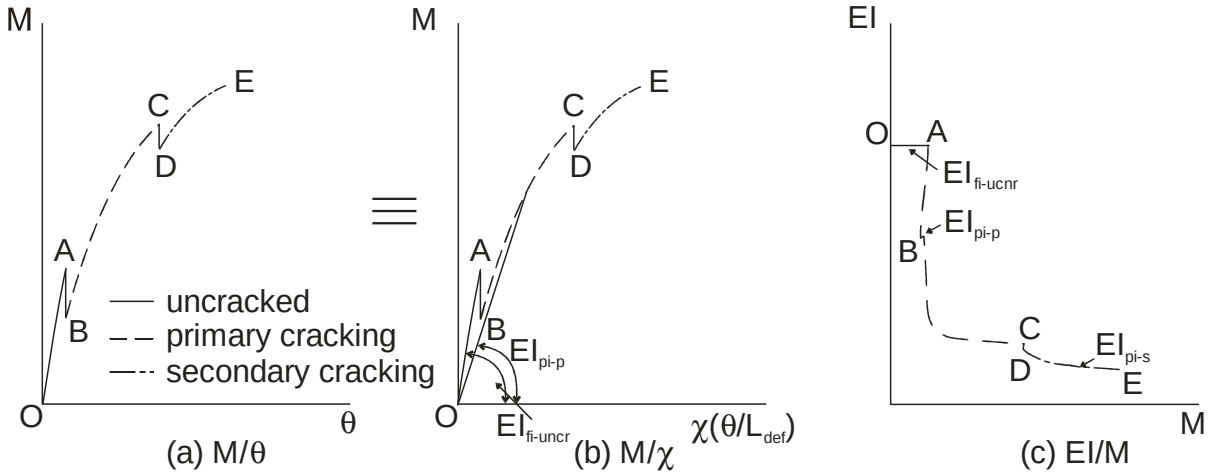

Figure 3: Equivalent M/χ and EI

The moment-rotation relationship in Fig. 3(a) can be converted into the moment-curvature (M/χ) relationship in Fig. 3(b) by dividing by the deformation length L_{def}. At the uncracked stage, the result obtained form this M/θ analysis and a traditional M/χ analysis are identical. The deformation length L_{def} used in the analysis is, therefore, irrelevant as any length will give the same M/χ. Furthermore, as both approaches are identical so too are the uncracked flexural rigidities ($EI_{fi\text{-}uncr}$), as shown in Fig. 3(c) which could also be obtained from the traditional transformed section approach. It is important to emphasise that both approaches are identical for uncracked segments, because, at the uncracked stage a traditional M/χ analysis does not rely on empirically derived factors for the model, such as those required to determine deflections in cracked members. Hence, the M/θ analysis conducted on a segment subjected to a constant moment can be used to determine the flexural rigidity of the cross section, which can in turn be used to determine the deflection of the member for any moment distribution.

Accommodating cracking

Now consider the case shown in Fig. 4(a) where the moment M_{seg} has increased to a level which causes the crack tip to intercept the reinforcing bar. Partial interaction theory must be used to describe the behaviour of the reinforcing bars because the load developed is now dependent on the slip of the bar at the crack face Δ_{reinf}, which in turn depends on the bond-slip (τ/δ) properties between the bar and the concrete surrounding it.

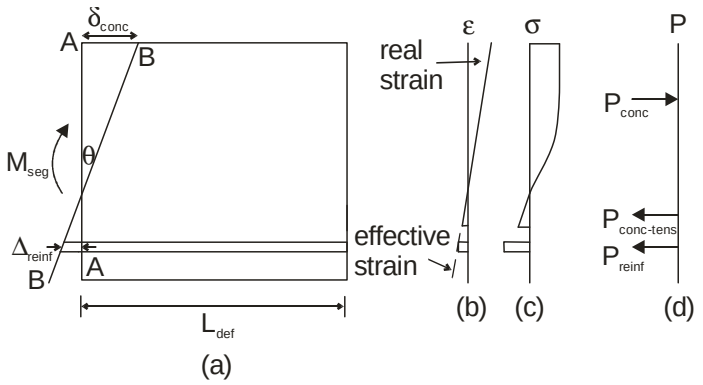

Figure 4: Cracked segment for M/θ analysis

The partial-interaction load-slip behaviour can be determined through the application of a well established partial interaction analysis technique [23,30] by considering the behaviour of reinforcement of total area A_r embedded with a total perimeter L_p in a prism of total area A_c as in Fig. 1(a) along the length of the member as in Fig. 1(b). The analysis is depicted in Fig. 5 where the prism in Fig. 1(b) is broken into elements of length L_s in Fig. 5 which are deliberately very small so that the slip along L_s can be assumed to be uniform. It is now a question of finding the relationship at the crack face, that is, at the left face of Element 1, between the reinforcement force P_{r1} and the slip at the crack face Δ_1.

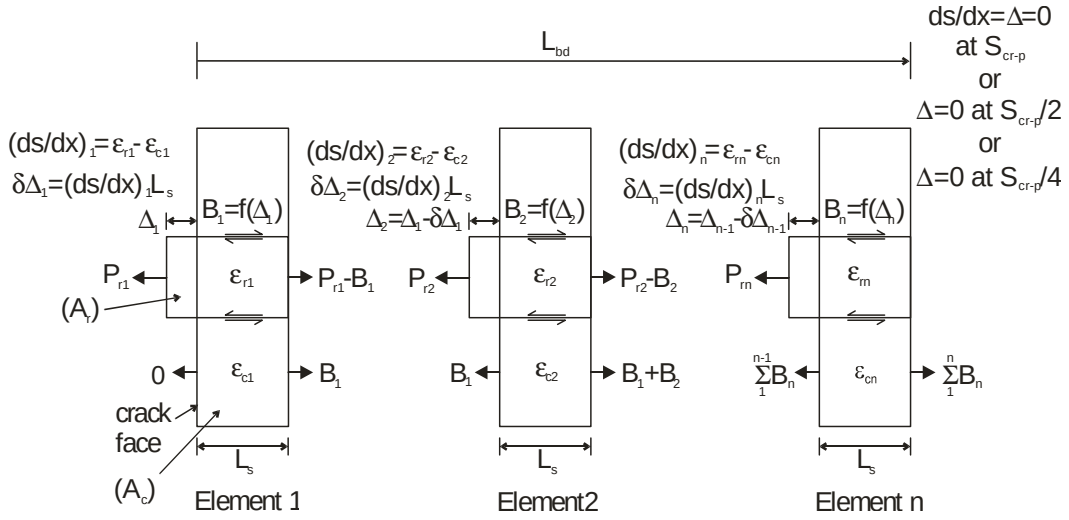

Figure 5: Partial interaction numerical approach

As an example under displacement control, the crack face slip Δ_1 in Fig. 5 could be fixed and the force in the reinforcement P_{r1} guessed. As the displacement of the bar Δ_1 has been set, the bond force in the first element B_1 can be determined from the known bond slip (τ-δ) properties, that is B_1 is equal to $L_pL_s\tau$ where τ depends on Δ_1 which have been defined for

both steel and FRP bars [31-33]. Hence, the force in the reinforcement in Element 1 varies from P_{r1} to P_{r1}-B_1, such that the mean stress, and consequently strain ε_{r1} can be determined. Furthermore, the force in the concrete in Element 1 varies from zero on the left side to B_1 on the right, so the mean strain in the concrete ε_{c1} can also be determined. The slip-strain in Element 1 $(ds/dx)_1$ is the algebraic difference in strain between that of the reinforcement and the concrete ε_{r1}-ε_{c1}, and the change in slip over Element 1, $\delta\Delta_1$, is the integration of the slip-strain over L_s, that is, $(\varepsilon_{r1}$-$\varepsilon_{c1})L_s$. Hence, both the slip and slip-strain in Element 1 are known. The analysis can then be repeated for Element 2 in which, on the left hand side, the force in the reinforcing bar P_{r2} is P_{r1}-B_1 and the force in the concrete P_{c2} is B_1. Furthermore, the slip of the reinforcement Δ_2 is Δ_1-$\delta\Delta_1$, from which the bond force B_2 can be derived. The analysis can then be repeated over subsequent elements to give the variation is slip Δ and slip strain ds/dx, and the initial guess for P_{r1} adjusted until a known boundary condition is achieved as explained below.

The partial interaction analysis depicted in Fig. 5 can be used to determine the primary crack spacing $S_{cr\text{-}p}$ because primary cracks form where the full interaction boundary conditions are met, that is, the slip-strain (ds/dx) and the slip Δ tend to zero at the same position. This corresponds to the length L_{bd} in Fig. 5. It is also important to note that this approach produces the minimum crack spacing as it is assumed that a varying moment distribution exists over the prism length. However it is possible to apply any desired crack spacing when carrying out the M/θ analysis.

The same analysis procedure is also employed to provide a relationship between the slip of the reinforcement Δ_{reinf} in Fig. 4(a) and the load developed P_{reinf} in the reinforcement in Fig. 4(d). In this case, L_{def} in Fig. 1(b) is $S_{cr\text{-}p}/2$ so that in Fig. 5 the boundary condition at L_{bd} from the crack face is now $\Delta = 0$ at $S_{cr\text{-}p}/2$ as shown. This analysis in turn can be used to predict the load at which secondary cracks form, that is, when the strain in the concrete at $S_{cr\text{-}p}/4$ equals the cracking strain. Similarly when the partial interaction analysis is carried out with the boundary condition that the slip of the bar $\Delta = 0$ at $S_{cr\text{-}p}/4$, then the tension stiffening (P/Δ) behaviour of the secondary cracks is given. It should also be noted that although debonding has not been considered here, as we are dealing with a serviceability limit, debonding of FRP bars can occur due to the high bond stiffness compared to ribbed steel bars. Debonding is more likely to occur following secondary cracking as for a given slip of the bar the total bond force must be higher in order to reach the boundary condition of $\Delta = 0$ over the length $S_{cr}/4$ instead of over $S_{cr}/2$ which is the case for primary cracking.

Having derived the partial interaction behaviour of the reinforcing bars, the analysis of the cracked segment in Fig. 4(a) can proceed in the same manner as that for the uncracked segment. The applied moment M_{seg} causes a change in deformation from A-A to B-B with a rotation θ. This deformation profile can be converted to a strain profile, shown in Fig. 4(b), by dividing by the deformation length L_{def}, which in the case of the cracked segment must be equal to half the primary crack spacing, that is, $S_{cr\text{-}p}/2$. In the compressive and uncracked

tension regions, the strains are real strains and, therefore, the stresses in Fig. 4(c) and internal forces in Fig. 4(d) can be determined through the application of any appropriate stress-strain relationship. In the cracked tension region, the slip of the reinforcement Δ_{reinf} can be determined from simple geometry, and for the given slip, the load developed determined through the application of the partial-interaction theory described above and illustrated in Fig. 5. Knowing all the internal forces, the maximum deformation in the concrete can again be adjusted until internal equilibrium is achieved.

The above analysis gives a single point on the M/θ relationship in Fig. 3(a) and must be repeated for increasing rotations to generate the curve B-C. If secondary cracking takes place the same analysis procedure is followed, but the deformation length L_{def} is equal to $S_{cr\text{-}p}/4$ and the partial-interaction load slip behaviour of the bar must be obtained using the boundary conditions for secondary cracking. This analysis gives the M/θ relationship in Fig. 3(a) from point D-E. The cracked segment analysis can be applied until the maximum strain in the concrete reaches the strain ε_{pk} at the peak stress f_c. As the purpose of this paper is to derive closed form solutions to describe serviceability behaviour, concrete softening will not be considered. However a numerical model which accounts for concrete softening using shear friction theory can be found in Visintin et al. (2012a).

Again it is possible to convert the M/θ relationship into an equivalent M/χ relationship, as in Fig. 3(b), by dividing the rotations by the deformation length L_{def}. Importantly, this M/χ relationship derived from a M/θ analysis is not the same as those obtained from a standard M/χ analysis. This is because when cracked, the M/θ approach produces an equivalent curvature which simulates the cracking processes seen in practice, that is, using the mechanics of partial- interaction theory, the slip of the reinforcing relative to the concrete which is responsible for both concrete cracking and crack widening is simulated. Thus the M/θ approach can be used to derive equivalent flexural rigidities for primary $EI_{pi\text{-}p}$ and secondary $EI_{pi\text{-}s}$ cracking, as in Fig. 3(c), which are different from the cracked flexural rigidity $EI_{fi\text{-}cr}$ found using typical approaches such as transformed sections which assumes full interaction.

Having described the PI M/θ approach for a segment using a numerical approach, we will now consider how, by assuming that at serviceability material properties remain linear-elastic, a closed form approach can be constructed.

SEGMENTAL M/θ CLOSED FORM SOLUTIONS

As it has been established that the behaviour predicted by the M/θ and traditional M/χ analyses are identical prior to cracking, the uncracked flexural rigidity determined using transformed sections ($EI_{fi\text{-}uncr}$) can be used in a mechanics based determination of deflections prior to cracking. However, after cracking, as illustrated in the segment in Fig. 6, partial-interaction behaviour as illustrated by Fig. 5, needs to be used in order to simulate the

mechanics of crack formation and widening because the reinforcement slips relative to the concrete. As we are still dealing with the behaviour at serviceability, a linear bond-slip (τ-δ) characteristic is also assumed, that is, the bond stiffness $k_e = \tau/\delta$ is constant. Closed form solutions for the partial-interaction behaviour in Fig. 5 have been developed for the case of a linear bond-slip (τ-δ) characteristic [28] and are given in Appendix A. These are used in the following segmental analyses to develop a closed form solution for the flexural rigidity of the cracked segment in Fig. 6.

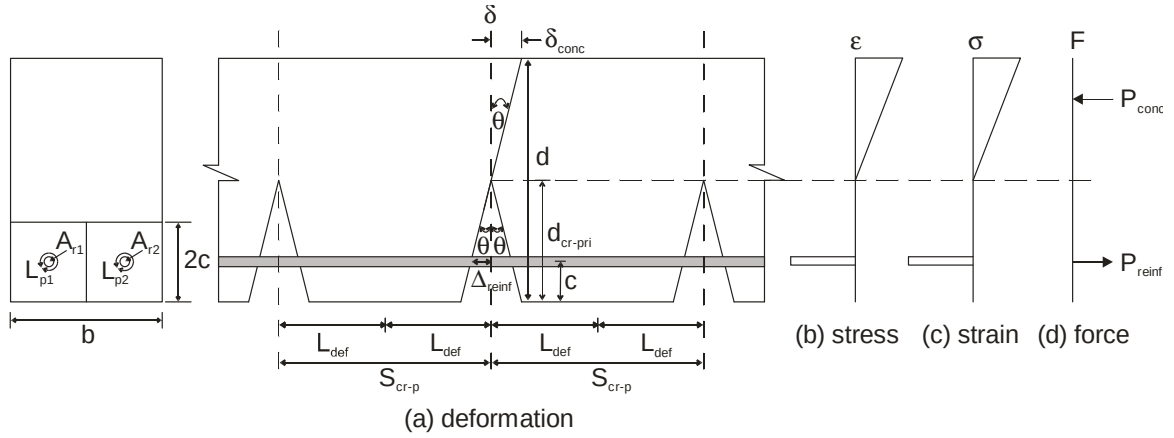

Figure 6: Idealisation for closed form solutions

For the tension region in Fig. 6, the crack rotation is given by

$$\theta = \frac{\Delta_{\text{reinf}}}{d_{cr-p}-c} \tag{2}$$

where Δ_{reinf} is the reinforcement slip relative to the crack face, $d_{cr\text{-}p}$ is the depth of the crack when it is a primary crack and $d_{cr\text{-}p}$-c is the distance of the reinforcement from the crack apex. Similarly for the compression region

$$\theta = \frac{\delta_{conc}}{d-d_{cr-p}} \tag{3}$$

where δ_{conc} is the maximum deformation in the compression region and *d* is the depth of the beam.

From Eqs. 2 and 3

$$\delta_{conc} = \frac{\Delta_{\text{reinf}}(d-d_{cr-pri})}{d_{cr-pri}-c} \tag{4}$$

The maximum strain in the concrete is therefore

$$\varepsilon_{conc} = \frac{\delta_{conc}}{L_{def}} \tag{5}$$

where, L_{def} is half the crack spacing, which for a linear ascending bond stress distribution, as shown in Appendix A, is

$$L_{def} = \frac{1}{\lambda_1} \tag{6}$$

in which,

$$\lambda_1 = \sqrt{k_e \beta_2} \tag{7}$$

where k_e is the bond stiffness τ/δ of the linear bond-slip and β_2 is given by

$$\beta_2 = \frac{L_p}{A_r}\left(\frac{1}{E_r} + \frac{A_r}{E_c A_c}\right) \tag{8}$$

where: A_c is the area of concrete surrounding the reinforcing bars which interact with it, as illustrated in Fig. 6, this area can be taken as the product of the width of the section b and twice to cover to the centre of the bar c; A_r is the sum of all the cross sectional areas of the reinforcing bars within A_c; L_p is the sum of all the perimeters of the reinforcing bars within A_c; E_r is the modulus of the reinforcing bars; and E_c the modulus of the concrete.

The force developed within the concrete compression region, P_{conc} in Fig. 6, can be determined as follows from Eqs. 5 and 6

$$P_{conc} = \frac{0.5\Delta_{\text{reinf}}\left(d - d_{cr-p}\right)^2 \lambda E_c b}{\left(d_{cr-p} - c\right)} \tag{9}$$

For the tensile reinforcement, the force developed for a given slip Δ_{reinf} using PI theory is given by Eq. 10 (Appendix A).

$$P_{reinf} = \frac{\Delta_{\text{reinf}} A_r E_r \lambda_1}{\tanh(1)} \tag{10}$$

As $P_{conc} = P_{reinf}$, from Eq. 9 and Eq. 10 the crack height is given by

$$d_{cr-p} = \frac{dbE_c \tanh(1) + A_r E_r \pm \sqrt{2dbE_c A_r E_r \tanh(1) + A_r^2 E_r^2 - 2bE_c A_r E_r c \tanh(1)}}{bE_c \tanh(1)} \tag{11}$$

Knowing the crack height, the moment in the section is simply

$$M = -P_{conc}\left(\frac{d - d_{cr-p}}{3}\right) + P_{reinf}(d - c) \tag{12}$$

Substituting Eqs. 9 and 10 into Eq. 12, the rotation for a given moment is

$$\theta_{pi-p} = \frac{6M\tanh(1)}{[E_c b\tanh(1)(-d^3+3d^2d_{cr-p}-3dd_{cr-p}^2+d_{cr-p}^3)+6A_rE_r(dd_{cr-p}-d_{cr-p}c-dc+c^2)]\lambda_1} \quad (13)$$

and knowing that the curvature is equal to θ/L_{def} gives the curvature

$$\chi_{pi-p} = \frac{6M\tanh(1)}{E_c b\tanh(1)(-d^3+3d^2d_{cr-p}-3dd_{cr-p}^2+d_{cr-p}^3)+6A_rE_r(dd_{cr-p}-d_{cr-p}c-dc+c^2)} \quad (14)$$

and hence the equivalent cracked flexural rigidity can be given by

$$EI_{pi-p} = \frac{E_c b\tanh(1)(-d^3+3d^2d_{cr-p}-3dd_{cr-p}^2+d_{cr-p}^3)+6A_rE_r(dd_{cr-p}-d_{cr-p}c-dc+c^2)}{6\tanh(1)} \quad (15)$$

The cracked flexural rigidity given by Eq. 15 is applicable for primary cracking, which occurs following first cracking. The moment at which primary cracks first occur (M_{cr}) is taken as the lesser of that obtained through a standard full-interaction transformed section analysis and that obtained from a partial interaction analysis (Appendix A) as follows

$$P_{reinf-cr-p} = \frac{A_rE_r\lambda_1^2\delta_1 f_t A_c}{\tau_{max}L_p} \quad (16)$$

The primary cracking moment can therefore be given by Eq. 17

$$M_{cr-p} = P_{reinf-cr-pr}\left(\tfrac{2}{3}d + \tfrac{1}{3}d_{cr}-c\right) \quad (17)$$

which simplifies to Eq. 18 when the load in the reinforcement to cause primary cracking is given by Eq. 16.

$$M_{cr-p} = \frac{(E_cA_c+A_rE_r)f_t(2d+d_{cr}-3c)}{3E_c} \quad (18)$$

Similarly, the secondary cracking load is given by (Appendix A)

$$P_{reinf-cr-s} = \frac{A_rE_r\lambda_1^2\delta_1 f_t A_c}{0.352\tau_{max}L_p} \quad (19)$$

and, hence, as above the secondary cracking moment is given by

$$M_{cr-s} = P_{reinf-cr-sec}\left(\tfrac{2}{3}d + \tfrac{1}{3}d_{cr} - c\right) \tag{20}$$

which simplifies to

$$M_{cr-s} = \frac{125(E_c A_c + A_r E_r) f_t (2d + d_{cr} - 3c)}{132 E_c} \tag{21}$$

Once the secondary cracking moment is reached, the crack spacing is half the primary crack spacing (Appendix A). As described for the numerical procedure, and shown in Appendix A for the closed form solutions, the change of boundary condition changes the load developed in the bar for a given slip to that in Eq. 22.

$$P_{reinf} = \frac{\Delta_{\text{reinf}} A_r E_r \lambda_1}{\tanh(0.5)} \tag{22}$$

This change means the crack height, rotation, curvature and flexural rigidity also change as shown; the derivation being identical to that for primary cracking.

$$d_{cr\_s} = \frac{2dbE_c \tanh(0.5) + A_r E_r \pm \sqrt{4dbE_c A_r E_r \tanh(0.5) + A_r^2 E_r^2 - 4bE_c A_r E_r c \tanh(0.5)}}{2bE_c \tanh(0.5)} \tag{23}$$

$$\theta_{pi-s} = \frac{3M \tanh(0.5)}{[E_c b \tanh(0.5)(-d^3 + 3d^2 d_{cr-s} - 3d d_{cr-s}^2 + d_{cr-s}^3) + 3A_r E_r (d d_{cr-s} - d_{cr-s} c - dc + c^2)]\lambda_1} \tag{24}$$

$$\chi_{pi-s} = \frac{6M \tanh(0.5)}{E_c b \tanh(0.5)(-d^3 + 3d^2 d_{cr-s} - 3d d_{cr-s}^2 + d_{cr-s}^3) + 3A_r E_r (d d_{cr-s} - d_{cr-s} c - dc + c^2)} \tag{25}$$

$$EI_{pi-s} = \frac{E_c b \tanh(0.5)(-d^3 + 3d^2 d_{cr-s} - 3d d_{cr-s}^2 + d_{cr-s}^3) + 3A_r E_r (d d_{cr-s} - d_{cr-s} c - dc + c^2)}{6 \tanh(0.5)} \tag{26}$$

Importantly, it can be seen that the flexural rigidity when considering partial interaction for primary ($EI_{pi\text{-}p}$) and secondary cracking ($EI_{pi\text{-}s}$), as in Eqs. 15 and 26, is independent of the bond-slip stiffness ($k_e = \tau/\delta$). This is significant. Although we are allowing for the slip of the reinforcement relative to the concrete through the use of partial interaction theory, by making the assumption of a linear ascending bond characteristic, we do not need to define the bond properties to determine the flexural rigidity and consequently the load deflection behaviour. The independence of the flexural rigidity to the bond-slip stiffness can be explained through

the example presented in Fig. 7 where the closed form PI equations have been used to describe the M/θ, M/χ and M/EI behaviour of a segment of a beam. The beam has a cross section of width of 200 mm, depth of 300 mm and an elastic modulus for the concrete of 25MPa. The section has been reinforced with 3 16mm bars of elastic modulus of 200GPa and bond stiffness k_e of either 13.7 N/mm, which is a linear simplification of the nonlinear bond characteristic suggested by [31] for ribbed steel bars embedded in 30MPa concrete, or, 92.7 N/mm which is the linear simplification of the nonlinear bond characteristic for sand coated FRP bars [32].

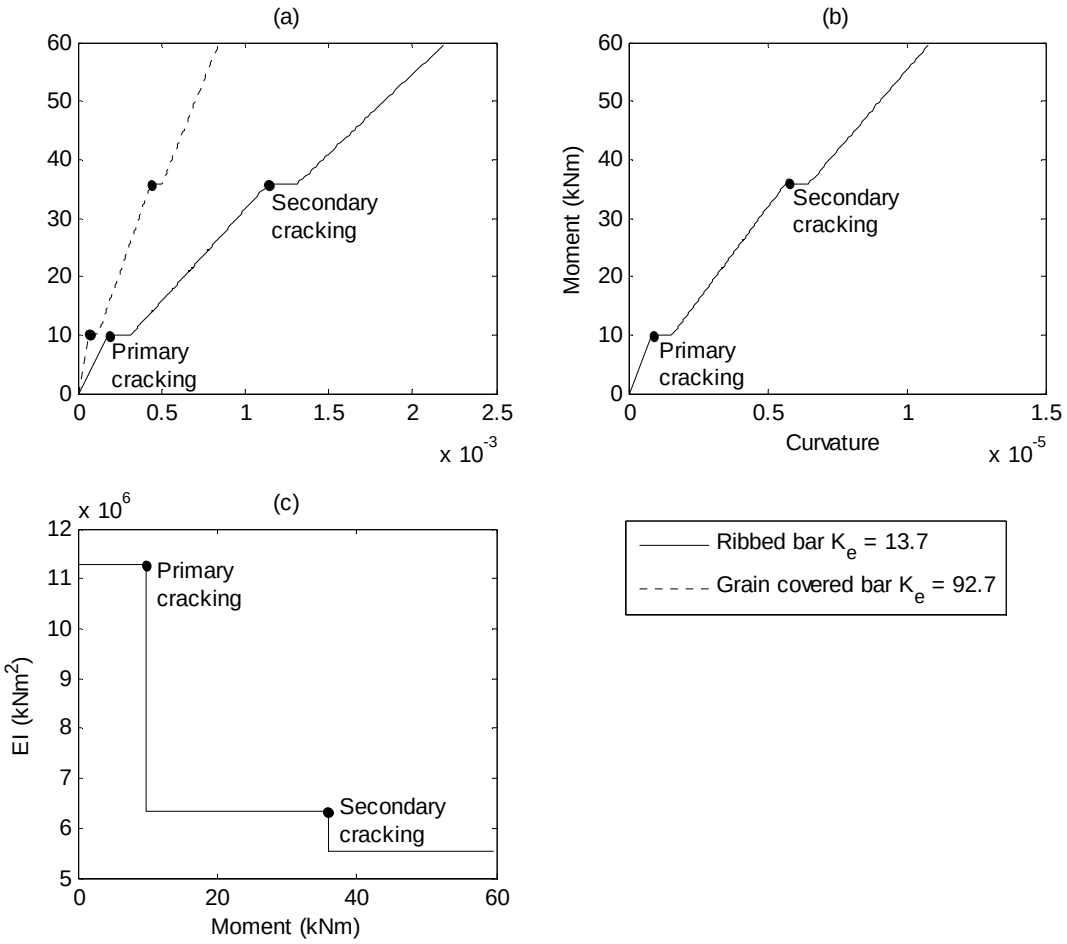

Figure 7: Influence of bond characteristic

If we consider a member reinforced with the bars of low bond stiffness of 13.7 N/mm, that is the ribbed bar, cracks form at a spacing of 404 mm and for the bar with a high bond stiffness of 92.7 N/mm, that is the sand coated bar, cracks form at a spacing of 155 mm. A segment reinforced with each type of bar, which is of a length of half the crack spacing, is taken and a moment applied as explained previously for the segmental analysis. For the segment with a

low bond stiffness, for any given moment following cracking, the slip of the reinforcement is greater than that of the segment with high bond stiffness and therefore the rotation, as shown in Fig. 7(a), is larger. Converting this rotation to a curvature by dividing by the segment length yields identical curvatures shown in Fig. 7(b). It can be seen that the curvature is independent of the bond characteristic, that is, both M/θ relationships yield identical M/χ relationships. This can also be shown by considering Eq. 6 and Eq. 13 which define the segment length and rotation of the segment for a given moment respectively. Both relationships are inversely proportional to λ, which is a function of the bond stiffness and so defining the curvature as the rotation per unit length of segment, that is, dividing Eq. 13 by Eq. 6 yields a curvature which is independent of λ and hence the bond properties. Finally, since the curvature is independent of the bond so too is the flexural rigidity of the segment, seen in Fig. 7(c). Similar behaviour was also noted in [27], where the deflection of a beam was determined by summing the discrete rotations about each crack. It was observed that with increasing bond stiffness more cracks formed but at each crack the discrete rotation reduced because the cracks were narrower and, hence, the overall behaviour became independent of the bond stiffness.

Hence, it can be seen in Fig. 7 that varying the bond-slip stiffness may vary the moment-rotation of a segment but does not vary the moment-curvature and consequently the flexural rigidity. This is because increasing the bond stiffness simply causes more cracks to occur but these cracks are narrower. Also of importance is the independence of the moment to cause primary and secondary cracking on the bond stiffness. As seen in Eqs.18 and 21 this is the case because the crack spacing is proportional to the bond stiffness, hence, for a stiff bond the crack spacing is small but the bond builds rapidly, and therefore, the load transferred from the bar to the concrete rapidly reaches that required to cause cracking. This can be shown mathematically by substituting Eqs. 7 and 8 into Eq. 16.

COMPARISON OF SECTIONAL PROPERTIES

The three major sectional properties that affect the deflection of a beam for short term loads are the uncracked flexural rigidity $EI_{fi\text{-}uncr}$, the cracked flexural rigidity EI_{cr} and the moment to cause cracking M_{cr}. The derivation of the uncracked flexural rigidity $EI_{fi\text{-}uncr}$ is based on the Euler-Bernoulli principle of plane sections remaining plane and its corollary of a linear strain profile, so that the M/θ and M/χ approaches give exactly the same values which can be obtained from transformed sections. The difficulty in quantifying deflection arises in the cracked properties, that is, EI_{cr} and M_{cr} and these are studied below for different elastic moduli, namely 200GPa and 40GPa, and varying reinforcement ratios.

Sectional flexural rigidity (EI_{cr})

It can be seen in Fig. 9 that for both the 200GPa and 40GPa reinforcement the flexural rigidity obtained from full interaction ($EI_{fi\text{-}cr}$) lies below that obtained from a partial interaction analysis for both primary cracking ($EI_{pi\text{-}p}$) and secondary cracking ($EI_{pi\text{-}s}$).

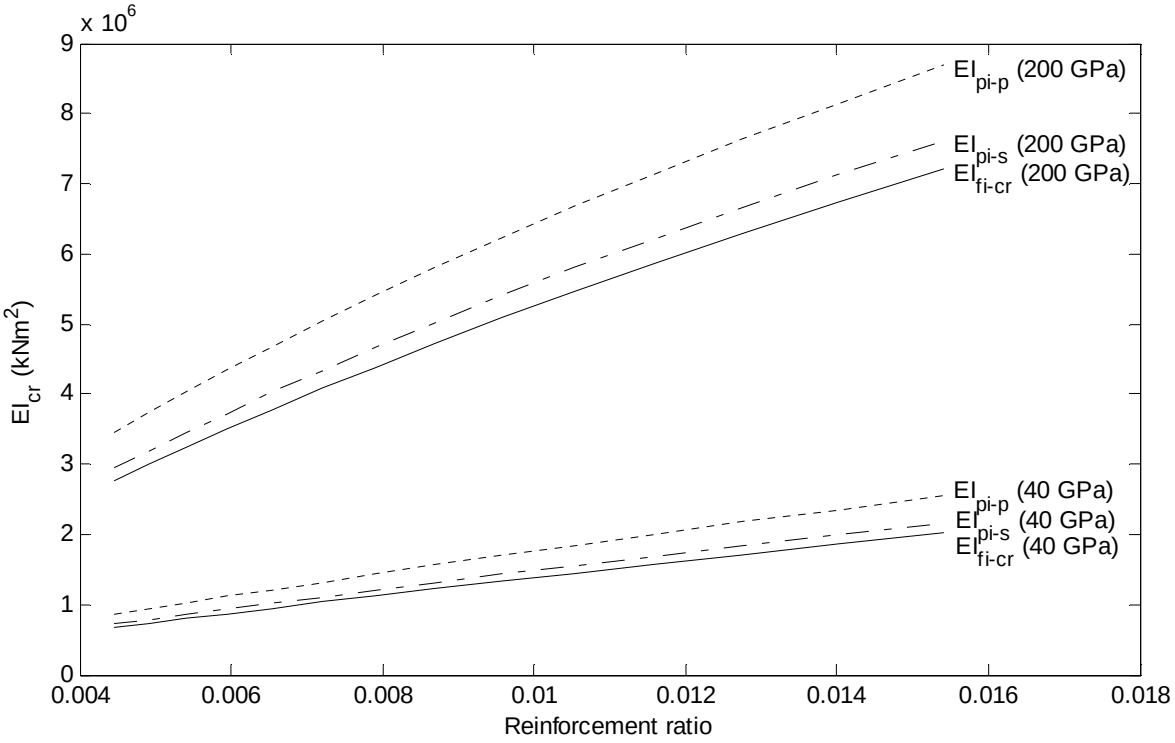

Figure 9: Variation in EI_{cr} for with reinforcement ratio and E_r.

Importantly, Fig. 9 shows the partial interaction approach does not predict a single flexural rigidity of the cracked section, but rather, the partial interaction flexural rigidity has a step change reduction as secondary cracking occurs that is from $EI_{pi\text{-}p}$ to $EI_{pi\text{-}s}$. To fully understand the implications of secondary cacking, the recognised randomness of cracking needs to be considered using the tension-stiffening analysis in Fig. 5.

The distance L_{bd} from the crack face in Fig. 5, is the distance where full-interaction ($ds/dx = \Delta = 0$) first occurs, that is beyond L_{bd} there is full-interaction. The region where there is full-interaction is important as this is where the maximum tensile stresses in the concrete occurs and, consequently, where there is the most likelihood of cracking. If we are dealing with a constant moment region, then all we know is that the primary crack spacing $S_{cr\text{-}p} \geq L_{bd}$. However if we are dealing with a moment gradient, then $S_{cr\text{-}p} \rightarrow L_{bd}$ as cracking would tend to occur where the moment is highest, that is towards the region where the initial crack face is. Hence, there is a degree of randomness in quantifying the primary crack spacing $S_{cr\text{-}p}$ in

Fig. 5. This degree of randomness flows onto the analysis of secondary cracks where the boundary condition is now $\Delta = 0$ at $S_{cr\text{-}p}/2$. Hence there is a degree of randomness, beyond that due to variation in material properties, in $EI_{pi\text{-}p}$ and $EI_{pi\text{-}s}$ in Fig. 9. The numerical segmental analysis provides the tools to study the effect of this randomness but is not the major focus of this paper.

As a simple example of the influence of crack spacing, consider the M/θ, M/χ and M/EI relationships shown in Fig. 10, which have been produced using the numerical approach for the 200x300mm cross section with an E_c of 25MPa and reinforced with 3 16mm bars with an E_r of 200 GPa and k_e of 13.7 N/mm. It can be seen in Fig. 10(c) that increasing the crack spacing from $S_{cr\text{-}p}$ to $1.2S_{cr\text{-}p}$ leads to an increase in the stiffness of the cracked section, but reduces the moment to cause secondary cracking. This increase in stiffness can be explained by considering the prism in Fig. A.2(b) in Appendix A. It can be seen that by increasing the crack spacing, the bond force builds over a greater bar length. Hence for a given slip, the load required to reach the boundary condition $\Delta = 0$ at $S_{cr\text{-}p}/2$ is reduced, thus a softer P/Δ relationship is obtained. This also means that the M/θ relationship, as in Fig. 10(a), softens for increasing crack spacing. As shown in Fig. 10(b), this does not, however, lead to a softer M/χ relationship; this is because the rotation takes place over a larger deformation length L_{def} in Fig. 4. As shown in Fig. 10(c), the stiffer M/χ relationship in turn leads to an increase in $EI_{pi\text{-}s}$ and $EI_{pi\text{-}s}$.

It is also important to note in Fig. 10(c) that the moment to cause secondary cracking has reduced. This reduction can again be explained by considering the numerical partial interaction analysis in Fig. 5. It is known that secondary cracking occurs once the strain in the concrete exceeds the tensile rupture strain at the boundary condition $\Delta = 0$ at $S_{cr\text{-}p}/4$. As the crack spacing is increased, for a given slip, the total bond force over the prism length $S_{cr\text{-}p}/4$ is higher, hence so too is the strain in the concrete strain. This means that the load in the reinforcement to cause secondary cracking is reduced and hence so too is the moment, as in Fig. 10(a). Importantly, this shows that $EI_{pi\text{-}cr}$ and $M_{cr\text{-}pi}$ are only independent of the bond τ/δ properties when considering the minimum crack spacing. If the randomness of cracking is allowed for by increasing the crack spacing, the cracked flexural rigidity is increased and the moment to cause secondary cracking is reduced, with the magnitude of these changes is depending on the bond properties. It can be seen that the effect of the random nature of cracking is complex but this partial interaction segmental analysis does provide a tool for studying it.

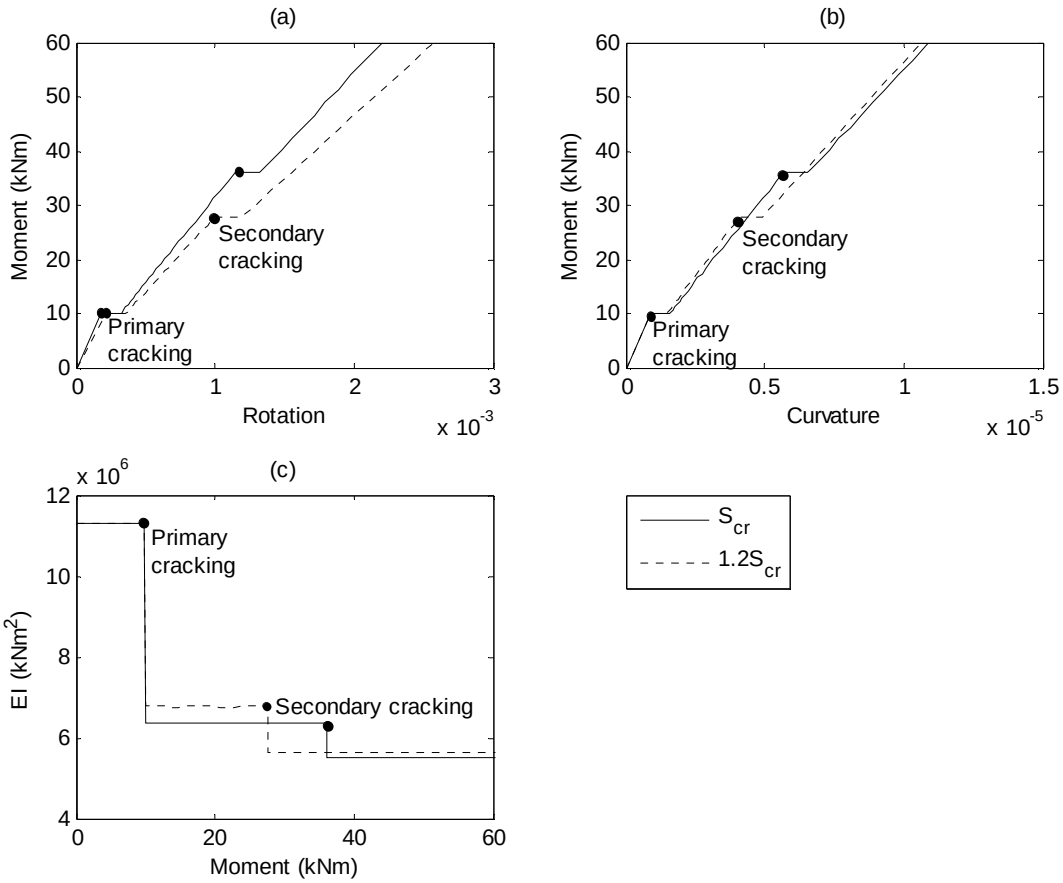

Figure 10: The influence of crack spacing on EI

Moment to cause cracking (M_{cr})

The cracking moment is important as it affects the extent of cracking along the span of a member. The full-interaction moment to cause cracking $M_{cr\text{-}fi}$ in Fig. 11 is based on the cross-sectional area of concrete, that is it ignores the reinforcement as recommended in codes. There is reasonable correlation with the partial-interaction values of $M_{cr\text{-}p}$, but it should be noted that for analysis the cracking moment is taken as the lesser of the $M_{cr\text{-}p}$ and $M_{cr\text{-}fi}$. However, as with the flexural rigidities discussed above, the major discrepancy is with the secondary cracks $M_{cr\text{-}s}$ and particularly for low reinforcement modulus such as for the 40 GPa reinforcement where secondary cracking, and the consequential major reduction in stiffness, can occur at relatively low moments. As outlined above, and shown in Fig. 10(c), the random nature of cracking can further decrease $M_{cr\text{-}s}$ from that shown in Fig. 11, leading to an earlier reduction in $EI_{pi\text{-}cr}$ and hence increase in member deflection.

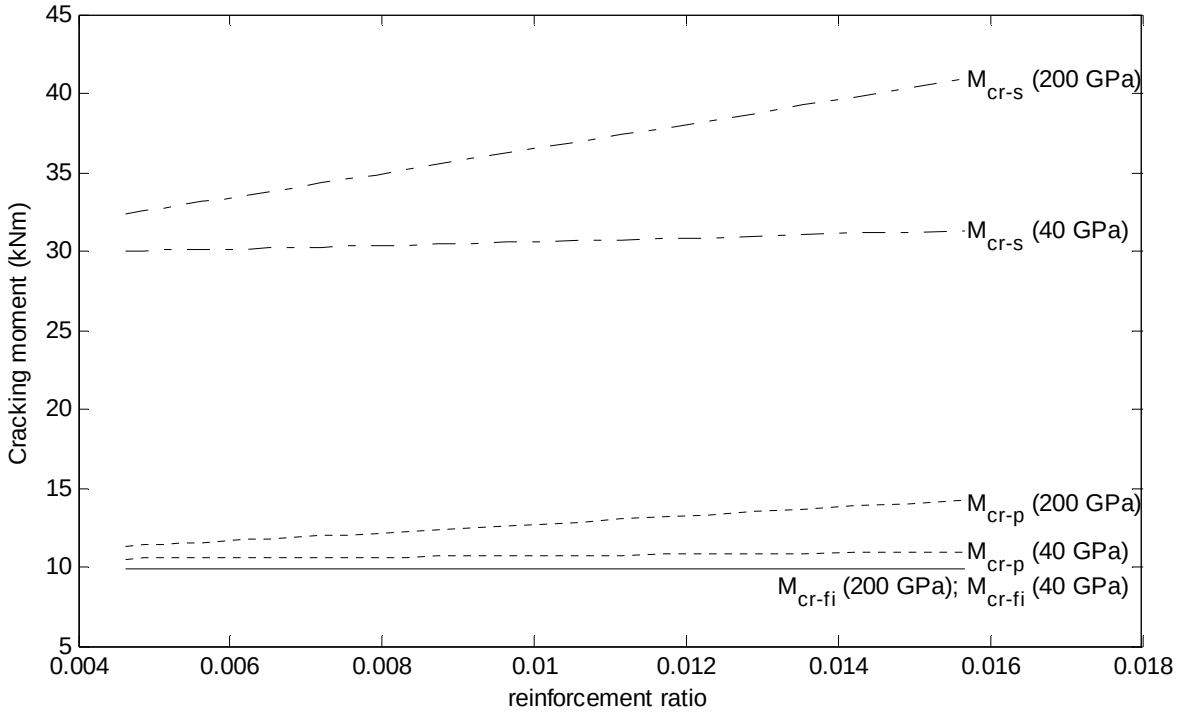

Figure 11: Variation in M_{cr} with reinforcement ratio and EI

MODELLING THE DEFLECTION OF BEAMS (EI_{eff})

Having determined the section properties $M_{cr,}$ $M_{cr\text{-}s}$ and $EI_{pi\text{-}cr}$ above, it is now a straightforward procedure to quantify the deflection, as illustrated in Fig. 12 for a simply supported beam with the point load P in Fig. 12(a) which induces the moment distribution M in Fig. 12(b). The primary and secondary cracking moments $M_{cr\text{-}p}$ and $M_{cr\text{-}s}$ define the extent of cracking in Fig. 12(b) where X_{uncr} is the uncracked region, $X_{cr\text{-}p}$ is the region where primary cracks occur and $X_{cr\text{-}s}$ is the region where both primary and secondary cracks occur. Within these regions, the flexural rigidities are as shown in Fig. 12(c) where $EI_{fi\text{-}uncr}$ is the full-interaction uncracked flexural rigidity from transformed sections, $EI_{pi\text{-}p}$ is the partial-interaction flexural rigidity in the region where only primary cracks occur and $EI_{pi\text{-}s}$ is the partial interaction flexural rigidity where both secondary and primary cracks exist. Dividing the flexural rigidities in Fig. 12(c) by the moment distribution M in Fig. 12(b) gives the variation in curvature in Fig. 12(d) which can be integrated to determine the deflection. It should be noted that the random nature of cracking has not been included in this analysis but as mentioned previously it could be included in a numerical simulation.

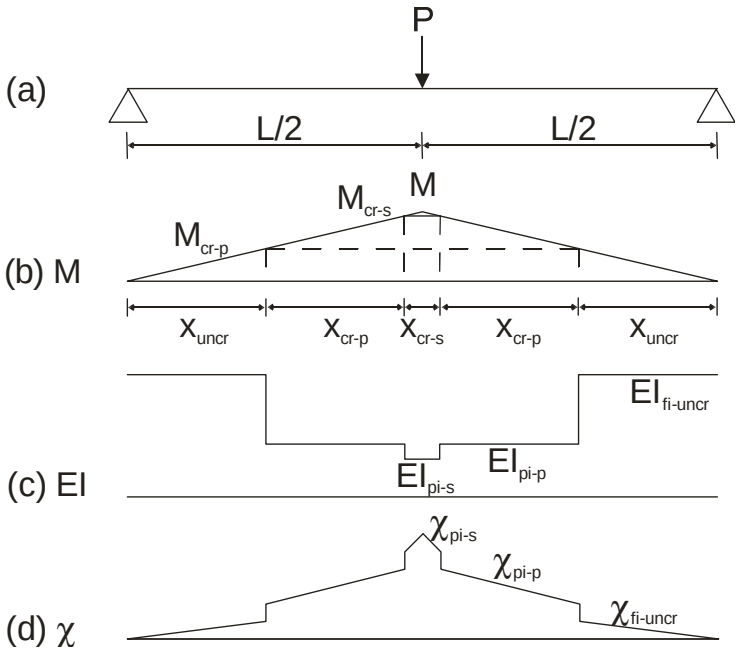

Figure 12: Deflection of a simply supported member

Using the moment area method, it is also possible to derive closed form solutions for determining the maximum deflection *y* at all load levels, that is uncracked y_{uncr}, cracked with only primary cracks y_{pi-p} and cracked with primary and secondary cracks y_{pi-s}. As an example, this has been carried out for the simply supported load case in Fig. 12, yielding Eqs. 27-29 where, M_{cr} is the lesser of the full interaction cracking moment M_{fi-cr} and the partial interaction primary cracking moment M_{cr-p}.

$$y_{uncr} = \frac{PL^3}{48EI_{fi-uncr}} \tag{27}$$

$$y_{pi-p} = \frac{64M_{cr}^3(EI_{pi-p}-EI_{fi-uncr})+P^3L^3EI_{fi-uncr}}{48EI_{fi-uncr}P^2EI_{pi-p}} \tag{28}$$

$$y_{pi-s} = \frac{64M_{cr}^3EI_{pi-s}(EI_{pi-p}-EI_{fi-uncr})+64EI_{fi-uncr}M_{cr-s}^3(EI_{pi-s}-EI_{cr-p})+P^3L^3EI_{pi-p}EI_{fi-uncr}}{48EI_{pi-s}EI_{pi-p}EI_{fi-uncr}P^2} \tag{29}$$

Finally by equating Eq. 28 and Eq. 29 with the uncracked elastic load case of Eq. 27, it is possible to solve for a single effective flexural rigidity $EI_{eff,}$ over the entire span of the member which accounts for the cracked and uncracked regions. This yields Eq. 30 for primary cracking, and Eq. 31 for primary and secondary cracking.

$$EI_{eff-p} = \frac{P^3 L^3 EI_{pi-p} EI_{fi-uncr}}{64M_{cr}^3 (EI_{pi-p} - EI_{fi-uncr}) + P^3 L^3 EI_{fi-uncr}} \quad (30)$$

$$EI_{eff-s} = \frac{EI_{pi-s} EI_{pi-p} EI_{fi-uncr} P^2 L^3}{64M_{cr}^3 EI_{pi-s} (EI_{pi-p} - EI_{fi-uncr}) + 64EI_{fi-uncr} M_{cr-s}^3 (EI_{pi-s} - EI_{pi-p}) + P^3 L^3 EI_{pi-p} EI_{fi-uncr}} \quad (31)$$

Also presented in Eqs. 32-34 are the deflections of a simply supported member subjected to 4 point loading and in Eq. 35 and Eq. 36 the effective flexural rigidities, where *a* is the distance from the support to the location of the point load.

$$y_{uncr} = \frac{Pa(4a^2 - 3L^2)}{24EI_{fi-uncr}} \quad (32)$$

$$y_{pi-p} = -\frac{8M_{cr}^3 (EI_{fi-uncr} - EI_{pi-p}) + P^3 a(4EI_{fi-uncr} a^2 - 3EI_{fi-uncr} L^2)}{24EI_{fi-uncr} EI_{pi-p} P^2} \quad (33)$$

$$y_{pi-s} = -\frac{8M_{cr} EI_{pi-s} (EI_{fi-uncr} - EI_{pi-p}) + 8EI_{fi-uncr} M_{cr-s} (M_{cr-s}^2 EI_{pi-p} - EI_{pi-s}) + P^3 EI_{fi-uncr} EI_{pi-p} a(4a^2 - L^2)}{24EI_{pi-s} EI_{pi-p} EI_{fi-uncr} P^2} \quad (34)$$

$$EI_{eff-p} = \frac{P^3 aEI_{fi-uncr} EI_{pi-p} (4a^2 - 3L^2)}{8M_{cr}^3 (EI_{fi-uncr} - EI_{pi-p}) + P^3 a(4EI_{fi-uncr} a^2 - 3EI_{fi-uncr} L^2)} \quad (35)$$

$$EI_{eff-s} = \frac{P^3 aEI_{fi-uncr} EI_{pi-p} EI_{pi-s} (4a^2 - 3L^2)}{8M_{cr} EI_{pi-s} (EI_{fi-uncr} - EI_{pi-p}) + 8EI_{fi-uncr} M_{cr-s} (M_{cr-s}^2 EI_{pi-p} - EI_{pi-s}) + P^3 EI_{fi-uncr} EI_{pi-p} a(4a^2 - L^2)} \quad (36)$$

DEFLECTION OF BEAMS

Comparison with design rules for member deflection

A simply supported beam of span 4 m with a central point load was used in the following analyses; the cross-section of the beam was the same as that used for the analyses in Fig. 7 that is, with a width of 200 mm, depth of 300 mm and E_c = 25 MPa. To investigate the influence of reinforcement modulus, the reinforcement has been considered to have either E_r = 40 GPa with k_e = 92.7 N/mm, or E_r = 200 GPa with k_e = 13.7 N/mm, and to investigate

reinforcement ratio the section has been reinforced with either 2 or 3No. 16 mm bars giving a reinforcement ratio of 0.74% or 1.1% respectively.

Firstly let us consider the cross section with 1.1% reinforcing and a reinforcement modulus of 200GPa. Fig. 13(a) shows the variation in effective flexural rigidity (EI_{eff}) derived using Eqs. 30 and 31, as well as EI_{eff} derived from the ACI approach [34] given by the following equations

$$I_{eff} = \left(\frac{M_{cr}}{M}\right)^3 I_{fi-uncr} + \left[1 - \left(\frac{M}{M_s}\right)^3\right] I_{fi-cr};\ \ I_{eff} \leq I_{fi-uncr} \tag{37}$$

$$\beta_d = 0.5\left(\frac{E_r}{E_s} + 1\right) \tag{38}$$

in which Eq.38 is a reduction factor allowing for application to FRP bars. Furthermore, Fig. 13(a) shows a comparison with Bischoff's [2] approach, which is given by

$$I_{eff} = \frac{I_{cr}}{1-\left(1-I_{fi-cr}/I_g\right)(M_{cr}/M)^2} \tag{39}$$

It can be seen from Fig. 13(a) that for the 200 GPa bars there is a negligible difference in EI_{eff} when using either of the full interaction (FI) approaches, that is, the ACI or Bischoff's approach. This is in contrast to the partial interaction (PI) approach, which, immediately following primary cracking predicts approximately the same stiffness as the FI approaches but rapidly asymptotes to a stiffer EI_{eff} prior to secondary cracking. Following secondary cracking, it can be seen that EI_{eff} softens and approaches that of the fully cracked section predicted by the FI approaches. This behaviour is to be expected as both the PI and FI approaches predict the same cracking moment, and, as seen in Fig. 9, the PI approach predicts a higher cracked flexural rigidity for both primary and secondary cracking. Fig. 13(b) also shows that the PI approach predicts almost identical deflection y for a given moment M as the FI approaches immediately following primary cracking; this is despite the fact that, as show in Fig. 9, $EI_{cr\text{-}p}$ is significantly higher. This is because the extent of cracking from the FI analysis is larger than that from the PI analyses which offsets the difference in stiffnesses.

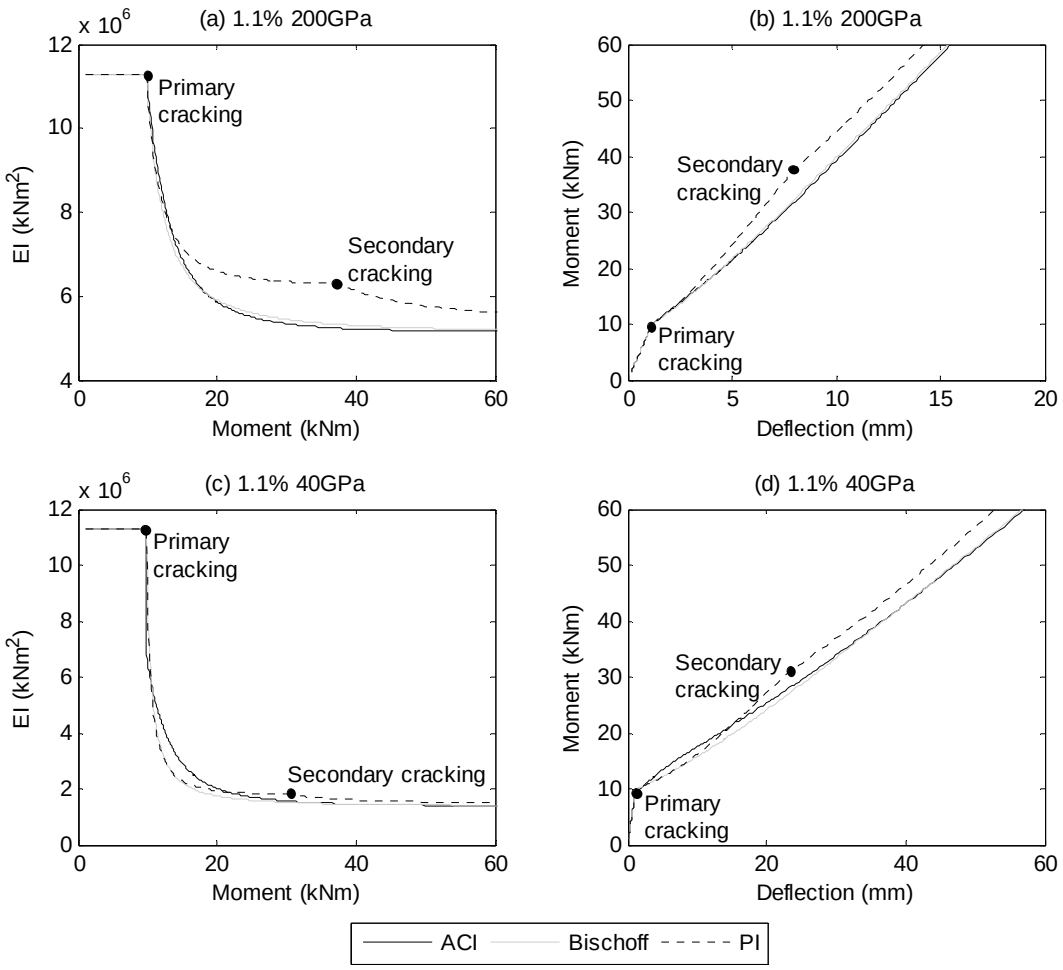

Figure 13: M/EI_{eff} and M/y for varying E_r

Now consider Fig. 13(c) which shows the effective flexural rigidity for the same cross section but this time reinforced with 40 GPa bars. Firstly considering the FI approaches, it can be seen that the ACI and Bischoff's approaches predict significantly different effective flexural rigidities following primary cracking, which in turn, as shown in Fig. 13(d), leads to a substantial difference in the deflection. It can also be seen in Fig. 13(c) that EI_{eff} predicted by Bischoff closely matches the PI approach. However since the cracked flexural rigidities are higher using the PI approach, as shown in Fig. 9, EI_{eff} becomes comparably stiffer as the applied moment increases. Again this suggests that using an elastic deflection equation for a beam with a single point load at mid span leads to an over prediction of the proportion of the beam which is cracked.

Now let us consider the influence of reinforcement ratio by reducing the ratio to 0.74%. Only the 40 GPa cross section will be considered here as it can be seen in Fig. 9 that for both the 200 GPa and 40 GPa bars the variation in behaviour with reinforcing ratio is similar. Fig. 14(a) shows that as was the case for 1.1% reinforcement in Fig. 13(c) Bishoff's approach

closely matches the PI approach immediately following primary cracking. This would again suggest that Bischoff's approach is better able to predict the deflection immediately following primary cracking. Considering Fig. 14(b) it can be seen that at approximately the moment at which secondary cracking is predicted in the PI approach, the FI approaches begin to rapidly converge on each other until both predict the same deflection when the beam is considered to be fully cracked. A comparison of the responses in Figs. 13(c) and (d) and in Figs.14 (a) and (b) show very little difference in behaviour occurs with the change in reinforcement ratio. This is because both the flexural rigidity if the section, and the moments to cause cracking, as shown in Figs. 9 and 11, change very little with reinforcing ratio.

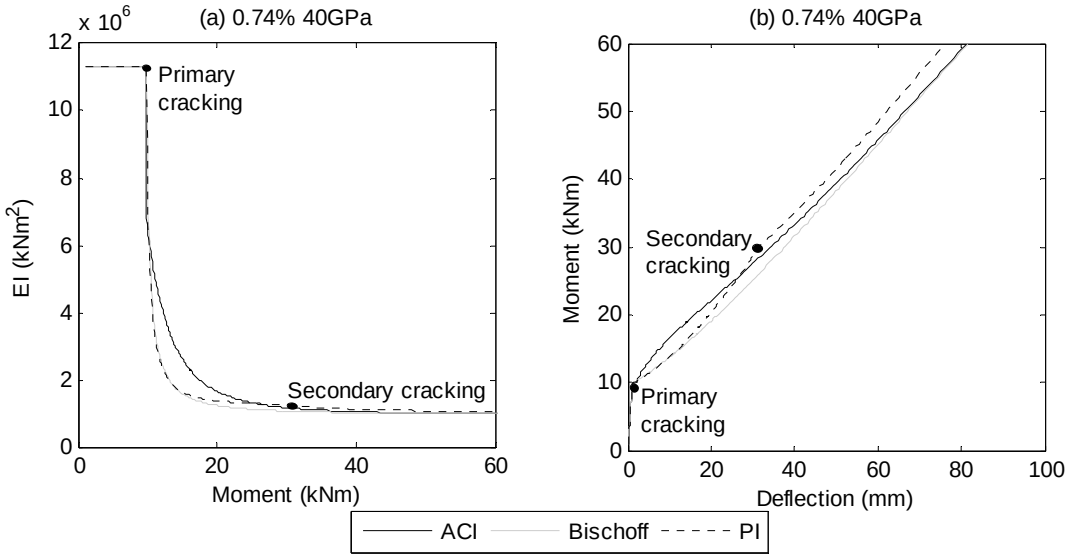

Figure 14: M/EI_{eff} and M/y for reduced reinforcement ratio

Finally, by considering the same 4m long member reinforced with 3 40GPa bars, this time loaded in 4-point bending, where the point loads are applied at 1.33 m centres, it is possible to investigate the influence of the loading configuration. By comparing Fig. 13(c) and Fig. 15(a), it can be seen that the FI approaches predict identical EI_{eff} in both loading scenarios. This is because they do not allow for the influence of the shape of the moment distribution when proportioning the uncracked and cracked segments of the member. This is not the case in the PI approach; hence, member stiffness is significantly lower following primary cracking because a greater portion of the beam is considered to be cracked. In Fig. 15(b) it can be seen that this translates to a significant step change in deflection following both primary and secondary cracking; this behaviour cannot be predicted using the FI approaches. It should also be remembered that the PI equations developed are based on the minimum crack spacing, and, as shown in Fig. 10(c), if the crack spacing is increased a minor increase in cross sectional stiffness is observed but a significant reduction in the cracking moment takes place. This combination may lead to a significant increase in member deflection.

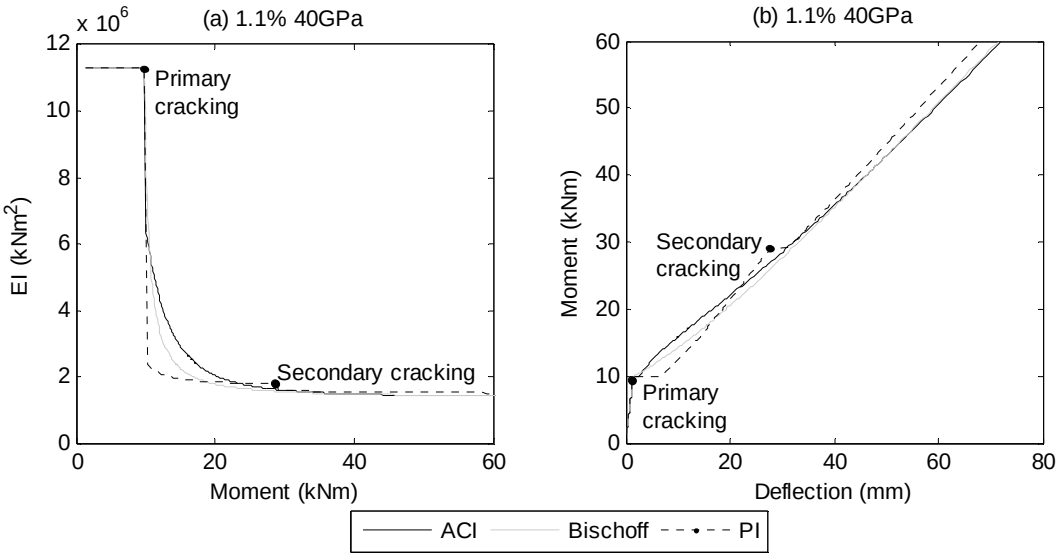

Figure 15: M/EI_{eff} and M/y when subjected to 4-point bending

Since the prediction of EI_{eff} using the FI approaches is independent of the moment distribution, it can also be concluded that empirically adjusting the coefficient of the M_{cr}/M ratio in Eqs. 37 and 39 may not lead to a generic improvement in the prediction of member deflection. This is because the moment distribution, which controls the proportion of the beam which is uncracked or cracked is ignored, and the use of an elastic deflection equation assumes a continuous distribution of curvature that cannot allow for the step changes associated with cracking which are shown in Fig. 12(d).

Comparison with experimental results

The PI approach has been compared to a pair of tests carried out by [35] on FRP reinforced beams under 4 point bending where the loads are applied at 300mm from the centre point. These beams had a span of 1800mm, a depth of 190mm, and were reinforced with 2 16mm ribbed GFRP bars with an elastic modulus of 64,153MPa. Beam C-216-D1 had a concrete strength of 56.3MPa, a width of 140mm and cover to the reinforcing of 20mm while beam C-216-D2 had a concrete strength of 61.7MPa a width of 160mm and cover to the reinforcing of 40mm.

Fig. 16 compares EI_{eff} predicted by the ACI, Bischoff's and the PI approaches, as well as their predicted deflections with the experimental results. It should be noted that to allow for some randomness of cracking, the PI approach has been presented for crack spacings S_{cr} and $1.2S_{cr}$. In Fig.s 16(a) and 16(c), it can be seen that the PI approach for both S_{cr} and 1.2Scr predict a far softer member response than the FI approaches immediately following primary cracking because a larger proportion of the beam is considered to be cracked. This in turn leads to the step change in deflection seen in Figs. 16(b) and 16(d). Similar behaviour is also

seen following secondary cracking. As the applied loads increase, however, the PI approach predicts a progressively stiffer response. It can also be noted from Figs. 16(b) that the increase in crack spacing from S_{cr} to $1.2S_{cr}$ significantly reduces the secondary cracking moment and hence between primary and secondary cracking the response for the PI approach with 1.2Scr is softer despite the stiffness of the section being higher. The PI approach tends to underestimate the deflection at high loads. However, this can be attributed to the effects of shrinkage which can be shown to considerably reduce the stiffness of the cracked section [29].

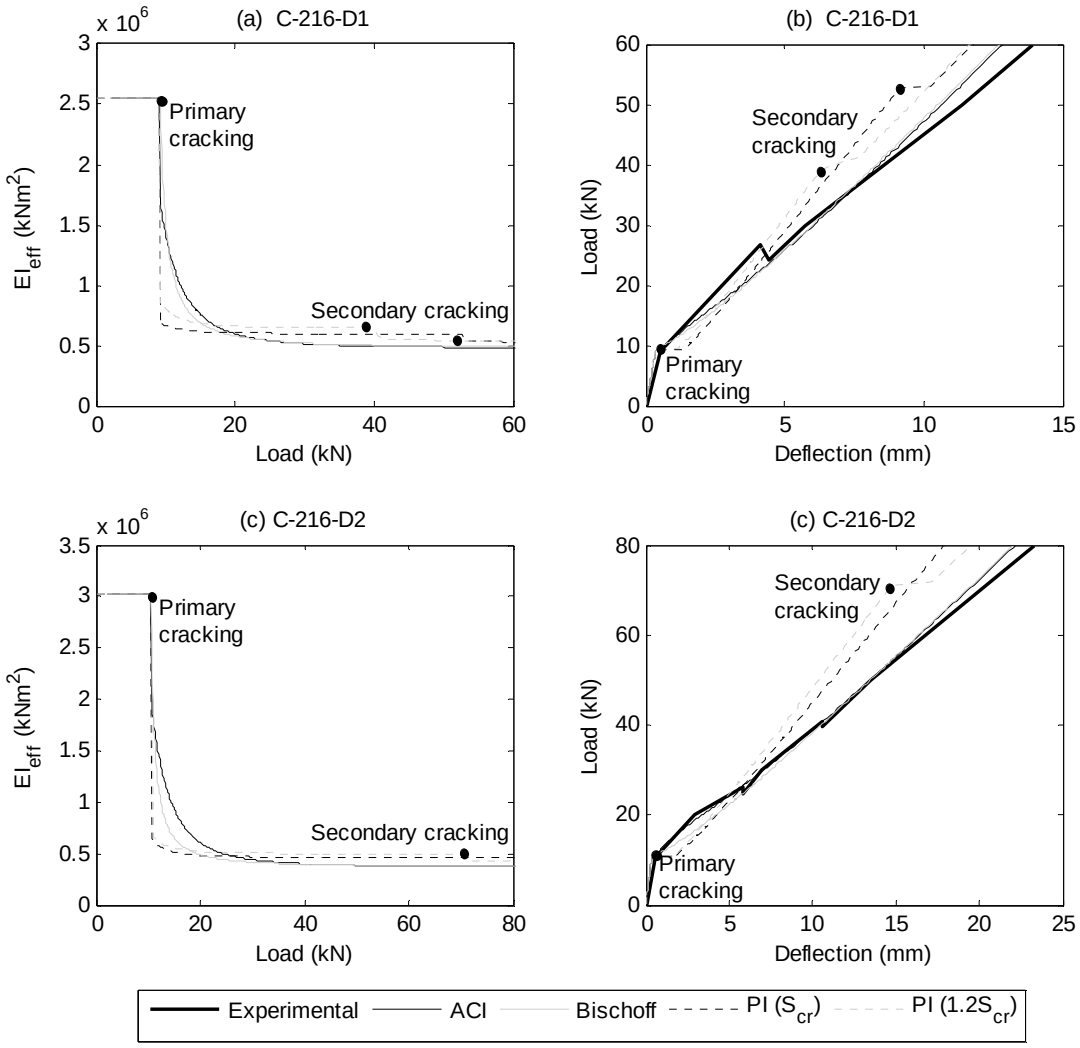

Figure 16: Comparison with tests by Barris et al. [35]

CONCLUSIONS

A serviceability partial-interaction approach that allows for slip between the reinforcement and concrete has been developed to quantify the flexural rigidity of a cracked section with

primary and secondary cracks and the moment to cause subsequent cracking. It has been shown how this partial-interaction procedure can be used to predict the minimum crack spacing and consequently used to give closed form solution for the serviceability deflection, as well as how it can be used to study the random component of cracking. It has also been shown how this partial-interaction approach can be used to derive closed form solutions for the effective flexural rigidity for use in design and how this depends on the distribution of the applied load. Surprising outcomes from this partial-interaction approach are that the flexural rigidity and the load to cause subsequent cracking are not dependent on the bond-slip stiffness at serviceability which should considerably simply the development of deflection rules for FRP reinforced members. This should be particularly useful for prediction the deflection of FRP reinforced members where a wide range of FRP material properties exist.

ACKNOWLEDGEMENTS

The financial support of the Australian research Council ARC Linkage Project LP 0883451 "Blast resistance of flexural high performance concrete members' and ARC Discovery project DP0985828 'A unified reinforced concrete model for flexure and shear' are gratefully acknowledged.

REFERENCES

[1] Branson DE. *Deformation of Concrete Structures*, McGraw 1977.

[2] Bischoff PH. Reevaluation of deflection prediction for concrete beams reinforced with steel and fiber-reinforced polymer bars. Journal of Structural Engineering 2005; 131(5):752-67.

[3] Sakai K, Yakuta Y. Moment-Curvature Relationships of Reinforced Concrete Members Subjected to Combined Bending and Axial Force. ACI Journal Proceedings 1980; 77(2):189-194.

[4] Gossman JS. Simplified Computations for Effective Moment of Inertia Ie and Minimum Thickness to Avoid Deflection Computations. ACI Journal 1980; 78(3):423-439.

[5] Al-Zaid R, Al-Shaikh AH, Abu-Hussein MM. Effect of Loading Type on the Effective Moment of Inertia of Reinforced Concrete Beams. ACI Structural Journal 1991; 88(2):184-190.

[6] Benmokrane B, Chaallal O, Masmoudi R. Flexural Response of Concrete Beams Reinforced with FRP Reinforcing Bars. ACI Structural Journal 1996; 91(2):46-55.

[7] Alsayed SH, Al-Salloum YA, Almusallam TH. Performance of glass fiber reinforced plastic bars as a reinforcing material for concrete structures. Composites Part B: engineering 2000; 31(6-7):555-567.

[8] Toutanji HA, Saafi M. Flexural behavior of concrete beams reinforced with glass fiber-reinforced (GFRP) bars. ACI Structural Journal 97(5):712-719.

[9] Yost RJ, Gross SP, Dinehart DW. Effective Moment of Inertia for Glass Fiber-Reinforced Polymer-Reinforced Concrete Beams. ACI structural Journal 2003; 100(6):732-739.

[10] Khalfallah S. Explaining the Riddle of Effective Moment of Inertia Models for FRP Concrete Beams. SBEIDCO - First International Conference on Sustainable Built Environment Infrastructure in Developing Countries ENSET Oran 2009.

[11] Bazant ZP, Oh BH. Deformation of Progressively Cracking Reinforced Concrete Beams. ACI Journal 81(3):268-278.

[12] Alwis WAM. Trilinear Moment-Curvature Relationship for Reinforced Concrete Beams. ACI Structural Journal 1990; 87(3):276-283.

[13] Hayder AR, Nayal R, Melhem H. Response prediction of concrete beams reinforced with FRP bars. Composite Structures 2004; 65(2):193-204.

[14] Bischoff PH, Gross PS. Equivalent Moment of Inertia Based on Integration of Curvature. Journal of Composites for Construction 2001; 15(3):263-273.

[15] Visintin P Oehlers DJ, Wu C. and Haskett M. A Mechanics Solution for Hinges in RC Beams with Multiple Cracks. Engineering Structures 2012; 36 March: 61-69.

[16] Gupta AK, Maestrini SR. Tension stiffening model for reinforced concrete bars. Journal of Structural Engineering 1990; 116(3):769-790.

[17] Wu Z, Yoshikawa H, Tanabe T. Tension stiffness model for cracked reinforced concrete. Journal of Structural Engineering 1991; 117(3):715-732

[18] Choi CK, Cheung SH. Tension stiffening model for planar reinforced concrete members. Computers & Structures 1996; 59 (1):179-190.

[19] Marti P, Alvarez M, Kaufmann W. and Sigrist V. Tension chord model for structural concrete. Structural Engineering International 1998; 8(4): 287-298.

[20] Yuan H, Teng JG, Seracino R, Wu ZS, Yao J. Full-range behavior of FRP-to-concrete bonded joints, Engineering Structures 2004; 26 (5):543-691.

[21] Oehlers DJ, Liu IST, Seracino, R. The gradual formation of hinges throughout reinforced concrete beams. Mechanics Based Design of Structures and Machines 2005; 33(3-4):375-400.

[22] Warner RF, Foster SJ, Kilpatrick AE. Reinforced Concrete Basics: Analysis and Design of Reinforced Concrete Structures. Pearson Education, Australia 2007.

[23] Haskett M, Oehlers DJ, Mohamed Ali MS. Local and global bond characteristics of steel reinforcing bars. Engineering Structures 2008; 30(2):376-383.

[24] Mohamed Ali MS, Oehlers DJ, Griffith MC, Seracino R. Interfacial stress transfer of near surface mounted FRP-to-concrete joints. Engineering Structures 2008; 30(7):1861-1868.

[25] Mohamed Ali MS, Oehlers DJ, Griffith MC. Shear transfer across cracks in FRP strengthened RC structures. ASCE Journal of Composites in Construction 2008; 12(4):416-424.

[26] Yankelevsky DZ, Jabareen M, and Abutbul AD. One-dimensional analysis of tension stiffening in reinforced concrete with discrete cracks. Engineering Structures 2008; 30:206-217.

[27] Muhamad R, Oehlers DJ, and Mohamed Ali MS. Discrete rotation deflection of RC beams at serviceability. Accepted Proc. ICE Structures and Buildings 2012.

[28] Muhamad R, Mohamed Ali MS, Oehlers DJ, and Griffith MC. The tension stiffening mechanism in Reinforced Concrete Prism. Accepted Advances in Structural Engineering 2012.

[29] Visintin P, Oehlers DJ, Haskett M. Partial-interaction time dependent behaviour of reinforced concrete beams Submitted to Magazine of Concrete Research 2012.

[30] Oehlers DJ, Mohamed Ali MS, Haskett M, Lucas W, Muhamad R. Visintin P, FRP reinforced concrete beams - a unified approach based on IC theory. ASCE Composites for Construction 2011; 15(3):293-303.

[31] CEB. *CEB-FIP Model Code 90*. London; 1992.

[32] Cosenza E, Manfredi G, Reakfonzo R, Behavior and Modeling of FRP to Concrete. Journal of Composites for Construction 1997; 1(2):40-51.

[33] Baena M, Torres L, Touron A, Barris C. Experimental study of bond behaviour between concrete and FRP bars using a pull-out test. Composites: Part B 2009; 40:784-797.

[34] ACI Committee 440. State-of-the-art report on fiber reinforced plastic FRP reinforcement for concrete structures. 1996; 65pp.

[35] Barris C, Torres LI, Turon A, Baena M, Catalan A. An experimental study of the flexural behavior of GFRP RC beams and comparison with prediction models. Composite Structures 2009; 91(3):286-295.

APPENDIX A: PARTIAL-INTERACTION TENSION-STIFFENING ANALYSIS

Governing equation

The fundamental equations for tension stiffening can be derived by considering the equations of equilibrium of a bonded joint such as that shown in Fig. 17(a) [28]. The equations governing this problem involve four fields: the axial stresses in the reinforcement (σ_r) and concrete (σ_c); the axial strains in the reinforcement (ε_r) and concrete (ε_c); the interface shear across the bonded length (τ) and the interface slip (δ) which is the difference between the axial displacement of the bar (u_r) and the concrete (u_c).

Examining Fig. A.1(b) and Fig. A.1(c) [28], the equilibrium equations for a prism under pure tension can be written as:

$$\frac{d\sigma_r}{dx} = \frac{\tau L_p}{A_r} \tag{A.1}$$

and

$$\frac{d\sigma_c}{dx} = -\frac{\tau L_p}{A_c} \tag{A.2}$$

and from Fig. A.1 (a) by equilibrium, the load acting at any section is:

$$P_r = \sigma_c A_c + \sigma_r A_r \tag{A.3}$$

where, A_r and A_c are the cross sectional areas of the reinforcing bar and prism respectively and L_p is the circumference of the reinforcement.

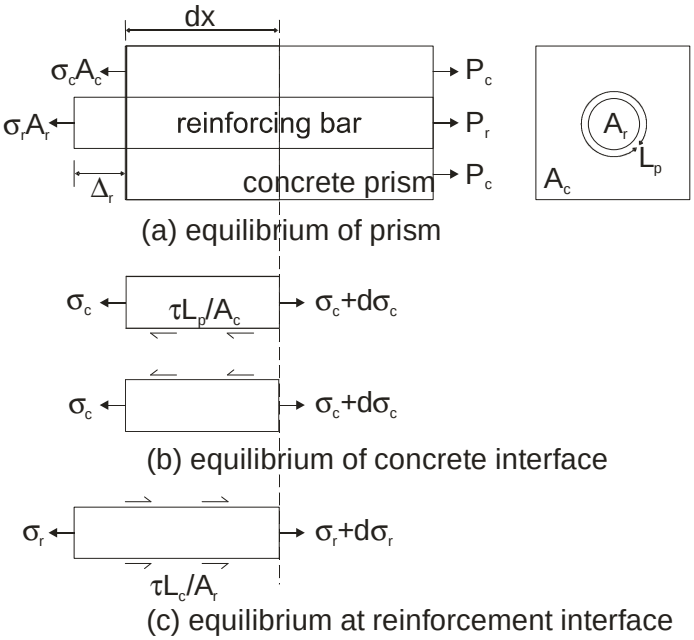

Figure A.1: Free body diagrams of partial interaction prism

The axial force P_r induces a relative slip between the bar and the surrounding concrete, that is,

$$\delta = u_r - u_c \tag{A.4}$$

Differentiating the slip δ gives the following slip strain

$$\frac{d\delta}{dx} = \frac{du_r}{dx} - \frac{du_c}{dx} \tag{A.5}$$

As $\frac{du_r}{dx}$ is simply the reinforcing strain and $\frac{du_c}{dx}$ is the concrete strain, and since the elastic moduli of the bar (E_r) and concrete (E_c) are known, the stress in the bar and in the concrete are as follows

$$\sigma_r = E_r \varepsilon_r = E_r \frac{du_r}{dx} \tag{A.6}$$

$$\sigma_c = E_c \varepsilon_c = E_c \frac{du_c}{dx} \tag{A.7}$$

Substituting Eqs. A.6 an A.7 into Eq. A.5 gives:

$$\frac{d\delta}{dx} = \frac{\sigma_r}{E_r} - \frac{\sigma_c}{E_c} \tag{A.8}$$

and differentiating yields

$$\frac{d^2\delta}{dx^2} = \frac{1}{E_r}\left(\frac{d\sigma_r}{dx}\right) - \frac{1}{E_c}\left(\frac{d\sigma_c}{dx}\right) \tag{A.9}$$

Substituting Eqs. A.1 and A.2 into Eq. A.9 gives the governing equation

$$\frac{d^2\delta}{dx^2} - \beta_2 \tau = 0 \tag{A.10}$$

where

$$\beta_2 = \frac{L_p}{A_r}\left(\frac{1}{E_r} + \frac{A_r}{E_c A_c}\right) \tag{A.11}$$

The governing equation (Eq. A.10) can then be solved using a known bond slip (τ-δ) relationship and knowing the boundary condition to the specific tension stiffening problem.

Crack spacing

Fig. A.2 [28] shows the boundary conditions for the formation of primary cracks. In the uncracked member, an initial crack is assumed to form at some location at x = 0; at the initial crack, the strain in the concrete equals zero and, therefore, the slip strain is simply the strain in the bar where the force is P_r, that is,

$$\frac{d\delta}{dx} = \frac{P_r}{A_r E_r} \text{ and } \delta = \Delta_r \text{ at } x = 0 \tag{A.12}$$

The minimum crack spacing S_p is then defined as the point of full interaction some distance from the crack face where both the slip strain and the slip tend towards zero, that is,

$$\frac{d\delta}{dx} = 0 \text{ and } \delta = 0 \text{ at } x = S_p \tag{A.13}$$

This point S_p represents the minimum crack spacing as it is the point at which the concrete stress is at its maximum, hence the crack can form anywhere in the full interaction region shown in Fig. A.2(a). The crack spacing is, however, taken to be equal to S_p, that is, the minimum value is taken, as beams are normally subjected to a moment gradient.

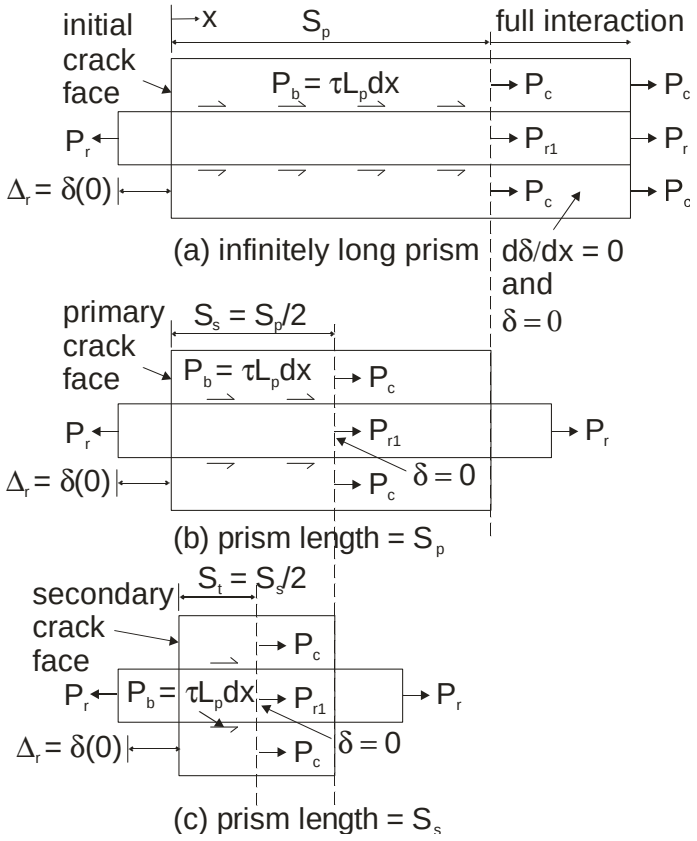

Figure A.2: Tension stiffening for concrete prism

Once a primary crack has formed at S_p from the initial crack in Fig. A.2, the problem now becomes that shown in Fig. A.2(b) which is that of a symmetrically loaded prism of length S_p. Since the prism is symmetrically loaded, the boundary condition at the midpoint of the prism, that is at the secondary crack spacing S_s becomes

$$\frac{d\delta}{dx} \neq 0 \text{ and } \delta = 0 \text{ at } x = S_p/2 = S_s \quad \text{(A.14)}$$

Finally if the bond is sufficiently strong such that secondary cracks can form at the midpoint of the prism of length S_s, that is at S_t in Fig. A.2(c), the boundary condition becomes

$$\frac{d\delta}{dx} \neq 0 \text{ and } \delta = 0 \text{ at } x = S_p/4 = S_t \quad \text{(A.15)}$$

Having now derived the boundary conditions for the formation of primary cracks, as well as tension stiffening for both primary and secondary cracks, it is possible to solve Eq. A.10 to determine the crack spacing and load-slip behaviour for the specific case of a linear ascending bond-slip.

Solutions for linear ascending bond slip characteristic

The bond slip for a linear ascending characteristic [17,20,24] can be written as

$$\tau = k_e \delta \quad \text{(A.16)}$$

where k_e is the stiffness of the bond slip (τ/δ) characteristic.

Substituting Eq. A.16 into Eq. A.10 yields

$$\frac{d^2\delta}{dx^2} - \beta_2 k_e \delta = 0 \quad \text{(A.17)}$$

which can be solved to give the following variation

$$\delta(x) = a\cosh(\lambda_1 x) + b\sinh(\lambda_1 x) \quad \text{(A.18)}$$

where

$$\lambda_1 = \sqrt{k_e \beta_2} \quad \text{(A.19)}$$

Differentiating Eq. A.18 yields

$$\frac{d\delta}{dx} = \lambda_1 a \sinh(\lambda_1 x) + \lambda_1 b \cosh(\lambda_1 x) \quad \text{(A.20)}$$

and substituting Eq. A.18 into Eq. A.16 gives

$$\tau(x) = k_e[a \cosh(\lambda_1 x) + b \sinh(\lambda_1 x)] \quad \text{(A.21)}$$

The constants *a* and *b* in Eqs. A.19 and A.21 can now be solved through the substitution of the boundary conditions as follows.

Crack spacing

Substituting the boundary conditions at the initial crack face, which are shown in Fig. A.2(a) and are given by Eq. A.12, into Eq. A.20 gives

$$b = \frac{P_r}{A_r E_r \lambda_1} \quad \text{(A.22)}$$

which along with the full interaction boundary conditions given in Eq. A.13 can be substituted in Eq. A.18 and Eq. A.20 yielding

$$a \cosh(\lambda_1 S_p) + \frac{P_r}{A_r E_r \lambda_1} \sinh(\lambda_1 S_p) = 0 \quad \text{(A.23)}$$

$$\lambda_1 a \sinh(\lambda_1 S_p) + \frac{P_r}{A_r E_r} \cosh(\lambda_1 S_p) = 0 \quad \text{(A.24)}$$

Since the hyperbolic equations have no analytical solution, it has been assumed the solution is achieved at 97% of the numerical solution and this gives a primary crack spacing of

$$S_p = \frac{2}{\lambda_1} \quad \text{(A.25)}$$

Load to cause primary cracking

Substituting Eq. A.25 back into Eq. A.22 yields

$$a = -\frac{P_r}{A_r E_r \lambda_1 (\tanh 2)} \quad \text{(A.26)}$$

The relationship between the force in the bar P_r at the initial crack located at x = 0 and the force in the bar P_{r1} and P_c at the initiation of the primary crack at x = S_p in Fig. A.2(a) can be written as

$$P_r - \int_{x=0}^{x=S_p} \tau L_p dx = P_{r1} \quad \text{(A.27)}$$

where,

$$P_r = P_{r1} + P_c \tag{A.28}$$

in which the integral in Eq. A.27 is the bond force and can be given by Eq. A.29 by solving Eq. A.27 and Eq. A.28 and in which the tensile cracking stress of the concrete is f_{ct}

$$\int_{x=0}^{x=S_{p,}S_s} \tau L_p dx = f_{ct} A_c \tag{A.29}$$

Since the full interaction condition is achieved at S_p it is also known that the strain in the reinforcement and the strain in the concrete are the same, and therefore,

$$P_{r1} = \frac{\sigma_c}{A_c} A_r E_r \tag{A.30}$$

Knowing the crack will form once the stress in the concrete equals the tensile cracking stress and substituting Eq. A.29 and Eq. A.30 into Eq. A.27 allows for the determination of the load to cause a principle crack $P_{r\_cr.}$

$$P_{r\_cr} = \frac{f_{ct}}{E_c} A_r E_r + f_{ct} A_c \tag{A.31}$$

For a linear ascending bond, the relationship between the bond force and the concrete force is given by Eq. A.28, and so substituting Eq. A.21 into Eq. A.29 gives the load to cause primary cracking based on partial interaction.

$$P_{r\_cr} = \frac{A_r E_r \lambda_1^2 \delta_1 f_{ct} A_c}{\tau_{max} L_p} \tag{A.32}$$

For the prism of length S_p shown in Fig. A.2(b), a secondary crack will form at $S_s = S_p/2 = 1/\lambda_1$ when the stress in the concrete reaches the tensile cracking stress and the same procedure is followed to determine the load to cause secondary cracking. Substituting Eq. A.22 and Eq. A.14 into Eq. A.18 gives the constraint *a* which in this case refers to a prism of length $S_{p.}$

$$a = -\frac{P_r}{A_r E_r \lambda_1} \tanh(1) \tag{A. 33}$$

Substituting Eq. A.32 and Eq. A.22 into Eq. A.21 and again into Eq. A.29 for the changed boundary conditions gives the load to cause a secondary crack as

$$P_{r\_cr} = \frac{A_r E_r \lambda_1^2 \delta_1 f_{ct} A_c}{0.352 \tau_{max} L_p} \quad \text{(A.34)}$$

Load slip behaviour

For a prism of length S_p, which corresponds to primary cracking, the slip Δ_r for a given load can be determined by substituting the constraints *a* and *b* given by Eq. A.33 and Eq. A.22 into Eq. A.18 where x = 0 to give

$$\Delta_r = \frac{P_r \tanh(1)}{A_r E_r \lambda_1} \quad \text{(A.35)}$$

Now considering the prism of length S_s in Fig. A2(c), by symmetry a tertiary crack will occur at $S_t = S_p/4 = 1/2\lambda_1$. Substituting Eq.A.22 and the boundary conditions for tertiary cracking as in Eq. A.15 into Eq. A.18 gives the unknown *a* in Eq. A.36.

$$a = -\frac{P_r}{A_r E_r \lambda_1} \tanh(0.5) \quad \text{(A.36)}$$

The slip for a given load for a prism of length S_s can then be given by Eq. A.37 which is obtained by substituting Eq. A.22 and Eq. A.36 into Eq. A.18 at x = 0.

$$\Delta_r = \frac{P_r \tanh(0.5)}{A_r E_r \lambda_1} \quad \text{(A.37)}$$

Statement of Authorship

The fundamental mechanisms that govern the flexural ductility of all RC members

Construction and Building Materials: invited paper

Oehlers, D.J.

Supervised research and wrote paper.

I hereby certify that the statement of contribution is accurate

Signed……..Date……

Visintin, P. (candidate)

Developed research presented, performed analysis for and wrote energy absorption section and assisted in manuscript evaluation.

I hereby certify that the statement of contribution is accurate

Signed…….Date……

Haskett, M.

Developed research presented and assisted in manuscript evaluation.

I hereby certify that the statement of contribution is accurate and I give permission for the inclusion of the paper in the thesis

Signed …….Date……

Sebastian, W.

Assisted in manuscript evaluation.

I hereby certify that the statement of contribution is accurate and I give permission for the inclusion of the paper in the thesis

Signed ……..…….Date……

The fundamental mechanisms that govern the flexural ductility of RC members

D. J. Oehlers, P. Visintin, M. Haskett and W. M. Sebastian

ABSTRACT

Flexural ductility in reinforced concrete members may be defined as concentrations of rotation at discrete positions. As such, it affects all aspects of reinforced concrete behaviour at all limit states including: serviceability deflections, sectional and member strengths, moment redistribution and collapse. The ductility design rules developed for steel reinforced concrete members that use a full-interaction (FI), that is no slip between the reinforcement and the adjacent concrete, moment curvature (M/χ) approach are empirically based as at least one major component of each model, not including the material properties, such as the hinge length or effective flexural rigidity (EI_{emp}) has to be determined through tests. Being empirically based, these ductility models for steel RC members can only be used within the bounds of the tests from which they were developed, and as such, are of little use beyond these bounds, such as for FRP RC members. As an example, it will be shown that steel RC members rely on the ductility of the steel material to achieve member ductility. In contrast even though FRP as a material is brittle, FRP RC members can be designed to be ductile through weak bond. To understand this problem, in order to find a solution, the fundamental principles that govern the flexural ductility of reinforced concrete members with any type of reinforcement are first described. To overcome the empiricism of the current FI M/χ approach, a mechanics based partial-interaction (PI), that is there can be slip between the reinforcement and the concrete, moment-rotation (M/θ) model has been developed using the well established theories of partial-interaction and shear-friction. It will be shown that this purely mechanics based PI M/θ model can quantify the deflection of members at all limit states that is at serviceability, ultimate and at collapse, as well as quantify moment redistribution and energy absorption. Furthermore, it will be shown that the results from the PI M/θ approach can be used to derive equivalent flexural rigidities (EI_{equ}) to replace the empirical flexural rigidities EI_{emp} required for the FI M/χ approach; such that the PI M/θ approach can be considered as an extension or refinement of the FI M/χ approach by eliminating empirical components such as the hinge lengths or effective flexural rigidities. Being mechanics based, this model can cope with any type of reinforcement such as any type of FRP, any bond-slip characteristic and even with fibre reinforced concrete.

Keywords: reinforced concrete; ductility; tension-stiffening; concrete softening; and partial-interaction.

INTRODUCTION

What is ductility? There is the classic concept which consists of linear elastic behaviour, O-A in Fig. 1, followed by unlimited perfect plasticity A-B. This can be applied to: the material within a member where the stress is maintained over A-B, that is the material ductility; to a section of a member where the curvature is maintained over A-B, that is the sectional ductility; and to a member where the rotation is maintained, that is the member ductility. Unfortunately, reinforced concrete members do not exhibit any of these classic properties as illustrated in Fig. 1. Cracking, creep and shrinkage generally occurs at an early stage so that rarely is there linear elasticity. Furthermore, there is no reason why there should be a plastic plateau, and even if one could be approximated, it is at best of limited length due to concrete softening or reinforcement failure; and of such a limited length that it can affect the overall behaviour of the member.

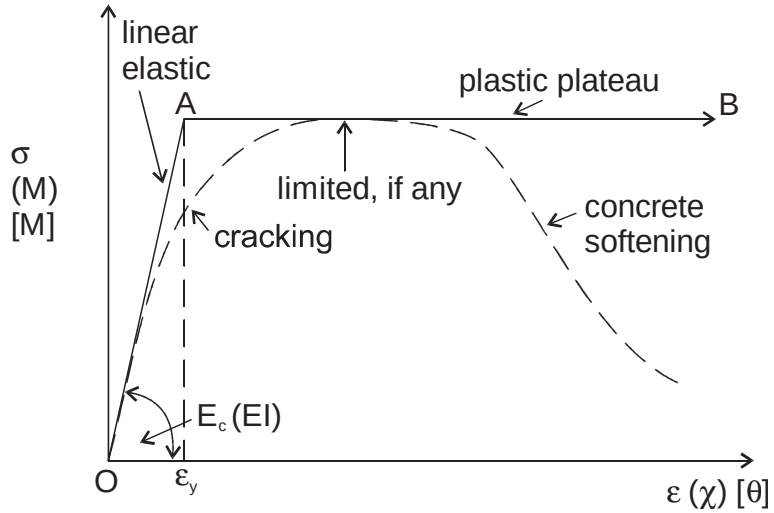

Fig.1 Ductility concepts

Member ductility is associated with concentrations of rotation often referred to as hinges or plastic hinges [1,2] which allow moment redistribution and energy absorption within members and frames. However, it may be worth noting that concentrations of rotation occur at all limit states after cracking has occurred, not just at the ultimate limit, causing a step change in member slope i.e. rotation between crack faces [3] across the crack. So when does ductility occur, or, what is ductility? A further problem is that material ductility does not necessarily provide sectional ductility, which does not necessarily provide member ductility. For example, there is no guarantee that using a ductile material will ensure member ductility and there is absolutely no reason to assume that a brittle material will automatically lead to a brittle structure. So what causes ductility?

To illustrate what actually occurs in practice, let us look at the behaviour of two span continuous beams reinforced internally with steel reinforcing bars but strengthened externally

over the hogging region with externally bonded (EB) fibre reinforced polymer (FRP) plates as in Fig. 2 [4,5]. FRP is a brittle material and EB plates are known to have a weak bond [6]. As such, guidelines tend to suggest that these FRP plated members should be treated as brittle so that no moment redistribution should be allowed. To evaluate the brittleness of the plated member, moment redistribution is a good gauge of ductility as it requires concentrations of rotation to occur. The variation of the percentage moment redistribution with the applied load, M_{static}, as a proportion of the theoretical ultimate load, $(M_{static})_u$, is shown in Fig. 3 for 7 beam tests; it is clear that large amounts of moment redistribution are occurring at ultimate. FRP is a brittle material, so if member ductility is directly related to material ductility, then there should, in theory, be no redistribution in Fig. 3. Therefore, what mechanism is providing this ductility? It can also be seen that moment redistribution does not only occur at the ultimate limit, but rather starts from the onset of cracking so that ductility occurs at all load levels. Once again, what mechanism is causing this ductility prior to the formation of "hinges" at ultimate.

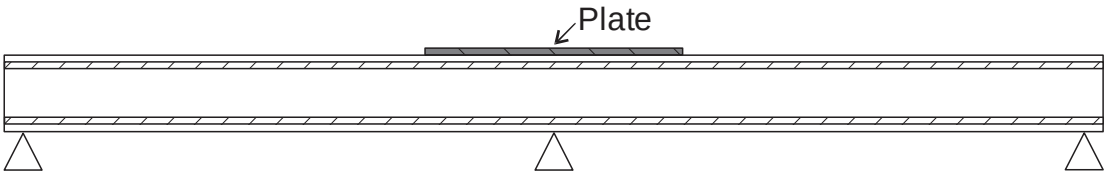

Fig. 2 Two span continuous beam strengthened with FRP plates

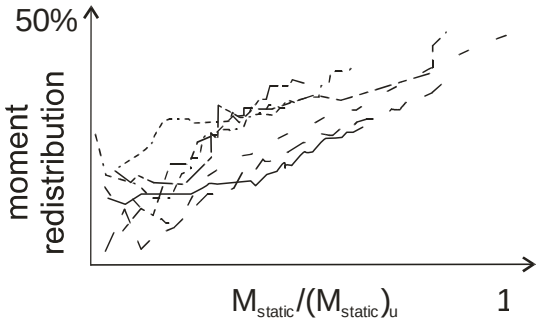

Fig. 3 Moment redistribution in beam with EB FRP plates

The results from two span continuous beams similar to those in Fig. 2, but this time strengthened with near surface mounted brittle FRP plates which have stronger and more ductile bond properties than FRP EB plates [6] are shown in Fig. 4 [5,7]. The results are similar to those in Fig. 3, which were strengthened with EB FRP plates, but are also in some ways better, showing in Fig. 4 large amounts of moment redistribution being maintained over wide ranges of load.

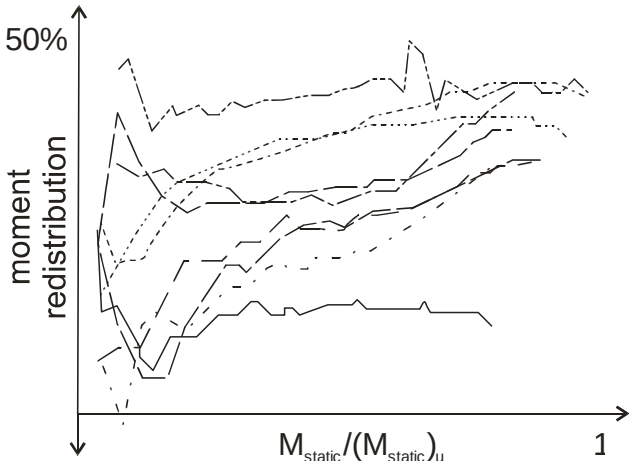

Fig. 4 Moment redistribution in beam with NSM FRP plates

What is providing the increasing ductility in Figs. 3 and 4? Fig. 5 shows the hogging region of the beam in Fig. 2 which has been strengthened with a longitudinal pair of NSM FRP plates the positions of which have been marked on the top surface [5]. Flexural/shear cracks which are as wide as the beam can be seen to be intercepting the FRP reinforcement. It can also be seen on the top surface between these flexural cracks a herringbone formation of much smaller cracks on either side of the NSM reinforcement. This herringbone formation of cracks is associated with debonding [6] and it will be shown that it is this debonding mechanism that allows these FRP reinforced beams to redistribute moment that is to act in a ductile fashion.

Fig. 5 Debonding of NSM plates

It is not just flexural cracking as in Fig. 5 that induces concentrations of rotation and consequently ductility but another major contributor to ductility is the formation of compression wedges as in Fig. 6 [8] which allows the concrete compression zone to accommodate within a member, for example, the large rotations between crack faces. It will be shown that it is this shear-friction mechanism associated with wedge formation [9] which also controls or limits the ductility, that is the ability to rotate.

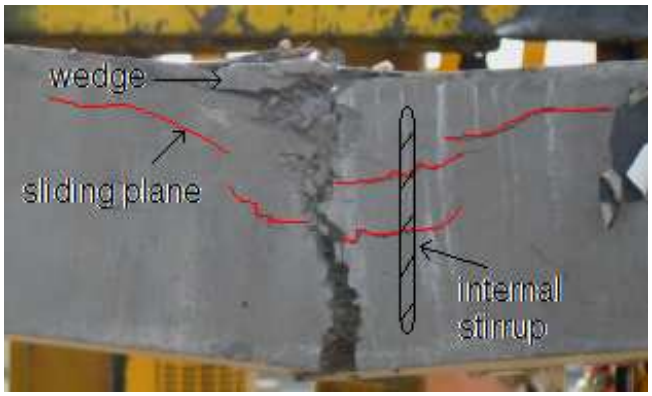

Fig. 6 Formation of wedges leading to concrete softening

It is suggested that member ductility is a mechanism and it can only be quantified through the study of the member ductility mechanism which is the subject of this paper. Hence material ductility by itself and sectional ductility by itself can never be used to quantify member ductility by themselves and as such these approaches will always have to resort to empirical components for the model. However once the member ductility mechanism has been quantified, it will be shown that it can be converted to convenient equivalent sectional properties or equivalent material properties for use in ductility analysis or design.

The fundamental mechanisms that control the behaviour of reinforced concrete members subjected to flexure and/or axial loads is first described. This section helps illustrate the importance of the partial-interaction (PI) bond-slip characteristics between the reinforcement and the concrete, that is the slip between the reinforcement and its adjacent concrete, which is often neglected. Although the same mechanisms can be extended to quantify the shear behaviour [10], it is felt that this is outside the scope of this paper. Methods for quantifying the ductility mechanism due to flexural cracking by considering the PI behaviour of a localised segment of the member are then explained. This section helps distinguish between the different debonding mechanisms that occur: that in which debonding is localised and does not reduce or limit the force in the reinforcement and which will be referred to as a 'strong' bond mechanism although 'strong' refers to the debonding mechanism and not the bond strength; and those in which debonding reduces or limits the force in the reinforcement and which will be referred to as a 'weak' bond mechanism in which 'weak' refers to the debonding mechanism and not the bond material strength. The ductility due to the concrete softening associated with the formation of wedges is then explained using shear-friction theory in the segmental approach. This helps illustrate how concrete softening is a mechanism that can be simulated using shear-friction theory. Finally the effect of the localised rotations which have been quantified through the segmental approach are applied to the analysis of members. This helps illustrate what is known in practice that ductility occurs as soon as flexural cracking or concrete softening occurs, and it also illustrates how these

ductility mechanisms can be applied to all RC members that is in theory to any type of concrete, to any type of reinforcement, with any bond-slip characteristics, and at any load stage from serviceability through to collapse.

FUNDAMENTAL MECHANISMS WITHIN RC MEMBERS

There would appear to be three fundamental mechanisms that contribute to the ductility of a member: (1) the interaction between flexural cracks through the reinforcement connecting the cracked regions; (2) concrete softening through the formation of wedges; and (3) confinement of the wedges through, for example, stirrups or FRP wrap.

(1) Flexural cracking in a beam

Let us consider the development of flexural cracks in an RC beam, although, the same principles apply to columns as well. To simulate the behaviour, we need a numerical model that simulates the bond-slip between the reinforcement and its adjacent concrete, that is partial-interaction, as this allows: cracks to widen; the gradual formation and development of cracks at discrete positions; and importantly the interaction between cracks [11-13]. This simulation requires a bond-slip property such as the idealised bond-slip property is shown in Fig. 7 where k_e is the elastic bond stiffness, $\tau_{b.max}$ is the maximum bond shear stress and s_f is the bond slip beyond which the shear stress is zero and it is, importantly, the slip at which debonding can be considered to commence.

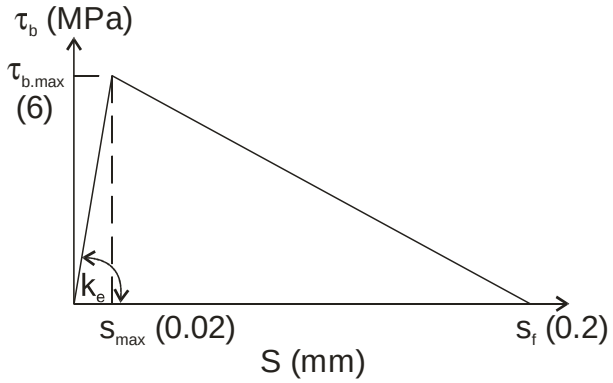

Fig. 7 Idealised bond-slip properties

A typical result of a numerical partial-interaction simulation of a loaded beam is illustrated in Fig. 8 [12]. The beam is initially uncracked on first loading. The central *initial crack* first forms where the moment is greatest and the load at which this occurs can be determined from elementary FI M/χ analyses such as used in transformed sections. The initial crack causes slip, that is partial-interaction, between the reinforcement and the concrete which controls the formation of the adjacent cracks referred to as the *primary cracks*. The region within which slip occurs has been labelled the partial-interaction region such that the slip s and slip-strain ds/dx are not zero. Beyond this region is the full-interaction region where both the slip and slip-strain are zero as shown. Between cracks, the slip reverses in direction as in A-B-C. If

the cracked region was in a constant moment region, then the slip distribution A-B would be equal and opposite to B-C as the force in the reinforcement at each crack is the same; this also occurs in tension-stiffening tests as in Fig. 9 [14,15]. From the primary crack to the full-interaction region in Fig. 8, slip is only in one direction D-E which is similar to that obtained in pull-tests [16,17].

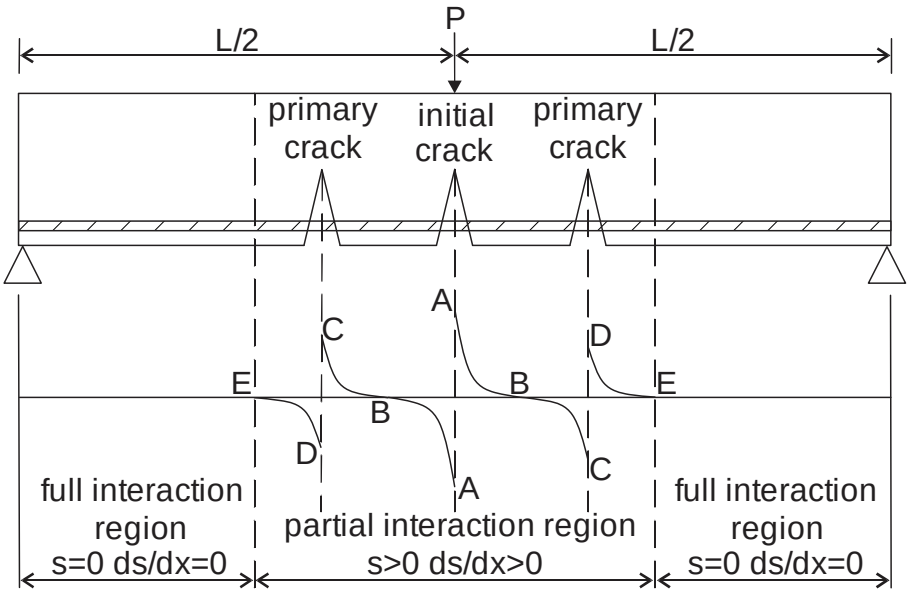

Fig. 8 Idealised behaviour of an RC beam

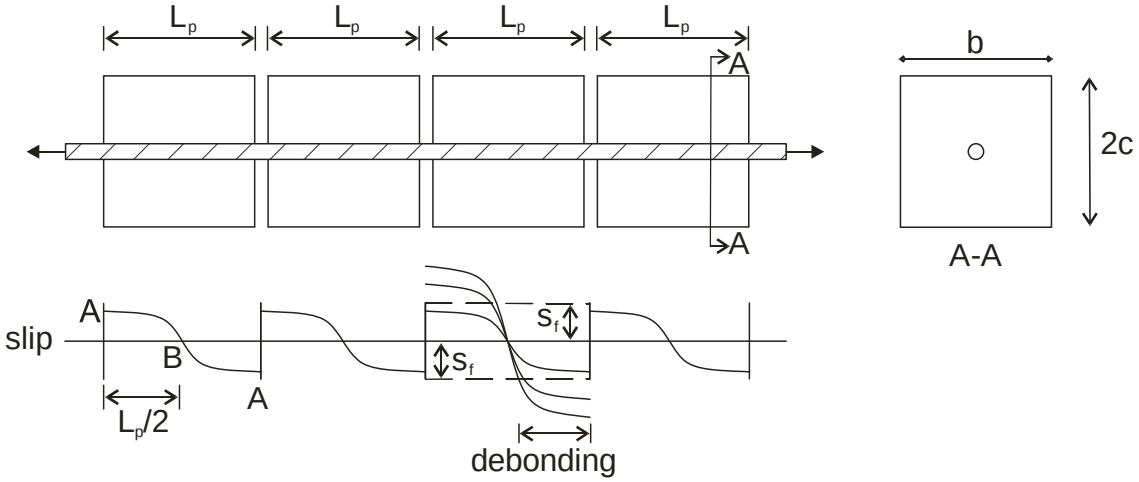

Fig. 9 Tension stiffening tests

Let us look at what happens after the formation of the initial crack in Fig. 8 [5,12]. The bond slip properties in Fig. 7 were used in which the maximum shear stress $\tau_{b.max}$ is 6 MPa and the slip at debonding s_f is 0.2 mm. The following results in Figs. 10 to 12 [12] are only for the region of the beam to the right of the initial crack in Fig. 8 as what happens to the left is a

mirror image. Furthermore, they are shown for increasing half crack widths s_{cr} that is at 0.05mm which is prior to debonding, 0.2mm which is at the onset of debonding and at 0.5mm in which debonding has occurred over O-C in Fig. 11. As the crack widens, the slip distribution gradually increases as in Fig. 10 causing the gradual build up of bond stress in Fig. 11 until the bond stress is fully developed at O-A-B at a half crack width of 0.2 mm; the force in the reinforcement to cause this full build up of the bond-stress is often referred to as the intermediate-crack (IC) debonding resistance P_{IC} and the strain in the reinforcement at the crack face at which this occurs is ε_{IC} in Fig. 12 [16,18,19]. Any further increase in the half crack width such as at 0.5 mm in Fig. 11 causes the bond stress distribution to move along the reinforcement from the fully developed O-A-B to C-D-E that is debonding occurs over O-C in Fig. 11 which is also shown in Fig. 12 as L_{dbd} where the strain in the reinforcement ε_{IC} remains constant. However, the shape of the bond stress distribution C-D-E remains unchanged whilst debonding, that is it is the same as when the bond is first fully developed as in O-A-B.

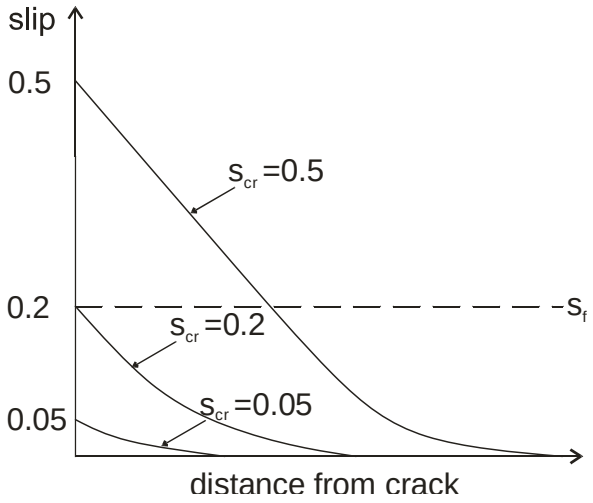

Fig. 10 Slip in beam with a single crack

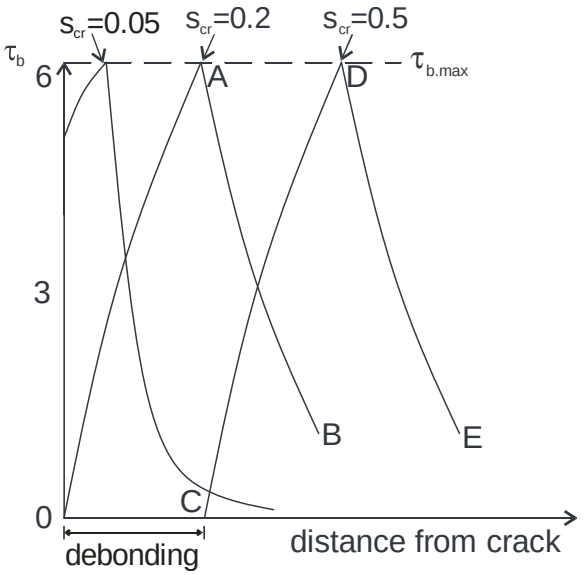

Fig. 11 Bond stress in beam with a single crack

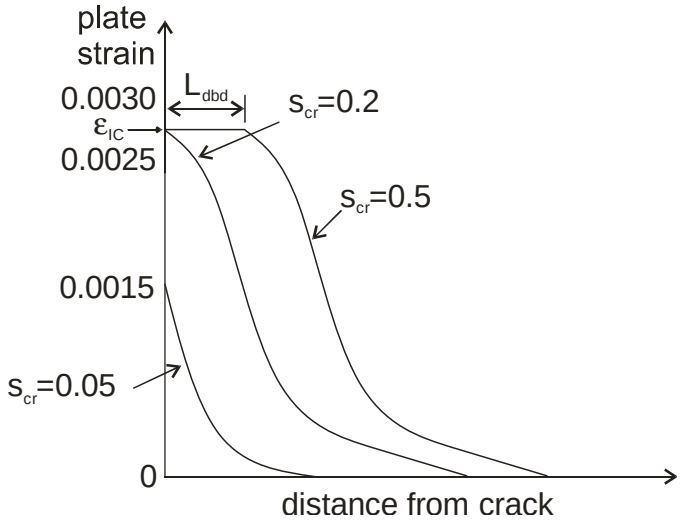

Fig. 12 Reinforcement strain in beam with single crack

Importantly, the half crack width, such as s_{cr} = 0.5 mm in Fig. 12, consists of two components. The half crack width at which the IC debonding resistance is first fully developed that is s_f, which in this case is 0.20 mm, and which occurs at a strain of ε_{IC} which is approximately 0.0027 in Fig. 12. Plus the extension of the plate over the debonded region L_{dbd}, that is, ε_{IC} $L_{dbd,}$ which in this case is approximately 0.3 mm. It can be seen that the crack widening due to debonding along L_{dbd} of 0.3 mm is the same order of magnitude as the half crack width of 0.20 mm required to induce the IC debonding resistance. This crack widening directly contributes to the rotation between crack faces and consequently the ductility. It is this combination of slips which can provide ductility in members which contain both brittle materials (e.g. FRP) and brittle bond characteristics (e.g externally bonded plates), suggesting that ductility can be greatly enhanced by debonding.

When multiple cracks form, the slip distribution in a segment between cracks starts off as in the reverse slip distribution A-B-C in Fig. 8. If the segment is in a constant moment region, then the slip distribution remains symmetrical as in Fig. 9 and debonding can occur within a segment when the slip exceeds the slip capacity of the reinforcement s_f in Fig. 9. However, each segment of length L_p between cracks acts individually, preventing debonding between segments even if the bond is weak. When multiple cracks form in a constant moment region, the force in the reinforcement at each crack location must be identical so that the slip distribution, and consequently the bond stresses, must be equal and opposite about B at $L_p/2$. This behaviour can also be assumed to apply in members with low moment gradients and to members with very strong bond where debonding between segments does not occur prior to the reinforcement yielding or the concrete crushing. In these circumstances, debonding can only occur within a segment as illustrated in Fig. 9 and the force in the reinforcement is not limited by the bond characteristics. As the force in the reinforcement is not limited by the bond, this behaviour will referred to as the *strong bond mechanism* and as has been explained it can occur not only with strong bond but also with weak bond should the variation in the stress resultants be favourable.

If the bond is weak and there is also a steep moment gradient, then the slip can vary as in Fig. 13 [12], where crack 1 is the initial crack and cracks 2 and 3 are primary cracks; these cracks divide the beam into segments as shown. The slip distribution A has a slip at the initial crack face of 0.19 mm, as can be seen at the intercept with the ordinate, and reverses in direction in Segments 1 and 2. Part of slip distribution B exceeds s_f but it still reverses in direction. At slip distribution C, the slip in Segment 1 is now in one direction and the step change shown is the total crack width of crack 2 which is about 0.67 mm. At slip distribution D, the slip on either side of crack 2 is the same so that crack 2 has now closed. It can be seen that debonding allows cracks to close.

The slip distributions in Fig. 13, induce the reinforcement strains in Fig. 14. As the reinforcement load is increased, the slips A, B and C in Fig. 13 induce the corresponding strain distributions in Fig. 14. The strains can exceed the IC debonding strain ε_{IC} as can be seen in distributions B and C but once the crack closes as in D in Fig. 13, then the strains are limited by ε_{IC} as in D in Fig. 14. Distributions A, B and C represent the *strong bond mechanism* whilst distribution D represents the *weak bond mechanism*. The more cracks there are, the closer the mechanism resembles that of a tension stiffening test in Fig. 9, where in theory, there is an unlimited strain capacity in the reinforcement due to the symmetry of the slip. However, as the cracks close, the mechanism moves from that of multiple cracking in Figs. 9 and 14 to that of a single crack in Fig. 12 where the IC debonding resistance and behaviour controls. Hence, the IC debonding behaviour for an individual crack is equal to, or

a lower bound to that which occurs in beams, and will provide a useful conservative design (Liu et al 2007a).

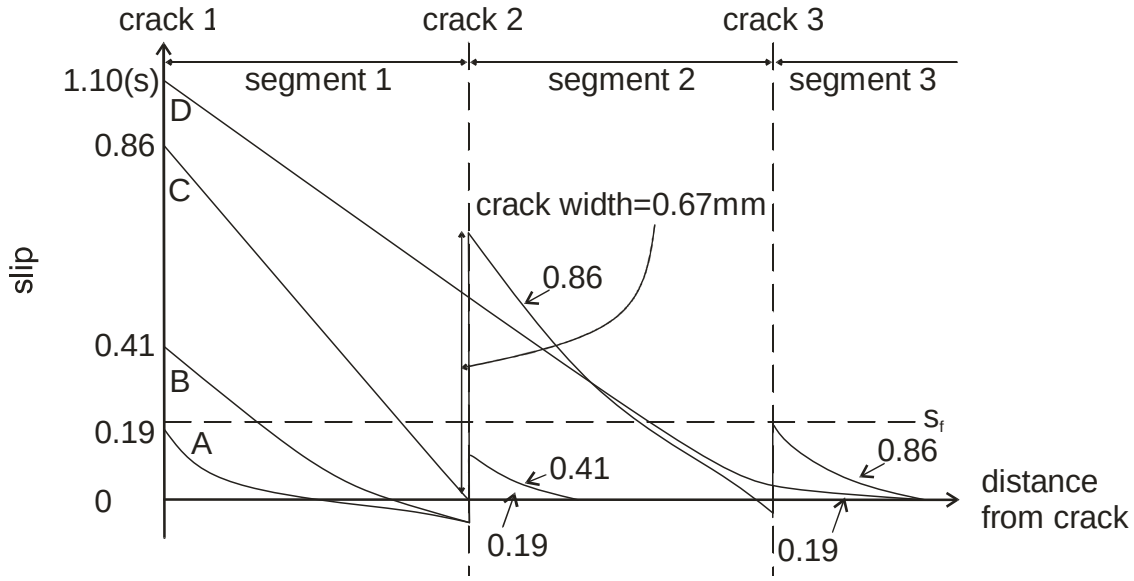

Fig. 13 Slip in a beam with multiple cracks

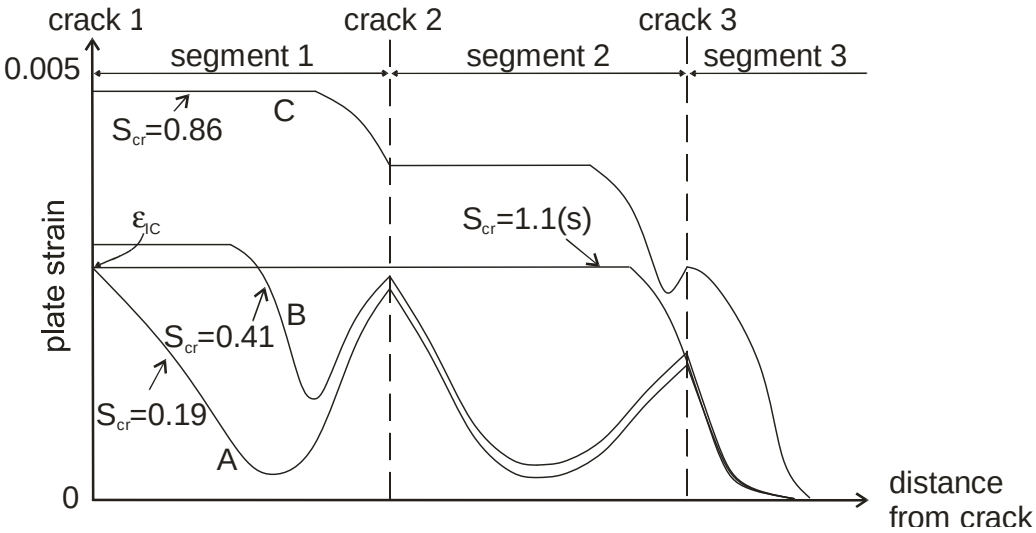

Fig. 14 Reinforcement strain in a beam with multiple cracks

(2) Concrete softening mechanism

The mechanisms responsible for providing ductility in the tension region have been explained previously. In order for a beam to be ductile, the compression region must also display ductility. Concrete resists excessive compressive strains beyond its material deformation capacity by forming wedges as in Fig. 6. In deep beams, these wedges tend to slide off soon after forming and this can severely reduce the member ductility at the ultimate

limit. In contrast, shallow beams can remain stable through large rotations even after a wedge has formed and allow the member to behave in a ductile fashion. It is known that internal steel stirrups such as that illustrated in Fig. 6, even when not required for shear, can further increase the flexural ductility by inhibiting the wedges from sliding off. The same effect can occur when the RC member is wrapped in either steel or FRP and this is often referred to as confinement. This concrete ductility and the effect of confinement on this ductility can be explained through a shear-friction mechanism [20-22].

Let us consider the behaviour of a cylinder or prism of height L_{pr} that is being subjected to an axial stress σ_{axl} and maybe a lateral stress σ_{lat} as in Fig. 15 [20]. It is common practice experimentally to measure the total axial contraction along A-A in Fig. 15(b) in order to plot the behaviour as a stress-strain relationship as in Fig. 16, in which there is an ascending branch, which may be considered as a material property, and a descending or softening branch, which is often considered to be size dependent and represents the formation of wedges.

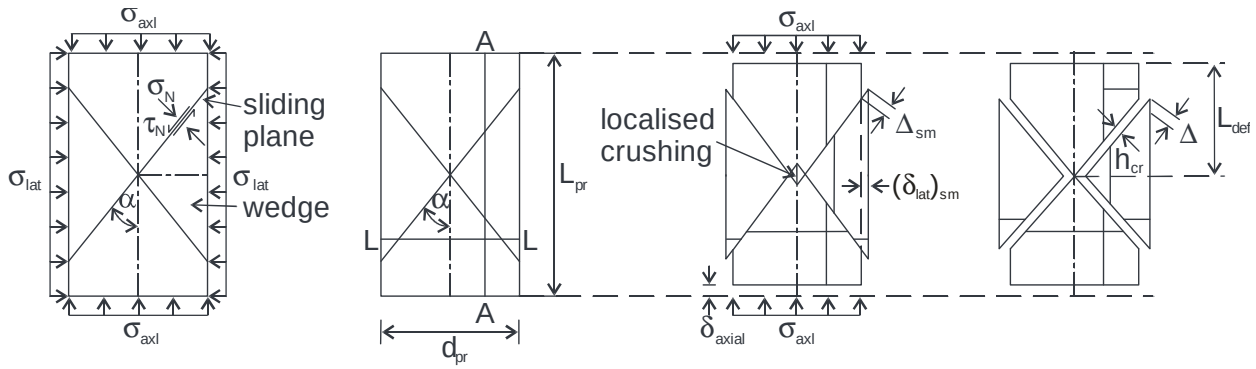

Fig. 15 Shear-friction mechanism

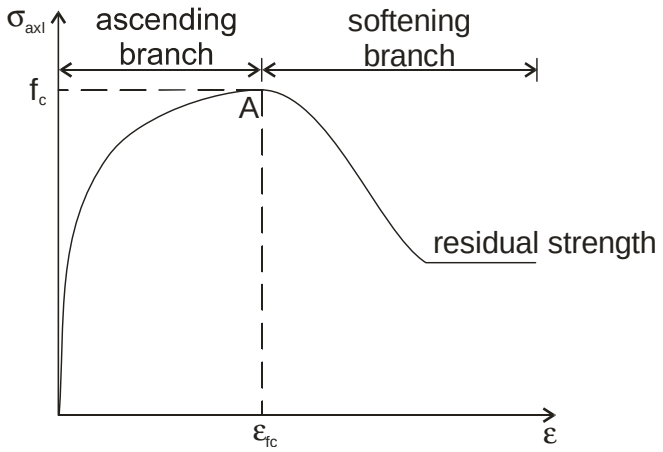

Fig. 16 Idealised concrete stress-strain relationship

The angle of a possible wedge, α in Fig. 15(a) depends on the Mohr Coulomb frictional properties as does the residual strength in Fig. 16 [9]. In the shear-friction mechanism, line A-A in Fig. 15(b) can keep contracting until the peak stress f_c at the strain ε_{fc} in Fig. 16 is achieved. The material itself cannot accommodate a strain greater than $\varepsilon_{fc,}$ that is, the material cannot accommodate a contraction greater than $\varepsilon_{fc}L_{pr}$. Hence if a greater contraction is required, then this is accommodated by sliding of the wedges Δ_{sm} as in Fig. 15(c) with a corresponding opening of the sliding planes due to aggregate interlock h_{cr} as in Fig. 15(d). The same can be said for the lateral dilation along L-L in Fig. 15(b) which is governed by the material Poisson effect ν and sliding Δ_{sm} and crack widening h_{cr}. The axial and lateral stresses σ_{axl} and σ_{lat} in Fig. 15(a) induce, through equilibrium, stresses normal to the sliding plane σ_N and shear stresses along the sliding plane τ_N which act in conjunction with Δ_{sm} and h_{cr}. These four parameters (σ_N, τ_N, Δ_{sm} and h_{cr}) are the shear friction properties as illustrated in Fig. 17 which when derived from prism tests as in Fig. 15 are for the case of initially uncracked concrete. They do not represent failure but are combinations of the shear-friction parameters that exist together much the same way as the stress-strain relationship in Fig. 16 are combinations that exist. It can be seen that softening in Fig. 16 is no longer considered to be purely a material property but rather a shear-friction mechanism, where excessive deformations are accommodated through the formation of wedges.

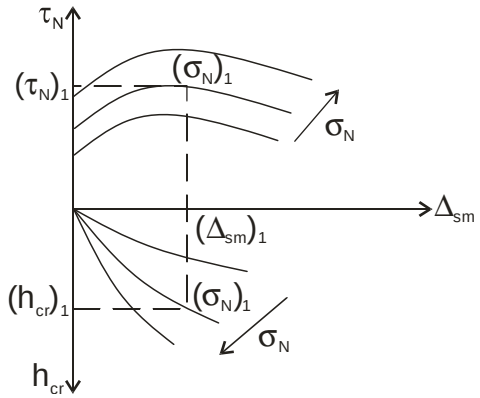

Fig. 17 Idealised shear friction properties

(3) Confinement of wedges

Let us now consider the situation when a reinforcing bar crosses a sliding plane such as would occur if a the stirrup crosses the sliding plane formed by the wedge as illustrated in Fig. 6. The behaviour, illustrated in Fig. 18, is governed by both shear-friction theory and by partial-interaction theory [10,23]. For example, let us impose a crack width h_{cr} on the mechanism in Fig. 18. The reinforcing bar slips $h_{cr}/2$ at each crack face. Knowing the bond-slip properties (τ/δ) and the material properties of the bar, the force in the bar P can be derived for that crack face slip $h_{cr}/2$ [17,24]. This induces an equal and opposite compressive force P across the sliding plane and consequently the normal confining stress σ_N is known.

Hence $(\sigma_N)_1$ and $(h_{cr})_1$ are known in Fig. 17 so there is only one vale of $(\Delta_{sm})_1$ and one value of $(\tau_N)_1$ that corresponds as illustrated in Fig. 17. Hence a combination of shear-friction theory and partial-interaction theory can be used to simulate the effect of confinement due to stirrups or FRP wrap on the concrete in compression, where the presence of stirrups or FRP wrap increases the normal force across the sliding plane, delaying concrete failure in the form of unstable sliding [23].

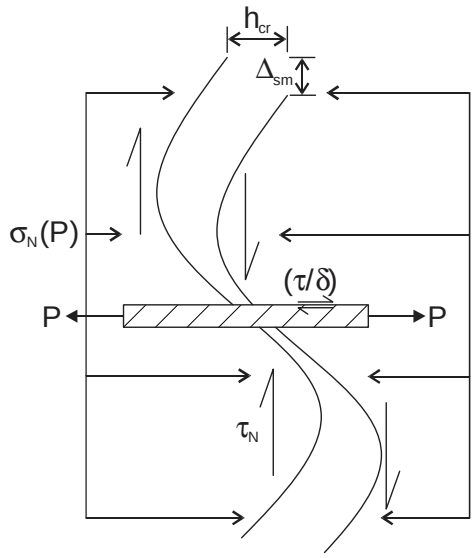

Fig. 18 Interaction between shear-friction and partial-interaction

SEGMENTAL ANALYSIS

The fundamental mechanisms within RC members described above, can be incorporated in a segmental analysis procedure [22, 25] to quantify the variation in flexural rigidity (EI) of a section for use in design. In order to do this, let us consider the behaviour of a short segment of a member of length $2L_{def}$ as illustrated in Fig. 19, which is subjected to an applied constant moment M and axial load P. As this segment is symmetrically loaded, the deformations at both the ends from A-A to C-C, which cause a rotation θ, are equal and opposite. Hence through symmetry, the mid-section of the segment B-B can be considered to remain stationary and the deformation to the right is identical to that on the left.

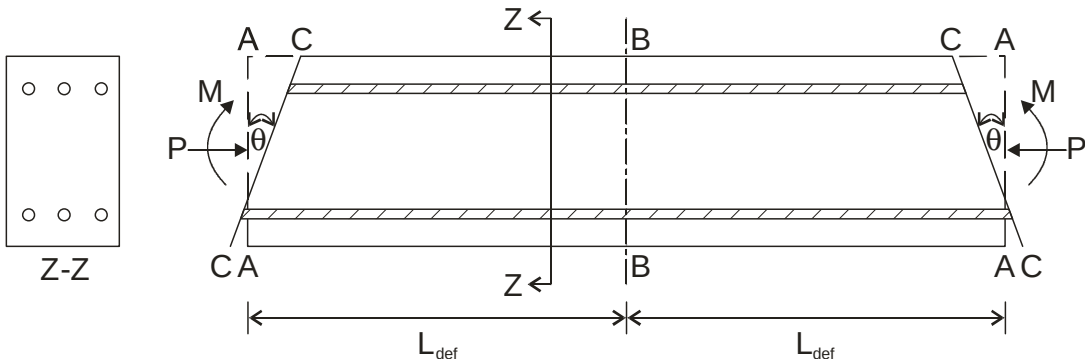

Fig. 19 Segment of a member

Segmental analysis of an uncracked element

First consider a segment which is uncracked as in Fig. 20 which corresponds to the right hand side of the segment in Fig. 19. Let us impose a rotation θ as shown in Fig. 20(a) in order to determine the moment M corresponding to this rotation for a known axial load P. The deformation from A-A to C-C induces the strain profile in Fig. 20(b) which can be used with the material properties to derive the stress distribution in Fig. 20(c), and consequently the force distribution in Fig. 20(d). It is a question of moving the deformation C-C in Fig. 20(a) up and down until the forces in Fig. 20(d) are in longitudinal equilibrium with P, after which the moment can be derived from Fig. 20(d) for the imposed rotation θ. This rotation can be divided by L_{def} to get the curvature χ and the moment divided by this curvature to get the flexural rigidity EI corresponding to the applied moment M and axial force P. The rotation can be increased to derive the $\tilde{M}\theta$ A-B of the uncracked section in Fig. 21(a), the M/□ relationship A-B in Fig. 21(b) prior to cracking and subsequently EI of the uncracked section as in Fig. 21(c). Importantly this segmental moment-rotation (M/θ) analysis prior to cracking or softening gives exactly the same results as the full-interaction (FI) moment-curvature (M/χ) analysis [26] that is commonly used by structural engineers, simply because the M/θ analysis is being used in its FI form.

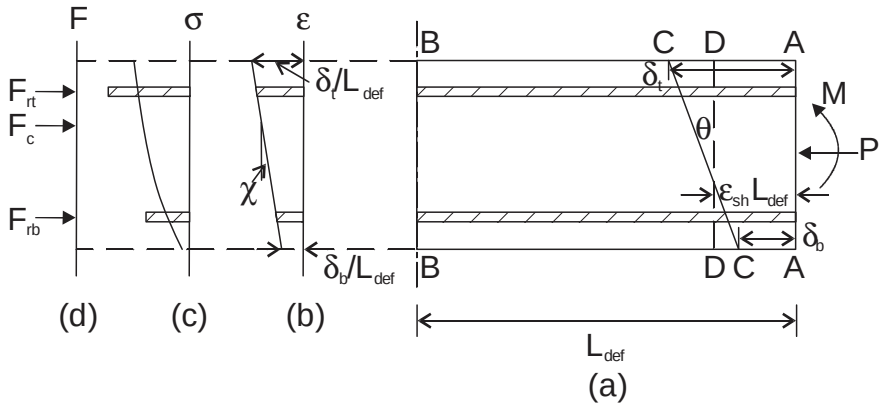

Fig. 20 Segmental analysis without cracking or softening

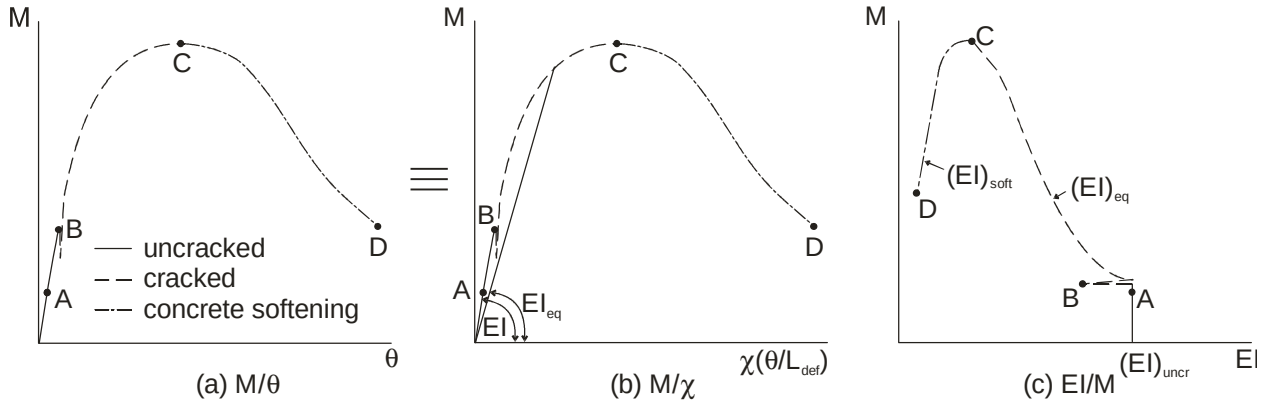

Fig. 21 Variations in member properties

It is very easy to include the effect of concrete shrinkage in this segmental analysis [27]. For example, a concrete shrinkage strain of ε_{sh} would cause the unrestrained concrete to contract by $\varepsilon_{sh}L_{def}$ to D-D in Fig. 20(a). Hence the concrete deformation along C-C should now be measured relative to D-D and not A-A, whilst that for the reinforcement should still be measured relative to A-A; in other respects, the analysis is the same and will yield a flexural rigidity that automatically allows for concrete shrinkage [27].

Single crack segmental analysis – weak bond mechanism

Let us now keep rotating the segment in Fig. 20(a) until the concrete tensile strain in Fig. 20(b) causes cracking. We will assume that a single crack develops at the centre as shown in Fig. 22(a). The analysis above the crack tip in Fig. 22 is exactly as that in Fig. 20, in that the forces above the crack tip depend on the material properties, that is, their stress-strain relationships. Below the crack tip, the force in the reinforcing bar F_{rb} depends on the interaction between the reinforcing bar, the crack width and the surrounding concrete. This behaviour is referred to as tension-stiffening and depends on the bond-slip (τ/δ) characteristics of the reinforcement.

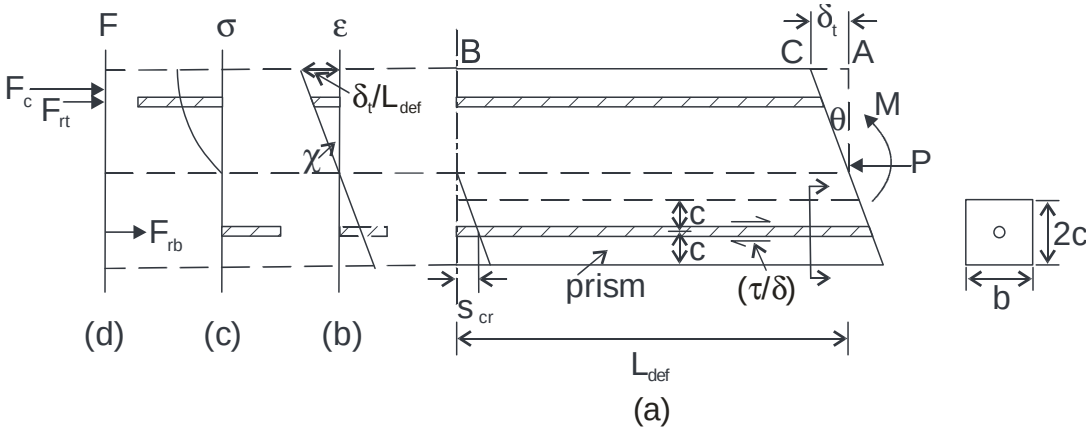

Fig. 22 Segmental analysis with a single crack

Tension-stiffening is often studied [15, 18, 28-39] by considering the partial-interaction behaviour of a reinforcing bar embedded in a concrete prism as indicated in Fig. 22(a).

The prism in Fig. 22(a) is shown in Fig. 23 where c is the cover provided to the reinforcement, b the section width and the bond-slip is τ/δ. The force in the reinforcement F_{rb} causes the reinforcement to slip relative to the crack face by s_{cr}. This interface slip diminishes along the length of the reinforcement, until at some point shown at the distance L_{FI} from the face, the slip tends to zero after which there is full-interaction. Over this region L_{FI}, the axial stress in the concrete builds up to its maximum value as in C in Fig. 23(d). As $F_{rb,}$ and consequently s_{cr} is increased, the bond stresses increase and reach their maximum distribution shown as C in Fig. 23(c). The load in the reinforcement corresponding to this slip and stress distribution is the IC debonding resistance $F_{IC,}$ and this force occurs at a specific crack face slip $s_{IC,}$ (s_f in Fig. 7) and reinforcement strain ε_{IC} Any imposed crack face slip greater than $s_{IC,}$ shown as Δ_s in Fig. 23(b), can only be accommodated by debonding along the length $L_{dbd,}$ such that the increase in slip beyond $s_{IC,}$ that is Δ_s, is equal to $\varepsilon_{IC}L_{dbd}$ and is accommodated over the partial-interaction region L_{pi}. It can be seen that debonding is a form of plasticity as the force P_{IC} is maintained with increasing reinforcement slip allowing increasing beam rotation.

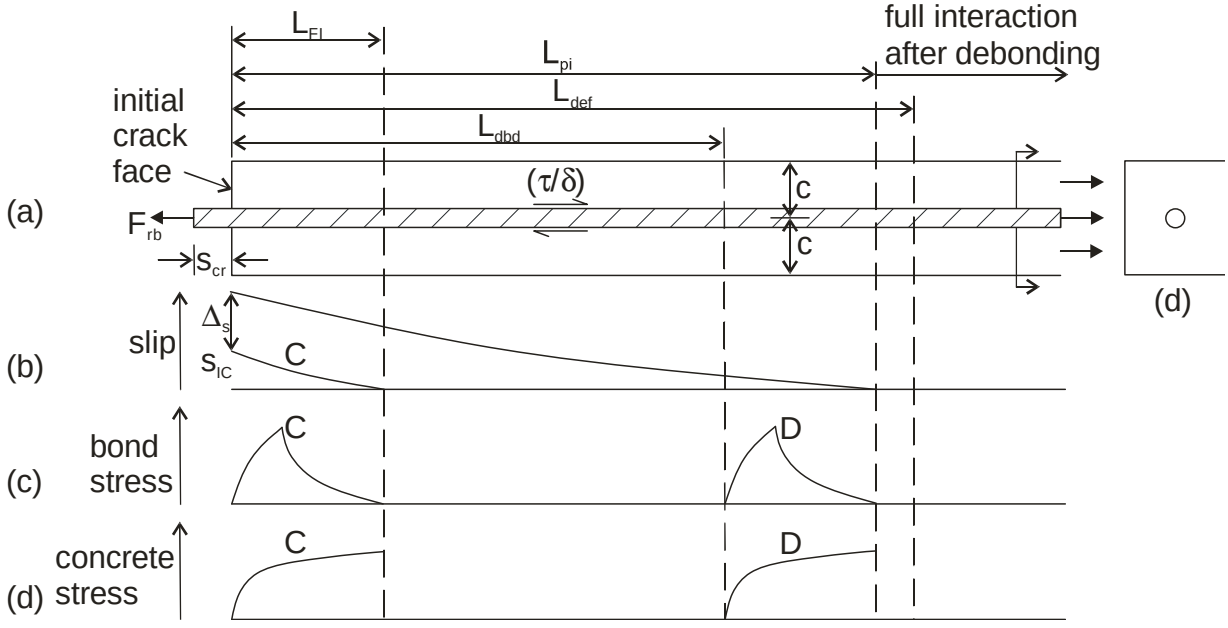

Fig. 23 Tension-stiffening behaviour with single crack.

The relationship between the reinforcement force F_{rb} and the slip at the crack face s_{cr} in Fig. 23 can be derived from numerical procedures which can cope with any bond-slip characteristic [24,33] and any material property, including reinforcement yield and strain-

hardening. Closed form solutions for specific shapes of bond-slip characteristics [37] and allowing for yield [33, 29] have also been developed. These partial-interaction approaches can then be used to derive F_{rb} in Fig. 22 where the segmental length L_{def} in Fig 22 must be greater than the length L_{FI} in Fig. 23 from the tension stiffening analysis. To accommodate debonding in the segmental analysis procedure, the length L_{def} in Fig. 22 must exceed L_{pi}. Using this analysis procedure, the variation in flexural rigidity for increasing moments post cracking can be determined, shown as B-C in Fig. 21. Hence, the segmental approach automatically allows for the variation in flexural rigidity due to tension-stiffening. It may also be worth noting that the inclusion of shrinkage in the tension-stiffening behaviour in Fig. 23 is very easy as the shrinkage strain is simply an additional slip-strain [27]. Concrete creep is also very easily accommodated in Fig. 22 by changing the concrete modulus and, hence, the time dependent variations in concrete can easily be incorporated both prior to and after cracking.

Steel reinforcing ribbed bars generally have good bond such that the reinforcement yields prior to debonding. The tension-stiffening models described above show that the slip at yield is relatively small, but, that yielding can increase this slip by an order of magnitude [33]. The same tension stiffening models show that FRP EB plates reach their IC debonding resistance at small slips, but, this can be increased by an order of magnitude through localised debonding around the crack face that is over a localised region L_{dbd} in Fig. 23. Hence, steel reinforced beams rely on steel material ductility for member ductility, and this is in contrast to FRP RC members which rely on weak bond.

Double crack segmental analysis – strong bond mechanism

The deformation imposed on the segment in Fig. 20 can be increased until cracks occur at both ends of the segment as shown in Fig. 24 where the crack spacing which is the segment length in Fig. 19 is now $2L_{def}$. From the single crack tension stiffening behaviour in Fig 23, the transfer of bond stresses from the bar to the adjacent concrete reduces the force in the bar as we travel away from the crack face, and correspondingly increases the tensile stresses in the concrete as shown at C in Fig. 23(d) until concrete cracking occurs. Hence this analysis gives the load in the reinforcement to cause primary cracking and, hence, the moment in the beam at which primary cracks occur. Primary cracks develop at L_{FI} in Fig. 23(d) and when the stress in the concrete exceeds the tensile capacity of the concrete. The load at the initial crack face corresponding to the formation of this crack is $F_{rb\text{-}pi}$. The corresponding minimum crack spacing is $L_{cr\text{-}pi}$ which occurs at the position of full-interaction that is L_{FI} [22,25]. Hence, the segment length $2L_{def}$ in Fig. 19 is the crack spacing L_{FI}. The left hand side of the segment in Fig. 19 is shown in Fig. 24 where L_{def} is $L_{FI}/2$.

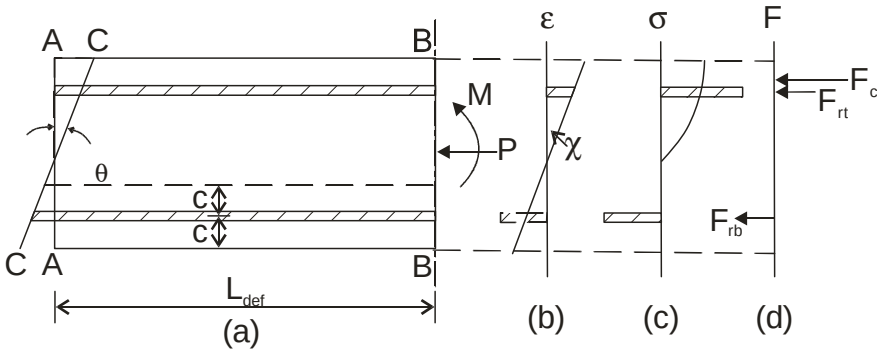

Fig. 24 Segmental analysis with a pair of cracks

After these primary cracks have developed on each side of the initial crack, the force in the reinforcement is now derived from the PI tension-stiffening analysis in Fig. 25(a), where the boundary condition is that the slip at mid-length is zero as in Fig. 25(b). The bond stress is also symmetrical as in Fig. 25(c). The region over which it acts can diminish from that in A where the bond stress acts over the whole length of reinforcement because the slip does not exceed s_f, to that in B where it acts over the region C-O-C where the slip is less than or equal to s_f. It can be seen that as the force in the reinforcement is increased, the bond force reduces but it does not limit the force in the reinforcement; this is the strong bond mechanism.

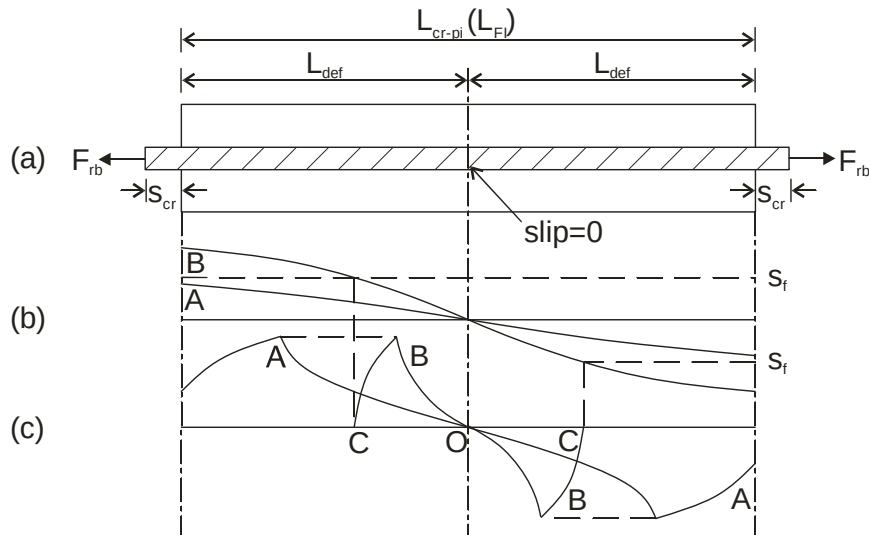

Fig. 25 Tension-stiffening behaviour with a pair of cracks.

The tension-stiffening analysis described above provides the relationship between crack width and reinforcement forces when primary cracks have formed, and is used in the segmental analysis in Fig. 24 to derive the sectional properties in regions of multiple cracks, that is, region B-C in Fig. 21. Numerical procedures are also available for the tension-stiffening and moment-rotation analyses [8,16,22,24,25,27,33] as well as closed form solutions [38]. It can be seen that the fundamental difference between the behaviour of a

single crack in Fig. 22 and that of multiple cracks in Fig. 24 are the tension stiffening behaviours shown in Figs. 23 and 25.

Segmental analysis with concrete softening

Concrete softening can be incorporated into the segmental analysis through the use of a softening stress-strain relationship if a reliable softening branch and its associated hinge length can be found. An alternative is to use shear-friction theory, which unlike softening stress-strain relationships and hinge lengths models the actual behaviour.

Compression wedges can also be incorporated into the segmental model as in Fig. 26(a). Let us impose a deformation B-B such that the deformation divided by L_{def} induces the effective strains D-E in Fig. 26(b). Let the maximum compressive strain that the concrete can resist as a material be ε_{fc} as in Fig. 16. Hence, the portion of the member below the strain of ε_{fc} in Fig. 26(b) can accommodate this deformation purely through material contraction; so the force in this concrete F_c in Fig. 26(d) can be determined from the ascending stress-strain relationship in Fig. 16. However, the portion above ε_{fc} in Fig. 26(b) cannot accommodate this deformation purely through material contraction, so a wedge of depth d_w must form to accommodate this non-material deformation through the mechanism of wedge sliding. At the base of the wedge, the entire deformation imposed on the segment can be accommodated by material straining and, hence, the wedge deformation Δ is zero. In contrast, the top of the wedge slides a maximum value of Δ_m as shown in Fig. 26(a). For the shear-friction analysis, it is convenient to slice the wedge into *n* small elements of depth d_e and to assume that the slip within an element is constant as shown in Fig. 26(e).

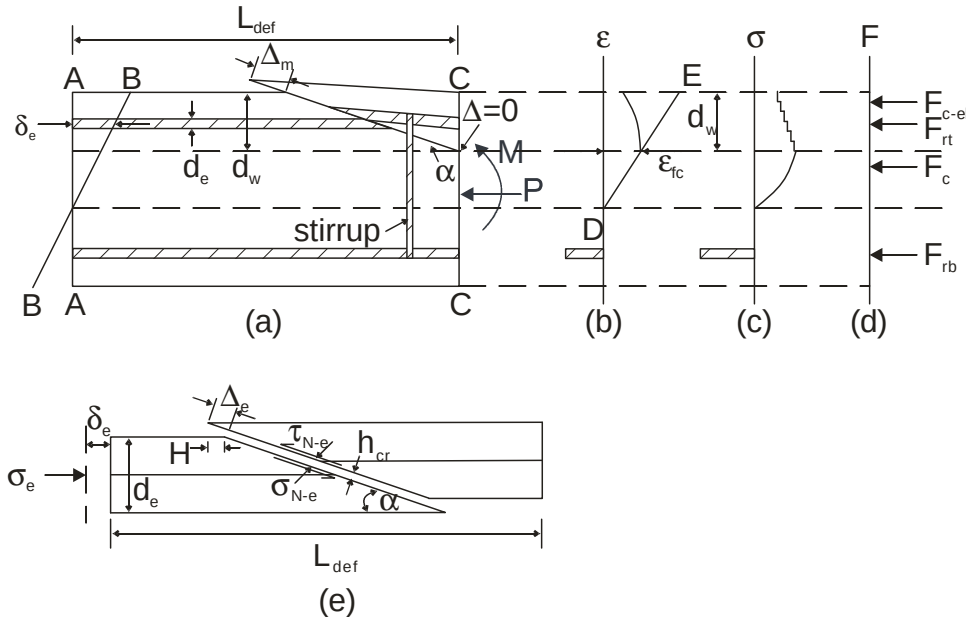

Fig. 26 Segmental analysis with concrete softening

The behaviour of the shear-friction wedge in Fig. 26(e) is identical to that in the top right hand corner of the prism in Fig. 15. The element of depth d_e in Fig. 26(a) is required to contract by δ_e as shown and which is also shown in Fig. 26(e). Let us guess that the axial stress in this element is σ_e so that from the material properties the strain is ε_e. Hence the contraction to be accommodated by sliding H_e is $\delta_e - \varepsilon_e L_{def}$. Depending on the angle of the wedge α [9] this has a sliding component Δ_e. Furthermore for an axial stress σ_e and the known angle α, $\sigma_{N\text{-}e}$ and $\tau_{N\text{-}e}$ are known through equilibrium as in Fig. 16(a). To determine whether this guess of σ_e is correct, we have to use the shear friction properties in Fig. 17.

To illustrate how a solution is found, let us first assume that the component of h_{cr} in Fig. 26(e) in the horizontal direction is negligible in comparison with the component of the slip Δ that is H in the horizontal direction; this is found to be the case in practice where the crack width component in the horizontal direction is at least an order of magnitude smaller than the sliding component H. Using Fig. 17. For the required Δ_e from above, that is $(\Delta_{sm})_1$ in Fig. 17 equals Δ_e, and the required σ_e from above, that is $(\sigma_N)_1$ in Fig. 17 equals σ_e, can be derived a value of $(\tau_N)_1$ in Fig. 17. If $(\tau_N)_1$ is not equal to the required $\tau_{N\text{-}e}$ from above, then the initial guess of σ_e has to be changed, that is iterated, until it is. If a more accurate analysis that incorporates crack widening h_{cr} is required, then this analysis also gives $(h_{cr})_1$ for Δ_e to $(\Delta_{sm})_1$ in Fig. 17 so that the contribution of h_{cr} on the contraction can be incorporated. However, a further iteration is required to converge.

This segmental analysis can also incorporate confinement. For example if steel stirrups crossed the wedge sliding plane as in Fig. 26(a) and they could be assumed to have yielded, then the confining stress σ_{lat} is known and this could be included in the equilibrium component of the analysis as in Fig. 16(a). This is equivalent to a hydrostatically or actively confined concrete. If the hydrostatic pressure is not known directly, then a more thorough analysis is to assume the vertical component of h_{cr} in Fig. 26(e) is the crack width and use partial-interaction analysis as depicted in Fig. 18 to determine the force in the reinforcement and consequently σ_{lat}. This can now be done only because the shear-friction properties as in Fig. 17 fully define the equilibrium and compatibility components.

The inclusion of concrete softening into the segmental analysis will give C-D in Fig. 21(a). As explained before, this can be converted to equivalent curvatures and flexural rigidities for the falling branch properties C-D in Figs. 21(b) and (c) for use in design. Care must be taken in using falling branch properties. As with all falling branch properties, these falling branch properties must be used in a defined length of member which in this case is L_{def} in Fig. 26 which must encompass the softening wedge [25]. It can be seen that the analysis can be done for any length L_{def} but the material properties extracted are peculiar to that length only, that is they will only give the correct rotations or hinge rotations for segments of that length only.

ANALYSIS OF MEMBERS

It has been shown how the effects of tension-stiffening, debonding, concrete softening and concrete confinement can be simulated in a PI M/θ segmental analysis to give sectional properties such as curvatures or flexural rigidities. The next step is to use these properties in the ductility design of members or frames which includes both energy absorption and moment redistribution.

Simply supported beam – energy absorption

To illustrate the application of this analysis procedure in evaluating ductility in the form of energy absorption in an RC member, let us consider the example of a simply supported beam with a uniformly distributed load, a 5m span and a cross section of 300mm x 200mm reinforced with 2No. 16 mm bars in the tension region. A PI M/θ segmental analysis with double cracks, that is a strong bond mechanism has been assumed, has been used to derive the M/EI relationship in Fig. 27 for this section.

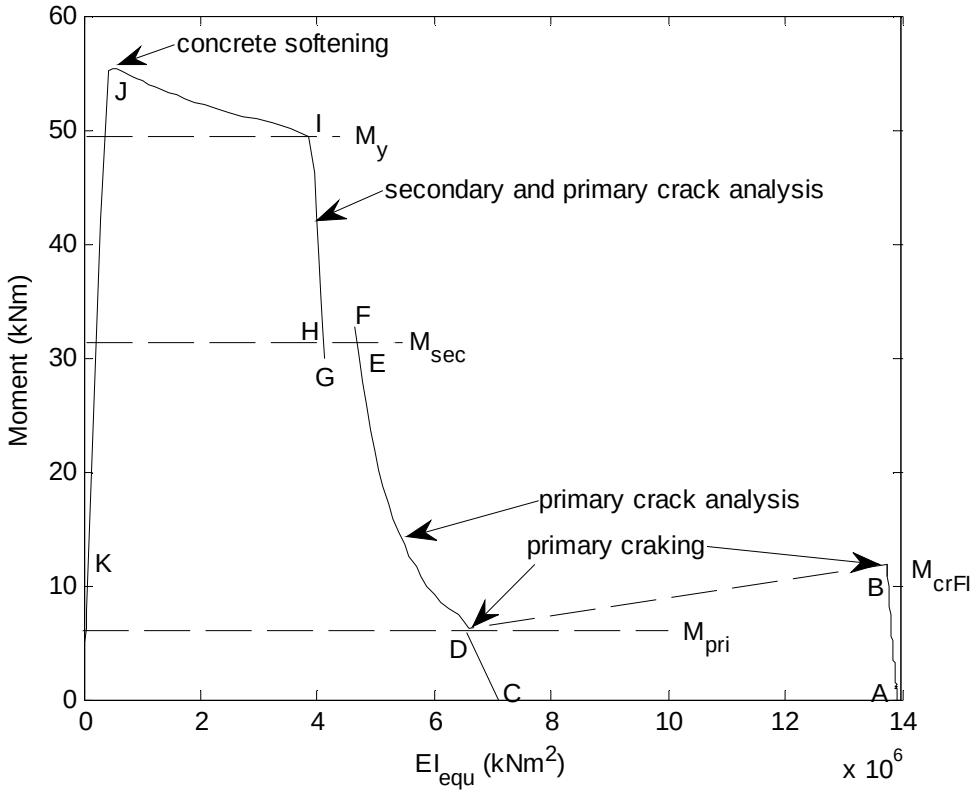

Fig. 27: Variation in $(EI)_{equ}$ from a PI M/θ analysis

Line A-B in Fig. 27 is the flexural rigidity of the uncracked section. $M_{cr\text{-}FI}$ at B is the moment to cause the initial crack from a FI M/χ analysis or the FI M/θ analysis in Fig. 20. M_{pri} at D is the moment to cause a primary crack from the PI M/θ analysis in Fig. 22 using the tension-

stiffening component in Fig. 23. Subsequent primary cracking after the initial crack has formed depends on the lesser of M_{pri} and $M_{cr\text{-}FI}$. The variation C-D-E-F is from a PI M/θ analysis in which L_{def} in Fig. 24 is half the primary crack spacing and the tension stiffening component is from Fig. 25. The same analysis gives the moment at which secondary cracks form that is M_{sec} at Point E. The variation G-H-I-J is from the same analysis as that for C-D-E-F except that L_{def} in Fig. 24 is now a quarter the primary crack spacing. The steel reinforcement yields at I and the concrete starts to soften at J. In this analysis, confinement of the wedge is ignored which leads to a rapid reduction in moment along J-K.

For a specific applied load and consequently distribution of moment, can be derived, using the sectional properties in Fig. 27, the variation in EI along the member for specific applied loads as illustrated in Fig. 28(a). Prior to cracking, Line A, the flexural rigidity of the uncracked section EI_{uncr} applies throughout. Line B is where primary cracks have formed at the centre or mid-span but remains uncracked on either side. Line C is where there are primary and secondary cracks at the centre, with primary cracking on either side and the uncracked region is very small. In Line D, softening at the centre further reduces EI. It can be seen in Fig. 28 how the centre of the beam softens, that is sectional softening when EI reduces, from the very early stages of loading which assists in the ability to absorb energy. The variation in EI in Fig. 28(a) can be used to derive the deflections in Fig. 28(b).

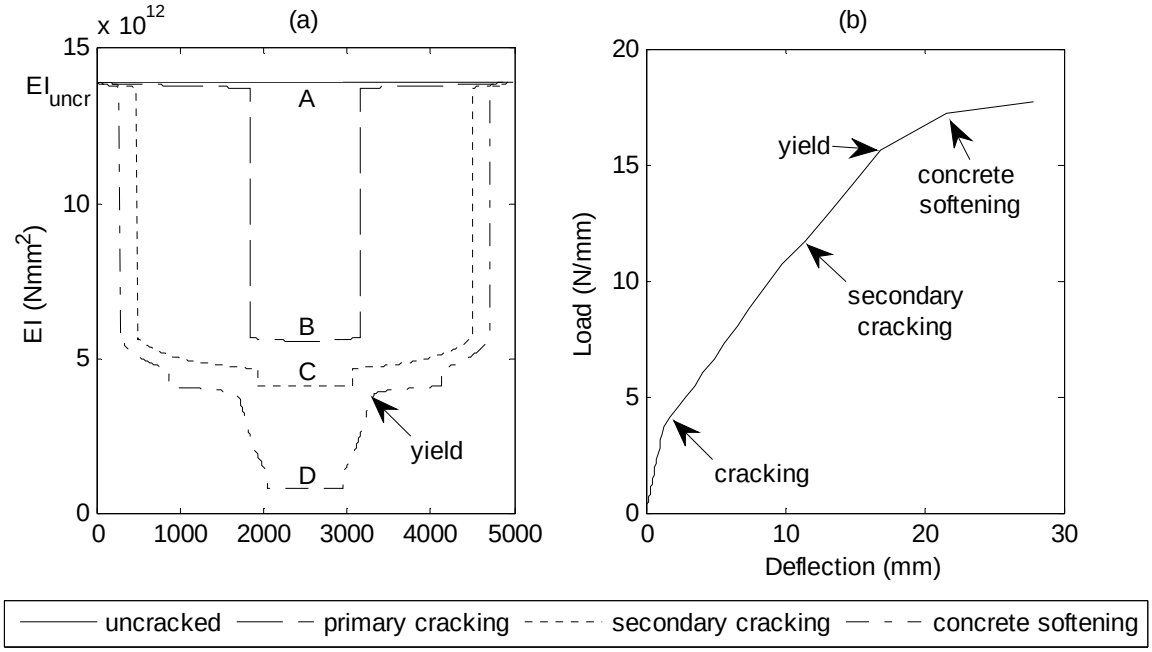

Fig. 28: Energy absorption in a simply supported beam

Continuous beam – energy absorption and moment redistribution

The simply supported beam in the previous example has now been built in at its ends. The variation in EI is shown in Fig. 29(a) for increasing loads from A to C. The results from Fig.

29(a) have been used to plot the deflection in Fig. 29(b). It can be seen in both figures in Fig. 29 that softening occurs at an early stage and in particular in Fig. 29(a) where sectional softening is concentrated in relatively small areas which is conducive to moment redistribution as this requires concentrations of rotation. Furthermore, this concentration of softening occurs at low loads which explains why moment redistribution occurs at very early stages of loading as in Figs. 3 and 4.

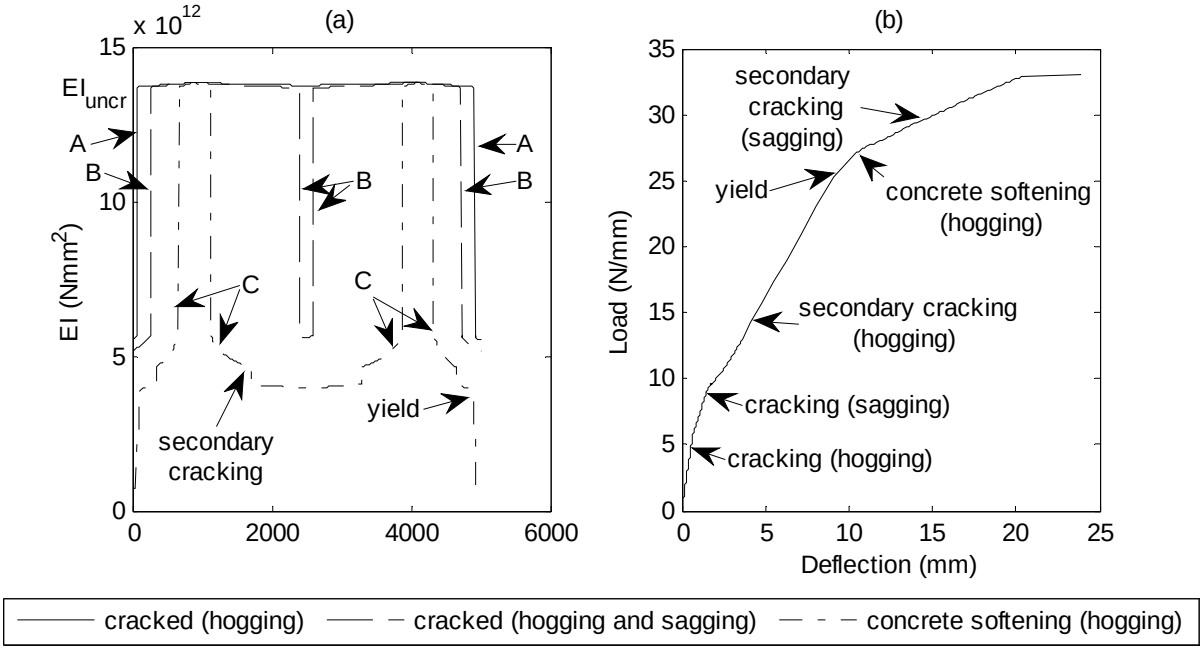

Fig. 29: Energy absorption in a built in beam

The ability of a statically indeterminate member to redistribute moment has been defined mathematically through structural mechanics [40-42]. The percentage moment redistribution at all stages of loading is a function of the concentration of rotation ($\square_{conc}$) and moment (M) that is at all stages of loading as well as other properties of the member such as span, load distribution and serviceability flexural rigidities.

As can be seen in Fig. 30, the PI M/θ segmental analysis gives the moment M and rotation θ in a segment at all stages of loading. The rotation when there are secondary cracks appear to be less than when there are primary cracks alone this is because the rotation when there are secondary cracks is calculated for a segment that is half the length as that for the primary cracks. The information in Fig. 30 can be used to quantify the concentration of rotation θ_{conc} required for a moment redistribution analysis [40-42]. Hence these analyses can be used to quantify moment redistribution without the need for empirical approach such as the neutral axis depth factor currently used in practice.

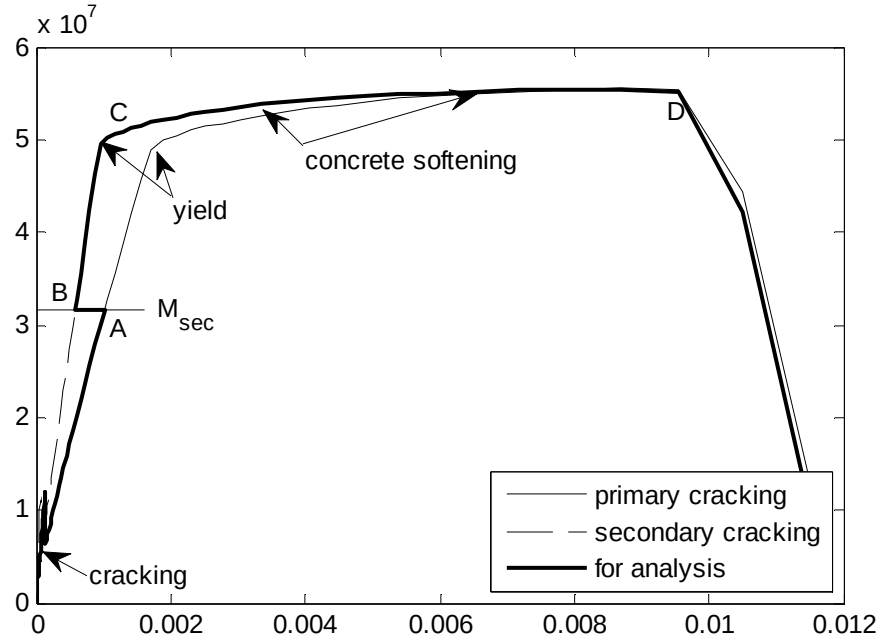

Fig. 30: M/θ of a segment

General application to members and frames

It has been shown how ductility can be quantified through PI M/θ segmental analyses. Furthermore that there are two segmental analyses that have to be considered. The single crack segmental analysis which allows for debonding along a member which has been referred to as the *weak bond mechanism* approach as the moment and rotation are limited by debonding. Furthermore, there is the double crack segmental analysis in which the behaviour is not limited by debonding and as such has been referred to as the *strong bond mechanism.*

The question is how do we use these two approaches in the analysis of a member or a frame. It is suggested that the *weak bond mechanism* approach be used to determine whether debonding along a member will occur. If this *weak bond analysis* shows that debonding does not occur, that is debonding along the member does not precede concrete crushing or reinforcement fracture, then *the strong bond mechanism* approach can be used throughout as in the examples above. If the *weak bond mechanism* analysis shows that debonding along the member will precede concrete crushing or reinforcement fracture then the sectional properties from this analysis should be used in the regions of the beam where the moments are at a maximum to limit the force in the reinforcement but at the same time allowing for rotation. In the remainder of the beam the sectional properties from the *strong bond mechanism* analysis should be used.

CONCLUSIONS

It has been shown how partial-interaction, that is slip between the reinforcement and the concrete, affects the ductility of reinforced concrete members to such an extent that it may be considered vital in simulating and quantifying ductility. It has also been shown how ductility occurs at virtually all load stages and as such affects energy absorption and moment redistribution at all load stages. A partial-interaction moment-rotation approach has been described that can quantify ductility in terms of flexural rigidity at all load stages so the results can be used in standard full-interaction moment-curvature approaches. The partial-interaction moment-rotation approach is generic in that it can be applied to any type of reinforcement with any bond-slip characteristic and to any type of concrete. Hence it is suitable for quantifying the ductility of new types of reinforced concrete members such as those with FRP reinforcement and those with polymer fibre concrete.

ACKNOWLEDGEMENTS

The financial support of the Australian research Council ARC Linkage Project LP 0883451 "Blast resistance of flexural high performance concrete members' and ARC Discovery project DP0985828 'A unified reinforced concrete model for flexure and shear' are gratefully acknowledged.

REFERENCES

[1] Mattock AH. Rotational Capacity of Hinging Regions in Reinforced Concrete Beams, Proceedings of the International Symposium on Flexural Mechanics of Reinforced Concrete, Miami, Florida, ACI SP-12, 1964 pp. 143-181.

[2] Panagiotakos TB and Fardis MN. (2001) Deformations of reinforced concrete members at yielding and ultimate. ACI Struct J. 2001; 98(2):135–48.

[3] Bachmann H. Influence of shear and bond on rotational capacity of reinforced concrete beams. Publications, IABSE, Zurich, 1970: 30(Part II): 11-28.

[4] Oehlers DJ, Ju G, Liu I and Seracino R. Moment redistribution in continuous plated RC flexural members. Part 1: neutral axis depth approach and tests. Engineering Structures 2004; 26, pp2197-2207.

[5] Liu I.S.T. Intermediate crack debonding of plated reinforced concrete beams. PhD thesis, Dept. of Civil and Environmental Engineering, The University of Adelaide 2005.

[6] Seracino R, Raizal Saifulnaz MR, and Oehlers DJ. Generic debonding resistance of EB and NSM plate-to-concrete joints". ASCE Composites for Construction 2007; 11 (1), Jan-Feb, 62-70.

[7] Liu IST, Oehlers DJ and Seracino R. Tests on the ductility of reinforced concrete beams retrofitted with FRP and steel near surface mounted plates. ASCE Journal of Composites for Construction 2006; March/April, Vol.10, No.2, pp106-114.

[8] Haskett M, Oehlers DJ, Mohamed Ali MS, and Wu C. Rigid body moment-rotation mechanism for reinforced concrete beam hinges. Engineering Structures 2009; 31 1032-1041.

[9] Mohamed Ali MS, Oehlers DJ, and Griffith, M.C. The residual strength of confined concrete. Advances in Structural Engineering 2010; Vol. 13, No. 4, pp603-618.

[10] Lucas W, Oehlers DJ and Mohamed Ali MS. Formulation of a shear resistance mechanism for inclined cracks in RC beams. ASCE Journal of Structural Engineering 2011; Vol. 137, Issue 12, Dec, pp1480-1488.

[11] Oehlers DJ, Liu IST and Seracino R. The gradual formation of hinges throughout reinforced concrete beams. Mechanics Based Design of Structures and Machines 2005; 33, pp375-400.

[12] Liu IST, Oehlers DJ, and Seracino R. Study of intermediate crack debonding in adhesively plated beams. ASCE Composites for Construction 2007; Vol.11, No.2, April 1, pp 175-183.

[13] Mohamed Ali MS, Oehlers DJ and Griffith MC Simulation of plastic hinges in FRP plated RC beams. ASCE Composites for Construction 2008; Vol.12, Issue 6, Nov-Dec, pp 617-625.

[14] Wu HQ and Gilbert RI. An experimental study of tension stiffening in reinforced concrete members under short-term and long-term loads. UNICIV Report No. R-449 The University of New South Wales.

[15] Fields K, Bischoff PH. Tension Stiffening and Cracking of High-Strength Reinforced Concrete Tension Members. ACI Structural Journal 2004; 101(4):447-456.

[16] Oehlers DJ, Haskett M, Wu C, and Seracino R. Embedding NSM FRP plates or improved IC debonding resistance", ASCE Journal of Composites for Construction 2008; November/December, Vol 12, No. 6, pp.635-642.

[17] Haskett M, Oehlers DJ, Mohamed Ali MS. Local and global bond characteristics of steel reinforcing bars. Engineering Structures 2008; 30(2):376-383.

[18] Yuan H, Teng JG, Seracino R, Wu ZS, Yao J. Full-range behavior of FRP-to-concrete bonded joints. Engineering Structures 2004; 26 (5):543-691.

[19] Seracino R., Jones NM, MSM, Ali. Page MW and Oehlers DJ. Bond strength of near-surface mounted FRP-to-concrete joints ASCE Composites for Construction 2007; July/August pp401-409

[20] Haskett M, Oehlers DJ, Mohamed Ali, MS, and Sharma SK. Evaluating the shear-friction resistance across sliding planes in concrete. Engineering Structures 2011; 33, pp 1357-1364.

[21] Haskett M, Oehlers DJ, Mohamed Ali MS, and Sharma SK. The shear friction aggregate interlock resistance across sliding planes in concrete. Magazine of Concrete Research 2010, Vol. 62, Issue 12, December, pp 907-924.

[22] Visintin P, Oehlers DJ, Wu C, and Haskett M. A mechanics solution for hinges in RC beams with multiple cracks. Engineering Structures 2012; Vol. 36, pp 61-69.

[23] Lucas W, Oehlers DJ, Mohamed Ali MS and Griffith MC, The FRP reinforced concrete shear-friction mechanism. Accepted special edition Advances in Structural Engineering 2012.

[24] Oehlers DJ, Mohamed Ali MS, Haskett M, Lucas W, Muhamad R, and Visintin P, FRP reinforced concrete beams – a unified approach based on IC theory". ASCE Composites for Construction 2012; May/June, Vol. 15, No. 3, pp293-303.

[25] Visintin P, Oehlers DJ, Haskett M, and Wu C. A moment-rotation approach for analysing the behaviour of RC columns. Submitted Computers and Structures 4/1/12.

[26] Oehlers, D.J. Teaching the fundamental principles in reinforced concrete design. Australian Journal of Structural Engineering 2007; Vol. 7, No.3, pp 99-108.

[27] Visintin P, Oehlers DJ, Haskett M. Partial-interaction time dependent behaviour of reinforced concrete beams Submitted to Magazine of Concrete Research 2012.

[28] Gupta AK, Maestrini SR. Tension stiffening model for reinforced concrete bars. Journal of Structural Engineering 1990; 116 (3): 769-790.

[29] Wu Z, Yoshikawa H, Tanabe T (1991). Tension stiffness model for cracked reinforced concrete. Journal of Structural Engineering 1991; 117(3):715-732

[30] Choi CK, Cheung SH. (1996) Tension stiffening model for planar reinforced concrete members" Computers & Structures 1996; 59 (1):179-190.

[31] Marti P, Alvarez M, Kaufmann W and Sigrist V. Tension chord model for structural concrete. Structural Engineering International 1998; 8(4): 287-298.

[32] Warner RF, Foster SJ, Kilpatrick AE. Reinforced Concrete Basics: Analysis and Design of Reinforced Concrete Structures. Pearson Education, Australia 2007.

[33] Haskett M, Oehlers DJ, Mohamed Ali and Wu C. Yield penetration hinge rotation in reinforced concrete beams. ASCE Structural Journal 2009*;* 135(2):130-138.

[34] Mohamed Ali MS, Oehlers DJ, Griffith MC, Seracino R. Interfacial stress transfer of near surface mounted FRP-to-concrete joints. Engineering Structure 2008; 30(7):1861-1868.

[35] Mohamed Ali MS, Oehlers DJ, Griffith MC. Shear transfer across cracks in FRP strengthened RC structures ASCE Journal of Composites in Construction 2008; 12(4):416-424.

[36] Stramandinoli RSB and La Rovere HL. An efficient tension-stiffening model for nonlinear analysis of reinforced concrete members. Engineering Structures 2008; 30:2069-2080.

[36] Yankelevsky DZ, Jabareen M, and Abutbul AD One-dimensional analysis of tension stiffening in reinforced concrete with discrete cracks. Engineering Structures 2008; 30:206-217.

[37] Muhamad R, Mohamed Ali MS, Oehlers DJ and Sheikh AH. Load-slip relationship of tension reinforcement in reinforced concrete members. Engineering Structures 2011; 33, pp1098-1106.

[38] Muhamad R, Mohamed Ali MS, Oehlers DJ, and Griffith MC. The tension stiffening mechanism in reinforced concrete prisms. Accepted International Journal of Advances in Structural Engineering, 10/2/12.

[39] Mohamed Ali MS, Oehlers DJ, Haskett M and Griffith MC. The discrete rotation in reinforced concrete beams". Submitted ASCE Journal of Engineering Mechanics 2012.

[40] Oehlers DJ, Haskett M, Mohamed Ali, MS, and Griffith MC. Moment redistribution in reinforced concrete beams", Proceedings of the Institution of Civil Engineers: Structures and Buildings, 2010; 163(3): p 165-176

[41] Haskett M, Oehlers DJ, Mohamed Ali MS, and Wu C. Analysis of moment redistribution in FRP plated RC beams. ASCE Composites in Construction 2010; 14(4): pp424-433, July/August.

[42] Haskett M, Oehlers DJ, and Mohamed Ali MS, Design for moment redistribution in RC beams retrofitted with steel plates. Advances in Structural Engineering 2010; 13(2): pp 379-391.

Chapter 4 – Concluding Remarks

In this body of work a new segmental M/θ analysis technique has been developed for both instantaneous and long term loading. Unlike the traditionally applied M/χ approaches which are typically based on the assumptions of plane sections remain plane at all locations and the corollary of a linear strain profile, the M/θ does not assume a linear strain profile. Using the well-established mechanics of partial interaction and shear friction theories, the M/θ approach simulates what is seen in practice, that is, the formation and gradual widening of cracks as the reinforcement slips relative to the concrete which encases it and the formation and failure of concrete softening wedges. Hence using partial-interaction and shear friction theories, the M/θ approach obviates the need for both empirically derived effective flexural rigidities and hinge lengths and has lead to the development of a new equivalent flexural rigidity which accounts for both concrete cracking and concrete softening and can be applied to both instantaneous and long term loading.

Being mechanics based, the M/θ approach can, in theory, be applied to any type of member, that is any cross section, with any concrete properties, and any reinforcement type with any bond characteristic. The M/θ approach has been applied to a wide range of member behaviour including: the instantaneous deflection of beams reinforced with both ductile steel and brittle fiber reinforced polymer bars; the cyclic behaviour of beams with steel reinforcing; the instantaneous deflection of laterally and eccentrically loaded columns, including those in which second order effects are considerable; and the long term deflection of simply supported beams.

Through these broad applications, it has been shown that the M/θ approach represents a widely applicable mechanics based solution to reinforced concrete analysis, capable of accurately predicting both instantaneous and long term deflections from serviceability through to peak loading and collapse, where the only empirically derived requirements are material properties. Hence, the moment rotation approach can be considered an extension of traditional analysis techniques in that it removes the need to empirically define effective flexural rigidities and hinge lengths to determine member behaviour.

Having developed a broad base for the application of the M/θ approach much research is to follow. Importantly the next step in this research is the inclusion of confinement using the approach outlined in Chapter 1; this is a particularly important consideration for the analysis of columns where the close stirrup spacings may mean confinement is high. It is also possible that this research into confinement could provide a new mechanics based approach to predicting the behaviour of sections confined with FRP wraps. Following on from the research on the instantaneous beams and column behaviour a further extension of the approach to allow for frame analysis is to follow including the adaptation of the M/θ approach to a finite element analysis framework.